



Numerical Simulation of Bubble Dynamics in Response to Acoustic Disturbances

THESIS

submitted in partial fulfillment of the requirements
for the degree of Doctor of Philosophy in Mechanical Engineering
of the Department of Mechanical and Industrial Engineering
University of Thessaly

By
KONSTANTINOS A. TSIGLIFIS
Dipl. Mechanical Engineer
University of Thessaly
Born on 23th Aug 1978
in Athens, Greece

Advisory Committee:
Assist. Prof. N. Pelekasis, supervisor
Prof. N. Vlachos
Prof. V. Bontozoglou

Volos, June 2007

UNIVERSITY OF THESSALY



**ΠΑΝΕΠΙΣΤΗΜΙΟ ΘΕΣΣΑΛΙΑΣ
ΒΙΒΛΙΟΘΗΚΗ & ΚΕΝΤΡΟ ΠΛΗΡΟΦΟΡΗΣΗΣ
ΕΙΔΙΚΗ ΣΥΛΛΟΓΗ «ΓΚΡΙΖΑ ΒΙΒΛΙΟΓΡΑΦΙΑ»**

Αριθ. Εισ.: 5486/1
Ημερ. Εισ.: 07-10-2007
Δωρεά: Συγγραφέα
Ταξιθετικός Κωδικός: Δ
620.106
ΤΣΙ

DEPARTMENT OF MECHANICAL AND INDUSTRIAL ENGINEERING

Numerical Simulation of Bubble Dynamics in Response to Acoustic Disturbances

By
KONSTANTINOS A. TSIGLIFIS

Approved by:

Assistant Professor Nikos Pelekasis, Mechanical & Industrial Engineering
University of Thessaly

Professor Nikos Vlachos, Mechanical & Industrial Engineering
University of Thessaly

Professor John Ekaterinaris, Mechanical & Aeronautic Engineering
University of Patras

Associate Professor Dimitris Valougeorgis, Mechanical & Industrial Engineering
University of Thessaly

Assistant Professor Spyros Karamanos, Mechanical & Industrial Engineering
University of Thessaly

Professor Anastassios Stamatelos, Mechanical & Industrial Engineering
University of Thessaly

Professor John Tsamopoulos, Chemical Engineering
University of Patras

© Copyright 2007 Konstantinos A. Tsiglifis

The approval of the Thesis by the Department of Mechanical and Industrial Engineering of the Polytechnic School of the University of Thessaly, does not imply acceptance of the author's beliefs (N.5343/32 – 202, 2)

ABSTRACT

The dynamic behavior and the fashion of collapse of a free bubble play a significant role in the phenomenon of single cavitation bubble luminescence (SCBL) and single bubble sono-luminescence (SBSL), in which light is emitted during its breakdown. In SCBL, the bubble is produced by the application of a laser pulse, in the host liquid, with a duration of 10^{-15} sec (femtosecond bubbles) and 10^{-9} sec (nanosecond bubbles). The resulting bubbles have size of the order of 5 and 500 μm , respectively. The femtosecond bubbles display severe elongation with regards to the axis of symmetry, while light is not emitted during their collapse. In contrast, the nanosecond bubbles exhibit almost spherosymmetric shape initially and collapse producing light. A parametric study is conducted on the fashion of collapse of bubbles, of various sizes, for weak or strong elongation and vanishing small or large internal overpressure, considering axisymmetric oscillations with weak viscous effects. Further, an effort is made to reproduce, as close as possible, respective SCBL and SBSL experiments, aiming to investigate the effect of the initial asymmetry on the fashion of collapse and the velocity of the resulting jet during collapse.

Recently, a significant number of applications in diagnostic and therapeutic medicine use the ability of microbubbles, encapsulated by an elastic membrane (contrast agents), to reflect the ultrasound waves. Initially, a model that predicts the backscatter signal of the microbubble as a function of the membrane properties, of the host liquid and the width and the frequency of the acoustic disturbances, is presented. This model predicts with accuracy the effect of the non linear membrane constitutive law on the microbubble response for large acoustic disturbances in comparison to experimental measurements.

The control of cohesion of microbubbles is desirable in several applications, such as in quantitative evaluation of heart blood flow (contrast perfusion imaging). In order to gain understanding regarding its cohesion range, the large-amplitude axisymmetric oscillation and collapse of an encapsulated microbubble is examined. The shear stresses that develop on the membrane due to the bending moments are accounted for, based on the shell stability theory, and are determined by the scalar bending modulus. This is a measure of the shell resistance to bending and is introduced as an additional parameter, due to the anisotropy of the membrane elasticity along the interface and perpendicular to it. With the help of stability analysis, it is feasible to estimate the range of the parameters for shape oscillations of the microbubble, as well as for the buckling of the shell. In combination with the model of the spherosymmetric oscillations, a theoretical tool is developed for the characterisation of a microbubble with regards to its membrane elasticity, bending resistance and viscosity. Phase diagrams are constructed where the regions of stable or unstable oscillation of a microbubble are defined. Finally, axisymmetric simulations of the interaction of the external flow field and the encapsulated microbubble are performed, implementing a hybrid boundary-finite element method, in order to determine the conditions under which a jet is created during the oscillation of the microbubble; a phenomenon which is observed when a microbubble oscillates near the walls of neighbouring tissues.

ACKNOWLEDGEMENTS

First of all, I would like to express my gratitude to my supervising Professor Nikos Pelekasis for his guidance, moral support and the countless hours spent diligently answering my questions. As a teacher, he will go above and beyond what is necessary so as to achieve his objective. His own passion for research has inspired me to follow in his footsteps. For all of these reasons I am greatly indebted to him.

Further, I would like to acknowledge the rest of the members of my supervising committee. I would like to begin by recognizing Professor N. Vlachos for his constructive criticism, as well as his efforts to publicize my work. With regard to Professor V. Bontozoglou, I feel compelled to express my appreciations for helping me to comprehend the physics behind the mathematics and many fruitful discussions on transport phenomena.

Next, I would like to thank the remaining members of my examination committee, for their suggestions on improving my Thesis. A special thanks to Professor Karamanos for the insights I gained through his lesson 'Theory of Elastic Stability', which has proved to be of great help in completing the research for my thesis. An other special thanks is dedicated to Professor Valougeorgis for helping me grasp the deeper mathematical notions of integral equations, which were key in creating accurate mathematical models for my research.

The contribution of Dr. Reinhard Geisler and Dr. Robert Mettin, from the Drittes Physikalisches Institut Göttingen must also be acknowledged as their experiments on Laser induced bubbles provided valuable information which has been key in creating an accurate simulation model.

I must also note the Dr. Sboro, for providing the initial spark to delve into the area of contrast agents, as well as the numerous discussions on them.

I would also like to acknowledge G. Breyannis and N. Holevas for providing impeccable technical support and for teaching me the how to use Linux as well providing valuable feedback on how to improve my program writing.

I would also like to acknowledge my colleague Maria Vlachomhtrou for the endless hours of constructive discussion on the phenomena relevant to the dynamics of fluids which have fueled a tremendous amount of research. In addition, I would like to also to thank her for excellent corroboration on lab matters and for sharing the same anxieties. I also need to mention my colleagues P. Dalla and N. Chiotti for their flawless collaboration and contribution to my research on microbubbles.

In addition I would like to thank the people that have supported me emotionally through out my studies, namely Theoro Mitsogianni and Evangello Karaisko. They have both in their own way supported me, Evangelos with his humour and Theodoros with his strong sense of character and discipline.

Least but not least I would like to acknowledge my family for their support and understanding and foremostly my mother, Kyriaki, who is not with us anymore. This thesis is dedicated to Rena.

TABLE OF CONTENTS

CHAPTER		I. <i>Introduction</i>	1
	I.1	<i>General Background</i>	1
	I.2	<i>Collapse of Laser and Acoustically Induced Bubbles</i>	2
	I.3	<i>Oscillations and Collapse of Encapsulated Microbubbles (Contrast Agents) Subject to Ultrasound</i>	4
	I.4	<i>Structure of the Dissertation</i>	8
CHAPTER	II.	<i>Weak Viscous Oscillations and Break-up of Elongated Bubbles</i>	12
	II.1	<i>Problem Formulation</i>	12
		II.1.1 Irrotational Flow Field	15
		II.1.2 Weak viscous effects ($Oh \ll 1$)	17
		II.1.3 Energy Variation	19
	II.2	<i>Numerical Solution</i>	20
		II.2.1 Finite-Element Implementation	21
		II.2.2 Boundary-Element Implementation	21
		II.2.3 Integration in Time	23
		II.2.4 Validation of the Numerical Scheme	26
	II.3	<i>Results & Discussion</i>	30
	II.4	<i>Conclusions</i>	43
CHAPTER	III.	<i>Non-Linear Oscillations and Collapse of Elongated Bubbles Subject to Weak Viscous Effects: Effect of Internal Overpressure</i>	44
	III.1	<i>Problem Formulation and Solution Methodology</i>	45
		III.1.1 Governing Equations	45
		III.1.2 Simulations Protocol	46
		III.1.3 Numerical Methodology	47
	III.2	<i>Parametric Study</i>	48
		III.2.1 Micron sized bubbles, $P_{st} \sim 4$, $Oh^{-1} \sim 20$	48
		III.2.2 Millimeter sized bubbles, $P_{st} \sim 300$, $Oh^{-1} \sim 180$	60
	III.3	<i>Simulations of Experiments with Laser Bubbles</i>	65
		III.3.1 Simulations of Femto-Second Laser Bubbles	66
		III.3.2 Simulations of Nano-Second Laser Bubbles	69
	III.4	<i>Conclusions</i>	78

CHAPTER	IV.	<i>Numerical Simulations of the Collapse of Acoustically Driven Bubbles</i>	82
	IV.1	<i>Simulation of Single-Bubble Sonoluminescence (SBSL)</i>	82
	IV.2	<i>Conclusions</i>	90
CHAPTER	V.	<i>Non-Linear Radial Oscillations of Encapsulated Microbubbles Subject to Ultrasound: The Effect of Membrane Constitutive law</i>	91
	V.1	<i>Problem Formulation</i>	92
		V.1.1 Governing equations of the external liquid	94
		V.1.2 Modeling of the Mechanical Behavior of the Membrane-Constitutive Laws	95
		V.1.2.1 Kelvin-Voigt Model	96
		V.1.2.2 Strain Hardening and Strain Softening Materials	97
		V.1.3 Linear Theory	102
	V.2	<i>Numerical Implementation</i>	104
		V.2.1 Validation of the Numerical Scheme	104
	V.3	<i>Results and Discussion</i>	107
	V.4	<i>Conclusions</i>	126
CHAPTER	VI.	<i>Axisymmetric Oscillations and Collapse of an Encapsulated Microbubble Subject to Acoustic Disturbances</i>	130
	VI.1	<i>Problem Formulation</i>	131
		VI.1.1 The Lagrangian Representation of the Microbubble Interface	132
		VI.1.2 Interfacial Force Balance: Coupling of Hydrodynamic and Elastic forces	133
		VI.1.3 Interfacial Tensions and Bending Moments	136
		VI.1.4 Constitutive Equations for Elastic Tensions	137
		VI.1.5 Constitutive Equation for Bending Moments	139
		VI.1.6 Energy Variation	140
	VI.2	<i>Numerical Solution</i>	140
	VI.3	<i>Stability to Nonspherical Disturbances</i>	142
	VI.4	<i>Stability of Periodic Solutions</i>	147
		VI.4.1 Periodic Solutions of Autonomous Systems	147
		VI.4.2 The Monodromy Matrix	148
		VI.4.3 Discretization of the Equations: Derivation of the Residual Vector and the Jacobian Matrix	150

VI.4.4	Calculating the Monodromy Matrix	151
VI.4.5	Mechanisms of Losing Stability	151
VI.5	<i>Results and Discussion</i>	152
VI.5.1	Static Buckling Instability: Comparison with shell Theory	152
VI.5.1.1	Stability Analysis	152
VI.5.1.2	Numerical Simulations	155
VI.5.2	Dynamic Buckling and Parametric Instability: Comparison with Experiments and the Determination of the Scalar Bending Modulus $k_{B \text{ dim}}$	157
VI.5.2.1	Dynamic Buckling Instability – The Case of MP1950 Microbubble	159
VI.5.2.2	Parametric Instability	167
VI.5.3	Phase diagram for an encapsulated microbubble and the Onset of the Jetting Phenomenon	170
VI.6	<i>Conclusions</i>	177
	<i>Appendix</i>	179
	<i>References</i>	182

LIST OF FIGURES

Figure II.1: Initial shape of the bubble for the symmetric (——) and the assymmetric (-----) case.	13
Figure II.2: Time evolution of the coefficients of Legendre modes P_0 and P_2 for the decomposition of the position of the interface f ; $S=0.8$, $P_{St}=4.1$, $Oh \rightarrow 0$, $\varepsilon_B=0$, with 100 elements in the region $0 \leq \theta \leq \pi$.	27
Figure II.3: Time evolution of the coefficients of Legendre modes P_0 and P_2 for the decomposition of the position of the interface f ; $S=1.0$, $P_{St}=4.1$, $\varepsilon=0.5$, $\omega_f = \omega_2 = 3.46$, $Oh^{-1}=20.5$, with 100 elements in the region $0 \leq \theta \leq \pi$.	28
Figure II.4: Time evolution of the shape of the bubble (a) in the beginning of the motion, (b) during jet formation and (c) during collapse; $S=0.6$, $P_{St}=4.1$, $Oh^{-1}=1000$, with 75 and 100 elements in the region $0 \leq \theta \leq \pi/2$.	29
Figure II.5: Comparison between time variation of the total kinetic and potential energy and dissipation; $S=0.6$, $P_{St}=4.1$, $Oh^{-1}=1000$, with 100 elements in the region $0 \leq \theta \leq \pi/2$.	30
Figure II.6: Bubble shapes for the inviscid case with $S=0.8$, $\varepsilon_B=0$ and 50 elements in the region $0 \leq \theta \leq \pi/2$.	31
Figure II.7: Bubble shapes for the case with $S=0.8$, $\varepsilon_B=0$, $Oh^{-1}=500$ and 50 elements in the region $0 \leq \theta \leq \pi/2$.	31
Figure II.8: Time evolution of the coefficients of Legendre modes: (a) P_0 , $Oh^{-1}=1000$, (b) P_0 , $Oh^{-1}=500$, (c) P_2 , $Oh^{-1}=1000$ and (d) P_2 , $Oh^{-1}=500$, for the case with $S=0.8$ $\varepsilon_B=0$ and 50 elements in the region $0 \leq \theta \leq \pi/2$.	33
Figure II.9: Time evolution of the shape of the bubble (a) in the beginning of the motion, (b) during jet formation and (c) during collapse; $S=0.6$, $P_{St}=4.1$, infinite Oh^{-1} , with 100 elements in the region $0 \leq \theta \leq \pi/2$.	34
Figure II.10: Time evolution of the distance D , raised to the $3/2$ power, between the dimples that are formed on countercurrent jets when $\varepsilon_B = 0$ and (a) $S=0.6$, Oh^{-1} infinite, (b) $S=0.6$, $Oh^{-1}=1000$, (c) $S=0.55$, Oh^{-1} infinite and (d) $S=0.55$, $Oh^{-1}=1000$; 100 and 130 elements were used in the region $0 \leq \theta \leq \pi/2$ for the cases with $S=0.6$ and 0.55 , respectively.	35
Figure II.11: Close-up on the solution vector in the vicinity of the dimple shortly before collapse when $S=0.62$, $\varepsilon_B=0$, $Oh^{-1} \rightarrow \infty$; (a) shape of the interface with 100 elements in the region $0 \leq \theta \leq \pi/2$ and (b) shape of the interface, (c) normal velocity, (d) tangential velocity and (e) liquid pressure with 150 elements in the region $0 \leq \theta \leq \pi/2$.	37
Figure II.12: Bubble shapes for the case with $S=0.6$, $\varepsilon_B=0$, $Oh^{-1}=400$ and 100 elements in the region $0 \leq \theta \leq \pi/2$.	38
Figure II.13: Time evolution of the shape of the bubble (a) in the beginning of the motion, (b) during jet formation and (c) during collapse; $S=0.55$, $P_{St}=4.1$, infinite Oh^{-1} , with 130 elements in the region $0 \leq \theta \leq \pi/2$.	39
Figure II.14: Time evolution of the shape of the bubble (a) in the beginning of the motion, (b) during jet formation and (c) during collapse; $S=0.55$, $P_{St}=4.1$, $Oh^{-1}=1000$, with 130 elements in the region $0 \leq \theta \leq \pi/2$.	40
Figure II.15: Comparison of jet thickness and bubble size with (a) increasing initial elongation, $S=0.6$ and 0.55 , $Oh^{-1}=1000$ and (b) increasing viscous effects, Oh^{-1} =infinite and 600, $S=0.6$.	40

- Figure II.16:** Time evolution of the shape of the bubble (a) in the beginning of the motion, (b) during jet formation and (c) during collapse; $S=0.6$, $P_{St}=4.1$, infinite Oh^{-1} , $\varepsilon_B=0.05$, with 100 elements in the region $0 \leq \theta \leq \pi/2$. 41
- Figure II.17:** Time evolution of the shape of an asymmetric bubble (a) in the beginning of the motion, (b) during jet formation and (c) during collapse; $P_{St}=4.1$, $Oh^{-1}=800$, $k=1.2$, $\ell = 5.55$, $\varepsilon_B=0$, with 150 elements in the region $0 \leq \theta \leq \pi$. 43
- Figure III.1:** Time evolution of (a) bubble shapes, (b) numerically obtained shape mode decomposition and (c) evolution of bubble radius and shape mode decomposition based on stability analysis; $S=0.99$, $P_{St}=4.1$, $\varepsilon_B=2$, $Oh^{-1}=20$, with 100 elements in the region $0 \leq \theta \leq \pi/2$. 49
- Figure III.2:** Time evolution of (a) bubble shapes in the beginning of the motion, (b) bubble shapes during collapse, (c) numerically obtained shape mode decomposition and (d) evolution of bubble radius and shape mode decomposition based on stability analysis; $S=0.99$, $P_{St}=4.1$, $\varepsilon_B=2$, $Oh^{-1}=40$, with 150 elements in the region $0 \leq \theta \leq \pi/2$. 50
- Figure III.3:** Time evolution of (a) bubble shapes during collapse, (b) numerically obtained shape mode decomposition and (c) evolution of bubble radius and shape mode decomposition based on stability analysis; $S=0.99$, $P_{St}=4.1$, $\varepsilon_B=2$, $Oh^{-1}=200$, with 150 elements in the region $0 \leq \theta \leq \pi/2$. 52
- Figure III.4:** Time evolution of the shape of the bubble (a) in the beginning of the motion, (b) during jet formation and (c) during collapse; $S=0.7$, $P_{St}=4.1$, $\varepsilon_B=2$, $Oh^{-1}=20$, with 200 elements in the region $0 \leq \theta \leq \pi/2$. 53
- Figure III.5:** Time evolution of the numerically obtained shape mode decomposition when $Oh^{-1}=20$, $S=0.7$, $P_{St}=4.1$, $\varepsilon_B=2$. 54
- Figure III.6:** Time evolution of the dimensional normal velocity of the bubble tip when $Oh^{-1}=20$, $S=0.7$, $P_{St}=4.1$, $\varepsilon_B=2$. 54
- Figure III.7:** Time evolution of the distance D , raised to the $3/2$ power, between the dimples that are formed on counter-propagating jets when $Oh^{-1}=20$; $\varepsilon_B=2$ and $S=0.7$. 55
- Figure III.8:** Time evolution of the shape of the bubble (a) in the beginning of the motion, (b) during jet formation and (c) during collapse; $S=0.45$, $P_{St}=4.1$, $\varepsilon_B=2$, $Oh^{-1}=20$, with 350 elements in the region $0 \leq \theta \leq \pi/2$. (d) mesh refinement with 200 and 350 elements in the region $0 \leq \theta \leq \pi/2$. 56
- Figure III.9:** Time evolution of the shape of the bubble (a) in the beginning of the motion, (b) during jet formation and (c) during collapse; $S=0.45$, $P_{St}=4.1$, $\varepsilon_B=2$, $Oh^{-1}=1000$, with 350 elements in the region $0 \leq \theta \leq \pi/2$. (d) mesh refinement with 200 and 350 elements in the region $0 \leq \theta \leq \pi/2$. 57
- Figure III.10:** Time evolution of the numerically obtained shape mode decomposition when $S=0.45$, $P_{St}=4.1$, $\varepsilon_B=2$ and $Oh^{-1}=20$ and 1000. 58
- Figure III.11:** Time evolution of the distance D , raised to the $3/2$ power, between the dimples that are formed on counter-propagating jets when $Oh^{-1}=1000$; $\varepsilon_B=2$ and $S=0.45$. 58
- Figure III.12:** Time evolution of the dimensional (a) normal velocity of the bubble tip when $Oh^{-1}=20$ and 1000 and (b) relative normal velocity of the pinching parts of the bubble's interface when $Oh^{-1}=1000$; $S=0.45$, $P_{St}=4.1$, $\varepsilon_B=2$. 60
- Figure III.13:** (a) Bubble shape during collapse, and time evolution of (b) numerically obtained shape mode decomposition and (c) evolution of bubble radius and shape mode decomposition based on stability analysis; $S=1$, $P_{St}=295$, $\varepsilon_B=10$, $Oh^{-1}=174$, with 300 elements in the region $0 \leq \theta \leq \pi/2$. 62

Figure III.14: (a) Bubble shape during collapse, and time evolution of (b) numerically obtained shape mode decomposition and (c) evolution of bubble radius and shape mode decomposition based on stability analysis; $S=1$, $P_{St}=295$, $\varepsilon_B=2$, $Oh^{-1}=174$, with 200 elements in the region $0 \leq \theta \leq \pi/2$. 62

Figure III.15: Time evolution of (a) bubble shapes in the beginning of the motion, (b) bubble shapes during collapse and (c) numerically obtained shape mode decomposition; $S=0.99$, $P_{St}=295$, $\varepsilon_B=10$, $Oh^{-1}=174$, with 200 elements in the region $0 \leq \theta \leq \pi/2$. 63

Figure III.16: Time evolution of (a) bubble shapes in the beginning of the motion, (b) bubble shapes during collapse and (c) numerically obtained shape mode decomposition; $S=0.9$, $P_{St}=295$, $\varepsilon_B=10$, $Oh^{-1}=174$, with 200 elements in the region $0 \leq \theta \leq \pi/2$. 64

Figure III.17: Time evolution of the dimensional normal velocity of the bubble tip with increasing initial elongation, $S=0.99, 0.9$ and 0.7 ; $P_{St}=295$, $\varepsilon_B=10$ and $Oh^{-1}=174$. 65

Figure III.18: (a) Frame sequence depicting the collapse of a bubble generated via a femtosecond laser pulse. The host liquid is water at normal pressure and temperature conditions. The width of each frame corresponds to $150\mu\text{m}$. The first frame is captured at $t_i=100$ ns while subsequent frames are captured at a time interval of 400 ns. The laser pulse is applied from the left and imparts $0.8 \mu\text{J}$ to the host liquid. All the frames are reproduced from [12]. (b) Simulations of shape oscillations of femto-second laser bubbles in water; $S=0.34$, $P_{St}=4.1$, $\varepsilon_B=9$, $Oh^{-1}=3$, with the number of elements in the region $0 \leq \theta \leq \pi/2$ ranging between 350 and 600 as the simulation progresses. Dimensionless times correspond to the instants at which the equivalent frames of Figure III.18(a) were recorded. (c) 5×5 and 45×45 enlargements of the last shape shown in III.18(b). 68

Figure III.19: Simulations of shape oscillations of femto-second laser bubbles in water during collapse; $S=0.34$, $P_{St}=4.1$, $\varepsilon_B=9$, $Oh^{-1}=20$, with 500 elements in the region $0 \leq \theta \leq \pi/2$. 68

Figure III.20: Time evolution of the dimensional normal velocity of the bubble tip of a femtosecond laser bubble; $S=0.34$, $P_{St}=4.1$, $\varepsilon_B=9$, $Oh^{-1}=3$. 69

Figure III.21: (a) Frame sequence depicting the collapse of a bubble generated via a nanosecond laser pulse. The host liquid is water at normal pressure and temperature conditions. The width of each frame corresponds to 4mm . The first frame is captured at $t_i=2 \mu\text{s}$ while subsequent frames are captured at a time interval of $30 \mu\text{s}$. The laser pulse is applied from the left and imparts $3.8(4) \text{mJ}$ to the host liquid. All the frames are reproduced from [12]. (b) Simulations of shape oscillations of nano-second laser bubbles in water; $S=1$, $P_{St}=295$, $\varepsilon_B=81$, $Oh^{-1}=174$. (c) Simulations of shape oscillations of nano-second laser bubbles in water; $S=0.98$, $P_{St}=295$, $\varepsilon_B=81$, $Oh^{-1}=174$. In the simulations 200 elements were used in the region $0 \leq \theta \leq \pi/2$. Indicated dimensionless times correspond to the instants at which the equivalent frames of figure III.21(a) were recorded. (d) 3100×3100 enlargement of the last shape shown in III.21(b) and (e) 125×125 and 1125×1125 enlargements of the last shape shown in III.21(c). 71

Figure III.22: Last numerically obtained shape when $S=1, 0.99, 0.98, 0.95$ and 0.9 . 72

Figure III.23: Shape mode decomposition of nano-second laser bubbles in water, on (a) numerically obtained shapes and (b) evolution of bubble radius and shape mode decomposition based on stability analysis; $S=0.98$, $P_{St}=295$, $\varepsilon_B=81$, $Oh^{-1}=174$. 73

Figure III.24: (a) Simulations of shape oscillations of femto-second laser bubbles in water during collapse, (b) time evolution of the dimensional normal velocity of the bubble tip of a femtosecond laser bubble; $S=0.8$, $P_{St}=295$, $\varepsilon_B=81$, $Oh^{-1}=174$. 74

Figure III.25: (a) Interfacial and jet speed during collapse of a nanosecond laser bubble and (b) evolution of the normal velocity distribution along the bubble interface; $S=0.98$, $P_{St}=295$, $\varepsilon_B=81$, $Oh^{-1}=174$.

76

Figure III.26: (a) Frame sequence depicting the collapse of a bubble generated via a nanosecond laser pulse. The host liquid is 5% water solution of acetone at normal pressure and temperature conditions. The width of each frame corresponds to 4mm. The first frame is captured at $t_1=2 \mu s$ while subsequent frames are captured at a time interval of $30 \mu s$. The laser pulse is applied from the left and imparts $3.8(4) mJ$ to the host liquid. All the frames are reproduced from [12]. (b) Simulations of shape oscillations of nano-second laser bubbles in 5% water solution of acetone; $S=0.98$, $P_{St}=302$, $\varepsilon_B=81$, $Oh^{-1}=176$, $P_G(t=t_1)=304$. (c) Simulations of shape oscillations of nano-second laser bubbles in 5% water solution of acetone; $S=0.98$, $P_{St}=302$, $\varepsilon_B=81$, $Oh^{-1}=176$, $P_G(t=t_1)=1404$. In the simulations 200 elements were used in the region $0 \leq \theta \leq \pi/2$. Indicated dimensionless times correspond to the instants at which the equivalent frames of figure III.26(a) were recorded. (d) 123×123 enlargement of the last shape shown in III.26(b) and (e) 7×7 enlargements of the last shape shown in III.26(c).

78

Figure III.27: (a) Blow up on the bubble shape near the equator during collapse and (b) evolution of the pressure distribution on the liquid side along the bubble interface during collapse; $S=0.98$, $P_{St}=295$, $\varepsilon_B=81$, $Oh^{-1}=174$.

81

Figure IV.1: (a) Photographic series of a trapped sonoluminescing bubble in a water-glycerin mixture driven at 21.4 kHz. The top row presents the bubble dynamics at an interframe time of ca. $2.5 \mu s$. The bottom row shows the bubble collapse with five-fold temporal resolution ($500 ns$ interframe time). The scale of image is indicated by the ruler ($100 \mu m$). (b) Radius-time curve from photographic observations. A numerically calculated curve is superimposed on the experimental data point (open circles). The calculation is based on the following parameters: driving frequency, $f_0=21.4 kHz$; ambient pressure, $p_0=1 bar$; driving pressure, $P_{Ac}=1.32 bar$; vapor pressure, $p_v=25 mbar$; equilibrium radius, $R_{Eq}=8 \mu m$; density of the liquid, $\rho=1000 kg m^{-3}$; viscosity, $\eta=0.006 N s m^{-2}$; surface tension, $\sigma=0.07 N m^{-1}$. The gas within the bubble is assumed to obey the adiabatic equation of state of an ideal gas with ratio of the specific heats of 1.33. All figures are reproduced from [13].

84

Figure IV.2: (a) Interfacial shape at collapse of a single-bubble in a water-glycerin mixture. (b) Time variation of the first five even Legendre modes of the bubble shape during the entire simulation and (c) during collapse; $S=0.96$, $P_{St}=5.714$, $\varepsilon=1.32$, $\omega_f=0.364$, $Re=3.9$.

85

Figure IV.3: (a) Interfacial shape during the collapse phase of a single-bubble in a water-glycerin mixture. (b) Time variation of the first five even Legendre modes of the bubble shape during the entire simulation and (c) during collapse; $S=0.96$, $P_{St}=5.714$, $\varepsilon=1.32$, $\omega_f=0.364$, $Re=23.7$.

86

Figure IV.4: (a) Interfacial velocity when $Re=23.7$ and $Re=3.9$ and (b) jet velocity during collapse when $Re=23.7$; $S=0.96$, $P_{St}=5.714$, $\varepsilon=1.32$, $\omega_f=0.364$.

87

Figure IV.5: (a) Interfacial shape at collapse of a single-bubble in water. (b) Time variation of the first five even Legendre modes of the bubble shape during the entire simulation and (c) during collapse; $S=0.96$, $P_{St}=5.714$, $\varepsilon=1.1$, $\omega_f=0.364$, $Re=23.7$.

88

Figure IV.6: (a) Interfacial shape at collapse of a single-bubble in water. (b) Time variation of the first five even Legendre modes of the bubble shape during the entire simulation and (c) during collapse; $S=0.99$, $P_{St}=5.714$, $\varepsilon=1.1$, $\omega_f=0.364$, $Re=23.7$.

89

- Figure V.1:** Schematic diagram of a contrast agent (a) at equilibrium and (b) at the unstressed state and at equilibrium. 94
- Figure V.2:** Isotropic tension: principal tension T/G_s as a function of relative area change. Comparison of the linear Hooke (H) law and the nonlinear Mooney-Rivlin (MR) and Skalak (SK) laws (adapted from Barthes et al.⁵⁰); $\nu_s=1/2$ denotes the 2d surface Poisson ratio. 100
- Figure V.3:** Evolution of the external microbubble radius with time for a sinusoidal pressure disturbance with amplitude $\varepsilon = 0.05$, (a) on-resonance with $\nu_f = 2.8$ MHz and (b) off-resonance with $\nu_f = 5$ MHz, as obtained from linear theory and from simulations with the three different types of membranes; $\mu_s = 0.6$ kgm⁻¹s⁻¹, $G_s = 35$ MPa, $R'_0 = 3$ μ m, $\delta' = 15$ nm, $b=0.5$ and $C=1$. 105
- Figure V.4:** Scattering cross section vs external forcing frequency as obtained from linear theory and from simulations with the three different types of membranes; $\mu_s = 0.6$ kgm⁻¹s⁻¹, $G_s = 35$ MPa, $R'_0 = 3$ μ m, $\delta' = 15$ nm, $b=0.5$ and $C=1$. 106
- Figure V.5:** Total scattering cross section vs external forcing frequency, when $\varepsilon=0.5, 1, 1.5$ and 2 , for (a) a free bubble, (b) a KV, (c) an MR ($b = 0$) and (d) an SK ($C = 1$) membrane; $\mu_s = 0.6$ kgm⁻¹s⁻¹, $G_s = 35$ MPa, $R'_0 = 3$ μ m, $\delta' = 15$ nm. 109
- Figure V.6:** Harmonic components of the scattering cross section vs. forcing frequency for (a) a free bubble, and (b) a KV, (c) an MR ($b = 0$) and (d) an SK ($C = 1$) membrane, when $G_s=35, 70$ and 105 MPa; $\mu_s = 0.6$ kgm⁻¹s⁻¹, $R'_0 = 3$ μ m, $\delta' = 15$ nm, $\varepsilon = 1$. 111
- Figure V.7:** Harmonic components of the scattering cross section vs. forcing frequency for (a) a free bubble, and (b) a KV, (c) an MR ($b = 0$) and (d) an SK ($C = 1$) membrane, when $G_s=35, 70$ and 105 MPa; $\mu_s = 0.6$ kgm⁻¹s⁻¹, $R'_0 = 3$ μ m, $\delta' = 15$ nm, $\varepsilon = 2$. 112
- Figure V.8:** Time evolution of the (a), (b) external microbubble radius and (c), (d) interfacial velocity when $G_s=35$ and 105 MPa, respectively, and $\varepsilon=1$ and 2 , for an MR membrane ($b = 0$) on-resonance, $\nu_f = 2.7$ and 4.4 MHz, respectively; $\mu_s = 0.6$ kgm⁻¹s⁻¹, $R'_0 = 3$ μ m, $\delta' = 15$ nm. 115
- Figure V.9:** Time evolution of the (a), (b) external microbubble radius and (c), (d) interfacial velocity when $G_s=35$ and 105 MPa, respectively, and $\varepsilon=1$ and 2 , for an SK membrane ($C = 1$) on-resonance, $\nu_f = 3.4$ and 5.6 MHz, respectively; $\mu_s = 0.6$ kgm⁻¹s⁻¹, $R'_0 = 3$ μ m, $\delta' = 15$ nm. 116
- Figure V.10:** Harmonic components of the scattering cross section vs. forcing frequency for an MR membrane with $b=0$ and 1 ; $\mu_s = 0.6$ kgm⁻¹s⁻¹, $G_s = 35$ MPa, $R'_0 = 3$ μ m, $\delta' = 15$ nm, $\varepsilon = 2$. 118
- Figure V.11:** Harmonic components of the scattering cross section vs. forcing frequency for an SK membrane with $C=1$ and 5 and nonzero residual stresses at $t=0$, $u'_{Eq} = u'(t' = 0) = -30, 0$ and 30 nm; $\mu_s = 0.6$ kgm⁻¹s⁻¹, $G_s = 35$ MPa, $R'_0 = 3$ μ m, $\delta' = 15$ nm, $\varepsilon = 2$. 118
- Figure V.12:** Effect of membrane viscosity on the harmonic components of the scattering cross section vs. forcing frequency for (a) a KV, (b) an MR ($b = 0$) and (c) an

SK ($C=1$) membrane, with $\mu_s = 0.6$ and $1.6 \text{ kgm}^{-1}\text{s}^{-1}$; $G_s = 35 \text{ MPa}$, $R'_0 = 3 \text{ }\mu\text{m}$, $\delta' = 15 \text{ nm}$, $\varepsilon = 2$. 120

Figure V.13: Effect of the surrounding fluid on the harmonic components of the scattering cross section vs. forcing frequency for (a) a KV, (b) an MR ($b=0$) and (c) an SK ($C=1$) membrane. $\mu_l = 0.001 \text{ kgm}^{-1}\text{s}^{-1}$ and $c = 1500 \text{ m/s}$ for water whereas $\mu_l = 0.004 \text{ kgm}^{-1}\text{s}^{-1}$ and $c = 500 \text{ m/s}$ for blood with a 5×10^{-4} microbubble volume fraction; $\mu_s = 0.6 \text{ kgm}^{-1}\text{s}^{-1}$, $G_s = 35 \text{ MPa}$, $R'_0 = 3 \text{ }\mu\text{m}$, $\delta' = 15 \text{ nm}$, $\varepsilon = 2$. 121

Figure V.14: First harmonic component of the scattering cross section vs. forcing frequency for (a) a KV, (b) an MR ($b=0$) and (c) an SK ($C=1$) membrane; $\mu_s = 0.6 \text{ kgm}^{-1}\text{s}^{-1}$, $G_s = 35 \text{ MPa}$, $R'_0 = 1 \text{ }\mu\text{m}$, $\delta' = 15 \text{ nm}$, $\varepsilon = 0.5$. 122

Figure V.15: First harmonic component of the scattering cross section vs. forcing frequency for (a) a KV, (b) an MR ($b=0$) and (c) an SK ($C=1$) membrane; $\mu_s = 0.6 \text{ kgm}^{-1}\text{s}^{-1}$, $G_s = 35 \text{ MPa}$, $R'_0 = 2 \text{ }\mu\text{m}$, $\delta' = 15 \text{ nm}$, $\varepsilon = 0.5$. 123

Figure V.16: Harmonic components of the scattering cross section vs. forcing frequency for (a) a KV, (b) an MR ($b=0$) and (c) an SK ($C=1$) membrane; $\mu_s = 0.6 \text{ kgm}^{-1}\text{s}^{-1}$, $G_s = 35 \text{ MPa}$, $R'_0 = 4 \text{ }\mu\text{m}$, $\delta' = 15 \text{ nm}$, $\varepsilon = 2$. 124

Figure V.17: Harmonic components of the scattering cross section vs. forcing frequency for (a) a KV, (b) an MR ($b=0$) and (c) an SK ($C=1$) membrane; $\mu_s = 0.6 \text{ kgm}^{-1}\text{s}^{-1}$, $G_s = 35 \text{ MPa}$, $R'_0 = 5 \text{ }\mu\text{m}$, $\delta' = 15 \text{ nm}$, $\varepsilon = 2$. 125

Figure V.18: Comparison between experimental measurements and predictions based on the Church-Hoff, the constant elasticity, the Newtonian and the strain softening model, of the fundamental and subharmonic signals when (a), (b) $\omega_f = 2\pi \cdot 2 \text{ MHz}$ and (b), (d) $\omega_f = 2\pi \cdot 4.4 \text{ MHz}$, for Sonazoid microbubbles. The data from experimental measurements as well as the predictions from the Church-Hoff, the constant elasticity and the Newtonian models are reproduced from Sarkar et al.⁴⁷ 128

Figure VI.1: Geometrical configuration of an encapsulated microbubble in the context of the present study. 131

Figure VI.2: Time evolution of the periodic solution $\vec{y}^*(t)$ whose the initial vector \vec{z}^* is perturbed with \vec{d}_0 . 149

Figure VI.3: Contours of the overpressure $P^{\text{overpressure}}$ that the membrane feels in respect to the appearing mode n considering a) Mooney-Rivlin law ($b=1$) and b) Skalak law ($C=1$); $R_{Eq} = 1.5 \text{ }\mu\text{m}$, $G_s = 133 \text{ MPa}$, $\delta = 15 \text{ nm}$, $\mu_s = 0.3 \text{ Pa}\cdot\text{s}$, $k_{B\text{dim}} = 1.496 \cdot 10^{-16} \text{ Nm}$, $\nu=0.5$. 153

Figure VI.4: Time evolution of the (a) microbubble radius, (b) dimensional overpressure, (c) shape mode decomposition based on dynamic stability analysis for a Mooney-Rivlin membrane, $b=1$, $\varepsilon=0.547$, (d) time evolution of the dimensional overpressure and (e) shape mode decomposition based on dynamic stability analysis for a Mooney-Rivlin membrane, $b=1$, $\varepsilon=0.537$; $R_{Eq} = 1.5 \text{ }\mu\text{m}$, $G_s = 133 \text{ MPa}$, $\delta = 15 \text{ nm}$, 154

$\mu_s = 0.3 \text{ Pa}\cdot\text{s}$, $k_{B\text{dim}} = 1.496 \cdot 10^{-16} \text{ Nm}$, $\nu=0.5$, $\rho_l = 998 \text{ kg/m}^3$, $P'_{st} = 101325 \text{ Pa}$, $\mu_l = 0$, $C_l \rightarrow \infty$, $\gamma=1.4$, type of pressure perturbation in the far field: $P'_\infty = P'_M(1 + \varepsilon)$. 155

Figure VI.5: Eigenvectors that correspond to the first negative eigenvalue, (a) of radius and (b) of angle θ of the particles; $S=1, R_{Eq} = 1.5 \mu m, G_s = 133 MPa, \delta = 15 nm, k_{Bdim} = 1.496 \cdot 10^{-16} Nm, \nu=0.5, P'_{Overpressure} = 53800 Pa$ for a Mooney-Rivlin membrane, $b=1, 200$ elements in the region $0 \leq \theta \leq \pi$.

156

Figure VI.6: Simulation of the oscillations of a contrast agent whose shell obeys the Mooney-Rivlin constitutive law with $b=1$. (a) Microbubble shape during collapse, (b) time evolution of the radial position of the interfacial particle with $\theta=0$, (c) numerically obtained shape mode decomposition during the entire simulation and (d) during collapse; $S=1, R_{Eq} = 1.5 \mu m, G_s = 133 MPa, \delta = 15 nm, \mu_s = 0.3 Pa \cdot s, \nu=0.5, k_{Bdim} = 1.496 \cdot 10^{-16} Nm, \rho_l = 998 \frac{kg}{m^3}, P'_{st} = 101325 Pa, \mu_l = 0, C_l \rightarrow \infty, \varepsilon=0.547, \gamma=1.4$, type of pressure perturbation in the far field: $P'_\infty = P'_{st} (1 + \varepsilon)$

157

Figure VI.7: Optical frame images and evolution of the diameter of the oscillation and fragmentation of a contrast agent microbubble (MP1950). The bubble has an initial diameter of $3 \mu m$, shown in (a). The image in (h) shows the diameter of the bubble as a function of time, and dashed lines indicate the times at which the two-dimensional frame images in (a)-(g) were acquired relative to the (h) image. The time interval between Figs. VI.5(b) and VI.5(f) is $80 ns$ while the shutter duration used in Figs. VI.5(b)-VI.5(f) is $50 ns$. All the frames are reproduced from [70].

159

Figure VI.8: Simulation with weak viscous effects of the oscillations of the contrast agent considering it as a free surface. (a) Last microbubble shape from the simulation, (b) time evolution of the microbubble diameter; $S=1, R_{Eq} = 1.5 \mu m, \rho_l = 998 \frac{kg}{m^3}, \mu_l = 0.001 Pa \cdot s, C_l \rightarrow \infty, \sigma = 0.677 \frac{N}{m}, P'_{st} = 101325 Pa, \gamma=1.07, \varepsilon=12, \nu_f = 2.4 MHz$, type of pressure perturbation in the far field: $P'_\infty = P'_{st} [1 + \varepsilon \cos(2\pi\nu_f t')]$, 100 elements in the region $0 \leq \theta \leq \pi/2$.

160

Figure VI.9: Mode $n=4$ (top) and mode $n=5$ (bottom) vibrations for small microbubbles of $1.4 \mu m$ diameter. The transmit frequency is $19 MHz$. All the frames are reproduced from [112].

162

Figure VI.10: Simulation of the oscillation and collapse of the contrast agent considering it as a shell following Mooney-Rivlin constitutive law $b=1$, (a) Microbubble shape during collapse, (b) time evolution of the microbubble diameter, (c)-(d) numerically obtained shape mode decomposition, (e)-(f) evolution of bubble radius and shape mode decomposition based on stability analysis, (g) comparison between time variation of the kinetic energy, work, membrane elastic energy, surface energy and dissipation due to the membrane viscosity, (h) time evolution of the $P'_{Overpressure}$ that the shell feels; $S=1, R_{Eq} = 1.5 \mu m, G_s = 590 MPa, \delta = 1 nm, \mu_s = 1.32 Pa \cdot s, k_{Bdim} = 3.45 \cdot 10^{-13} Nm, b=0, \nu=0.5, \rho_l = 998 \frac{kg}{m^3}, \mu_l = 0, C_l \rightarrow \infty, P'_{st} = 101325 Pa, \sigma = 0.051 \frac{N}{m}, \gamma=1.07, \varepsilon=12, \nu_f = 2.4 MHz$, type of pressure perturbation in the far field: $P'_\infty = P'_{st} [1 + \varepsilon \cos(2\pi\nu_f t')]$

164

Figure VI.11: Simulation of the oscillation of the contrast agent considering it as a shell. (a) Last microbubble shape from the simulation, (b) time evolution of the

microbubble diameter; $S=1$, $R_{Eq} = 1.5 \mu m$, $G_s = 590 MPa$, $\delta = 1 nm$,
 $\mu_s = 1.32 Pa \cdot s$, $k_{Bdim} = 6.89 \cdot 10^{-13} Nm$, $b=0$, $v=0.5$, $\rho_l = 998 \frac{kg}{m^3}$, $\mu_l = 0$, $C_l \rightarrow \infty$,
 $P'_{st} = 101325 Pa$, $\sigma = 0.051 \frac{N}{m}$, $\gamma=1.07$, $\varepsilon=12$, $\nu_f = 2.4 MHz$, type of pressure
 perturbation in the far field: $P'_\infty = P'_{st} [1 + \varepsilon \cos(2\pi\nu_f t')]$ 165

Figure VI.12: The effect of the forcing frequency on the buckling instability. (a) Last microbubble shape from the simulation, (b) numerically obtained shape mode decomposition, (c) time evolution of the $P'_{Overpressure}$ that the shell feels, (d) evolution of bubble radius and shape mode decomposition based on stability analysis, (e) time evolution of the distribution of transverse shear tension q' ; $S=1$,
 $R_{Eq} = 1.5 \mu m$, $G_s = 590 MPa$, $\delta = 1 nm$, $\mu_s = 1.32 Pa \cdot s$, $k_{Bdim} = 3.45 \cdot 10^{-13} Nm$, $b=0$,
 $v=0.5$, $\rho_l = 998 \frac{kg}{m^3}$, $\mu_l = 0$, $C_l \rightarrow \infty$, $P'_{st} = 101325 Pa$, $\sigma = 0.051 \frac{N}{m}$, $\gamma=1.07$,
 $\varepsilon=33$, $\nu_f = 500 kHz$, type of pressure perturbation in the far field:
 $P'_\infty = P'_{st} [1 + \varepsilon \sin(2\pi\nu_f t')]$ 167

Figure VI.13: Parametric Instability – Subharmonic Resonance during the oscillation of an encapsulated microbubble. (a) Time evolution of the $P'_{Overpressure}$ that the shell feels, (b) evolution of bubble radius and shape mode decomposition based on stability analysis, (c) Last microbubble shape from the simulation, (d) numerically obtained shape mode decomposition; $S=1$, $R_{Eq} = 1.5 \mu m$, $G_s = 174 MPa$, $\delta = 1 nm$,
 $\mu_s = 1.32 Pa \cdot s$, $k_{Bdim} = 1.25 \cdot 10^{-13} Nm$, $b=1$, $v=0.5$, $\rho_l = 998 \frac{kg}{m^3}$, $\mu_l = 0$, $C_l \rightarrow \infty$,
 $P'_{st} = 101325 Pa$, $\sigma = 0.051 \frac{N}{m}$, $\gamma=1.07$, $\varepsilon=12$, $\nu_f = 11.66 MHz$, type of pressure
 perturbation in the far field: $P'_\infty = P'_{st} [1 + \varepsilon \cos(2\pi\nu_f t')]$ 169

Figure VI.14: Parametric Instability – Harmonic Resonance during the oscillation of an encapsulated microbubble. (a) Time evolution of the $P'_{Overpressure}$ that the shell feels, (b) evolution of bubble radius and shape mode decomposition based on stability analysis; $S=1$, $R_{Eq} = 1.5 \mu m$, $G_s = 174 MPa$, $\delta = 1 nm$, $\mu_s = 1.32 Pa \cdot s$, $k_{Bdim} = 1.25 \cdot 10^{-13} Nm$, $b=1$,
 $v=0.5$, $\rho_l = 998 \frac{kg}{m^3}$, $\mu_l = 0$, $C_l \rightarrow \infty$, $P'_{st} = 101325 Pa$, $\sigma = 0.051 \frac{N}{m}$, $\gamma=1.07$,
 $\varepsilon=6.5$, $\nu_f = 5.83 MHz$, type of pressure perturbation in the far field:
 $P'_\infty = P'_{st} [1 + \varepsilon \cos(2\pi\nu_f t')]$ 170

Figure VI.15: Phase diagram for an encapsulated microbubble, MP1950, with scalar bending modulus (a) $k_{Bdim} = 3 \cdot 10^{-14} Nm$ and (b) $k_{Bdim} = 1 \cdot 10^{-13} Nm$; $G_s = 520 MPa$, $\delta = 1 nm$,
 $\mu_s (sPa) \cdot \delta (nm) = 1.34 R_{Eq} (\mu m) - 0.69$, $b=0$, $v=0.5$, $\rho_l = 998 \frac{kg}{m^3}$, $\mu_l = 0.001 Pa \cdot s$,

$C_l = 1540 \text{ m/s}$, $P'_{st} = 101325 \text{ Pa}$, $\sigma = 0.051 \text{ N/m}$, $\gamma = 1.07$, $v_f = 2.4 \text{ MHz}$, type of pressure perturbation in the far field: $P'_\infty = P'_{st} [1 + \varepsilon \cos(2\pi v_f t')]$ 171

Figure VI.16: Ultrasound jet development in an experimental microbubble (Mechanical Index MI=1.2). Each image frame corresponds to a $38 \times 30 \mu\text{m}^2$ area. Interframe time $0.33 \mu\text{s}$ and exposure time is 10 ns . All the frames are reproduced by [116]. 172

Figure VI.17: Simulation of the oscillation and collapse of the contrast agent following Mooney-Rivlin constitutive law with small initial shape perturbation of the second mode, (a) initial microbubble shapes, (b) microbubble shapes during collapse, (c)-(d) numerically obtained shape mode decomposition for the cases $b=1$, $\varepsilon=7$, $P_2=-0.05$ and $b=0$, $\varepsilon=4$, $P_2=-0.1$ respectively, (e)-(f) evolution of bubble radius and shape mode decomposition based on stability analysis for the cases $b=1$, $\varepsilon=7$, $w_2=-0.05$ and $b=0$, $\varepsilon=4$, $w_2=-0.1$, respectively, (g) time evolution of the velocity of the poles for the two cases; $S=1$, $R_{Eq} = 1.5 \mu\text{m}$, $G_s = 590 \text{ MPa}$, $\delta = 1 \text{ nm}$, $\mu_s = 1.32 \text{ Pa}\cdot\text{s}$,

$k_{Bdim} = 1.75 \cdot 10^{-14} \text{ Nm}$, $v=0.5$, $\rho_l = 998 \text{ kg/m}^3$, $\mu_l = 0$, $C_l \rightarrow \infty$, $P'_{st} = 101325 \text{ Pa}$, $\sigma = 0.051 \text{ N/m}$, $\gamma = 1.07$, $v_f = 2.4 \text{ MHz}$, type of pressure perturbation in the far field: $P'_\infty = P'_{st} [1 + \varepsilon \cos(2\pi v_f t')]$ 174

Figure VI.18: Simulation of the oscillation and collapse of the contrast agent following Mooney-Rivlin constitutive law ($b=1$) with small initial shape perturbation of the second mode, $P_2 = -0.05$, (a) microbubble shape during collapse, (b) numerically obtained shape mode decomposition, (c) evolution of bubble radius and shape mode decomposition based on stability analysis; $S=1$, $R_{Eq} = 1.5 \mu\text{m}$, $G_s = 590 \text{ MPa}$, $\delta = 1 \text{ nm}$,

$\mu_s = 1.32 \text{ Pa}\cdot\text{s}$, $k_{Bdim} = 1.75 \cdot 10^{-14} \text{ Nm}$, $v=0.5$, $\rho_l = 998 \text{ kg/m}^3$, $\mu_l = 0$, $C_l \rightarrow \infty$, $P'_{st} = 101325 \text{ Pa}$, $\sigma = 0.051 \text{ N/m}$, $\gamma = 1.07$, $v_f = 2.4 \text{ MHz}$, $\varepsilon=5.5$, type of pressure perturbation in the far field: $P'_\infty = P'_{st} [1 + \varepsilon \cos(2\pi v_f t')]$. 176

Figure VI.19: Simulation of the oscillation of the contrast agent following Mooney-Rivlin constitutive law ($b=1$) with small initial shape perturbation of the second mode, $P_2 = -0.05$, (a) numerically obtained shape mode decomposition, (b) evolution of bubble radius and shape mode decomposition based on stability analysis; $S=1$, $R_{Eq} = 1.5 \mu\text{m}$, $G_s = 590 \text{ MPa}$, $\delta = 1 \text{ nm}$, $\mu_s = 1.32 \text{ Pa}\cdot\text{s}$, $k_{Bdim} = 1.75 \cdot 10^{-14} \text{ Nm}$, $v=0.5$,

$\rho_l = 998 \text{ kg/m}^3$, $\mu_l = 0$, $C_l \rightarrow \infty$, $P'_{st} = 101325 \text{ Pa}$, $\sigma = 0.051 \text{ N/m}$, $\gamma = 1.07$, $v_f = 2.4 \text{ MHz}$, $\varepsilon=5$, type of pressure perturbation in the far field: $P'_\infty = P'_{st} [1 + \varepsilon \cos(2\pi v_f t')]$. 176

LIST OF TABLES

Table I.1: Schematic diagram of the models developed in the context of the thesis.	11
Table III.1 (a): Collapse pattern for micrometer size bubbles depending on the parameter range	79
Table III.1 (b): Collapse pattern for millimeter size bubbles depending on the parameter range	80
Table V.1: Resonance frequency of the first harmonic component as a function of area dilatation modulus and acoustic amplitude, recovered from numerical simulations. The rest of the problem parameters are provided in Figures V.5 –V.7.	113
Table V.2: Comparison of the resonance frequency as obtained via equations (V.32) and (V.34), for different equilibrium radii; $G_s=35$ MPa, $\mu_s = 0.6 \text{ kgm}^{-1}\text{s}^{-1}$ and $\delta' = 15 \text{ nm}$.	126

CHAPTER I

INTRODUCTION

I.1 General background

Bubble oscillations and collapse has been a field of research since the early twentieth century when Lord Rayleigh¹ first studied the spontaneous generation and collapse of bubbles, in an effort to explain the damage of propellers of high speed boats and submarines. He described the process of cavitation in which bubbles are generated as a result of changes in the local pressure field. Such acoustically generated bubbles can oscillate quite violently and subsequently collapse and damage the propeller's surface. This is a spherically symmetric type of collapse that is predicted by the well-known Rayleigh-Plesset equations² and is associated with the emission of sound during its last stages.

Asymmetric bubble collapse was addressed later on^{3,4} in order to assess the destructive effect of jet formation during collapse near a solid boundary. This was facilitated by resorting to the boundary integral formulation that requires discretization of the bubble-liquid interface and the rigid or free boundaries that interact with the bubble, rather than the entire flow domain. This is of course possible in the potential flow regime that is applicable to the case of collapsing bubbles. The destructive effect of the shock wave that is generated by the spherical implosion of a collapsing bubble and of the jet that is formed during asymmetric collapse, have been captured and verified experimentally^{5,6} with high-speed photography and they are both known to contribute to plastic deformation of nearby material. Recent advances in computational and cinematographic observation techniques have afforded capturing the details of collapse and in particular the formation of toroidal^{7,8} bubbles at jet impact in the presence of a solid boundary.

Nowadays, bubble oscillation and collapse is the key factor to a number of applications in many fields of technology. Inertia cavitation created by the rapid oscillation and collapse of a free bubble, may occur in devices such as propellers and pumps and causes a great deal of noise, component damage, vibrations, and loss of efficiency. Although cavitation is undesirable in many circumstances, this is not always the case. For example, supercavitation is under investigation as a means to envelop underwater vehicles by a cloud of cavitating bubbles, thereby reducing or eliminating contact with water. Such vehicles can travel significantly faster than conventional submarines. Cavitation can also be useful in ultrasonic cleaning devices. These devices induce cavitation using sound waves and use the collapse of the cavitation bubbles to clean surfaces via shock wave or jet impact. Used in this manner, the need for sometimes environmentally harmful chemicals can be reduced in many industrial and commercial processes that require cleaning as a step. In industry, cavitation is often used to homogenize, or mix and break down suspended particles in a colloidal liquid compound, such as paint mixtures, or milk. Many industrial mixing machines are based upon this design principle. Cavitating water purification devices have also been designed, in which the extreme conditions of cavitation can break down pollutants and organic molecules. Spectral analysis of light emitted in sonochemical reactions reveal chemical and plasma based mechanisms of energy transfer. The light emitted from cavitation bubbles is termed sonoluminescence. Cavitation also plays an important role for the destruction of kidney stones in shock wave lithotripsy.

Recently, besides free or cavitation bubbles, whose interface with the host fluid is treated as a free surface, a number of applications in medical science make use of the ability of contrast agents to reflect the ultrasound waves. Ultrasound contrast agents are gas-filled microbubbles that are surrounded by an elastic membrane, in order to prevent gas diffusion and dissolution in blood, and that are administered intravenously to the systemic circulation. The echogenicity difference between the gas in the microbubbles and the soft tissue surroundings of the body is immense. Thus, ultrasonic imaging using microbubble contrast agents enhances ultrasound backscatter, or reflection of the ultrasound waves, to produce a unique sonogram with increased contrast due to the high echogenicity difference. Contrast enhanced ultrasound can be used to image blood perfusion in organs, to measure blood flow rate in the heart and other organs, just to name a few among a wide variety of applications. In fact, the spectrum of potential applications of encapsulated microbubbles in medicine is ever-growing. Targeting ligands that bind to receptors characteristic of intravascular diseases (e.g. cancer) can be conjugated to microbubbles, enabling the microbubble complex to accumulate selectively in areas of interest, such as diseased or abnormal tissues. This form of molecular imaging, known as targeted contrast enhanced ultrasound, will only generate a strong ultrasound signal if targeted microbubbles bind in the area of interest. Targeted contrast enhanced ultrasound can potentially have many applications in both medical diagnostics and medical therapeutics. However, the targeted technique has not yet been approved for clinical use; it is currently under preclinical research and development.

I.2 Collapse of laser and acoustically induced bubbles

The details of bubble collapse have recently been singled out as a key factor in the context of single bubble sono-luminescence⁹ (SBSL) and single cavitation bubble luminescence¹⁰ (SCBL) experiments, where light is emitted during the final stages of collapse of a bubble that is generated and held captive via acoustic bubble traps or strong laser pulses, respectively. The initial shape of bubbles induced via laser pulses is easier controlled hence bubbles generated in this fashion are often used as a means to examine the effect of sphericity during collapse on the level of light emission^{11,12}. Thus, it was found¹¹ by comparing the collapse of a free bubble against that of a bubble in the vicinity of a solid boundary via a high speed image converted camera, that in the former arrangement light emission is stronger owing to the higher sphericity of collapse. In fact, it was found that shock-wave emission is not necessarily connected with a luminescence event in cases for which collapse was not violent enough, as for example in the presence of a nearby solid boundary. The pulse duration in these experiments was on the order of a few nanoseconds and the bubbles that were generated had sizes on the order of 1 mm while being more or less spherical. More recently employment of femtosecond, 10^{-15} s, laser pulses became possible¹² in which case the bubbles that are generated are much smaller in size, on the order of a few micrometers, with more pronounced asymmetries in their initial geometry, i.e. they exhibited an initial elongation along their axis of symmetry. Such bubbles were observed¹² to collapse asymmetrically in a water solution without any light emission, whereas bubbles produced by the nanosecond laser pulses collapsed in a more or less spherically symmetric fashion¹² and this process was accompanied by strong light emission. Thus, the importance of sphericity in SCBL was corroborated. The fact that cavitation

luminescence needs a highly spherical bubble collapse^{11,12} bears significance on the mechanism behind light emission which may be associated with the formation of a pair of diverging-converging shock waves propagating in the host liquid¹³. In particular, the existence of a converging shock wave can account for the temperature and pressure conditions that are necessary for light emission at the bubble collapse site. On the other hand jet formation is also known to take place during even a mildly aspherical bubble collapse both from experimental^{11,14} and numerical^{15,16} studies. In fact, it has been shown experimentally that light emission can take place as the jet collides with the opposite bubble surface¹¹, provided that the bubble is not originally too close to the neighboring solid boundary, and thus jet impact has also been held responsible for light emission¹⁷, by causing "fracturing" of the surrounding liquid, i.e. water in most cases.

In the case of SBSL, there are theories that claim that neither shock wave formation nor jet impact is necessary for providing the energy localization that is needed for light emission. Recent studies^{18,19} have shown that adiabatic compression during the collapse phase of a bubble that is acoustically trapped and performs stable oscillations, is enough for generating the appropriate environment for light emission. On the other hand there are theories^{17,20} that assert that even when the bubble shape is initially spherical, asymmetric collapse happens at the last stages giving rise to jet formation and impact. Simulations of bubbles translating with a traveling wave exhibit jet formation upon collapse, accompanied by the appearance of toroidal bubbles^{15,21}. The experiments that have been performed on SBSL cannot clearly demonstrate what pattern prevails at the final stages, due to the enormous velocity of the bubble interface as well as to the extremely small bubble size at the final collapse stages. Nevertheless, it is believed¹⁷ that, irrespective of the more or less spherical nature of bubble pulsations, sphericity is lost during the very last stages of collapse and this is corroborated by experimental investigations^{22,23} indicating that sonoluminescence occurs within a parameter range, in terms of bubble size and sound amplitude, that is adjacent to that corresponding to shape instabilities.

It is not within the scope of the present study to determine the dominant mechanism behind light emission in single cavitation bubble luminescence (SCBL) and single bubble sono-luminescence (SBSL). Rather, it is intended at providing a parametric study on the details of bubble collapse for different bubble sizes, under conditions of weak or strong elongation and vanishing small or large overpressure, and at shedding some light on the degree of sphericity and on the mechanics of jet formation and impact during bubble collapse by simulating experiments¹² with laser and acoustically generated bubbles as realistically as possible.

In addition, calculations of the interfacial and jet velocities may enlighten the effect of the shock wave on the production of luminescence, even if the present model cannot simulate the generated shock wave and doesn't take into account dissipation due to compressibility. It is also interesting to correlate the appearance of shape instabilities, as predicted asymptotically^{24,25} for acoustically levitated bubbles, with shape deformation and break-up as predicted numerically when the assumption of spherosymmetry is relaxed and the effect of viscous dissipation inside the boundary layer surrounding the bubble is taken into account.

In a different context, it is of interest to investigate the possibility that during bubble collapse or break-up universalities exist that may or may not be of the same nature as those obtained in the case of capillary pinch-off of initially elongated inviscid drops^{26,27}. Clearly, the existence of volume oscillations in the case of bubbles

complicates the dynamics and the initial energy allocation between the breathing mode and higher modes corresponding to shape deformation will play an important role in the long-time behavior of the bubble. As will be seen in the following sections, for small initial overpressures and moderate initial elongations bubble break-up will occur when the Reynolds number, based on the bubble size, surface tension and liquid viscosity, becomes larger than a threshold value. For axisymmetric bubbles with fore-aft symmetry, during break-up two countercurrent jets are formed on either side of the axis of symmetry connecting the two poles, that impinge upon each other on the equatorial plane which is also a plane of symmetry in this case. The final stages of the break-up process closely resemble the dynamics of two colliding drops²⁸ despite the absence of the strong lubricating effect of the pressure inside the bubble. In addition, the relevant time and space scales at this stage of the motion do not depend on the initial conditions of the problem and seem to obey the same universal law that governs capillary pinch-off of elongated drops.

A hybrid boundary-finite element method is used in order to solve for the velocity potential and shape deformation of axisymmetric bubbles. Weak viscous effects are included in the computations by retaining first-order viscous terms in the normal stress boundary condition and satisfying the tangential stress balance. Details on the model equations and assumptions as well as the numerical methodology and the relevant dimensionless parameters are given in a following chapter.

I.3 Oscillations and collapse of encapsulated microbubbles (contrast agents) subject to ultrasound

In recent years, a large number of ultrasound biomedical applications make use of or come across of micro-bubbles effects. Such bubbles can either arise spontaneously in an irradiated object, biological tissue, blood, an aqueous suspension of biological cells, etc., or be injected into the object encapsulated as contrast agents in order to enhance the ultrasound scatter from it^{29,30}. In the following, we will refer to such bubbles as micro-bubbles or contrast agents in order to distinguish them from free or cavitation bubbles. Today such micro-bubbles are clinically established markers of vascularity and are used for quantitative blood flow and volume measurements³⁰. Ongoing research has revealed their potential for quantification of microvasculature and perfusion³¹. Clinical applications for contrast-enhanced ultrasound expand beyond perfusion imaging. Recent developments of site-targeted micro-bubbles allows for drugs or genes to be carried into or onto them, while controlled disturbance or even disruption of their encapsulating membrane upon the application of ultrasound fields, appears to enhance focal release³². In the same context, the encapsulating membrane of cells that lie in the vicinity of cavitating micro-bubbles is subjected to straining that stretches or may even rupture it as a result of the tensile strain that develops. It is of great importance to establish the critical parameter range, normally the Mechanical Index (MI), for micro-bubble induced sonoporation that separates simple straining of the cell membrane accompanied by pore opening, from lysis and irreversible damage of the cell, e.g. ultrasound induced haemolysis of red blood-cells³³.

Proper understanding of the physical mechanism of the above applications requires modelling of the pulsation and deformation of insonated micro-bubbles, alone and in the vicinity of biological cells or tissue. Efficient acquisition and processing of

the scattered pressure signal is the determining factor in modern perfusion imaging modalities. The common approach of most studies modelling contrast agents is a direct transfer of the achievements of classical physical acoustics to biological systems. In the pioneering studies of micro-bubble pulsations in blood flow, contrast agents are commonly described by various forms of the Rayleigh-Plesset equation^{34,35,36}. In one of the earlier attempts to model a contrast agent Church³⁴ used a generalized Rayleigh-Plesset model that accounted for the finite shell thickness and viscoelastic properties. In this manner he was able to show, in the limit of small amplitude acoustic disturbances and using the Kelvin-Voigt constitutive law that predicts the stresses developing on the cell membrane for small displacements, the effect of shell properties on the resonance frequency and sound attenuation in a liquid containing micro-bubbles. Adopting a slightly different approach de Jong et al.³⁵ and Frinking & de Jong³⁶ modelled the micro-bubble shell as a membrane of infinitesimal thickness and used semi-empirical laws³⁶ or simple linear models³⁵ for the description of shell elasticity and viscosity. In addition they utilized expressions derived from linear theory³⁷ in order to model acoustic, thermal and viscous damping of the scattered pressure signal as well as damping due to internal shell friction. They conducted simulations in the linear and nonlinear regime of acoustic disturbances and thus were able to point out the importance of higher harmonics in the scattered signal (signals from contrast agents are less susceptible to contamination from higher harmonics than free bubbles due to the encapsulating membrane) as well as the effect of viscoelastic properties of the shell on the bubble response. Based on sound attenuation and scattering data from direct measurements with actual contrast agent populations subject to weak acoustic disturbances, they were able to obtain an estimate for the shell elasticity modulus and friction. However, upon comparing the predictions of their model with the available scattering data obtained at higher acoustic pressures, they reported failure to predict the dependence of scattering cross section on increasing acoustic pressure. Sboros et al.³⁸ reached a similar conclusion when they compared the same models against their own measurements. In the same study as well as elsewhere³⁹ it was seen that when the Gilmore and Herring models⁴⁰ were employed better predictions for high acoustic pressures were possible. The Gilmore and Herring models are essentially adaptations of the classical Rayleigh-Plesset model describing free bubble oscillations, which account for liquid compressibility when large or very large fluid velocities develop as a result of the pulsating micro-bubble, respectively⁴⁰. The above models as well as other models that account for the non-Newtonian properties of blood⁴¹ are successful in predicting micro-bubble behavior within a certain parameter range, but they fail to provide reliable predictions over wide ranges of the relevant parameters as they are characterized by a significant degree of empiricism in the description of the membrane. An effort towards a more rigorous theoretical description of radial pulsations of micro-bubbles in blood flow was made by Khismatullin & Nadim⁴². In that study the radial motion of a micro-bubble that is encapsulated by a viscoelastic membrane and surrounded by a slightly compressible viscoelastic liquid was examined, assuming that the viscoelastic properties of the shell and the liquid are described by the Kelvin-Voigt and the 4-constant Oldroyd models, respectively. In this fashion they were able to calculate resonance frequencies and damping coefficients for linearly pulsating micro-bubbles. As was already shown elsewhere^{34,43}, because of membrane elasticity resonance occurs at higher frequencies than for the case free bubbles. In addition, it was seen that the resonance frequency also depends significantly on viscous damping in the host liquid. However, their theory⁴² is

restricted to small-amplitude oscillations only, hence the effect of the appearance of higher harmonics and sub harmonics was restricted to the second harmonic response. As was already seen this is a recurring issue with models of contrast agents, namely their predictive value at large acoustic pressures.

The above models as well as other models that are extensively used in the literature, e.g. the Church-Hoff model⁴⁴, are obtained by the Kelvin-Voigt model, originally proposed by Church³⁴, when the shell thickness is taken to be much smaller than its radius. Such models are only valid for small shell displacements, strictly speaking, they are successful in predicting micro-bubble behavior within a certain parameter range, but they fail to provide reliable predictions over wide ranges of the relevant parameters because they are restricted by the validity range of the membrane description. As an alternative approach, following Edwards et al.⁴⁵, Chatterjee & Sarkar⁴⁶ and Sarkar et al.⁴⁷ modeled the effect of shell dilatational elasticity through interfacial tension and its variation with shell interfacial area, while also including the effect of dilatational shell viscosity through a Newtonian viscoelastic model for the membrane material. The above authors discuss the merits of this approach in comparison with the Church-Hoff model, but they also point out the need to account for material softening as a result of excessive area dilatation when large acoustic disturbances or very large frequencies are employed. At this point, it should be stressed that all the above models ignore changes in the material with varying MI, adopting a type of Hooke's law for the material's mechanical behaviour. However, most materials exhibit a varying elasticity modulus when they are subject to external disturbances of increasing intensity or increasing frequency. Thus, there are materials, called strain hardening, whose stress-strain relationship exhibits a steeper slope as deformations increase, corresponding to an increased apparent elasticity modulus. A characteristic example of this type of material is that of the lipid bi-layer that forms the red blood cell membrane as well as certain polymers that are used in the manufacturing of contrast agents. On the other hand, if the stress-strain slope is reduced as deformations increase the material is called strain softening, e.g. rubber is a characteristic example. Such behaviour is accounted for by the constitutive law describing the membrane material. The Skalak law⁴⁸ belongs to the class of constitutive laws describing materials that are strain hardening by nature and it is widely used⁴⁹ for describing the mechanical behavior of the red blood cell membrane, while the Mooney-Rivlin law is often used to characterize strain softening materials. The importance of these material properties has already been recognized in the modeling of blood cells or capsules in general⁵⁰, where by the term capsule we refer to drops surrounded by an elastic membrane. Such particles are often produced by the pharmaceutical or the cosmetic industry. A number of studies with simulations of blood cells or capsules, based on the above membrane properties among other aspects of the proposed model, have appeared in the last two decades with significant success in explaining their actual dynamic behavior^{49,50,51,52}. Emelianov et al.⁵³ took into consideration the effect of different constitutive laws on the dynamics of a gas bubble, when the surrounding elastic medium extends to infinity. It is the scope of the present study to introduce this perspective in the literature of contrast agent modeling. It should also be stressed that all the existing studies neglect the effect of membrane residual stresses. In other words, even though a micro-bubble may be at equilibrium its membrane may carry residual stresses, possibly as a result of a previous measurement cycle or in the form of residual stresses after their encapsulation process is over. The effect of residual stresses on the micro-bubble response is expected to be

larger when a membrane constitutive law is used that deviates from Hookean behavior. This is due to the fact that such material behavior alters the apparent membrane elasticity, which is a parameter that determines the micro-bubble dynamic behavior.

Microbubble destruction is the key to many of the techniques used or under evaluation in the clinic. For example, by destroying contrast microbubbles with a high-amplitude acoustic pulse and then observing the refill of microbubbles at lower acoustic pressure levels, information on the kinetics of flow can be obtained. Contrast enhancement will return to regions of rapid flow faster than to regions of slow flow. Wei³¹ introduced the concept of using the destruction of microbubbles and the rate of signal return to map perfusion quantitatively. In recent years, this technique has been applied in a number of organs^{54,55}. The acoustic rupture of contrast microbubble shells has also been proposed as a means to release more strongly-scattering, free bubbles that provide a short-lived but unique acoustic signature for imaging⁵⁶. Several researchers are exploring microbubbles as drug delivery vehicles, which can be concentrated in a specific area for localized treatment⁵⁷. Local, controlled delivery of drugs such as chemotherapeutic agents which can be systemically toxic should significantly reduce undesirable side effects. Researchers have shown that encapsulated microbubbles designed for transporting therapeutic agents can be ruptured with an acoustic pulse⁵⁸. Such acoustic delivery could be applied to contrast microbubbles concentrated at a desired treatment site in vivo. At the same time there exist applications, such as sonoporation⁵⁹, where microbubble cohesion is preferred.

The general goal of this study is to emphasize the flow structure interaction aspect of contrast agent dynamics by cross-examining the effect of non-linearity in the membrane viscoelastic behavior along with that of external liquid attributes such as viscosity, compressibility and nonlinearity in the acoustic disturbance. As a first step in this direction, the model employed for the description of a free spherosymmetric bubble⁶⁰ that properly accounts for weak compressibility of the surrounding liquid when the Mach number is small but non-zero, is coupled with different constitutive laws modelling the encapsulating shell. The latter is modelled as a membrane of small or infinitesimal thickness via one of the three membrane constitutive laws that were mentioned above, i.e. the Kelvin-Voigt, Mooney-Rivlin and Skalak laws. It should be noted that the last two laws formally collapse to the Kelvin-Voigt model as the membrane displacement tends to zero. The fluid and structure problems are coupled at the microbubble interface where stress continuity is imposed.

In order to define the threshold of the external disturbances above which the microbubble breaks up, as well as the number of the free bubble fragments, one has to relax the assumption of spherosymmetry in the model by allowing axisymmetric or three-dimensional deformation of the interface with infinitesimal thickness. Similar studies have been conducted using boundary elements techniques in order to investigate the dynamic behavior of a red blood cell or capsule^{49,61} when $Re \rightarrow 0$. The present study aims at establishing the range of cohesion and the collapse mechanism such as, static buckling, dynamic buckling, Rayleigh - Taylor instability or parametric instability, rupture of the membrane due to excessive tensile tensions, for a pulsating micro-bubble whose membrane follows the Mooney-Rivlin or Skalak law. If possible, we also wish to predict the number of the ensuing fragments allowing axisymmetric deformation of the interface.

The stability of spherical microbubble pulsations is first examined with regards to external acoustic disturbances. In this case, infinitesimal deformations in the

microbubble shape are imposed in a similar fashion with M.S. Plesset⁶² and it is examined whether the spherical surface is stable, or whether non-spherical shape perturbations should be expected to grow as the microbubble pulsates. In addition, the stability of periodic spherically symmetric pulsations is examined, in a manner similar to that previously employed for free bubbles⁶³. The elastic stresses that develop on the shell due to the bending moments are accounted for, based on the shell stability theory⁶⁴, and are determined by the scalar bending modulus, $k_{B \text{ dim}}$. This is a measure of the shell resistance to bending and is introduced as an additional parameter, due to the anisotropy of the membrane elasticity along the interface and perpendicular to it⁶⁵. Once this parameter is known the resonance frequencies for shape oscillations of the microbubble could be predicted as well as conditions for its break-up could be established. The two constitutive laws that are employed in the spherically symmetric model are implemented here also.

Finally, a numerical model is developed, implementing a hybrid boundary-finite element method in order to solve for the velocity potential and shape deformation of an axisymmetric microbubble, coupled with an axisymmetric viscoelastic model for the encapsulating shell. The latter is taken to be a thin shell with anisotropic elasticity along the interface, membrane elasticity, and perpendicular to it, bending elasticity. Details of collapse are investigated in connection with the interfacial topology, e.g. conditions for jet formation are sought in the parameter range of interest to medical applications.

I.4 Structure of the dissertation

As a first step towards simulating laser induced bubbles, the study in chapter II focuses on the break-up process of bubbles that are initially elongated along their axis of symmetry. The amount of initial overpressure is assumed to be either vanishing or small. In this fashion, an effort will also be made to examine the dynamics of bubble collapse for possible universalities. More specifically, in section II.1 the governing equations for the problem of the nonlinear oscillations and collapse of elongated bubbles subject to weak viscous effects are presented. The motion is decomposed in an irrotational part that is described via a boundary-integral representation⁶⁶, section II.1.1, and in a rotational part that is described via a boundary layer approach that is valid for weak viscous effects⁶⁷, section II.1.2. In section II.1.3, the variation of the total energy of the system is obtained including the effect of dissipation, and is used as an integral check on the accuracy of our calculations. Next, in section II.2, the numerical solution of the problem is presented and convergence tests along with validation tests are given. In section II.3, an extensive account of the results that were obtained numerically is presented and the effect of the basic parameters is discussed. Bubbles possessing fore-aft symmetry along the symmetry axis are examined and their long-term dynamic state is calculated as a function of the initial elongation, S , and Reynolds number, Re . Micron-sized bubbles are investigated and this size is reflected in the dimensionless static pressure in the far-field, $P_{St} = P'_{St} / (2\sigma / R)$, as well as in $Re = Oh^{-1} = (R\sigma\rho / \mu^2)^{1/2}$; R is the radius of a spherical bubble with the same volume as the initial volume of the elongated bubble, P'_{St} is the far field pressure taken to be equal to the atmospheric pressure, ρ and μ denote the density and viscosity, respectively, of the surrounding fluid taken to be water and σ denotes surface tension taken to be the interfacial air-water tension throughout this study. The effect of small

internal overpressures as well as that of initial asymmetries is also presented, while in section II.4 the results are discussed in the context of previous studies.

In chapter III, the details of nonlinear oscillations and collapse of elongated bubbles, subject to large internal overpressure are studied. In section III.1, a brief account is given of the specific features of the problem treated in this study, i.e. initial conditions and parameter range. In addition, the context in which the experiments with laser bubbles¹² (SCBL) are simulated here is outlined. In section III.2, a parametric study is carried out, of the process of bubble collapse in the appropriate parameter range determined by initial elongation, internal bubble overpressure, bubble size and viscosity. Different modes of collapse are obtained and the existence of universalities during pinch-off is investigated. In section III.3 an attempt is made to identify the types of bubble behavior obtained in the parametric study of section III.2 in the simulations of specific experiments with laser bubbles. The importance of initial elongation and overpressure on the details of bubble collapse will be emphasized, e.g. degree of sphericity during collapse and jet formation and impact, depending on the level of initial disturbances. Finally, in section III.4 conclusions will be drawn and directions for future research will be outlined.

In chapter IV, the details of nonlinear oscillations and collapse of acoustically driven bubbles (SBSL) are studied. In section IV.1, a brief account is given of the specific features of the problem of SBSL and results of simulations are shown obtained at conditions similar with experiments where luminescence takes place. The pattern of shape deformation, parametric vs. Rayleigh-Taylor instability, and collapse is captured, and the evolution of the interfacial and jet velocities during the last stages of collapse are calculated and compared. Finally, in section IV.2 the importance of initial elongation on the details of bubble collapse is emphasized, e.g. degree of sphericity during collapse and jet and microbubble formation depending on initial asymmetry, and conclusions are drawn.

In chapter V, the non-linear radial oscillations of encapsulated microbubbles subject to ultrasound are studied. A detailed account of the model employed for the description of the micro-bubble is given in section V.1. The numerical methodology is briefly presented in section V.2. It is the same approach that was used in a previous study of free bubble oscillations near and above the Blake threshold⁶⁸. The resonance frequency and scattering cross section of the micro-bubble are calculated for a wide parameter range in section V.3. Finally, in section V.4 conclusions are drawn on the relative importance of different aspects of the micro-bubble model, especially in the regime of large acoustic disturbances where the impact of the constitutive law on the interpretation of certain experimental observations is mostly evident. Finally, future directions of contrast agent modelling will be discussed.

In chapter VI, the axisymmetric oscillation and collapse of an encapsulated microbubble which is insonated in an inviscid fluid, is studied. The governing equations of the problem are presented in section VI.1, while a brief description of the numerical method which is applied for the solution of the equations is invoked in section VI.2. In section VI.3, the governing equations of the linearized problem with respect to non spherical disturbances are derived based on similar studies^{23,24,62,63,64}. In section VI.4, the stability of periodic spherosymmetric pulsations is studied through the calculation of the eigenvalues of the monodromy matrix⁶⁹, while in section VI.5 an attempt is made to compare with results of shell theory as regards to the appearance of static buckling instability. In addition, based on respective experimental observations of a contrast

agent destruction⁷⁰, a calibration of the physical properties of microbubble shell through the estimation of shear stress modulus and scalar bending modulus, is attempted. Different kinds of shape instabilities and collapses which are related to the dynamic nature of the microbubble oscillation are identified, such as the dynamic buckling and the parametric instability, while phase diagrams for an encapsulated microbubble that defines the regions marking the onset of instability, are constructed. Simulations of encapsulated bubbles are also conducted aiming at capturing extreme shape deformations, i.e. jet formation and details of break-up. Finally, in section VI.6 conclusions are drawn and future directions for modeling are posed.

An overview of the problems studied in the frame of this thesis is shown in Table 1. In this table the characteristics of the models developed and their applicability to the above-discussed cases, are outlined.

OVERVIEW OF PROBLEMS STUDIED IN THE FRAME OF THIS THESIS

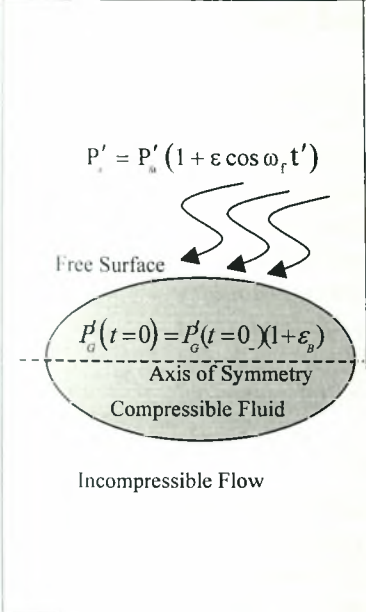
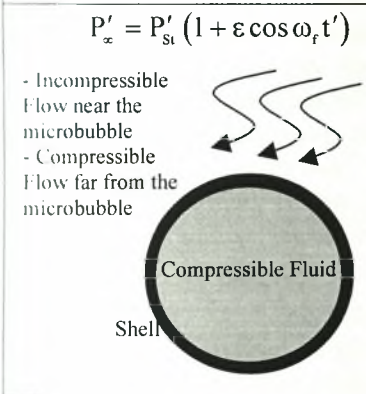
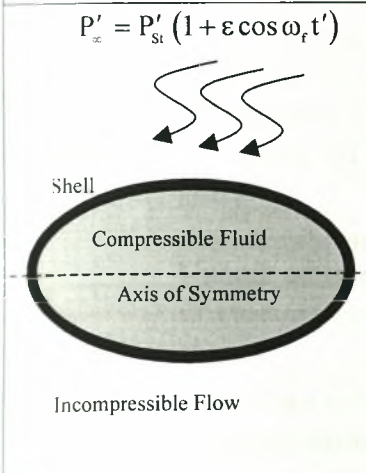
Schematic	Model Type	Model Applicability	Chapter
 <p>$P'_s = P'_a (1 + \varepsilon \cos \omega_f t')$</p> <p>Free Surface</p> <p>Axis of Symmetry</p> <p>Compressible Fluid</p> <p>Incompressible Flow</p>	<p>Axisymmetric potential flow Weak viscous effects, Lagrangian representation of the interface</p> <p>Free bubble undergoing isothermal or adiabatic oscillations</p> <p>Response under</p> <p>(a) Initial elongation and/or internal overpressure and</p> <p>(b) Initial elongation and acoustic disturbances</p>	<p>Prediction of the details of the bubble collapse under severe elongation (universalities)</p> <p>Prediction of the details of the bubble collapse under severe elongation and internal overpressure</p> <p>Prediction of the unstable modes for small deviations from sphericity</p> <p>Prediction of the details of bubble collapse under acoustic disturbances and initial elongation</p> <p>Prediction of the unstable modes for small deviations from sphericity</p>	<p>II</p> <p>III</p> <p>IV</p>
 <p>$P'_z = P'_{st} (1 + \varepsilon \cos \omega_f t')$</p> <p>- Incompressible Flow near the microbubble - Compressible Flow far from the microbubble</p> <p>Compressible Fluid</p> <p>Shell</p>	<p>Spherosymmetric potential flow</p> <p>Coupled shell and fluid dynamics, Non Linear elastic constitutive laws, Acoustic damping, External viscous effects, Spherosymmetric shell at equilibrium</p>	<p>Prediction of the backscatter signal from an encapsulated microbubble depending on the constitutive law of the shell, for large shell displacements</p>	<p>V</p>
 <p>$P'_z = P'_{st} (1 + \varepsilon \cos \omega_f t')$</p> <p>Shell</p> <p>Compressible Fluid</p> <p>Axis of Symmetry</p> <p>Incompressible Flow</p>	<p>Axisymmetric potential flow, Lagrangian representation of the interface</p> <p>Coupled shell and fluid dynamics, Non Linear elastic constitutive laws, Axisymmetric shell at equilibrium</p> <p>Elastic anisotropy (different bending and membrane elasticity)</p>	<p>Stability analysis to small axisymmetric interfacial perturbations</p> <p>Prediction of the eigenfrequencies of the unstable modes</p> <p>Stability of periodic pulsations</p> <p>Phase diagrams of the stability for specific contrast agents</p> <p>Prediction of the details of the collapse of an encapsulated microbubble under acoustic disturbances and for large deviations from sphericity</p>	<p>VI</p>

Table I.1: Schematic diagram of the models developed in the context of the thesis.

CHAPTER II

Weak Viscous Oscillations and Break-up of Elongated Bubbles

The weak viscous oscillations of a bubble are examined, in response to an elongation that perturbs the initial spherical shape at equilibrium. The flow field in the surrounding liquid is split in a rotational and an irrotational part. The latter satisfies the Laplace equation and can be obtained via an integral equation. A hybrid boundary-finite element method is used in order to solve for the velocity potential and shape deformation of axisymmetric bubbles. Weak viscous effects are included in the computations by retaining first-order viscous terms in the normal stress boundary condition and satisfying the tangential stress balance. An extensive set of simulations was carried out until the bubble either returned to its initial spherical shape, or broke up. For a relatively small initial elongation the bubble returned to its initial spherical state regardless of the size of the Ohnesorge number; $Oh = \frac{\mu}{(\rho R \sigma)^{1/2}}$. For larger

initial elongations there is a threshold value in Oh^{-1} above which the bubble eventually breaks up giving rise to a “donut” shaped larger bubble and a tiny satellite bubble occupying the region near the center of the original bubble. The latter is formed as the round ends of the liquid jets that approach each other from opposite sides along the axis of symmetry, coalesce. The size of the satellite bubble decreased as the initial elongation or Oh^{-1} increased. This pattern persisted for a range of large initial deformations with a decreasing threshold value of the Oh^{-1} as the initial deformation increased. As its equilibrium radius increases the bubble becomes more susceptible to the above collapse mode. The effect of initial bubble overpressure was also examined and it was seen that small initial overpressures, for the range of initial bubble deformations that was investigated, translate the threshold of Oh^{-1} to larger values while at the same time increasing the size of the satellite bubble.

II.1 PROBLEM FORMULATION

We want to investigate the nonlinear oscillations of a bubble that is initially elongated along its axis of symmetry from its spherical shape with radius R at static equilibrium, figure II.1. The interior pressure, P'_G , may be simultaneously increased but the magnitude of the disturbance, ε_B , will remain small in the context of this study:

$$P'_G(t=0) = P'_G(t=0_-)(1 + \varepsilon_B) \quad (\text{II.1})$$

It should be noted that throughout this study primed letters denote dimensional variables. In the absence of any acoustic disturbances, $\varepsilon=0$, the pressure in the far field acquires its static value, P'_{st} ,

$$P'_\infty = P'_{st} (1 + \varepsilon \cos \omega'_r t), \quad (\text{II.2})$$

with ω'_r denoting the dimensional forcing frequency of the disturbance. At equilibrium the fluid surrounding the bubble is quiescent and the pressure inside the bubble is connected to that in the far field via the Young-Laplace equation,

$$P'_G(t=0_-) - P'_{st} = \frac{2\sigma}{R} \quad (\text{II.3})$$

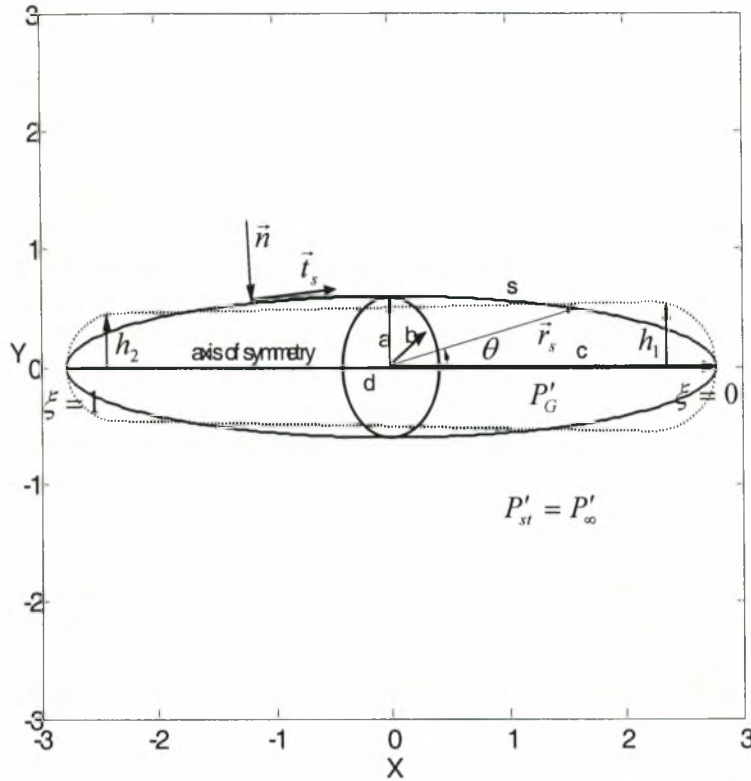


Figure II.1: Initial shape of the bubble for the symmetric (——) and the asymmetric (-----) case.

The shape of the bubble is assumed to be axisymmetric at all times while the disturbed shape at $t=0$ is characterized by fore-aft symmetry with respect to the equatorial plane, in most of the cases examined. In fact, we assume that the disturbed shape is that of an ellipsoid

$$\frac{y'^2}{a^2} + \frac{z'^2}{b^2} + \frac{x'^2}{c^2} = 1 \quad (\text{II.4})$$

with two equal semi-axis, $a=b$, in the equatorial plane, $y'z'$, and the third one, c , along the axis of symmetry, x' , characterizing the extend of initial elongation. For a given initial volume, V_0 , of the disturbed bubble we can calculate through the following relationships for the volume of a spherical and an ellipsoidal object, the equivalent radius R and the ratio c/R as a function of $S=a/R$, which is a parameter that will be used as a means to control the magnitude of initial elongation,

$$V_0 = \frac{4}{3} \pi R^3 = \frac{4}{3} \pi a^2 c \rightarrow R = \left(\frac{3V_0}{4\pi} \right)^{1/3}, \quad \frac{c}{R} = \frac{1}{(a/R)^2} = \frac{1}{S^2}. \quad (\text{II.5})$$

After introducing spherical coordinates,

$$y' = r' \sin \theta \cos \phi, \quad z' = r' \sin \theta \sin \phi, \quad x' = r' \cos \theta \quad (\text{II.6})$$

in equation (II.4), we obtain the following equation describing the initial shape of the bubble,

$$r = f(\theta, t = 0) = \frac{S}{\sqrt{S^6 \cdot \cos^2 \theta + \sin^2 \theta}}, \quad (\text{II.7})$$

where the azimuthal angle φ is set to zero without any loss of generality due to axisymmetry, and $r = r'/R$. When $S=1$ we recover the spherical shape whereas as S decreases the imposed elongation along the axis of symmetry becomes stronger. Nevertheless, the model presented here allows for asymmetric shapes, with regards to the y' axis as well. Such shapes are obtained by constructing an axisymmetric body consisting of two hemi-spheres that are attached on each one of the poles and are connected in the middle section of the body by a cone with variable radius. For a given volume, i.e. fixed R , and total initial elongation, $\ell = 2c/R$, we use the ratio between the radii of the two hemispheres, $k=h_1/h_2$, as a parameter controlling the degree of asymmetry. Thus, it can be easily shown that the ratio, s , between the radius, h_2 , of the cone's smaller hemisphere and R , is related to ℓ and k through the expression

$$\ell = \frac{4 - 2 \cdot s^3 \cdot (k^3 + 1) + s^3 \cdot (k + 1) \cdot (k^2 + k + 1)}{s^2 \cdot (k^2 + k + 1)} \quad (\text{II.8})$$

which uniquely determines the shape of the body (see also figure II.1). Having determined the initial geometry of the bubble the interior overpressure can be estimated provided the energy level of the laser pulse is known, possibly from experimental investigations. In this chapter we will assume small overpressure levels which amounts to small values of parameter ε_B .

The dynamics of a bubble subjected to the kind of disturbances presented above is normally described through the use of potential theory. If, however, one has to model situations with bubble sizes in the order of microns, then viscosity becomes the dominant dissipation mechanism and has to be accounted for. For bubbles oscillating in water with equilibrium radii ranging between 10 and 1000 μm the inverse Ohnesorge number varies, roughly, between 30 and 1000. This is the range of Oh^{-1} within which a theory that takes into account weak viscous effects would be applicable, provided there is no large-scale separation taking place in the liquid boundary layer surrounding the bubble's surface.

The equivalent radius R is assigned as the characteristic length of the problem thus giving, $r = r'/R$, $f = f'/R$, as the dimensionless distance from the origin of the spherical coordinate system and dimensionless location of the interface, respectively. In the absence of a characteristic velocity, surface tension is used in order to render velocity, pressure and time dimensionless, $\bar{V} = \bar{V}'/(\sigma/R/\rho)^{1/2}$, $p = p'/(2\sigma/R)$, $t = t'/(R^3/\sigma)^{1/2}$. Considering incompressible flow the dimensionless equations governing the motion in the ambient fluid and the deformation of the bubble read as follows:

Continuity equation expressing the differential mass balance,

$$\bar{\nabla} \cdot \bar{\mathbf{V}} = 0; \quad (\text{II.9})$$

Navier Stokes equations expressing the differential linear momentum balance

$$\frac{\partial \bar{\mathbf{V}}}{\partial t} + \bar{\mathbf{V}} \cdot \bar{\nabla} \bar{\mathbf{V}} = -2\bar{\nabla} P + \text{Oh} \nabla^2 \bar{\mathbf{V}}, \quad (\text{II.10})$$

where the effect of gravity is dropped due to the small size of the bubbles; kinematic condition forcing points on the surface to move with the fluid velocity

$$\vec{r} = \vec{r}_s : \frac{d\vec{r}_s}{dt} = \vec{V}, \quad (\text{II.11})$$

where \vec{r}_s denotes the position vector of a material point on the surface of the bubble; force balance on the interface,

$$\vec{r} = \vec{r}_s : -P_G \vec{n} - (-2P\underline{\underline{I}} + Oh\underline{\underline{\tau}}) \cdot \vec{n} = 2H\vec{n} = (-\vec{\nabla}_s \cdot \vec{n}) \vec{n}, \quad (\text{II.12})$$

where \vec{n} denotes the outwards pointing unit normal vector with respect to the fluid surrounding the bubble, $\vec{\nabla}_s$, H , denote the surface gradient and mean curvature on the

bubble's interface, respectively, and $\underline{\underline{I}}, \underline{\underline{\tau}} = \frac{\partial V_i}{\partial x_j} + \frac{\partial V_j}{\partial x_i}$, the unit and deviatoric stress

tensor, respectively;

quiescent flow conditions in the far field,

$$\vec{r} \rightarrow \infty : \vec{V} \rightarrow 0, \quad P \rightarrow P_\infty = P_{St}. \quad (\text{II.13a,b})$$

Due to negligible density and kinematic viscosity of the gas inside the bubble we take the bubble pressure to be uniform and drop the deviatoric part of the stress tensor on the side of the gas inside the bubble. In addition, owing to the very short time frame over which the phenomena that are investigated in the present study evolve, we can neglect heat transfer to and from the surrounding liquid, to a first approximation, and consider adiabatic oscillations. Consequently the variation of the bubble pressure with time is given by

$$P_G(t=0) \left(\frac{4}{3} \pi \right)^\gamma = P_G(t) V_G^\gamma(t), \quad (\text{II.14})$$

where γ denotes the polytropic constant, $1 \leq \gamma \leq 1.4$, and V_G the dimensionless instantaneous volume of the bubble; for an adiabatic process $\gamma=1.4$.

In order to capture the effect of viscosity for relatively large Oh^{-1} we first decompose the velocity and pressure fields in an irrotational and a rotational part,

$$\vec{V} = \vec{u} + \vec{U} \quad (\text{II.15})$$

$$P = p_{ir} + p \quad (\text{II.16})$$

where,

$$\vec{u} = \vec{\nabla} \Phi, \quad \vec{U} = \vec{\nabla} \times \vec{A}, \quad (\text{II.17a,b})$$

with $\vec{\nabla} \times \vec{u} = 0$, $\vec{\nabla} \cdot \vec{A} = 0$; it can be seen that a decomposition of this type is possible for any flow field without any loss in generality⁷¹. When the flow is characterized by axial symmetry the vector potential is of the form,

$$\vec{A} = A(r, \theta) \vec{e}_\phi \quad (\text{II.18})$$

where \vec{e}_ϕ is the unit vector in the azimuthal direction. Next we present the formulation for the scalar, Φ , and vector potential, \vec{A} .

II.1.1 Irrotational flow field

Introducing decomposition (II.15) in the continuity equation we obtain, using (II.17a,b),

$$\vec{\nabla} \cdot \vec{u} + \vec{\nabla} \cdot (\vec{\nabla} \times \vec{A}) = 0 \rightarrow \nabla^2 \Phi = 0. \quad (\text{II.19})$$

Thus we recover the well-known result that the scalar velocity potential satisfies the Laplace equation. In an effort to capture more complicated bubble shapes for which Eulerian description would be multi-valued, we adopt the Lagrangian formulation for

the description of the motion of particles occupying the bubble's interface. As the irrotational pressure and velocity fields must satisfy Bernoulli's equation, the latter can be combined with the normal force balance in the absence of viscous dissipation,

$$2P_G - 2p_{ir} = 2H \quad (II.20)$$

to give the dynamic condition describing the evolution of the velocity potential on the bubble's surface,

$$\frac{D\Phi}{Dt} = \frac{1}{2} \left[\left(\frac{\partial\Phi}{\partial n} \right)^2 + \frac{\Phi_\xi^2}{r_\xi^2 + r^2\theta_\xi^2} \right] + 2P_{st} - 2P_G - 2H \quad (II.21)$$

In the above equation

$$\frac{D\Phi}{Dt} = \frac{\partial\Phi}{\partial t} + \vec{u} \cdot \vec{\nabla}\Phi = \frac{\partial\Phi}{\partial t} + |\vec{u}|^2, \quad (II.22)$$

while ξ is a Lagrangian coordinate that identifies particles on the interface and is related to the arclength, s , of the interface by

$$\frac{\partial s}{\partial \xi} = (r_\xi^2 + r^2\theta_\xi^2)^{1/2}, \quad 0 \leq \xi \leq 1; \quad (II.23)$$

ξ as a subscript denotes partial differentiation. It should be pointed out that, in the context of Lagrangian formulation, both the scalar and the vector velocity potentials, Φ and A , as well as the r and θ coordinates of Lagrangian particles on the interface will be functions of ξ . Then, the mean curvature H is given by,

$$-2H = \frac{1}{r^2\theta_\xi \sin\theta} \left\{ \frac{\sin\theta(2r^2\theta_\xi^2 + r_\xi^2)}{(r^2\theta_\xi^2 + r_\xi^2)^{1/2}} - \frac{\partial}{\partial \xi} \left[\frac{rr_\xi \sin\theta}{(r^2\theta_\xi^2 + r_\xi^2)^{1/2}} \right] \right\}. \quad (II.24)$$

Owing to axisymmetry the derivatives with respect to ξ should satisfy the following conditions:

$$\frac{\partial r}{\partial \xi} = \frac{\partial\Phi}{\partial \xi} = \frac{\partial^2\Phi}{\partial \xi \partial n} = \frac{\partial^2\theta}{\partial \xi^2} = 0, \quad \text{at } \xi = 0,1 \quad (II.25)$$

corresponding to the two poles of the coordinate system.

Following Pelekasis & Tsamopoulos⁶⁶, we recast the Laplace equation in an integral form involving quantities evaluated at the interface, i.e. we introduce the boundary integral formulation of the Laplace equation:

$$\begin{aligned} \Phi(\hat{r}, \hat{\theta}, t) + \int_0^1 [\Phi(r, \theta, t) - \Phi(\hat{r}, \hat{\theta}, t)] \frac{\partial G}{\partial n}(\hat{r}, \hat{\theta}, r, \theta) r \sin\theta (r_\xi^2 + r^2\theta_\xi^2)^{1/2} d\xi = \\ \int_0^1 \frac{\partial\Phi}{\partial n}(r, \theta, t) G(\hat{r}, \hat{\theta}, r, \theta) r \sin\theta (r_\xi^2 + r^2\theta_\xi^2)^{1/2} d\xi \end{aligned} \quad (II.26)$$

where hatted coordinates, \hat{r} , $\hat{\theta}$, depend on the location of the field point $\hat{\xi}$ and are not subject to integration. The above equation relates the scalar velocity potential to its normal derivative at the interface and can be obtained by applying Green's third identity on the Laplace equation and allowing the field point, where the potential is evaluated, to approach the interface. G and $\partial G/\partial n$ denote the axisymmetric free space singular kernel of the Laplace equation and its normal derivative, respectively. The latter possesses a non-integrable $1/p$ singularity, with p denoting the distance between the source and field points on the bubble's interface. The difference between the values of the potential at the field and source points has been introduced in equation (II.26) in order to

circumvent this singularity⁷². It should also be pointed out that the integrals in equation (II.26) are line integrals along the instantaneous generating curve of the axisymmetric interface between the bubble and the surrounding fluid. As will be seen in section II.3 this has a beneficial impact in the efficiency of calculations.

II.1.2 Weak viscous effects ($Oh \ll 1$)

When Oh is small the rotational part of the velocity field forms a boundary layer near the bubble's surface, where dissipation and inertia balance each other, so that the boundary condition of zero shear rate is satisfied at the interface. In order to capture this effect we introduce a new orthogonal coordinate system based on the arc-length s and azimuthal angle ϕ , as they are defined on the instantaneous position of the interface, and the distance, n , along the normal direction on any point in the interface. In this triply orthogonal coordinate system consisting of a Lamé group of surfaces based on the shape of the interface we know⁷³ that the metric along the normal direction is $h_n=1$ whereas those in the other two directions are, $h_t = 1 + O(n)$, $h_\phi = r \sin \theta + O(n)$, for an axisymmetric shape. Consequently, within a boundary layer, where ζ is small, the metrics are everywhere the same with those evaluated on the interface. For the same reason, the two unit vectors that are tangent to the family of surfaces parallel to the interface, and whose direction varies along the normal to the interface, within the boundary layer will be, roughly, identical to those defined on the interface. Thus, the gradient operator is defined in the boundary layer as,

$$\bar{\nabla} = \bar{\nabla}_s + \bar{n} \frac{\partial}{\partial n} + O(n) \approx \bar{t} \frac{\partial}{\partial s} + \frac{\bar{e}_\phi}{r \sin \theta} \frac{\partial}{\partial \phi} + \bar{n} \frac{\partial}{\partial n} \quad (II.27)$$

where $\bar{\nabla}_s$ is the surface gradient defined on the bubble's interface, \bar{t} is the unit vector tangent along the generating curve of the axisymmetric interface and r, θ , are the coordinates that determine the instantaneous shape of the interface. The approximate expression for the gradient operator becomes exact when applied on the interface.

Next, following Lundgren & Mansour⁶⁷ we introduce the decomposition of the velocity field in the tangential force balance to get,

$$\bar{t} \cdot \left[\bar{\nabla} \bar{V} + (\bar{\nabla} \bar{V})^T \right] \cdot \bar{n} = \bar{t} \cdot \bar{\nabla} \bar{u} \cdot \bar{n} + \bar{n} \cdot \bar{\nabla} \bar{u} \cdot \bar{t} + \bar{t} \cdot \bar{\nabla} \bar{U} \cdot \bar{n} + \bar{n} \cdot \bar{\nabla} \bar{U} \cdot \bar{t} = 0. \quad (II.28)$$

Due to the irrotationality of \bar{u} we get

$$\bar{t} \cdot \bar{\nabla} \bar{U} \cdot \bar{n} + \bar{n} \cdot \bar{\nabla} \bar{U} \cdot \bar{t} = -2 \bar{t} \cdot \bar{\nabla} \bar{u} \cdot \bar{n}. \quad (II.29)$$

Upon introduction of the gradient operator as defined in equation (II.27) and appropriate differentiation of the unit vectors we obtain

$$\frac{\partial U_t}{\partial n} + \frac{\partial U_n}{\partial s} + U_t L = -2 \left(\frac{\partial u_n}{\partial s} + u_t L \right) = -2 \left(\frac{\partial^2 \Phi}{\partial n \partial s} + \frac{\partial \Phi}{\partial s} L \right), \quad (II.30)$$

where L is one of the fundamental magnitudes of the second kind⁷³ (see also the appendix for more details on the coordinate system) and t, n as subscripts on U or u denote the corresponding component of the velocity vector. Both velocity fields satisfy continuity which, when written for the rotational flow field, takes the form,

$$\frac{1}{r \sin \theta} \frac{\partial}{\partial s} (U_t r \sin \theta) - U_n \left(L + \frac{N}{r^2 \sin^2 \theta} \right) + \frac{\partial U_n}{\partial n} = 0 \quad (II.31)$$

where N is another fundamental magnitude of the second kind. Since n is small inside the boundary layer formed by the rotational velocity field, from equation (II.31) we deduce that $U_t \gg U_n$. Consequently, setting n to be of order δ inside the boundary layer

and considering that the right hand side of (II.30) is an order one quantity, the normal derivative of the tangential component of the rotational velocity field becomes the dominant term on the left hand side of equation (II.30), which now reads

$$\frac{\partial U_t}{\partial n} = -2 \left(\frac{\partial^2 \Phi}{\partial n \partial s} + \frac{\partial \Phi}{\partial s} L \right), \quad U_t = O(\delta). \quad (\text{II.32})$$

Then, from continuity $U_n = O(\delta^2)$.

The goal of this approach is to account for the effect of viscosity through the use of quantities that are evaluated on the bubble's surface. To this end we introduce equation (II.15) in the equations of motion and get

$$\frac{DU_t}{Dt} - \vec{U} \cdot \frac{D\vec{t}}{Dt} + \vec{U} \cdot \vec{\nabla} \vec{u} \cdot \vec{t} = -\frac{\partial p}{\partial s} + Oh \frac{\partial^2 U_t}{\partial n^2} \quad (\text{II.33})$$

$$\frac{DU_n}{Dt} - \vec{U} \cdot \frac{D\vec{n}}{Dt} + \vec{U} \cdot \vec{\nabla} \vec{u} \cdot \vec{n} = -\frac{\partial p}{\partial n} + Oh \frac{\partial^2 U_n}{\partial n^2} \quad (\text{II.34})$$

for the tangential and normal directions, respectively, after eliminating the irrotational part of the equations and the tangential component of viscous dissipation. Taking into account the small thickness of the boundary layer surrounding the interface, the order of magnitude of the different velocity components and dropping derivatives along the tangential direction taken to be much smaller than those along the normal, we obtain an estimate for the size of the boundary layer, $\delta \sim Oh^{1/2}$, and the rotational part of the pressure, $p \sim \delta^2$, while equation's (II.33) and (II.34) become,

$$\frac{DU_t}{Dt} + U_t \vec{t} \cdot \vec{\nabla} \vec{u} \cdot \vec{t} = Oh \frac{\partial^2 U_t}{\partial n^2} + O(\delta^2) \quad (\text{II.35})$$

$$U_t \vec{t} \cdot \frac{D\vec{n}}{Dt} - U_t \vec{t} \cdot \vec{\nabla} \vec{u} \cdot \vec{n} = \frac{\partial p}{\partial n} + O(\delta^2). \quad (\text{II.36})$$

Employing equation (II.17b) the components of \vec{U} can be expressed in terms of the vector potential \vec{A} as,

$$U_t = -\frac{\partial A}{\partial n}, \quad U_n = \frac{1}{r \sin \theta} \frac{\partial}{\partial s} (r \sin \theta A), \quad (\text{II.37})$$

which makes A an $O(\delta^2)$ quantity. Next, we substitute the above expressions in the equations of motion, (II.35) and (II.36), and integrate across the boundary layer, where the vortical part of the velocity and pressure fields vanish, to get the variation of the vector potential with time as well as the pressure on the surface of the bubble:

$$\frac{DA}{Dt} = A \left(\vec{n} \cdot \vec{\nabla} \vec{u} \cdot \vec{n} - \vec{t} \cdot \vec{\nabla} \vec{u} \cdot \vec{t} \right) - Oh \frac{\partial U_t}{\partial n} \quad (\text{II.38})$$

$$p = A \left(\vec{t} \cdot \vec{\nabla} \vec{u} \cdot \vec{n} \right) \quad (\text{II.39})$$

Finally, we introduce the irrotational normal force balance in equation (II.12) to get the corrected expression for the evolution of the scalar velocity potential including weak viscous effects

$$\frac{D\Phi}{Dt} = \frac{u^2}{2} + 2P_\infty - 2P_G + 2p - 2H - 2Oh \left(\vec{n} \cdot \vec{\nabla} \vec{u} \cdot \vec{n} \right). \quad (\text{II.40})$$

As mentioned in the beginning of this subsection this approach was first introduced by Lundgren & Mansour⁶⁷ and has been used ever since by other investigators as well, most notably Boulton-Stone & Blake⁷⁴.

Before we summarize the equations that we solve in order to capture the dynamic behavior of the bubble, we have to emphasize that we work with variables that are evaluated on the surface and that can be calculated by solving the interfacial equations presented above. For example, the tangential component of the vortical part of the velocity field is given via the normal derivative of the vector potential. The latter cannot be obtained by solving a differential equation defined solely on the interface. Consequently, since the location of a free surface is determined purely by its normal velocity, with the tangential component operating as a mapping function that controls the relative position of the Lagrangian particles on the free surface, we move the particles in the following fashion

$$\frac{d\vec{r}_s}{dt} = \vec{u} + U_n \vec{n}. \quad (\text{II.41})$$

Consequently, instead of material points we refer to marker points that move according to the above expression without any loss in accuracy as far as the bubble shape is concerned. In terms of spherical coordinates, through which we describe the position of the particles, we have

$$\frac{dr}{dt} = \frac{(u_n + U_n)r\theta_s + u_t r_s}{\sqrt{r_s^2 + r^2\theta_s^2}}, \quad \frac{d\theta}{dt} = \frac{u_t r\theta_s - (u_n + U_n)r_s}{r\sqrt{r_s^2 + r^2\theta_s^2}} \quad (\text{II.42a,b})$$

where subscript s denotes partial differentiation with respect to the arc-length s of the generating curve of the axisymmetric interface and $\frac{d}{dt} = \frac{\partial}{\partial t} + (\vec{u} + U_n \vec{n}) \cdot \vec{\nabla}$. In the same fashion and in order to move the particles in a consistent manner, the equations describing the evolution of the scalar and vector potential become

$$\frac{d\Phi}{dt} = \frac{u^2}{2} + u_n U_n + 2P_\infty - 2P_G + 2A(\vec{t} \cdot \vec{\nabla} \vec{u} \cdot \vec{n}) - 2H - 2Oh(\vec{n} \cdot \vec{\nabla} \vec{u} \cdot \vec{n}) \quad (\text{II.43})$$

$$\frac{dA}{dt} = A(\vec{n} \cdot \vec{\nabla} \vec{u} \cdot \vec{n} - \vec{t} \cdot \vec{\nabla} \vec{u} \cdot \vec{t}) - Oh \frac{\partial U_t}{\partial n}. \quad (\text{II.44})$$

In the last equation the additional term $U_n \frac{\partial A}{\partial n}$ has been dropped from the right hand side as it is of higher order, $O(\delta^3)$. Overall, equation's (II.42a,b), (II.43), (II.44), along with the integral equation (II.26), equation (II.14) that prescribes the variation of the pressure inside the bubble, the boundary conditions due to axisymmetry, i.e. equation (II.25) with the additional condition of vanishing vector potential at the poles, $A(0,t)=A(\pi,t)=0$, and the initial conditions (II.1), (II.2), (II.7) and (II.8) provide the complete formulation of the dynamic behavior of the bubble. All the variables that are involved are evaluated on the surface, which, in view of the axisymmetry, renders the problem one-dimensional. More details on the proper evaluation of the variables in the frame of the boundary fitted coordinate system that is used, are given in the Appendix.

II.1.3 Energy variation

Starting from the identity

$$\iiint_V \frac{\partial \Phi}{\partial t} \nabla^2 \Phi dV = 0, \quad (\text{II.45})$$

and performing integration by parts we obtain

$$\iint_A \frac{\partial \Phi}{\partial t} \frac{\partial \Phi}{\partial n} dA - \frac{1}{2} \iiint_V \frac{\partial}{\partial t} [(\vec{\nabla} \Phi)^2] dV = 0 \quad (\text{II.46})$$

Invoking the Reynolds transport theorem we get,

$$\frac{1}{2} \frac{d}{dt} \iiint_V [(\vec{\nabla} \Phi)^2] dV = \iint_A \frac{\partial \Phi}{\partial t} \frac{\partial \Phi}{\partial n} dA + \frac{1}{2} \iint_A (\vec{\nabla} \Phi)^2 (u_n + U_n) dA \quad (\text{II.47})$$

Finally, integration by parts on the left hand side integral and introduction of the dynamic boundary condition (II.43) provides the energy balance for the dynamics of the bubble

$$\begin{aligned} \frac{1}{2} \frac{d}{dt} \iint_A \Phi \frac{\partial \Phi}{\partial n} dA - \frac{1}{2} \iint_A u^2 U_n dA + \iint_A \frac{\partial \Phi}{\partial n} (2H + 2P_G - 2P_{St}) dA = \\ \iint_A 2p \frac{\partial \Phi}{\partial n} dA - \frac{2}{\text{Re}} \iint_A \frac{\partial \Phi}{\partial n} \frac{\partial u_n}{\partial n} dA. \end{aligned} \quad (\text{II.48})$$

The first two integrals on the left hand side signify variations in the total kinetic energy of the system including the effect of the vortical velocity field. The first integral on the right hand side represents energy loss due to the rotational part of the pressure whereas the second integral represents classical dissipation due to vorticity near a zero shear surface. In the limit as $\text{Re} = \text{Oh}^{-1}$ tends to infinity the energy balance for inviscid⁶⁶ bubble oscillations is recovered.

$$\frac{d}{dt} \left[\frac{1}{2} \iint_A \Phi \frac{\partial \Phi}{\partial n} dA + \iint_A dA + V \left(P_G + \frac{2P_{St}}{\gamma - 1} \right) \right] = 0 \quad (\text{II.49})$$

II.2 NUMERICAL SOLUTION

The numerical solution of the equation set presented at the end of section II.1.2 is obtained in a fashion similar to the one adopted by Pelekasis & Tsamopoulos⁶⁶ for the case of two interacting bubbles. More specifically, the Boundary Integral formulation was used in the Eulerian frame of reference, in order to establish a connection between the scalar potential and its normal derivative at the interface, whereas the Lagrangian representation was adopted for the motion of surface marker points in order to capture the evolution with time of the scalar and vector potentials. This requires solution of partial differential equations involving time and only one spatial dimension, as a combined result of axisymmetry and the use of boundary integral formulation. To this end, the azimuthal dependence has been integrated out of Eq. (II-26) thus leaving an integral equation of the first kind for the normal derivative of the scalar potential, given the potential, defined along the generating curve of the bubble's surface. Since the early studies in modeling cavitating bubbles⁷⁵ next to a solid or a free surface the boundary integral method has extensively been used for capturing bubble oscillations, collapse or breakup^{21,76}. For a review article on the boundary integral method for potential flow problems and comparative studies on the efficiency of different boundary integral formulations the interested reader is referred elsewhere^{77,78}.

II.2.1 Finite-Element Implementation

The Galerkin/finite-element method is used for transforming the kinematic and dynamic boundary conditions from partial differential equations to initial value equations. To this end, the corresponding unknown variables (r, θ, Φ, A) are represented as a finite sum of unknown coefficients multiplied by a set of prespecified basis functions that are nonzero only over a few elements of the domain. The weak formulation results upon multiplication of Eqs. (II.42a,b), (II.43) and (II.44) by each basis function in turn and integration over the domain. Integration by parts is also carried out whenever it is possible in order to eliminate the second derivative, appearing in the surface curvature term. Four Gauss integration points are used for the evaluation of integrals over each element. This ensures that any numerical error is controlled by the interpolation of unknown functions rather than by numerical integration⁷⁹.

The cubic B-splines are used as a basis functions which are nonzero over four elements at most and guarantee continuity of the function along with its first and second derivatives⁸⁰. Since $B_i(\xi = \xi_j) \neq \delta_{ij}$, the coefficients, a_i, b_i, c_i, d_i of the B-spline representation

$$\begin{aligned} r(\xi, t) &= \sum_{i=0}^{N+1} a_i(t) B_i(\xi), \\ \theta(\xi, t) &= \sum_{i=0}^{N+1} b_i(t) B_i(\xi), \\ \Phi(\xi, t) &= \sum_{i=0}^{N+1} c_i(t) B_i(\xi), \\ A(\xi, t) &= \sum_{i=0}^{N+1} d_i(t) B_i(\xi), \end{aligned} \tag{II.50}$$

are different from the values of the unknown functions at the nodes. Consequently, this representation will require an additional matrix multiplication in order to obtain the nodal values of the functions. The coefficients corresponding to fictitious nodes outside the domain, namely, $a_0, a_{N+1}, b_0, b_{N+1}, c_0, c_{N+1}, d_0, d_{N+1}$ are expressed in terms of coefficients in the interior nodes by using boundary conditions. Since B-splines extend over four elements, they give rise to a banded matrix with a bandwidth of seven and require more calculations for the construction of the system matrix. These small disadvantages are outweighed by the increased accuracy and smoothness of the solution. This is because B-splines are $O(h^4)$ and $O(h^3)$ accurate in interpolating a smooth function and its first derivative, respectively.

II.2.2 Boundary-Element Implementation

The boundary integral equation (II.26) is discretized in a fashion similar to that of the differential equations previously described, and the corresponding unknown is written as

$$\frac{\partial \Phi}{\partial n}(\xi, t) = \sum_{i=0}^{N+1} g_i(t) \cdot B_i(\xi)$$

By letting the field point $\hat{\xi}$ approach each one of the nodal points and integrating through all the elements related to the source point ξ , N equations are obtained. The axisymmetric kernels G and $\frac{\partial G}{\partial n}$ are given in spherical coordinates as

$$G = \frac{K(m)}{\pi\sqrt{a+b}} \quad (\text{II.51})$$

and

$$\begin{aligned} \frac{\partial G}{\partial n} = n_r \frac{\partial G}{\partial r} + n_\theta \frac{\partial G}{\partial \theta} \frac{1}{r(\xi)} = \frac{1}{2r\pi\sqrt{a+b}} \left[\frac{r^2(\hat{\xi}) - r^2(\xi)}{a-b} E(m) - K(m) \right] n_r + \\ \frac{r(\hat{\xi})}{\pi\sqrt{a+b}} \left[\frac{4 \cos[\theta(\xi)] \sin[\theta(\hat{\xi})]}{a+b} \frac{dK}{dm} - \frac{\sin[\theta(\xi) + \theta(\hat{\xi})]}{a-b} E(m) \right], \end{aligned} \quad (\text{II.52})$$

where,

$$\begin{aligned} a &= r^2(\xi) + r^2(\hat{\xi}) - 2r(\xi)r(\hat{\xi})\cos[\theta(\xi)]\cos[\theta(\hat{\xi})] \\ b &= 2r(\xi)r(\hat{\xi})\sin[\theta(\xi)]\sin[\theta(\hat{\xi})] \\ m &= \frac{2b}{a+b} \end{aligned} \quad (\text{II.53})$$

and $K(m)$ and $E(m)$ are the elliptic integrals of the first and second kind, respectively.

These integrals are approximated with less than 2×10^{-8} error by the expressions

$$\begin{aligned} K(m) &= \sum_{i=0}^4 A_i m_i' + \ln\left(\frac{1}{m_i}\right) \sum_{i=1}^4 C_i m_i' \\ E(m) &= 1 + \sum_{i=1}^4 D_i m_i' + \ln\left(\frac{1}{m_i}\right) \sum_{i=1}^4 E_i m_i' \end{aligned} \quad (\text{II.54})$$

where $m_i = 1 - m$ and A_i, C_i, D_i, E_i are constants given in [81]. When the field point $\hat{\xi}$ coincides with one of the source points ξ , the G kernel exhibits a logarithmic

singularity of the form $\ln\left(\frac{1}{a-b}\right) = \ln\left(\frac{1}{|\mathbf{x} - \hat{\mathbf{x}}|^2}\right)$, while the $\frac{\partial G}{\partial n}$ kernel exhibits a

stronger singularity of the form $|\mathbf{x} - \hat{\mathbf{x}}|^{-1}$. The former term is integrated by resorting to a 12-point logarithmic quadrature [79]. The latter term is rendered regular by the procedure described in the previous section. The remaining regular terms are integrated using the normal Gaussian quadrature with varying numbers of Gauss points as suggested in [82]. For further details, see Pelekasis et al.[72]

Despite the fact that reliable solvers of the full Navier-Stokes equations have also been developed the boundary integral method is still widely applied due to its superiority in capturing details of severely deformed interfaces, with high accuracy and minimum computational effort. The weak viscous correction of the boundary integral method, such as the one employed here, extends the validity of the standard potential theory formulation, to the extent that large displacement thickness effects are not present. This would be the case, for example, in situations with massive flow separation where the wake structure plays a central role in the dynamics, in which case resorting to the full Navier-Stokes becomes necessary. In the present study the appearance of liquid jets moving along the direction of elongation might entail such phenomena, but they occupy very thin regions and evolve very abruptly for any significant displacement thickness effect to alter the dynamic behavior captured by our numerical solution.

II.2.3 Integration in Time

The fourth order explicit Runge-Kutta time integration scheme was employed due to its better stability characteristics⁷². In fact, it was seen that, for small initial deformations, doubling the number of elements along the interface required, roughly, a four times smaller time step for numerical stability. Solution of the unknowns of the problem is done sequentially. Once the complete state of the bubble is known at a certain time instant the surface marker points are moved in the manner prescribed by equations (II.42a,b) and their new coordinates are obtained. The updated values of the two potential functions are obtained in the same way. Next, using the boundary integral equation (II.26) we get the normal derivative of the scalar potential. Finally the bubble volume is calculated, the interior pressure is advanced and the procedure is repeated until the bubble either breaks up or eventually returns to its equilibrium spherical shape. We are particularly interested in the dynamics of collapse or break-up. As explained in the following, mesh regriding takes place as time advances in order to prevent concentration of the marker points in certain regions of the interface leaving the rest of the interface misrepresented. Subsequently, the time step is adapted so that numerical stability is preserved.

Owing to the initial elongation and subsequent surface deformation, marker points are distributed in such a way as to prohibit large discrepancies in the element length while providing accurate discretization in regions of large curvature. This is accomplished by positioning the marker points along the interface so that the integral⁸³

$$\int_0^1 (1+d|-2H|)(r_\xi^2 + r^2\theta_\xi^2) d\xi \quad (II.55)$$

is minimized; d is a parameter controlling the concentration of grid points in regions of high curvature. It ranges from 10^{-2} to 10^{-3} as the number of elements increases from 80 to 160. Decreasing d amounts to reducing the emphasis placed upon curvature variations while regriding. As a result of this procedure the time step has to be adapted in order to maintain stability of the numerical scheme and properly resolve the capillary waves that arise as part of the dynamics of bubble deformation.

Initially, the dynamics is characterized by the high curvature regions around the two poles where the dimensionless radius of curvature is the smallest. Balancing the dynamic pressure with surface tension forces provides the proper time scale in this region as

$$\tau = \left(\frac{\rho R_0^3}{\sigma} \right)^{1/2}, \quad (\text{II.56})$$

where R_0 is the radius of curvature at the two elongated tips of the bubble. Consequently, in order to capture the dynamics in the early stages of the motion as parameter S decreases, since the minimum element size Δs_{\min} decreases with regridding, the time scale should also be decreased following the 3/2 power law mentioned above, $\Delta t \sim (\Delta s_{\min})^{3/2}$. This universal scaling law was also obtained in [27] in the context of capillary pinch-off of drops. In the present study the effect of initial elongation has to be accounted for as well. In practice, in order to respect the stability requirements of the Runge-Kutta time integrator which were found elsewhere⁷² to obey a quadratic law, $\Delta t \sim \Delta s_{\min}^2$, and to account for the decreasing radius of curvature as parameter S decreases, in the simulations to be presented hereafter the time step was initially set to $\Delta t = \Delta s_{\min}^2 S$. This scaling was found to be appropriate in the beginning of the bubble motion. Once the simulation commences, for a given value of S , the time step is adapted according to the following law:

$$\frac{\Delta t^{\text{new}}}{\Delta t^{\text{old}}} = \left(\frac{\Delta s_{\min}^{\text{new}}}{\Delta s_{\min}^{\text{old}}} \right)^\alpha \frac{H_{\min}^{\text{new}}}{H_{\min}^{\text{old}}} \quad (\text{II.57})$$

where H_{\min} is the minimum mean radius of curvature on the bubble's surface and α an adjustable parameter that is initially set to one. As time evolves, the time step has to be further reduced due to the appearance of two high-speed jets approaching each other along the axis of symmetry, hence parameter α has to be increased accordingly. During collapse areas with very small radius of curvature appear in the form of dimples that eventually touch at the equatorial plain. Accurate resolution of such areas requires further remeshing and time step adaptation, which is performed by further increasing α which had to become as large as 3 and 4. More specifically, in the beginning of the simulation the time step was in the order of 10^{-5} whereas during collapse it had to be dropped to 10^{-8} .

It should also be stressed that, for calculations with finite Oh^{-1} , marker points are used for tracking the evolution of the interface instead of Lagrangian particles. This is a result of our inability to evaluate the tangential component of the vortical velocity field solely based on quantities that are defined on the boundary. Nevertheless, this does not restrict the validity of our results since the shape of a free surface can always be found from information regarding the normal component of the velocity of particles residing on the interface. The tangential component simply acts as a function that maps points between the previous and the current location of the interface. This is a well-known result that has been used by previous investigators⁸⁴ in order to optimize the distribution of the grid points on the interface and avoid grid distortion. In the present study the potential part of the tangential component of the velocity of surface particles is used for updating the position of the interface, along with the normal component of the potential and vortical parts, without any compromise in numerical accuracy.

Numerical calculation of the azimuthal component of the vector potential, involves interpolation of second order derivatives of the scalar potential in a manner that is not amenable to reduction of order via integration by parts. Consequently, as the simulation proceeds, short wave instabilities tend to appear whose wavelength is on the order of minimum element size. Such short wave instabilities often appear in high Oh^{-1}

calculations^{67,72} and cannot be eliminated with mesh refinement alone. The standard procedure in order to circumvent this problem is to implement filtering of the higher modes while monitoring the energy of the system so that it is dissipated appropriately. Inviscid calculations do not exhibit such instabilities hence filtering is avoided. However, in all the simulations to be presented in the following where Oh^{-1} is taken to be large but finite, after a certain number of time steps the vector potential is filtered by introducing the fourth order derivative with respect to ξ ,

$$\frac{\partial A}{\partial t} = \lambda \frac{\partial^4 A}{\partial \xi^4}. \quad (II.58)$$

The above equation is discretized with the second order accurate fully implicit scheme,

$$A'_j = A_j + \frac{\lambda \Delta t}{\Delta \xi^4} (A'_{j+2} - 4A'_{j+1} + 6A'_j - 4A'_{j-1} + A'_{j-2}), \quad (II.59)$$

which possesses improved stability characteristics; $\lambda \Delta t / \Delta \xi^4$ was set to a large value, typically between 100 and 1000, for stability reasons. As will be seen in the numerical tests presented in the end of this section, this methodology allows for accurate and efficient evaluation of the vortical part of the flow, which is essential for handling weak viscous effects.

Another important aspect of the numerical methodology that is employed here has to do with the use of symmetry with respect to the equatorial plane in order to reduce the storage requirements and processing time for given level of accuracy. When the shape of the bubble is expected to remain symmetric throughout the simulation, the domain of discretization can be halved so that it includes only one of the two hemispheres, say the north. Consequently; and in view of axisymmetry, only half of the generating curve that connects the north and the south pole needs to be discretized and the size of the full matrix that has to be constructed and inverted for the calculation of the normal derivative of the scalar potential, becomes four times smaller which constitutes a significant reduction in the computational load. To this end, the same symmetry boundary conditions that were originally imposed at the south pole, equation (II.25), are now implemented at the equator where coordinate ξ' is set to one in the new formulation. In addition, integral equation (II.26) is rearranged to incorporate symmetry. More specifically, the single layer kernel, G , is symmetric when the shape of the interface is symmetric with respect to the equator and consequently the integral containing kernel G in equation (II.26) becomes

$$\int_0^1 \frac{\partial \Phi}{\partial n}(r, \theta, t) G(\hat{r}, \hat{\theta}, r, \theta) r \sin \theta (r_\xi^2 + r^2 \theta_\xi^2)^{1/2} d\xi = 2 \int_0^1 \frac{\partial \Phi}{\partial n}(r, \theta, t) G(\hat{r}, \hat{\theta}, r, \theta) r \sin \theta (r_\xi^2 + r^2 \theta_\xi^2)^{1/2} d\xi' \quad (II.60)$$

with $r, \theta, \hat{r}, \hat{\theta}$, defined along the line connecting the north pole with the equator. The double layer kernel on the other hand is not symmetric and as a result the integral containing $\partial G / \partial n$ becomes,

$$\begin{aligned}
& \int_0^1 \left[\Phi(r, \theta, t) - \Phi(\hat{r}, \hat{\theta}, t) \right] \frac{\partial G}{\partial n}(\hat{r}, \hat{\theta}, r, \theta) r \sin \theta (r_{\xi}^2 + r^2 \theta_{\xi}^2)^{1/2} d\xi = \\
& \int_0^1 \left[\Phi(r, \theta, t) - \Phi(\hat{r}, \hat{\theta}, t) \right] \frac{\partial G}{\partial n}(\hat{r}, \hat{\theta}, r, \theta) r \sin \theta (r_{\xi'}^2 + r^2 \theta_{\xi'}^2)^{1/2} d\xi' - \\
& \int_0^1 \left[\Phi(r, \omega, t) - \Phi(\hat{r}, \hat{\theta}, t) \right] \frac{\partial G}{\partial n}(\hat{r}, \hat{\theta}, r, \omega + \pi/2) r \sin \omega (r_{\xi''}^2 + r^2 \omega_{\xi''}^2)^{1/2} d\xi'',
\end{aligned} \tag{II.61}$$

where,

$$\omega = \theta - \pi/2 \leq \pi/2,$$

$$\Phi(r, \omega, t) = \Phi(r, \omega + \pi/2, t), \quad \frac{\partial \Phi}{\partial n}(r, \omega, t) = \frac{\partial \Phi}{\partial n}(r, \omega + \pi/2, t). \tag{II.62}$$

As the number of elements increases construction of the system matrix, which is full as is normally the case with the boundary integral methodology, becomes the most time consuming part of the computation taking up more than 80 % of the CPU time^{66,72}. In order to minimize computational time we resort to parallel strategies. In particular, the system matrix is constructed in a parallel fashion with different processors dedicated to different rows of the matrix. The algorithm is implemented on a LINUX Cluster with 4 Xeon processors with significant savings in processing time.

II.2.4 Validation of the Numerical Scheme

The validity of the above numerical implementation was investigated in a number of cases some of which are presented in this section. First of all the linear prediction of the breathing mode frequency was recovered when the initial elongation was relatively small, $S \sim 1$. Figure II.2 shows the time evolution of the zeroth Legendre mode, P_0 , that is associated with volume oscillations, and the second Legendre mode, P_2 , for a slightly elongated bubble, $S=0.8$, of equilibrium radius $R= 5.8 \mu\text{m}$ that is oscillating in water at atmospheric pressure; $P_{St}=4.1$, $\varepsilon_B=0$, water is taken to be inviscid and 100 elements are used for the discretization of the interface. Despite the moderate value of ε orthogonal decomposition of the shape in the Legendre eigenmodes reveals that P_0 and P_2 dominate and oscillate at a frequency that is slightly smaller than that predicted by linear theory,

$$\omega_0 = [6(P_{St} + 1)\gamma - 2]^{1/2}, \quad \omega_k = [(k^2 - 1)(k + 2)]^{1/2}, \quad k \geq 1, \tag{II.63}$$

as a result of inertia.

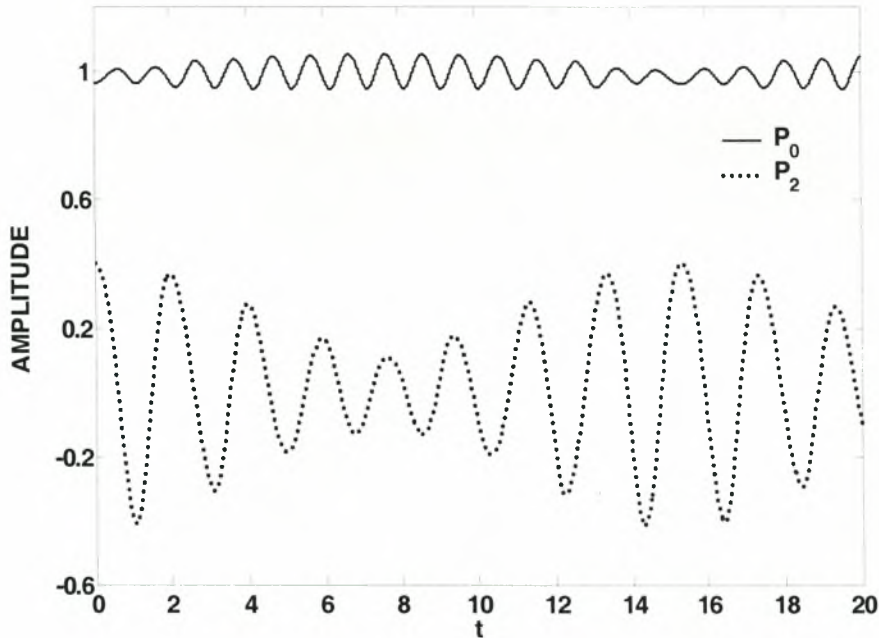


Figure II.2: Time evolution of the coefficients of Legendre modes P_0 and P_2 for the decomposition of the position of the interface f ; $S=0.8$, $P_{St}=4.1$, $Oh \rightarrow 0$, $\varepsilon_B=0$, with 100 elements in the region $0 \leq \theta \leq \pi$.

At a slower time scale there is exchange of energy between the two modes that is manifested in the beat exhibited in the oscillations of P_0 and P_2 in figure II.2. Physically this reflects the inward motion of the bubble along its two poles, as a result of the increased curvature in that region, which tends to restore its spherical shape at equilibrium. Subsequently, this motion is reversed due to the compressibility of the bubble and the whole cycle is repeated. The total energy remains constant, as expected in the absence of any damping mechanism, at the value predicted by integrating the governing equations over the entire flow domain, equation (II.49).

The effect of viscosity was also investigated by imposing a sinusoidal disturbance, of the type described by equation (II.2), on the static pressure in the far field. The forcing frequency is set to the dimensionless fundamental frequency of P_2 , $\omega_f = \omega_2$, S to 1 and ε to 0.5. Oh^{-1} was set to the value corresponding to a bubble with equilibrium radius $R = 5.8 \mu\text{m}$, i.e. $Oh^{-1} = 20.5$. Weak viscous analysis may not be exactly valid at this relatively low value, however it does provide us with a reliable estimate of viscous dissipation. In any case, this particular simulation was intended to serve as a test case for the behavior of the numerical scheme employed for calculating the vector potential and to establish the validity of the filtering scheme. The bubble is initially performing pure volume oscillations but eventually acquires a periodically deformed shape with P_0 and P_2 as the only eigenmodes and ω_2 as the corresponding frequency, figure II.3.

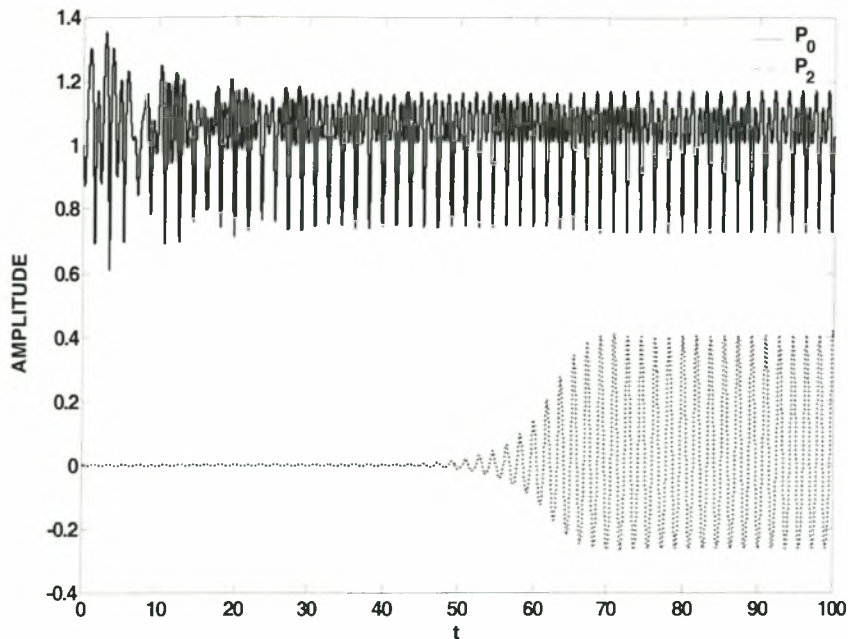


Figure II.3: Time evolution of the coefficients of Legendre modes P_0 and P_2 for the decomposition of the position of the interface f ; $S=1.0$, $P_{Si}=4.1$, $\varepsilon=0.5$, $\omega_f = \omega_2 = 3.46$, $Oh^{-1}=20.5$, with 100 elements in the region $0 \leq \theta \leq \pi$.

Finally, our numerical methodology was validated against mesh refinement for a rather demanding flow situation. Namely, the case with $S=0.6$ and $Oh^{-1}=1000$ was investigated and the evolution of the bubble shape and total energy was obtained from the initial stages of bubble motion until collapse, with 75 and 100 elements along half of the generating curve connecting the two poles in view of the symmetry of the shape, figures II.4(a) and II.4(c). The initial inward motion of the bubble along its axis of symmetry, as a result of the reduced curvature at the two poles, is accurately captured and, more importantly, the final stages of collapse are obtained with the formation of what seems to be two countercurrent liquid jets, figure II.4(b), that eventually meet at the equatorial plane. Dimple formation at the rounded ends of the two jets is clearly exhibited by the corresponding shapes, along with the formation of a small satellite bubble after collapse, figure II.4(c). More details on the physics of collapse are presented in the next section.

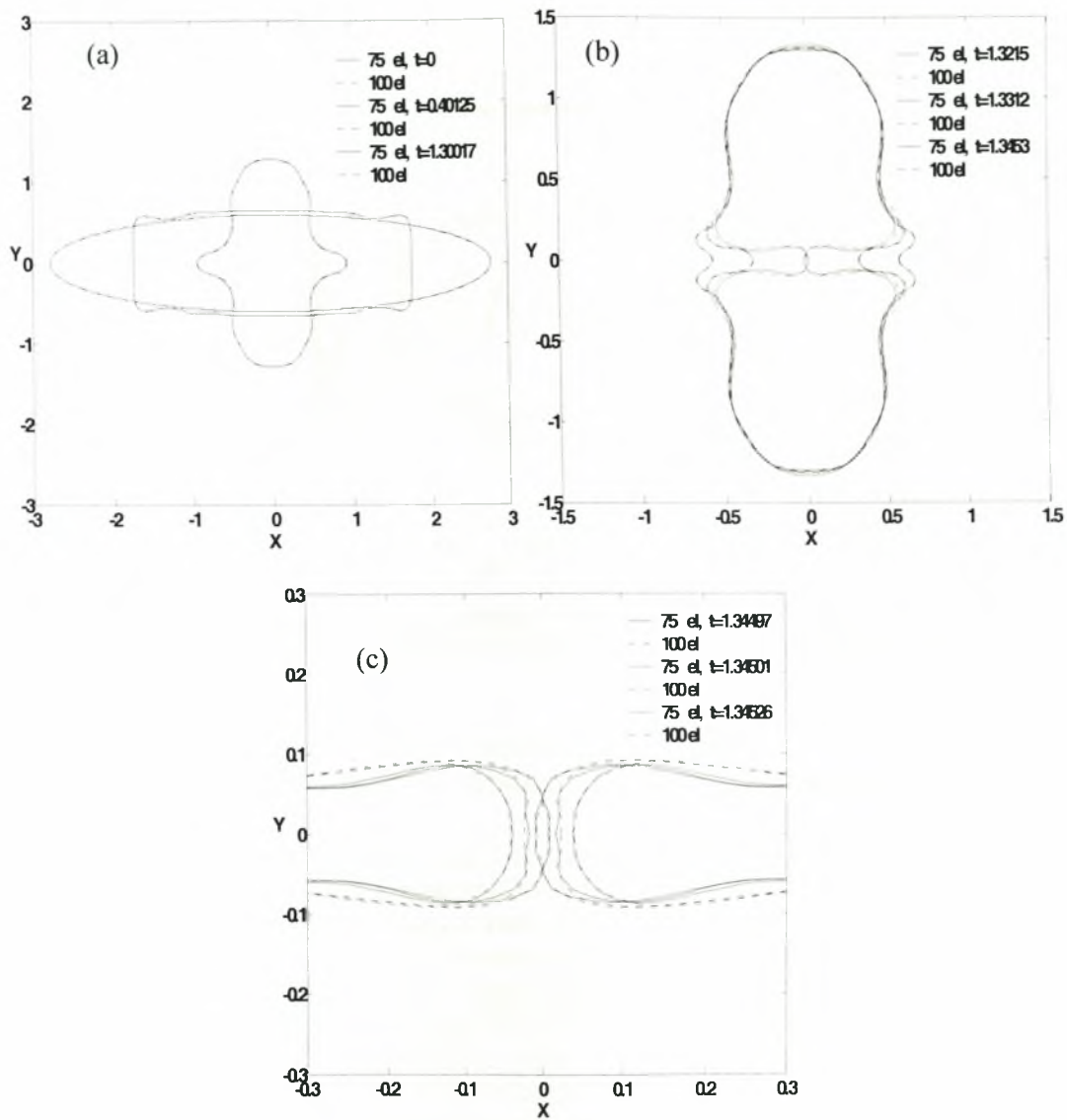


Figure II.4: Time evolution of the shape of the bubble (a) in the beginning of the motion, (b) during jet formation and (c) during collapse; $S=0.6$, $P_{St}=4.1$, $Oh^{-1}=1000$, with 75 and 100 elements in the region $0 \leq \theta \leq \pi/2$.

The variation of the total energy of the system is also monitored, figure II.5, as an additional means to check the validity of the numerical treatment of viscous effects. The time derivative of the kinetic and potential energy of the bubble is calculated numerically and compared against dissipation, in the manner shown in equation (II.48), with more than satisfactory agreement at least for the range of the calculation over which the kinetic energy does not change very abruptly. In the latter case numerical differentiation of the total kinetic energy becomes less accurate and monitoring of equation (II.48) quite difficult. From this stage on we have to resort to mesh refinement for establishing the validity of the numerical solution.

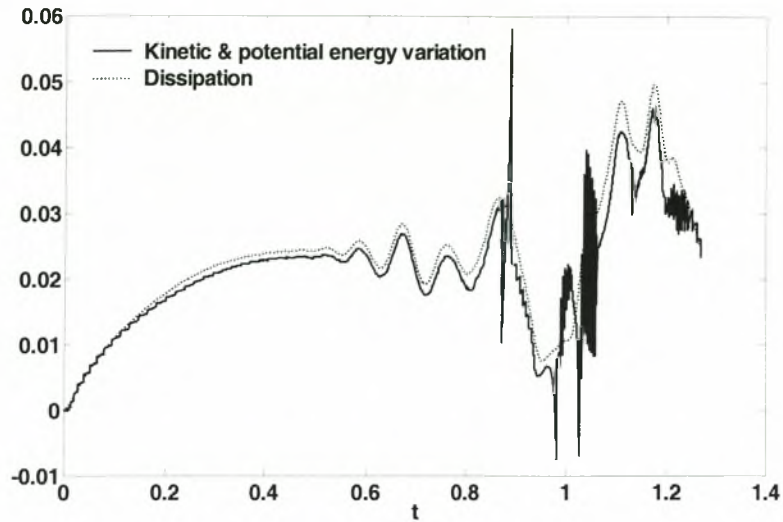


Figure II.5: Comparison between time variation of the total kinetic and potential energy and dissipation; $S=0.6$, $P_{St}=4.1$, $Oh^{-1}=1000$, with 100 elements in the region $0 \leq \theta \leq \pi/2$.

II.3 RESULTS & DISCUSSION

Based on the asymptotic analysis and the numerical methodology that were presented in the previous sections, a series of simulations was carried out in an effort to capture the initial dynamics as well as the final stages of collapse, whenever that was indeed the case, for small or large initial elongations. Inviscid oscillations as well as weak viscous effects were also accounted for by adjusting Oh . Finally the effects of small internal overpressure and initial fore-aft asymmetry in the bubble shape were included. The investigation of the possibility of different break-up mechanisms under the influence of very large internal overpressures and elongations, a situation that is closer to the physics of sonoluminescence, is analysed in a next chapter.

In this fashion it was found that, for small or moderate initial elongations, $S > 0.6$, of micron size bubbles, $R = 5.8 \mu\text{m}$, oscillating in water at atmospheric pressure, $P_{St} = 4.1$, and no internal overpressure, $\varepsilon_B = 0$, the dynamics is initially determined by the energy exchange between volume oscillations, dominated by P_0 , and shape oscillations, dominated by P_2 . This tendency is clearly exhibited in figure II.2, where the evolution of the corresponding modes is plotted vs. time, as well as in figure II.6 where the shape deformation of the bubble is followed for a number of periods of the breathing mode, $T_0 = 2\pi/\omega_0$, when $S = 0.8$ and viscous dissipation is neglected, $Oh \rightarrow 0$. In this case the bubble oscillates indefinitely, without breaking-up, while its shape is deformed in a manner determined by slow energy transfer to higher modes.

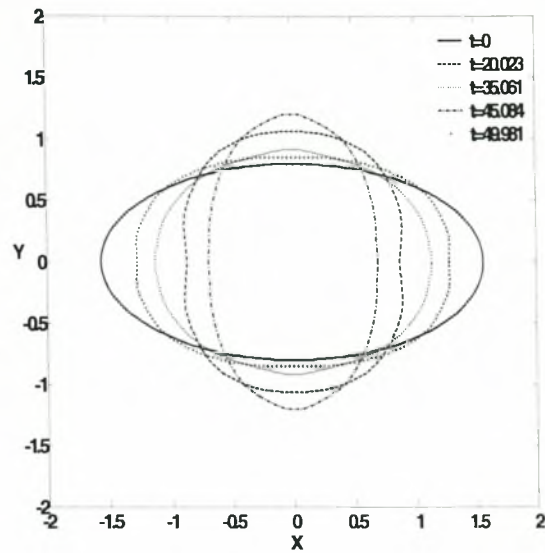


Figure II.6: Bubble shapes for the inviscid case with $S=0.8$, $\varepsilon_B=0$ and 50 elements in the region $0 \leq \theta \leq \pi/2$.

When viscous effects are included in the model the shape of the bubble eventually returns to its equilibrium spherosymmetric configuration, see figure II.7 for the case with $Oh^{-1}=500$.

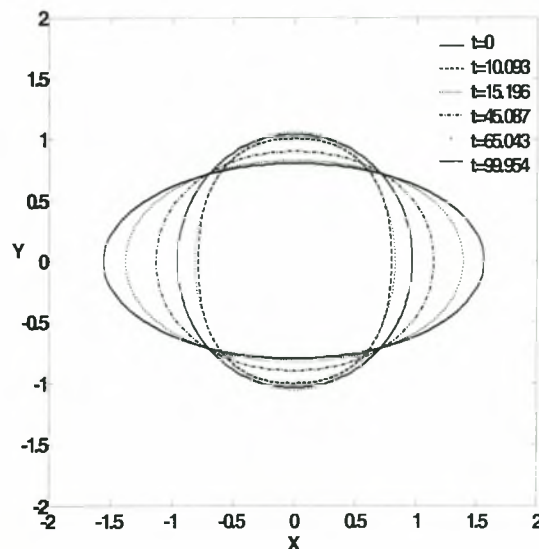


Figure II.7: Bubble shapes for the case with $S=0.8$, $\varepsilon_B=0$, $Oh^{-1}=500$ and 50 elements in the region $0 \leq \theta \leq \pi/2$.

This process occurs faster with decreasing Oh^{-1} . The slow “beat” between P_0 and P_2 with the final domination of P_0 , as a result of viscous damping, is shown in figures II.8(a) and II.8(b) for P_0 when $Oh^{-1}=1000$ and 500 and in figures II.8(c) and II.8(d) for P_2 and the same values of Oh^{-1} . This pattern was seen to persist for quite a wide range

of initial deformations until when $S=0.62$ and $Oh^{-1} \rightarrow \infty$ the two opposite ends of the bubble touch each other at the equatorial plane. In this case the kinetic energy that is acquired near the two poles of the bubble as they move towards each other due to the initial elongation, is just enough to overcome the reaction exercised by the gas inside the bubble, in the form of an increase in its interior pressure as a result of its compressibility. When viscous effects are included the bubble eventually settles to a sphere, as expected.

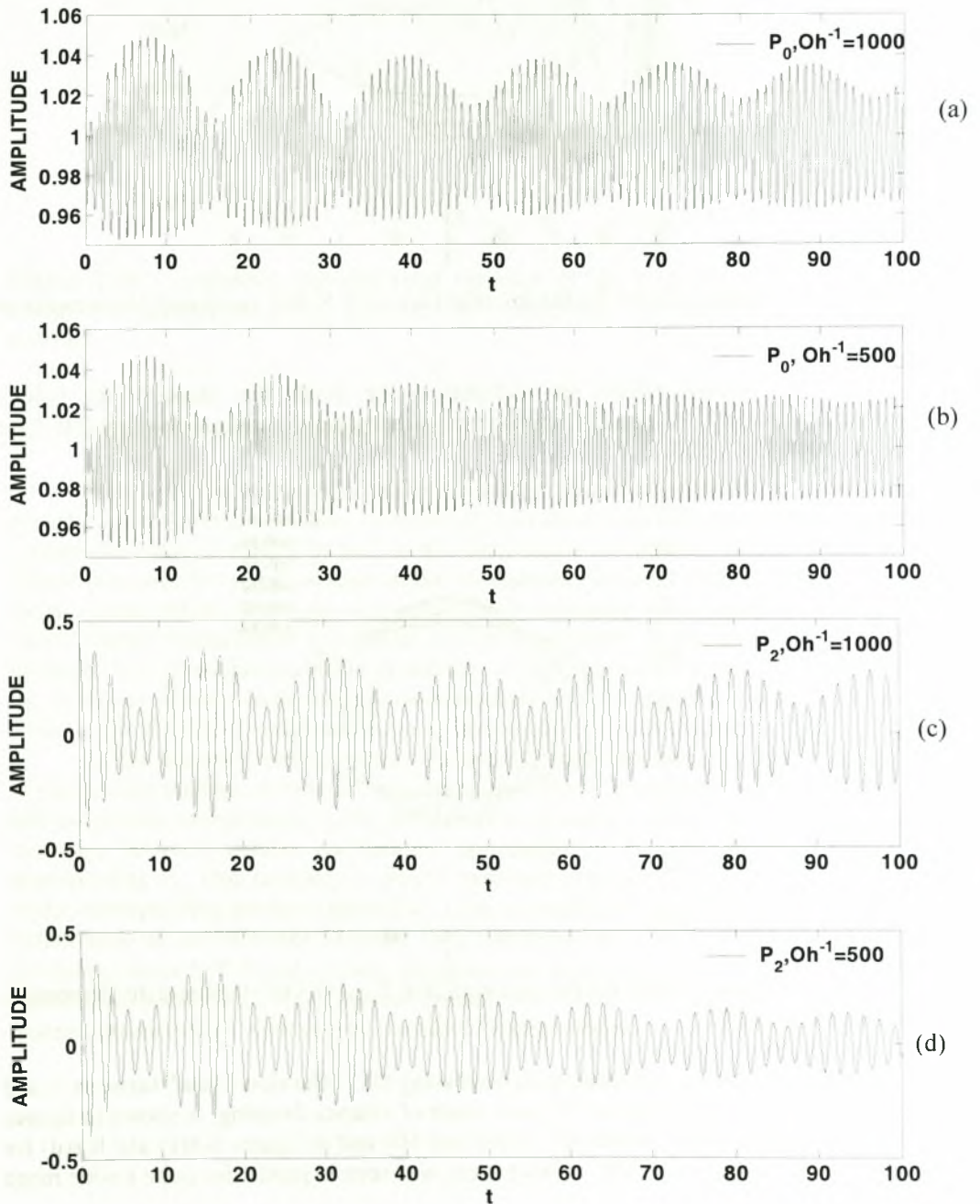


Figure II.8: Time evolution of the coefficients of Legendre modes: (a) P_0 , $Oh^{-1}=1000$, (b) P_0 , $Oh^{-1}=500$, (c) P_2 , $Oh^{-1}=1000$ and (d) P_2 , $Oh^{-1}=500$, for the case with $S=0.8$ $\varepsilon_\beta=0$ and 50 elements in the region $0 \leq \theta \leq \pi/2$.

As the initial elongation further increases, $S=0.6$, this interesting dynamic effect is more pronounced towards the final stages of the bubble collapse. The initially prolate shaped bubble soon acquires an oblate form, as was the case with smaller initial deformations, except that now the two poles exhibit more intense deformations, the regions near them are dominated by higher harmonics and consequently they undergo faster oscillations locally; see figure II.9(a) when $S=0.6$ and $Oh^{-1} \rightarrow \infty$. Eventually, two high-speed jets are formed at the two poles that approach each other along the axis of symmetry. As the two jets approach the equatorial plane they spread and form rounded ends that keep approaching, figure II.9(b), until they eventually collide.

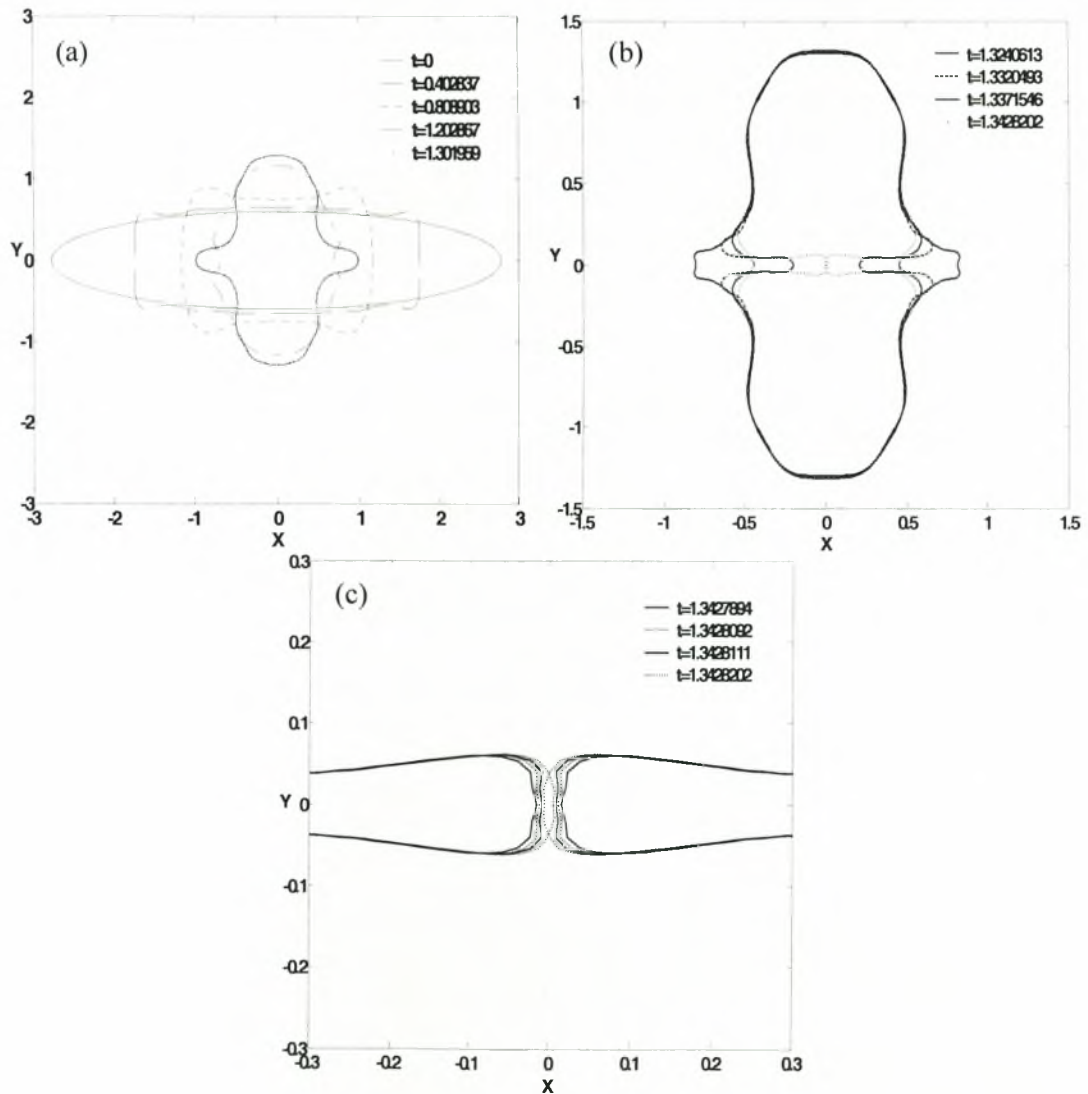


Figure II.9: Time evolution of the shape of the bubble (a) in the beginning of the motion, (b) during jet formation and (c) during collapse; $S=0.6$, $P_{St}=4.1$, infinite Oh^{-1} , with 100 elements in the region $0 \leq \theta \leq \pi/2$.

In the present study the film that is formed in the region between the two jet-tips that are approaching each other, exerts no lubrication force upon them owing to the negligible viscosity of the gas inside the bubble. Nevertheless, the two tips interact since they are part of the bubble's interface. Formally, this is exemplified by the integral form of Laplace's equation, which accounts for the interaction between different parts of the moving interface and how this reflects on the interfacial velocity. Thus, the tip of the two jets acquires a rounded shape due to its progressive deceleration as it approaches the equatorial plane, where the normal velocity vanishes if symmetry is to be respected. Since the tangential velocity is zero at the poles anyway, for axisymmetric shapes, a local pressure maximum is established there. Thus, fluid entering this region prefers to move in a direction other than that defined by the axis of symmetry. This signifies the formation of a pressure minimum off the axis of symmetry on the liquid side, which, given that the pressure is uniform inside the bubble, results in the appearance of a dimple with very high curvature on either side of the axis of symmetry. In the present study pressure variations inside the bubble follow changes in the bubble's volume, which occurs on a much slower time scale than the growth and approach of the dimples that appear on the two jets. Finally, the dimples that form on either side of the equator upon the rounded ends of the two jets approach each other until they touch, figure II.9(c), giving rise to a small satellite bubble, which occupies the region circumscribed by the dimples, that is surrounded by the rest of the bubble which has now acquired a toroidal shape.

Dimple formation is an effect that is also observed whenever two Newtonian liquid drops approach each other, whether they are coated by surfactants or not. It should be pointed out, however, that in the present study the minimum distance between the two rounded ends of the two jets eventually vanishes due to the absence of viscous stresses in the gas phase. In fact, final coalescence is also possible when two drops that are dispersed in another liquid are approaching each other, provided that normal viscous stresses and inertia effects are negligible⁸⁵ in the continuous phase.

An interesting aspect of the collapsing process of elongated bubbles concerns the existence of universalities in the period of time between dimple formation and the coalescence of the two jets when the dimples lying on opposite jets touch upon each other. This is a natural extension of previous studies^{26,27} on the capillary pinch-off in inviscid liquids. In the latter studies it was shown that the process of capillary break-up in liquid drops or jets, excluding viscous effects, is governed by the balance between surface tension and dynamic pressure in the manner illustrated by equation (II.56). In this fashion, it was shown that the radius of curvature of each neck on the interface where pinch-off occurs as well as the minimum distance between the two necks in the pinching region eventually vanish and, more specifically, the time to pinch-off scales with the $3/2$ power of either one of the above quantities. In the present study we show that this indeed is the case with the distance, D , between two approaching dimples lying on opposite jets and the time for bubble collapse. As can be seen from the close-up on the collapsing process shown in figure II.9(c), the dimples tend to become more acute as they approach, implying a vanishing radius of curvature as they touch, and the distance between them raised to the $3/2$ scales linearly with the time to collapse, figure II.10(a).

This is a result that is corroborated by mesh refinement, with the element size in the region around the dimples remaining much smaller than the minimum distance between them.

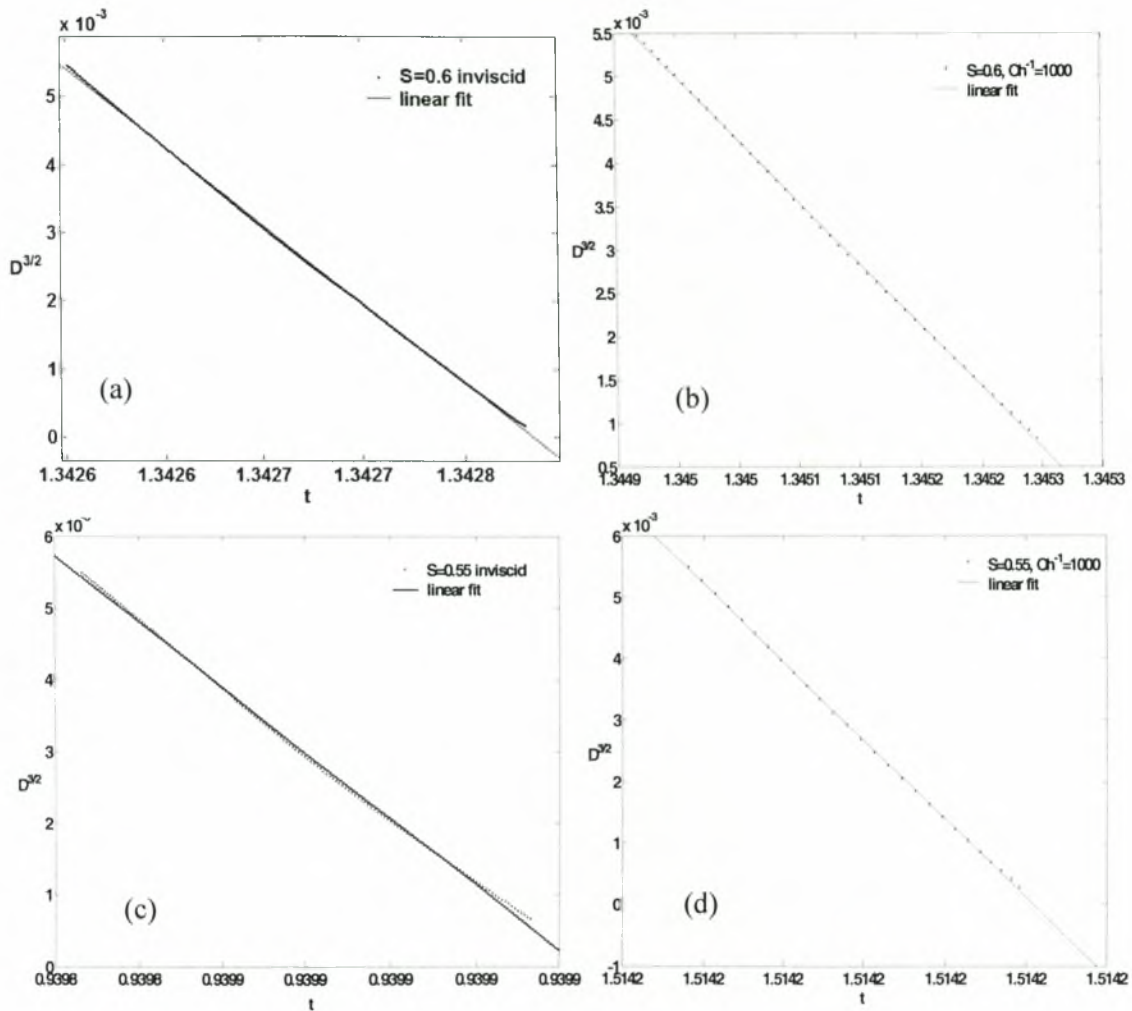
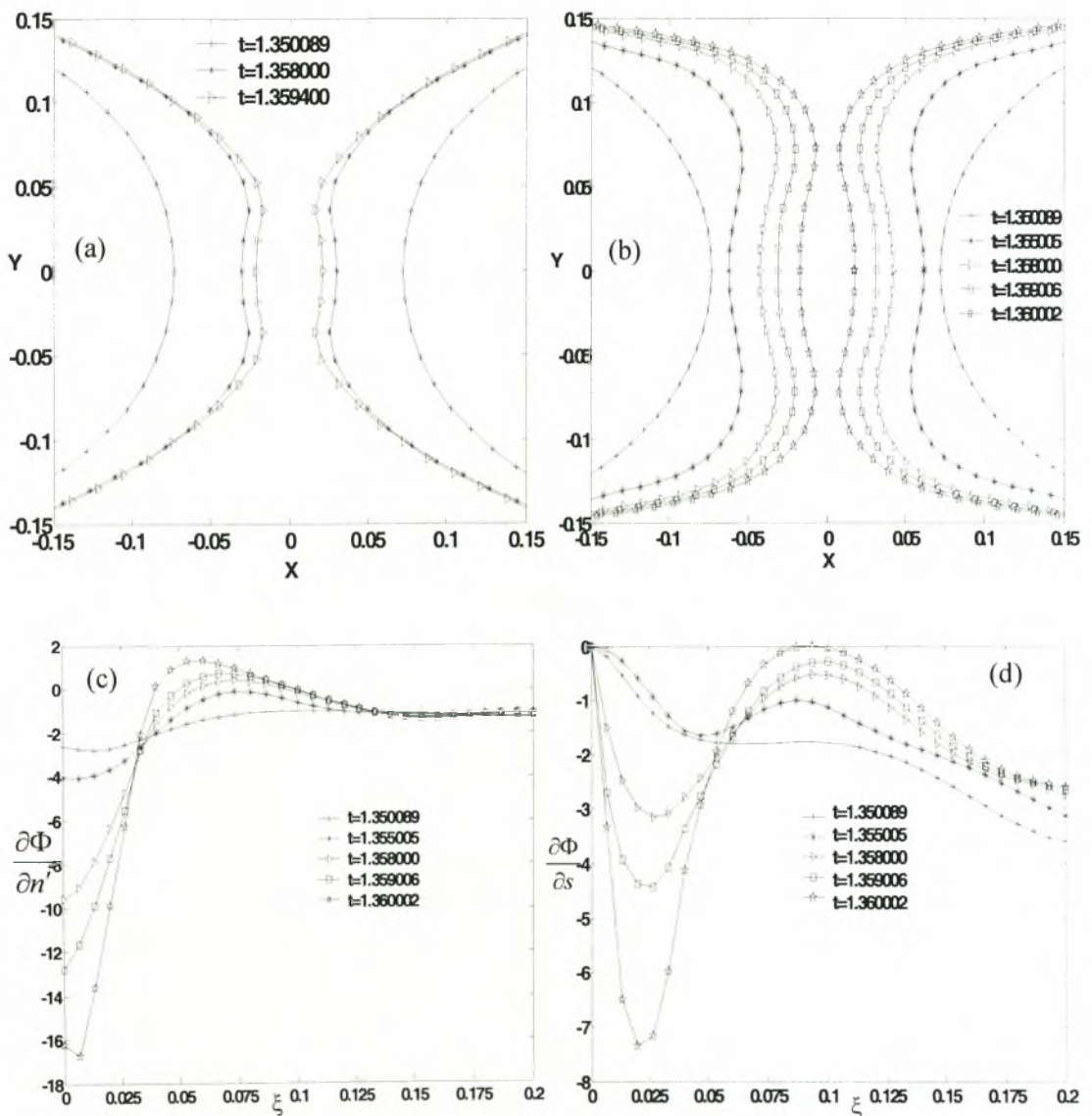


Figure II.10: Time evolution of the distance D , raised to the $3/2$ power, between the dimples that are formed on countercurrent jets when $\varepsilon_B = 0$ and (a) $S=0.6$, Oh^{-1} infinite, (b) $S=0.6$, $Oh^{-1}=1000$, (c) $S=0.55$, Oh^{-1} infinite and (d) $S=0.55$, $Oh^{-1}=1000$; 100 and 130 elements were used in the region $0 \leq \theta \leq \pi/2$ for the cases with $S=0.6$ and 0.55 , respectively.

In order to corroborate the breakup mechanism that was outlined above the inviscid case with $S=0.62$ was recalculated starting from a point in time for which a well-rounded jet tip is formed. This is the parameter value for which the microbubble is formed for the first time in the central region of the original bubble. The solution vector obtained up to that time with 100 elements placed along the generating curve connecting the north pole and the equator, was interpolated with 150 elements to produce a more accurate description of the interfacial shape and velocity. The time step was adapted according to equation (II.57) and the solution was advanced in time until a collapse took place. As illustrated by a close-up on the details of the bubble motion

shown in figure II.11, the basic features of the shape of the interface near the equator are reproduced by the refined mesh and the dimples are captured more accurately, figures II.11(a) and II.11(b); $\xi=1$ and 0 represent particles located at the equator and the north pole, respectively. The evolution of the overall bubble shape is not very different from that shown in figure II.9, hence it is not shown. As time advances the dimples tend to become more acute in shape and tend to eventually touch following the scaling law that was discussed in the previous paragraph. As soon as the dimple is formed, $t \approx 1.355$ from figure II.11(b), the pressure on the liquid side acquires a minimum figure II.11(e), which explains the increased curvature in the same area. The normal velocity, $\frac{\partial \Phi}{\partial n'}$ with n' pointing towards the liquid, in the vicinity of the dimple is negative indicating motion towards the equatorial plane, figure II.11(c).



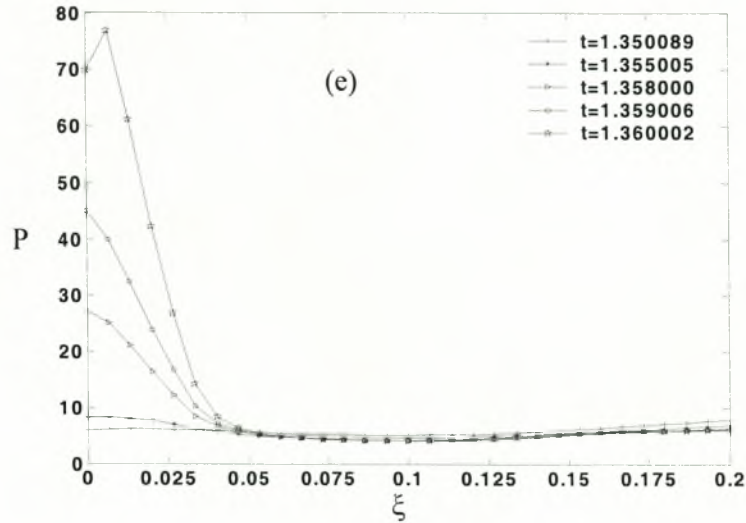


Figure II.11: Close-up on the solution vector in the vicinity of the dimple shortly before collapse when $S=0.62$, $\varepsilon_B=0$, $Oh^{-1} \rightarrow \infty$; (a) shape of the interface with 100 elements in the region $0 \leq \theta \leq \pi/2$ and (b) shape of the interface, (c) normal velocity, (d) tangential velocity and (e) liquid pressure with 150 elements in the region $0 \leq \theta \leq \pi/2$.

The persistence of the above pattern was investigated for varying Oh^{-1} and initial elongation S and it was seen to indeed occur until a critical Oh^{-1} , below which the motion of the two jets is damped strongly enough to prevent them from getting too close and coalescing to form the smaller satellite and the larger toroidal bubbles. The lowest value of Oh^{-1} for which the above mode of collapse was observed for the case with $S=0.6$, was found to be, $Oh^{-1}_{cr} \sim 600$. The sequence of bubble shapes as time elapses is shown in figures II.4(a)-II.4(c) from the beginning of the deformation until collapse, for the case with $Oh^{-1}=1000$. As expected, the increasing effect of viscosity decelerates the two jets and causes them to spread, in comparison with the inviscid simulation, before they become rounded at the tips and eventually touch. If Oh^{-1} is further decreased to 400 the bubble eventually returns to its equilibrium spherically symmetric configuration, figure II.12.

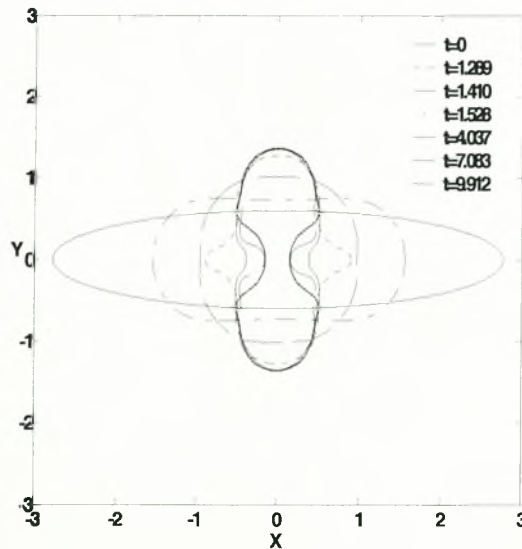


Figure II.12: Bubble shapes for the case with $S=0.6$, $\varepsilon_B=0$, $Oh^{-1}=400$ and 100 elements in the region $0 \leq \theta \leq \pi/2$.

Decreasing S to 0.55, which amounts to intensifying the initial elongation, results in two faster and narrower countercurrent jets. This is a result of the increased initial elongation that induces larger velocities in the vicinity of the two poles. The jets again form rounded ends as they approach each other until they eventually touch at the two protruding dimples, as illustrated in figures II.13(a)-II.13(c) for the inviscid case. The final stages of coalescence of the rounded ends of the two jets are governed by the scaling rule mentioned above, namely that the distance between opposite facing dimples, raised to the $3/2$ power, scales linearly with the time to pinch-off, figure II.10(c). Again, this behavior persists until a threshold value of $Oh^{-1} \sim 200$.

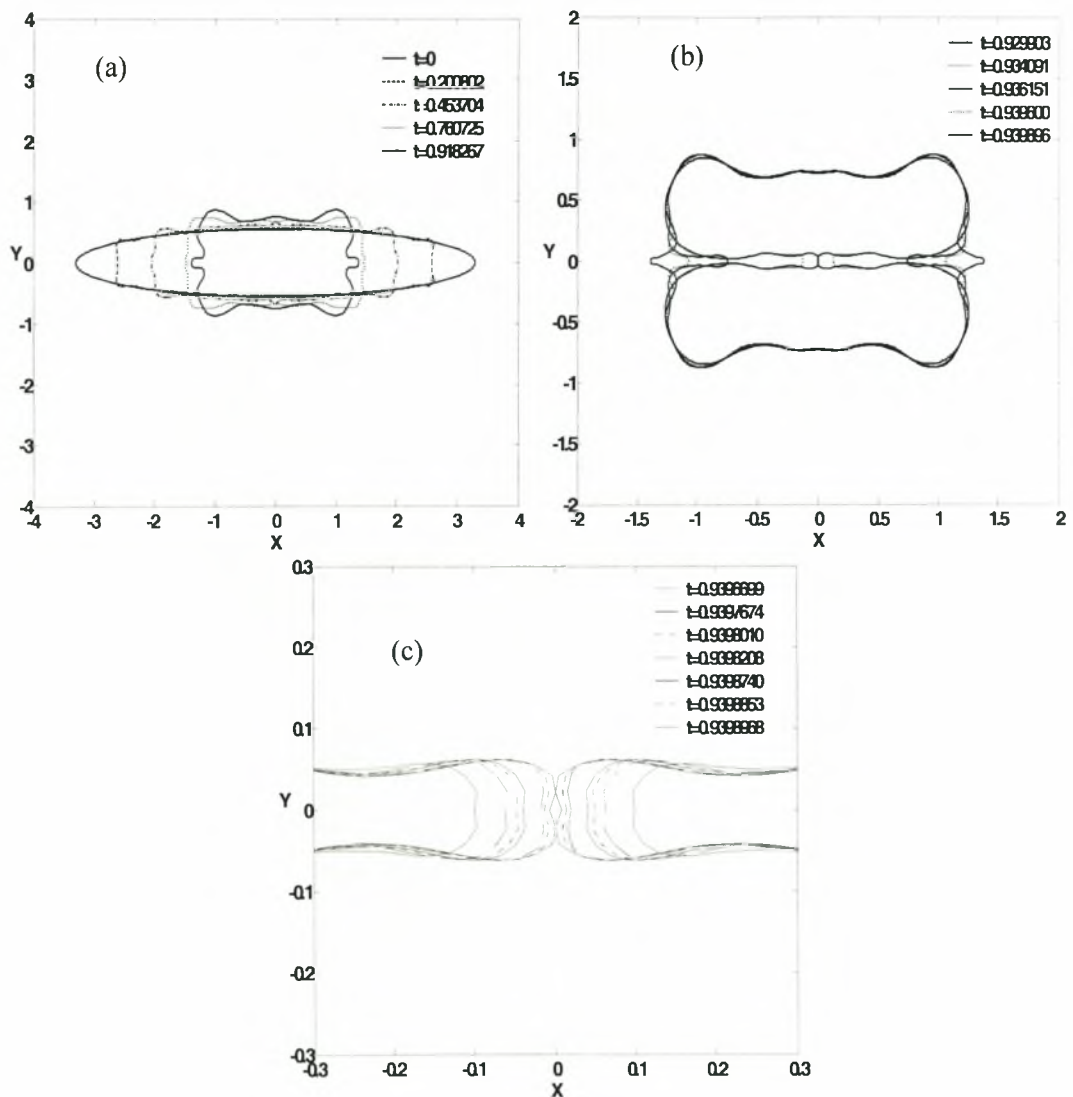


Figure II.13: Time evolution of the shape of the bubble (a) in the beginning of the motion, (b) during jet formation and (c) during collapse; $S=0.55$, $P_{St}=4.1$, infinite Oh^{-1} , with 130 elements in the region $0 \leq \theta \leq \pi/2$.

The evolution of deformed bubble shapes for the case with $Oh^{-1}=1000$ is illustrated in figures II.14(a)-II.14(c), from initial elongation until collapse. In this case the two countercurrent jets are thinner compared to the situation with $S=0.6$ and $Oh^{-1}=1000$ but thicker than the inviscid situation with $S=0.55$, as expected due to the smaller initial elongation and negligible viscous dissipation, respectively. The results with finite Oh^{-1} were examined as regards the universal scaling law governing the collapsing process and it was seen that the latter is more or less true for large but finite values of Oh^{-1} . This is illustrated in figures II.10(b) and II.10(d) where the minimum distance between the countercurrent jets, raised to the $3/2$ power, is plotted against time from pinch-off for the cases with $Oh^{-1}=1000$ and $S=0.6$ and 0.55 , respectively. As mentioned above, this pattern ceases to exist below a threshold value of Oh^{-1} at which point the bubble returns to the spherical shape.

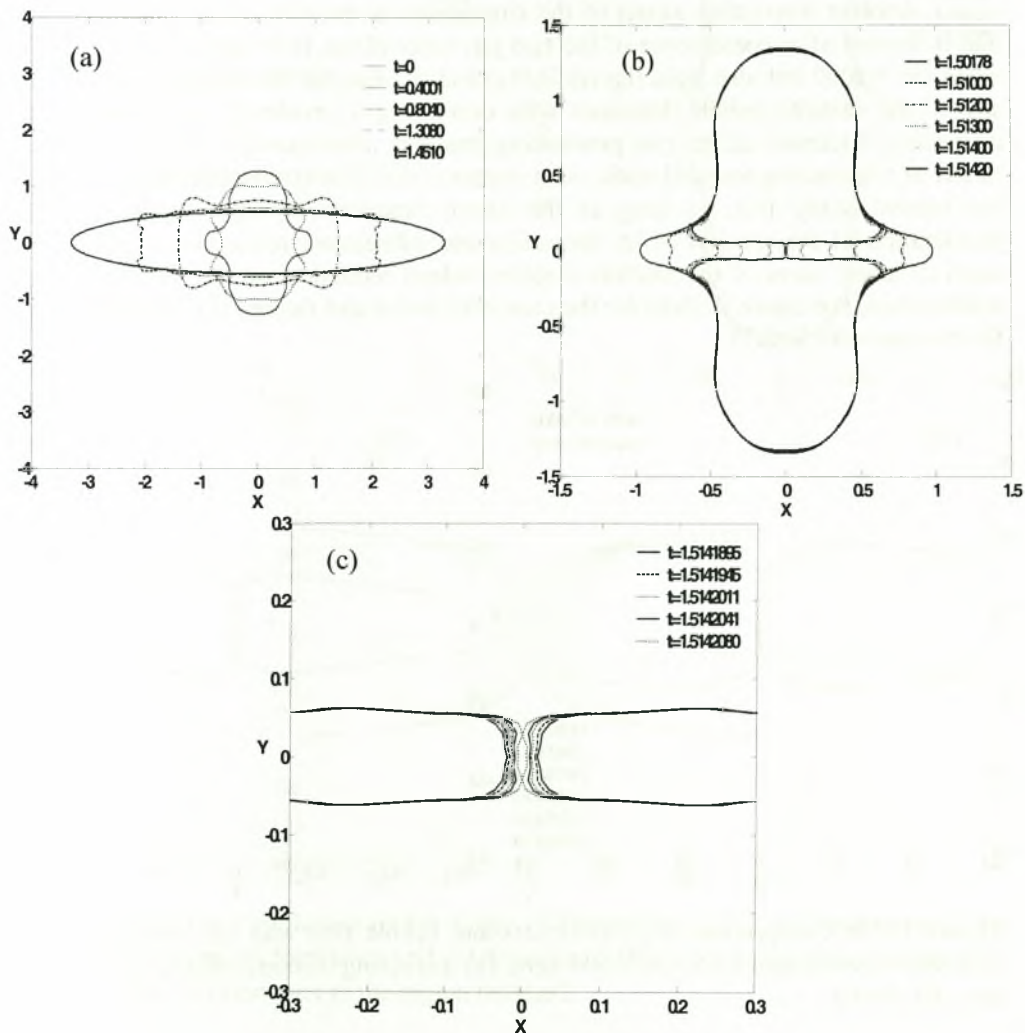


Figure II.14: Time evolution of the shape of the bubble (a) in the beginning of the motion, (b) during jet formation and (c) during collapse; $S=0.55$, $P_{St}=4.1$, $Oh^{-1}=1000$, with 130 elements in the region $0 \leq \theta \leq \pi/2$.

At this point it should be stressed that similar boundary integral studies on bubble breakup have been carried out by other investigators as well, in the presence of initial shape perturbations⁸⁶ and large initial overpressure⁷⁶ but under less severe initial elongation, hence the more prominent role of jet formation in the breakup process that was identified in the present study in comparison with Ref. 76 where jet formation was also captured. It should also be pointed out that as S decreases even further the motion at the two poles becomes so fast that the time step required for capturing the initial deformation and collapse phases of the bubble motion becomes prohibitively small. Consequently, we refrained from reducing S below 0.55. Nevertheless, we anticipate that with increasing initial elongation the mode of collapse will change as different phenomena may emerge. For example, already for the case with $S=0.55$ the tendency of the two jets to pinch-off before they coalesce is evident in figure II.13(b) where a distinct neck formation is observed as a result of the fast speed of approach.

Another interesting aspect of the simulations is the size of the satellite bubble that is formed after coalescence of the two jets takes place. It is seen in figure II.15(a) when $Oh^{-1}=1000$ but also from figures II.9(c) and II.13(c) for the inviscid case, that the size of the satellite bubble decreases with decreasing S , evidently as a result of the decreasing thickness of the two penetrating jets and, consequently, of the decreasing radius of the ensuing rounded ends. As a matter of fact it was identified as a pattern in the present study that, as long as the above described collapse mode persisted, deceleration of the process of jet formation and subsequent reduction of jet velocity leads to larger sizes of the satellite bubble. Indeed reduction of Oh^{-1} leads to larger bubble sizes, see figure II.15(b) for the case with $S=0.6$ and figures II.14(c) and II.13(c) for the case with $S=0.55$.

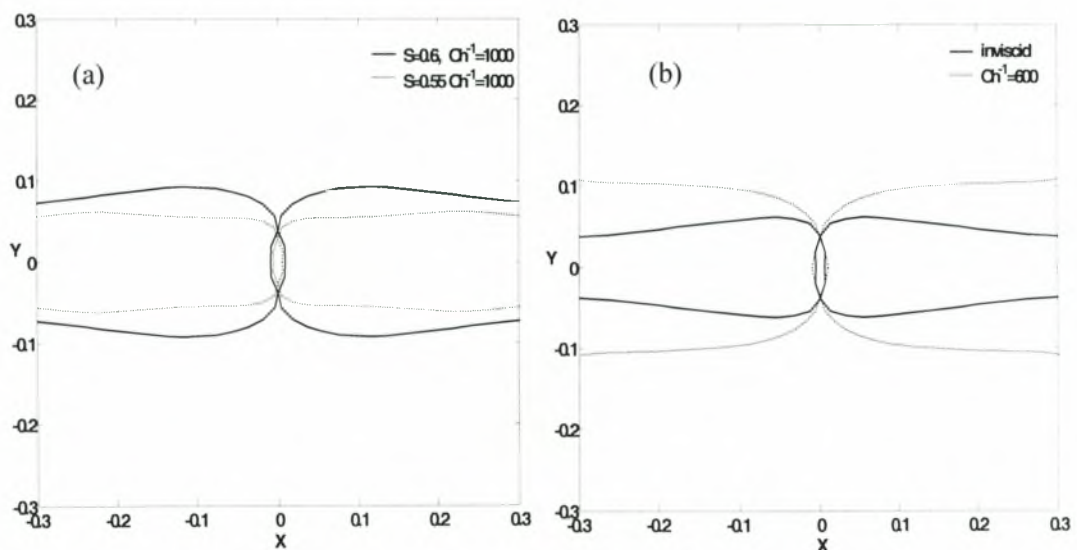


Figure II.15: Comparison of jet thickness and bubble size with (a) increasing initial elongation, $S=0.6$ and 0.55 , $Oh^{-1}=1000$ and (b) increasing viscous effects, $Oh^{-1}=\infty$ and 600 , $S=0.6$.

In fact, so does increasing the internal overpressure, ε_B . In this case the speed by which the elongated bubble retracts to the oblate shape is smaller, owing to the higher initial bubble overpressure, thus resulting to a thicker jet and, eventually, a larger satellite bubble. This is clearly illustrated in figures II.16(a)-II.16(c) that show the evolution of bubble shapes for inviscid oscillations with $S=0.6$ and $\varepsilon_B=0.05$. For such small values of ε_B the overall pattern of dynamic behavior does not change with the exception of Oh_{cr}^{-1} that now increases as a manifestation of the stabilizing influence of initial overpressure; when $\varepsilon_B=0.05$ $Oh_{cr}^{-1} \sim 1000$. The pattern that was identified in the above, regarding the scaling law relating the minimum distance between coalescing jets with the time to coalescence, $D^{3/2} \sim t$, is recovered and holds even for very large yet finite values of Oh^{-1} . Further increase of ε_B affects the dynamics of bubble break-up more drastically enriching the possible collapse mechanisms. Since this parameter range, as far as the internal overpressure is concerned, simulates better the physics of SCBL we will elaborate on it in a subsequent chapter.

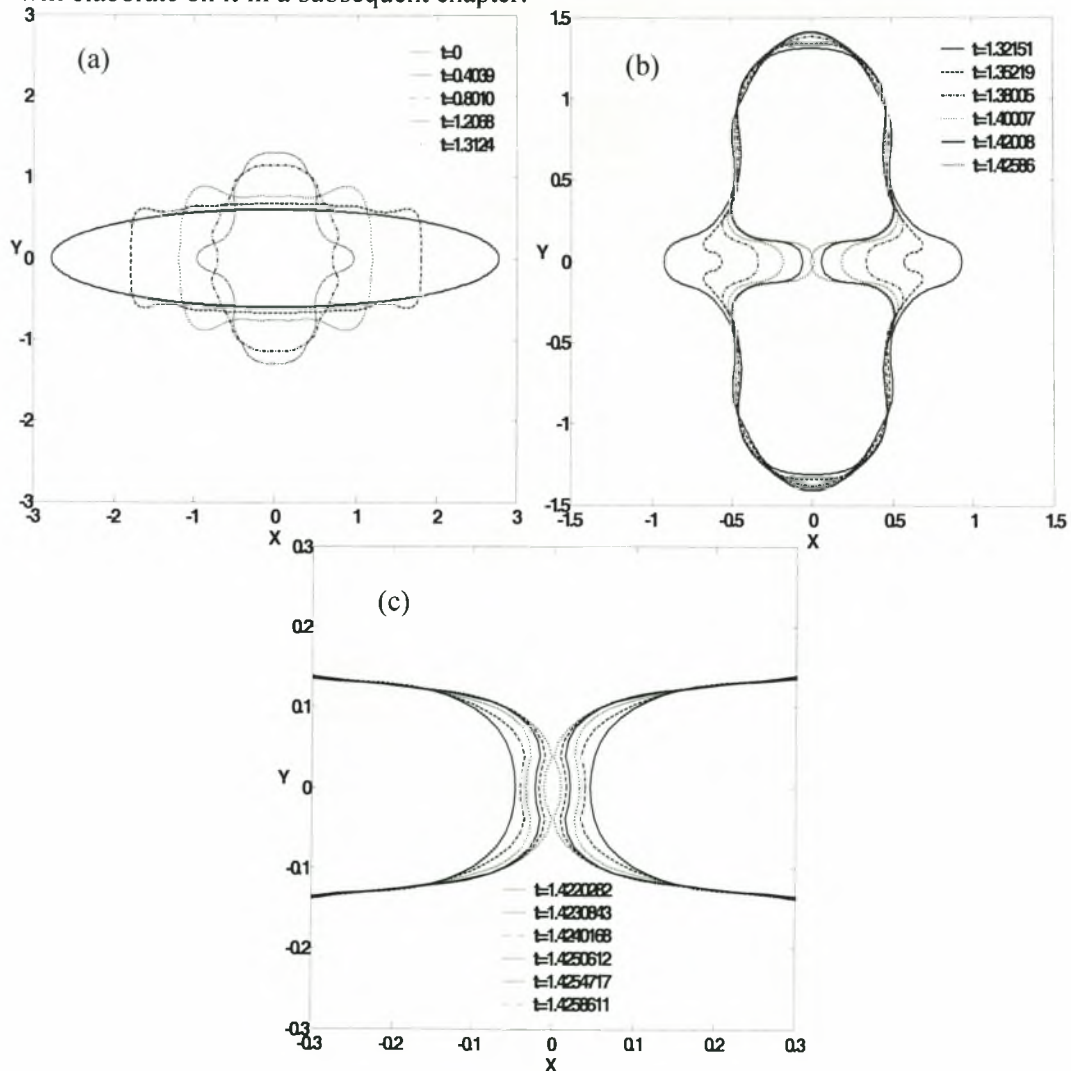


Figure II.16: Time evolution of the shape of the bubble (a) in the beginning of the motion, (b) during jet formation and (c) during collapse; $S=0.6$, $P_{St}=4.1$, infinite Oh^{-1} , $\varepsilon_B=0.05$, with 100 elements in the region $0 \leq \theta \leq \pi/2$.

The effect of asymmetry in the initial elongation was also investigated, by imposing the types of shapes that are portrayed in figure II.1. In this case the regions around the two poles are moving at a different speed, due to the difference in radius of curvature, with the one with the smaller radius moving faster. Once the shape of the bubble becomes roughly oblate these two regions perform out of phase oscillations until a jet is formed at the north pole, that moves along the axis of symmetry, penetrates the bubble and hits the opposite side of its interface forming a satellite and a larger toroidal bubble. This is illustrated in figures II.17(a)-II.17(c) for the case with $k=1.2$, $Oh^{-1}=800$, and the same initial elongation, $\ell = 2/(0.6)^2$, as for an ellipsoidal bubble with $S=0.6$. In this case the satellite bubble does not occupy the region at the intersection between the equatorial plane and the axis of symmetry. Rather, it appears off the equator, as the two dimples that are formed symmetrically with respect to the axis of symmetry on the rounded end of the penetrating jet touch upon the opposite side of the bubble. As the level of asymmetry decreases the bubble collapses closer to the equatorial plane.

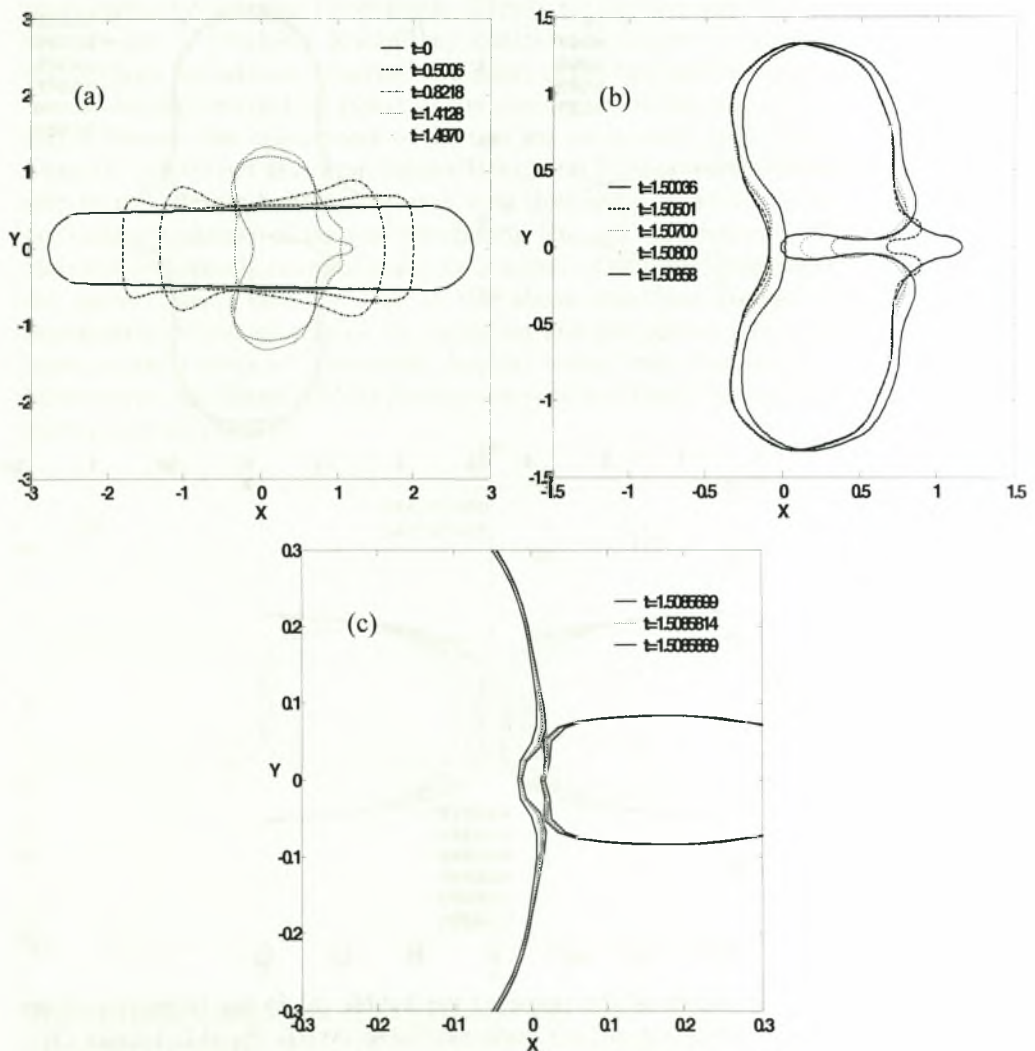


Figure II.17: Time evolution of the shape of an asymmetric bubble (a) in the beginning of the motion, (b) during jet formation and (c) during collapse; $P_{St}=4.1$, $Oh^{-1}=800$, $k=1.2$, $\ell = 5.55$, $\varepsilon_B=0$, with 150 elements in the region $0 \leq \theta \leq \pi$.

II.4 CONCLUSIONS

The effect of initial elongation on the dynamic behavior of a bubble that is suspended in a liquid at atmospheric pressure is investigated. The particular case of an air bubble suspended in water was simulated extensively and it was shown that beyond a certain range of initial elongations, $S \leq 0.6$, the long time configuration of the bubble is either spherically symmetric, $Oh^{-1} \leq Oh_{cr}^{-1}$, or collapsed consisting of a small satellite bubble occupying the region around the center and a larger toroidal bubble. The collapse mechanism is quite interesting and is characterized by the formation of two countercurrent jets penetrating the bubble from opposite ends and meeting at the equatorial plane. As they approach each other their ends become rounded and two dimples appear on each one of them that are symmetrically located with respect to the axis of symmetry. The final stages of coalescence of opposite facing dimples are governed by the balance between capillary and inertia forces responsible for the pinch-off process of liquid drops and jets. In fact, the $3/2$ scaling law describing the evolution of the minimum distance between approaching dimples against the time to pinch-off, was recovered for the inviscid case and large initial elongations, $0.55 \leq S \leq 0.6$, and was seen to be roughly valid for large values of Oh^{-1} . A small amount of initial overpressure was shown to stabilize the bubble by increasing the value of Oh_{cr}^{-1} . For the case of a micrometer-size air bubble suspended in water Oh^{-1} is not very large and consequently the theory presented here predicts that the bubble will eventually return to the spherically symmetric configuration. Nevertheless, as the size of the bubble increases Oh^{-1} and P_{St} both increase and it is seen that for an initial elongation characterized by $S=0.6$, a bubble with equilibrium radius on the order of 5 mm which amounts to $Oh^{-1} \sim 600$ and $P_{St} \approx 3500$, eventually collapses in the manner described above. In other words larger bubbles are more susceptible to collapse. In fact, it was found that when $P_{St}=3600$, $S=0.6$ and $\varepsilon_B=0$ the threshold value above which the bubble collapses is $Oh_{cr}^{-1} \sim 300$. It should also be pointed out that the combination of large initial elongations and substantial internal overpressures may extend the range over which the dynamic phenomena that were identified in the present study will manifest themselves. Larger initial overpressures are also expected to modify the long-term dynamics and probably give rise to different break-up mechanisms. This process is very important in the physics of sonoluminescence and will be investigated separately in a subsequent chapter.

CHAPTER III

Non-Linear Oscillations and Collapse of Elongated Bubbles Subject to Weak Viscous Effects: Effect of Internal Overpressure

The details of nonlinear oscillations and collapse of elongated bubbles, subject to large internal overpressure, are studied by a boundary integral method. Weak viscous effects on the liquid side are accounted for by integrating the equations of motion across the boundary layer that is formed adjacent to the interface. For relatively large bubbles with initial radius R_0 on the order of millimeters, $P_{St}=P_{St}'/(2\sigma/R_0)\sim 300$ and $Oh=\mu/(\sigma R_0\rho)^{1/2}\sim 200$, and an almost spherical initial shape, $S\sim 1$, Rayleigh-Taylor instability prevails and the bubble breaks-up as a result of growth of higher modes and the development of regions of very small radius of curvature; σ , ρ , μ and P'_{St} denote the surface tension, density, viscosity and dimensional static pressure in the host liquid while S is the ratio between the length of the minor semi-axis of the bubble, taken as an axisymmetric ellipsoid, and its equivalent radius R_0 . For finite initial elongations, $0.5\leq S<1$, the bubble collapses either via two jets that counter-propagate along the axis of symmetry and eventually coalesce at the equatorial plane, or in the form of a sink flow approaching the center of the bubble along the equatorial plane. This pattern persists for the above range of initial elongations examined and large internal overpressure amplitudes, $\varepsilon_B\geq 1$, irrespective of Oh number. It is largely due to the phase in the growth of the second Legendre mode during the afterbounce of the oscillating bubble, during which it acquires large enough positive accelerations for collapse to take place. For smaller bubbles with initial radius on the order of micrometers, $P_{St}\sim 4$ and $Oh\sim 20$, and small initial elongations, $0.75<S\leq 1$, viscosity counteracts P_2 growth and subsequent jet motion thus giving rise to a critical value of Oh^{-1} below which the bubble eventually returns to its equilibrium spherical shape, whereas above it collapse via jet impact or sink flow is obtained. For moderate elongations, $0.5\leq S\leq 0.75$, and large overpressures, $\varepsilon_B\geq 0.2$, jet propagation and impact along the axis of symmetry prevails irrespective of Oh . For very large elongations, $S<0.5$, and above a certain threshold value of Oh^{-1} the counter-propagating jets pinch the contracting bubble side-walls in an off-centered fashion. Simulations of laser induced bubbles were also performed. The collapse mode via jet propagation along the axis of symmetry is recovered for the case of femtosecond laser bubbles, initial radius on the order of μm . The severity and local activity of collapse via sink flow along the equatorial plane during pinching of nanosecond laser bubbles, initial radius on the order of mm , is pointed out as a result of an afterbounce instability in the presence of small initial elongations under large overpressures.

III.1 PROBLEM FORMULATION AND SOLUTION METHODOLOGY

III.1.1 Governing Equations

The problem addressed in the present study is similar to that in chapter II except for the initial conditions where specific attention is placed on the level of initial overpressure inside the elongated bubble,

$$P_G(t=0) = P_G(t=0_+)(1 + \varepsilon_B), \quad P_G(t=0_+) - P_{s1} = 1; \quad (III.1a,b)$$

ε_B denotes the amplitude of the internal overpressure and $P_{s1} = P'_{s1}/(2\sigma/R_0)$ the dimensionless static pressure but it can also serve as a measure of the bubble size. In the above equations as well as in the rest of this study the dimensionless formulation used in chapter II is adopted, with surface tension providing the characteristic time, velocity and pressure scales; when dimensional variables are introduced they will be denoted by primes. The regime of large internal overpressures is investigated that is characterized by $\varepsilon_B \sim 1$ or larger. The bubble is assumed to be an ellipsoid initially. The level of elongation is again characterized by the parameter $S=a/R_0$ with a , R_0 , denoting the length of the smaller semi-axis and the radius of a bubble with the same initial volume as the elongated bubble, respectively, figure II.1. As the negative deviation between S and unity increases, $S \leq 1$, then the initial elongation of the bubble is intensified. Based on the bubble sizes generated by nanosecond and femtosecond laser pulses in water the cases with $R=420$ and $5.8 \mu\text{m}$ are considered, corresponding to a dimensionless static pressure $P_{s1}=295$ and 4.1 , respectively. For bubbles of this size in water $Oh^{-1}=(\rho R_0 \sigma)^{1/2}/\mu$ is 174 and 20 , respectively. However, for completeness the parametric study is contacted in S , ε_B and Oh^{-1} , with the understanding that the analysis is strictly valid when $Oh^{-1} \gg 1$, i.e. when viscous forces are less important than surface tension.

In this fashion the problem formulation reads as follows. Lagrangian particles are employed for updating the location of the interface,

$$\frac{dr}{dt} = \frac{(u_n + U_n)r\theta_s + u_t r_s}{\sqrt{r_s^2 + r^2\theta_s^2}}, \quad \frac{d\theta}{dt} = \frac{u_t r\theta_s - (u_n + U_n)r_s}{r\sqrt{r_s^2 + r^2\theta_s^2}} \quad (III.2a,b)$$

where r , θ , denote the radial and polar spherical coordinates, the subscript s denotes partial differentiation with respect to the arc-length s of the generating curve of the axisymmetric interface, t and n are the tangential and normal components of the potential, $\bar{u} = \bar{\nabla}\Phi$, and vortical, $\bar{U} = \bar{\nabla} \times \bar{A}$, part of the fluid velocity and $\frac{d}{dt} = \frac{\partial}{\partial t} + (\bar{u} + U_n \bar{n}) \cdot \bar{\nabla}$; Φ , \bar{A} , denote the scalar and vector potentials associated with the fluid velocity.

Combining the Bernoulli equation with the normal force balance on the interface we obtain the following equation describing the time evolution of scalar potential on the interface.

$$\frac{d\Phi}{dt} = \frac{u^2}{2} + u_n U_n + 2P_x - 2P_G + 2A(\bar{t} \cdot \bar{\nabla} \bar{u} \cdot \bar{n}) - 2H - 2Oh(\bar{n} \cdot \bar{\nabla} \bar{u} \cdot \bar{n}) \quad (III.3)$$

This equation contains $O(Oh)$ corrections for the normal viscous stress and the vortical part of the pressure on the interface. The normal component, $u_n = \frac{\partial \Phi}{\partial n}$, of the potential

velocity field is obtained by recasting the Laplace equation in the form of an integral equation evaluated on the interface

$$\Phi(\hat{r}, \hat{\theta}, t) + \int_0^1 [\Phi(r, \theta, t) - \Phi(\hat{r}, \hat{\theta}, t)] \frac{\partial G}{\partial n}(\hat{r}, \hat{\theta}, r, \theta) r \sin \theta (r_\xi^2 + r^2 \theta_\xi^2)^{1/2} d\xi = \int_0^1 \frac{\partial \Phi}{\partial n}(r, \theta, t) G(\hat{r}, \hat{\theta}, r, \theta) r \sin \theta (r_\xi^2 + r^2 \theta_\xi^2)^{1/2} d\xi \quad (III.4)$$

where G and $\partial G/\partial n$ denote the axisymmetric free space singular kernels of the Laplace equation. Due to axisymmetry, $\bar{A} = A(r, \theta) \bar{e}_\theta$, and integrating the tangential component of the momentum equation across the boundary layer we obtain an equation describing the time evolution of the vector velocity potential evaluated on the interface,

$$\frac{DA}{Dt} = A(\bar{n} \cdot \bar{\nabla} \bar{u} \cdot \bar{n} - \bar{t} \cdot \bar{\nabla} \bar{u} \cdot \bar{t}) - Oh \frac{\partial U_t}{\partial n} \quad (III.5)$$

Equations (III.2)-(III.5), along with the appropriate boundary conditions enforcing axisymmetry at the two poles, provide the description of the bubble dynamics based solely on interfacial variables, including weak viscous effects.

As a means to analyze and cross check the numerical results, the equation describing shape instabilities⁶³ for an oscillating bubble is employed,

$$\ddot{a}_n + \left[3 \frac{\dot{R}}{R} + 2 \frac{Oh}{R^2} (n+2)(2n+1) \right] \dot{a}_n + (n-1) \left[-\frac{\ddot{R}}{R} + \frac{(n+1)(n+2)}{R^2} + 2 \frac{Oh \dot{R}}{R^3} (n+2) \right] a_n = 0 \quad (III.6)$$

where n denotes the Legendre mode under investigation and $R(t)$ is the time variation of the dimensionless bubble radius, which is predicted by the Rayleigh-Plesset (RP) equation for an initial disturbance of the form shown in eq. (III.1):

$$R\ddot{R} + \frac{3}{2} \dot{R}^2 = 2(P_{st} + 1)(1 + \varepsilon_B)R^{-\gamma} - 2P_{st} - 4Oh - 2 \quad (III.7)$$

The liquid is treated as incompressible and the gas inside the bubble as ideal with a polytropic constant γ . The above approximation is appropriate since the duration of the investigated phenomena is very short and consequently the boundary layer thickness can be approximated as $\delta' \sim \sqrt{vt'}$. Equation (III.6) is valid provided $\delta' \ll R_0$ or equivalently, $t \ll Oh^{-1}$, which is indeed the case in the context of the present study.

III.1.2 Simulations Protocol

Besides the parametric study, which aims at a description of the dynamics of the elongated bubble that is as general as possible, an attempt is also made at simulating specific experimental observations¹². This suffers from the uncertainty related to the exact distribution of the total energy that is imparted to the host fluid by the laser pulse, among different forms of energy. In particular, the largest part of the initial energy due to the laser pulse is consumed in order to locally form plasma, which then recombines to generate a gas and vapor filled bubble. Energy is also dissipated in the form of thermal and acoustic energy of the host fluid, and only a small part, roughly 10%, is converted to mechanical energy of the bubble which can then be quantified in terms of the internal overpressure when the bubble starts expanding at $t=0$. After the instant of bubble

inception and within a very short period of time, part of the liquid vapor cools down and re-condenses. It is assumed that this process is completed within the time interval $0 < t < t_1$, a few microseconds for nanosecond bubbles and a few hundreds of nanoseconds for femtosecond bubbles, needed to capture the first frame depicting the shape of the bubble. From this point onwards the bubble expands and collapses in a more or less isothermal fashion, except for the very last moments of collapse in which case large pressures and temperatures are generated. After the point of collapse the bubble rebounds and eventually settles to its equilibrium radius.

In order to simulate this process, first the equilibrium radius is estimated from the frame corresponding to the bubble equilibrium. Then, for given conditions in the quiescent fluid the internal bubble pressure is estimated and consequently, employing the adiabatic or isothermal ideal gas law, the pressure inside the bubble at $t=t_1$ can be calculated, $P_G(t=t_1)$, because its volume is also known at this time instant. However, this is not the original bubble overpressure $P_G(t=0_+)$ since condensation has already taken place before $t=t_1$, and the simulation cannot start at $t=t_1$ because the kinetic energy of the bubble is not known. As a result, the original overpressure at $t=0$, $P_G(t=0_+)$, is estimated by fitting the maximum bubble volume, V_{max} , before collapse. The simulation proceeds until $t=t_1$ at which point the pressure has to abruptly drop at the value $P_G(t=t_1)$ estimated at $t=t_1$ based on the equilibrium conditions. This is just a simple way to account for initial condensation of liquid vapor. It is not expected to be far from reality for a host liquid like water that does not exhibit excessive evaporation. From this point on the simulation continues, with given internal bubble pressure, shape and kinetic energy, until the point of collapse. It is also important to note that even for an overall spherical collapse a small amount of initial elongation is always present. Consequently, the bubble is allowed to be slightly elongated initially, and the effect that this bears on the details of collapse is monitored in section III.1.4 in view of the findings of the parametric study in section III.1.3.

III.1.3 Numerical Methodology

The numerical methodology employed for capturing the detailed bubble dynamics is explained in detail in section II.2. The kinematic and dynamic boundary conditions, equations (III.2) and (III.3), along with the equation describing the evolution of the vector potential, equation (III.5), are discretized via the finite element method and are integrated in time with the 4th order accurate Runge-Kutta method. Filtering is applied on the vector potential solution at every time step in order to eliminate short wave instabilities. The normal component of the potential velocity vector is calculated by applying the boundary element method on the integral equation (III.4). In order to accommodate the large initial elongations and overpressures of the bubble as well as the resulting large deformations and jet velocities use of symmetry is employed, when bubble geometry permits, along with parallel construction of the system matrix that arises as part of the boundary integral methodology. In fact, between 100 and 200 elements are used along half of the generating curve of the interface, $0 \leq \theta \leq \pi/2$, for moderate initial elongations, $S \geq 0.7$, whereas between 300 and 600 elements are used, in the same portion of the θ space, when the initial elongation becomes very large, $S \leq 0.6$. Finally, marker points are redistributed at every time step in order to properly resolve areas of high curvature. Subsequently, in order to avoid unstable evolution of marker

points the time step is adapted following the $\Delta t \sim \Delta S_{\min}^{5/2}$ rule for cases with explosive and almost spherosymmetric bubble collapse. The latter scaling arises in the context of the Rayleigh-Plesset equation when the velocity of a spherical bubble during collapse is evaluated⁷¹, $\dot{R} \sim R^{-3/2}$, which as R becomes vanishing small gives $\Delta t \sim \Delta R^{3/2}$. The latter scaling reflects the dominant balance between inertia and the pressure drop between the far field and the bubble interior. When the initial elongation is relatively large and the bubble collapse asymmetric the $\Delta t \sim \Delta S_{\min}^{3/2}$ time adaptation rule is employed as suggested by the universality law governing most of the collapse phase of such bubbles, already discussed in section II.2 and observed in the present study also.

III.2 PARAMETRIC STUDY

In section II.3 the dynamic behavior of elongated bubbles was examined with vanishing or small initial overpressure and the combined effect of initial elongation and viscous dissipation was investigated. It was thus seen that for small bubble will eventually return to its equilibrium spherical shape, whereas above a certain level of elongation, S smaller than, roughly, 0.6 for zero initial overpressure, a threshold value of Oh^{-1} exists above which the bubble eventually collapses via jet impact giving rise to a toroidal bubble surrounding a tiny microbubble that occupies the central region of the original bubble. Existence of a small initial overpressure does not significantly change this picture, stabilizing the bubble by increasing the critical Oh^{-1} number for jet impact. Overpressure essentially delays the process of jet formation by uniformly expanding the bubble, thus giving more time for viscosity to act and prevent impact. Large internal overpressures are expected to enrich the above dynamic pattern by adding large amounts of energy to the system that may then be converted to inertia with interesting consequences on the bubble dynamics. In this section the effect of large internal overpressure on the dynamics of micron and millimeter sized bubbles is investigated as a function of ε_B , S and Oh . These are very small bubbles and we expect viscous damping to be the dominant dissipation mechanism. In order to assist the analysis of the bubble behavior the formulas providing the resonance frequencies for volume and shape oscillations, as predicted by linear theory excluding any damping mechanism, are reproduced below,

$$\omega_0 = [6(P_{Si} + 1)\gamma - 2]^{1/2} \quad \omega_k = [(k^2 - 1)(k + 2)]^{1/2}, \quad k \geq 1, \quad (III.8)$$

III.2.1 Micron sized bubbles, $P_{Si} \sim 4$, $Oh^{-1} \sim 20$

We first consider bubbles with initial volume characterized by an indicative equivalent radius of 5.8 μm , generated in water at normal conditions, 20° C and 1 bar, in which case $P_{Si} \approx 4.1$. For bubbles of this size oscillating in water $Oh^{-1} \approx 20$. Nevertheless a parametric study was conducted by varying Oh , in order to capture the effect of viscous dissipation on the break-up mechanism. We consider initial overpressure levels that are characterized by values of ε_B on the order of 1 or larger. In particular, the case with $\varepsilon_B = 2$ was examined for a wide range of initial elongations and viscous dissipation levels. For small initial elongations, $S \geq 0.7$, typically between 100 and 200 elements were used in the half theta space and the dimensionless time step varied within one calculation between 5×10^{-4} and 10^{-5} . For large initial elongations, $S \approx 0.45$, typically 350

elements were used in the half theta space and the dimensionless time step varied within one calculation between 10^{-5} and 5×10^{-6} .

When the initial elongation is negligible, $S \sim 1$, the bubble performs a number of volume oscillations during which it gradually becomes more and more deformed due to the onset of higher non-spherical harmonics. Eventually, it settles to its equilibrium spherical shape under the action of viscous dissipation, figure III.1(a). Plotting the shape mode decomposition as a function of time indicates gradual decay and this is corroborated by stability analysis, via equations (III.6)-(III.7), of the second spherical harmonic i.e. the second Legendre polynomial (P_2) in the context of axisymmetric disturbances; see also figures III.1(b) and III.1(c).

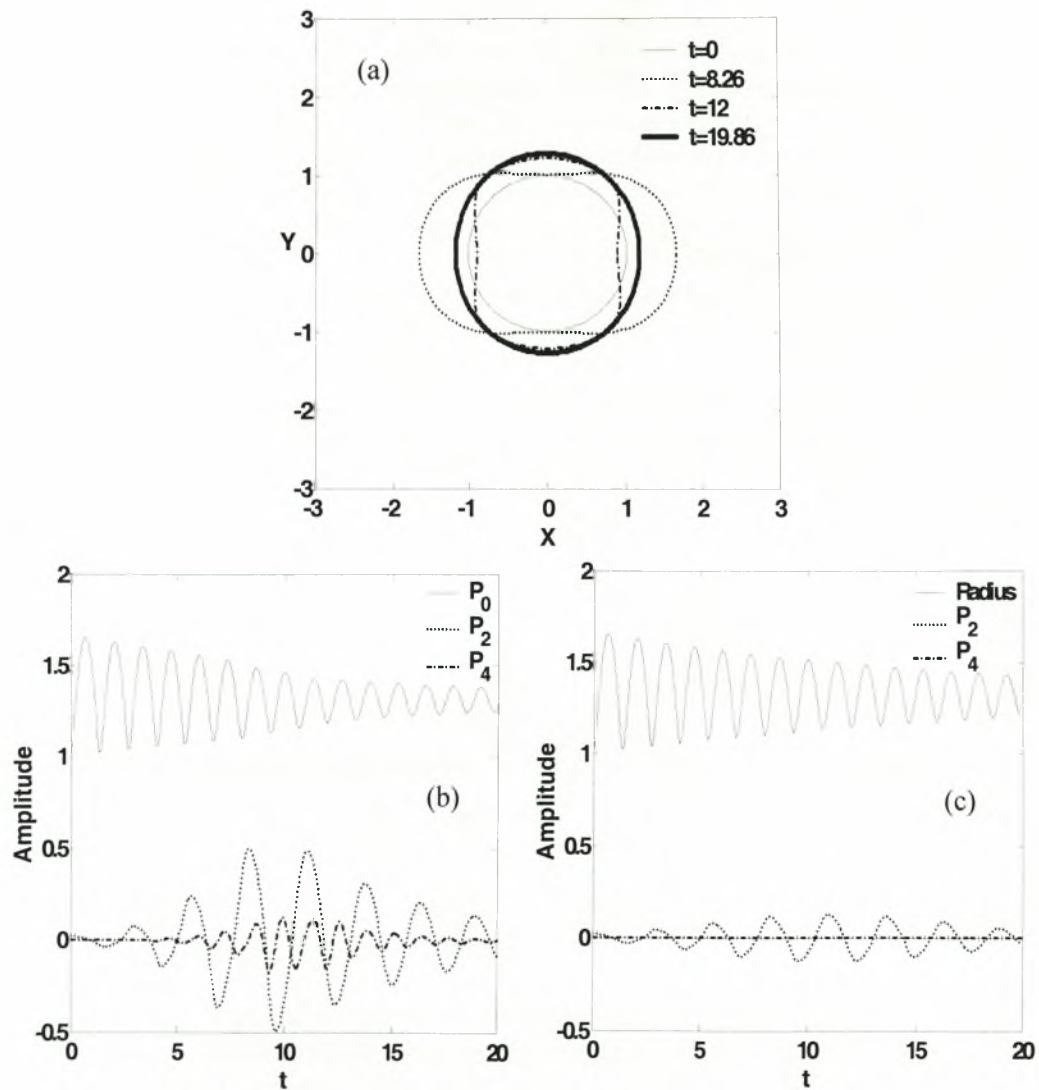


Figure III.1: Time evolution of (a) bubble shapes, (b) numerically obtained shape mode decomposition and (c) evolution of bubble radius and shape mode decomposition based on stability analysis; $S=0.99$, $P_{St}=4.1$, $\varepsilon_B=2$, $Oh^{-1}=20$, with 100 elements in the region $0 \leq \theta \leq \pi/2$.

When the effect of viscous dissipation is mitigated, larger Oh^{-1} , while the rest of the problem parameters remain the same the time required for returning to the spherosymmetric configuration becomes longer, until a threshold value of Oh^{-1} is reached above which the bubble pinches off via jet formation and impact in the manner described in section II.3 for small overpressures, see figures III.2(a) and III.2(b) for the case with $Oh^{-1}=30$. The mode decomposition is also depicted as obtained from the numerically calculated bubble shape as well as the stability analysis, figures III.2(c) and III.2(d).

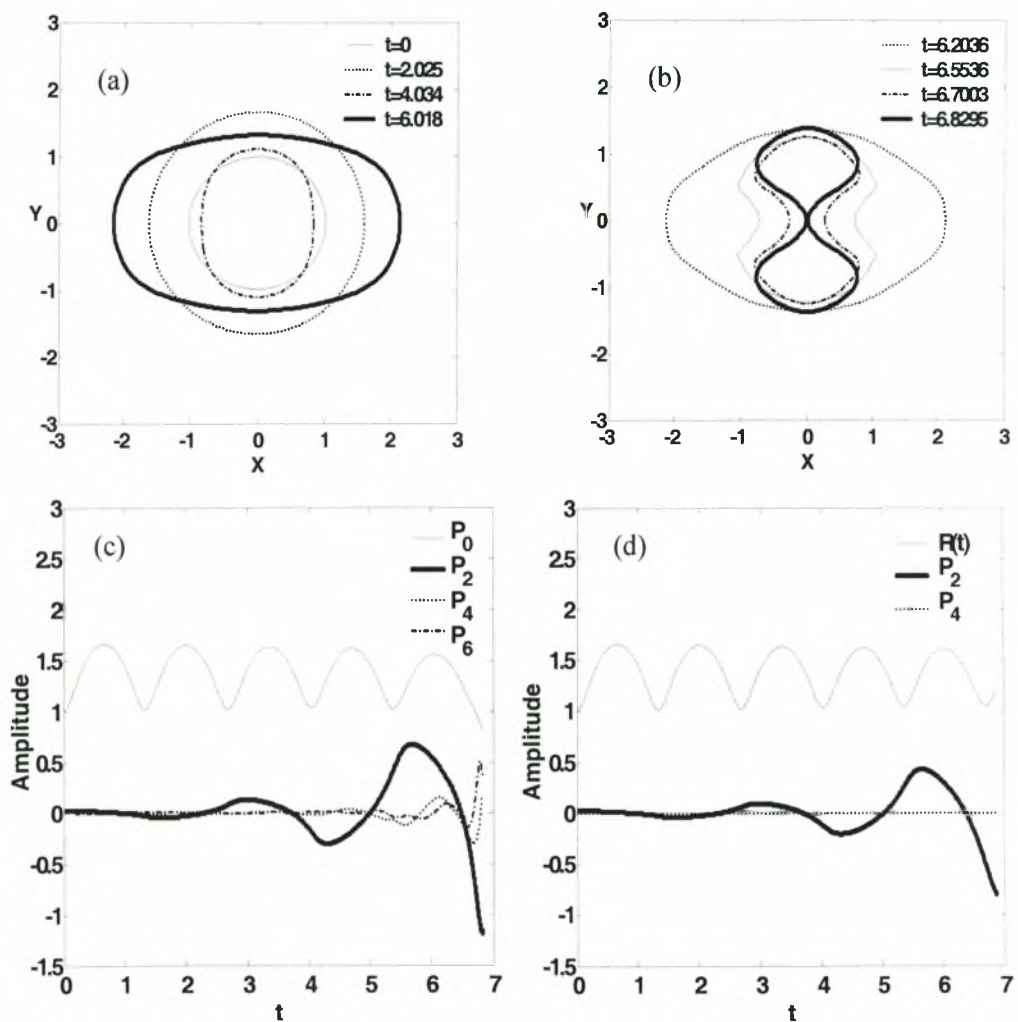
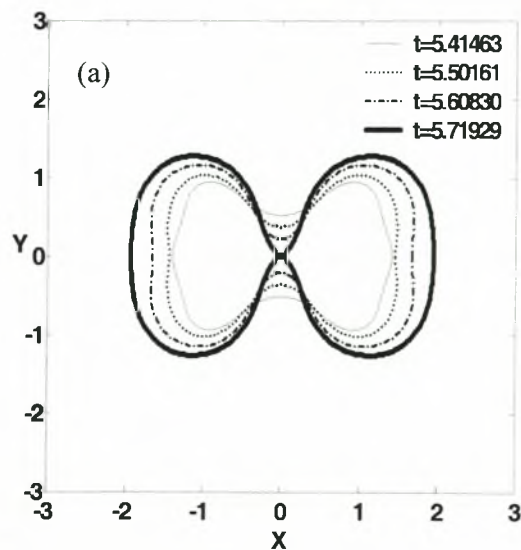


Figure III.2: Time evolution of (a) bubble shapes in the beginning of the motion, (b) bubble shapes during collapse, (c) numerically obtained shape mode decomposition and (d) evolution of bubble radius and shape mode decomposition based on stability analysis; $S=0.99$, $P_{St}=4.1$, $\epsilon_B=2$, $Oh^{-1}=40$, with 150 elements in the region $0 \leq \theta \leq \pi/2$.

In both figures P_2 exhibits gradual growth during the collapse phase of volume pulsations indicating the onset of an afterbounce instability⁶³. The latter lies between the Rayleigh-Taylor instability, it is also associated to positive gas accelerations during bubble collapse but is not as explosive, and the parametric instability, it also exhibits gradual growth but does not require as many cycles to appear. It should also be stressed that, based on equation (III.8) $\omega_0 \approx 6.4$, which is almost twice the resonance frequency of P_2 , $\omega_2 \approx 3.4$, indicating the possibility for parametric excitation.

When the initial overpressure increases, $\varepsilon_B=10$, the threshold in Oh^{-1} for jet impact decreases also, due to faster growth of P_2 , until it covers almost the entire range of Oh number. The rest of the even Legendre modes are either stable or grow but not as fast as P_2 that dominates the dynamics. It is important to note that when the internal overpressure is small or absent jet formation and impact is heavily dependent on the inertia imparted to the bubble poles due to the initial elongation. As ε_B increases significantly, in contrast to the situation with small initial overpressure ($\varepsilon_B \ll 1$) in which case collapse via jet impact is stabilized, this process is assisted by P_2 growth as a result of the afterbounce instability that allows for jet impact even at very low initial elongations, $S=0.99$, provided viscous damping is not strong enough to eventually overwhelm shape instability. The fashion by which jet impact takes place depends on the phase in the P_2 growth pattern for which its amplitude is large enough for impact to take place. When the amplitude of P_2 grows in time it does so in the manner shown in figure III.2, gaining in size during each collapse phase of the pulsating bubble while exhibiting alternating sign with increasing number of pulsation cycles. Thus, when collapse occurs during the positive phase in the P_2 growth cycle it manifests itself in the form of a sink flow along the equatorial plane that is directed towards the center of the bubble on the axis symmetry. Figure III.3 illustrates this behavior when $Oh^{-1}=200$.



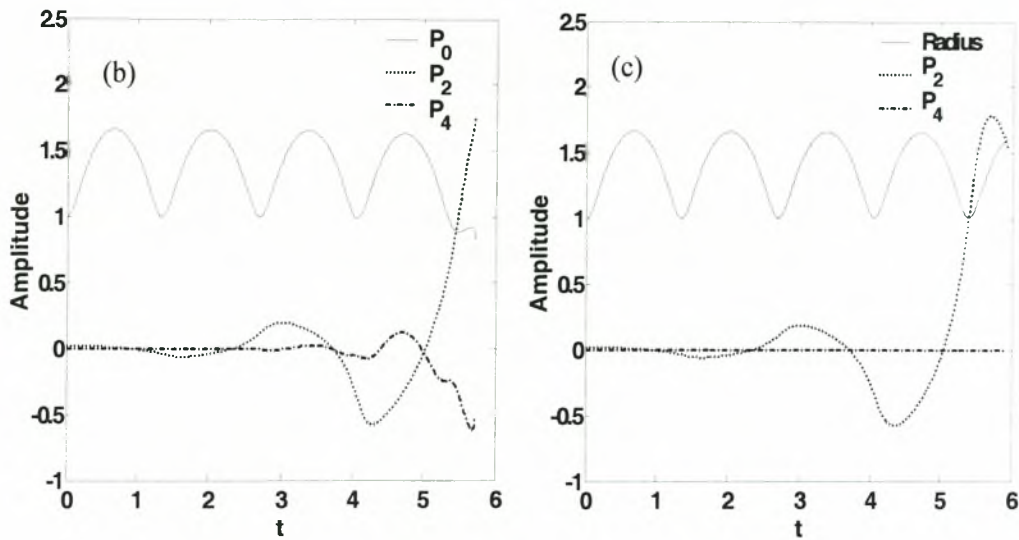


Figure III.3: Time evolution of (a) bubble shapes during collapse, (b) numerically obtained shape mode decomposition and (c) evolution of bubble radius and shape mode decomposition based on stability analysis; $S=0.99$, $P_{St}=4.1$, $\varepsilon_B=2$, $Oh^{-1}=200$, with 150 elements in the region $0 \leq \theta \leq \pi/2$.

When the opposite happens, negative P_2 amplitudes, the jets propagate along the axis of symmetry and coalesce on the equator. The latter is the type of behavior that we obtain in section II.3 as well as in most cases presented in this study for relatively large elongations, in which case the initial content of P_2 in the bubble shape is quite substantial, prolate, so that when the shape of the bubble becomes oblate, negative P_2 content, for the first time the propagating jets are fast enough to cause impact. The former type of collapse leads to a different final topology that consists of two larger bubbles and a tiny one occupying the center of the original bubble, i.e. it is not associated with the formation of a toroidal bubble. A collapse mode of this type was also obtained in the context of bubble interaction with a tip vortex or plane boundaries^{76,87}. In the latter two studies the original bubble is seen to collapse on the axis of symmetry before it splits to form two smaller bubbles, which then collapse on their own. The simulations indicate a strong pressure signal in the host liquid in the vicinity of the bubble during the primary collapse followed by a stronger signal during the collapse of the smaller bubbles. The first signal was thought to be an artifact of the numerical process of splitting the bubble. However, its presence is corroborated by the simulations presented here, showing locally a peak pressure accompanying dimple formation during collapse.

As the initial elongation increases the centered collapse mode via jet impact persists until it occupies the entire range of Oh , $0.5 \leq S \leq 0.75$ when $\varepsilon_B \geq 2$. Within this range of elongations the bubble always collapses with the two jets coalescing at the equatorial plain irrespective of Oh , see figure III.4 for $S=0.7$ and $Oh^{-1}=20$, with the understanding that as Oh^{-1} decreases the onset of collapse is decelerated. The shape mode decomposition, figure III.5, confirms the above described pattern of P_2 growth.

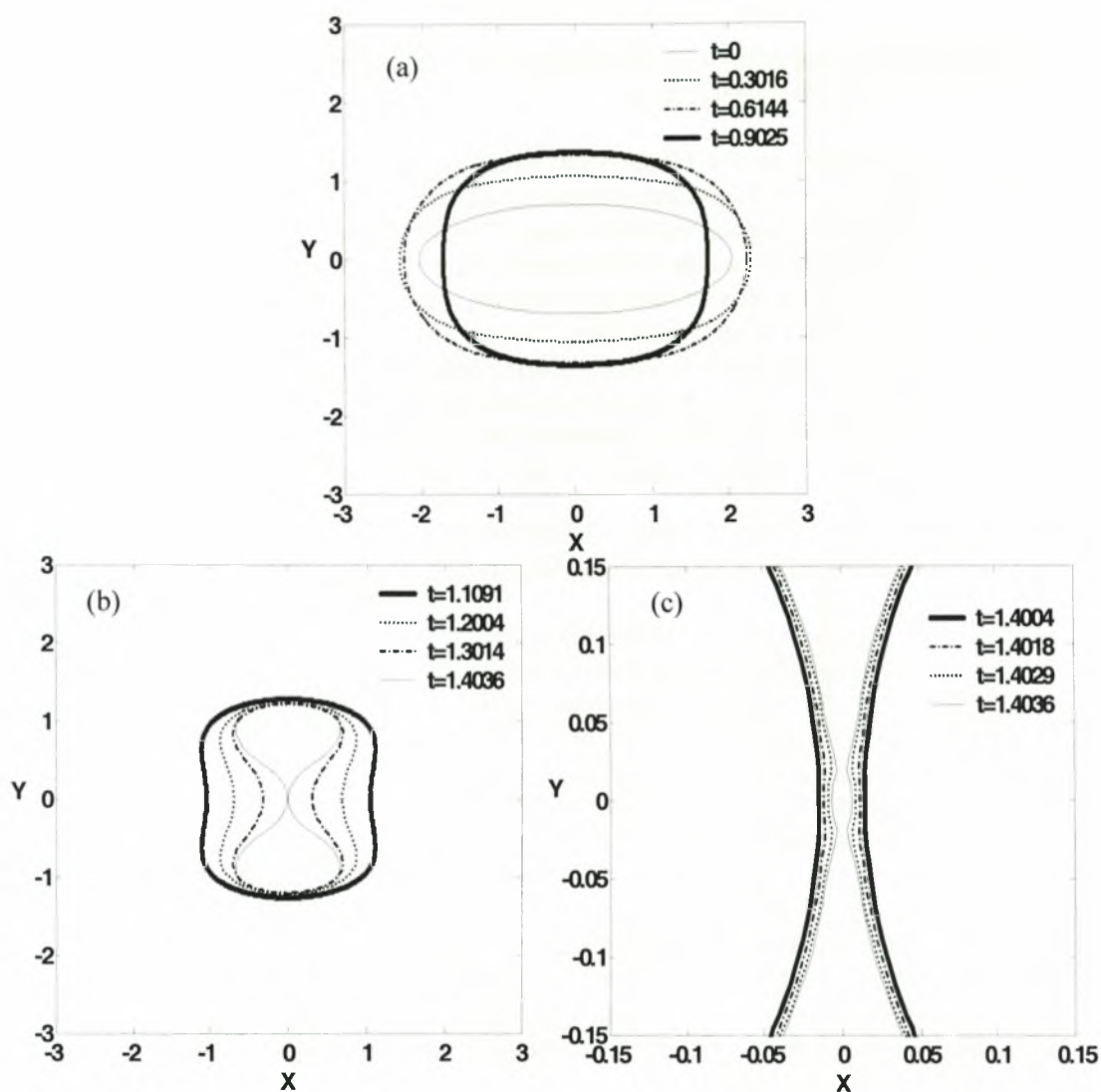


Figure III.4: Time evolution of the shape of the bubble (a) in the beginning of the motion, (b) during jet formation and (c) during collapse; $S=0.7$, $P_{St}=4.1$, $\epsilon_B=2$, $Oh^{-1}=20$, with 200 elements in the region $0 \leq \theta \leq \pi/2$.

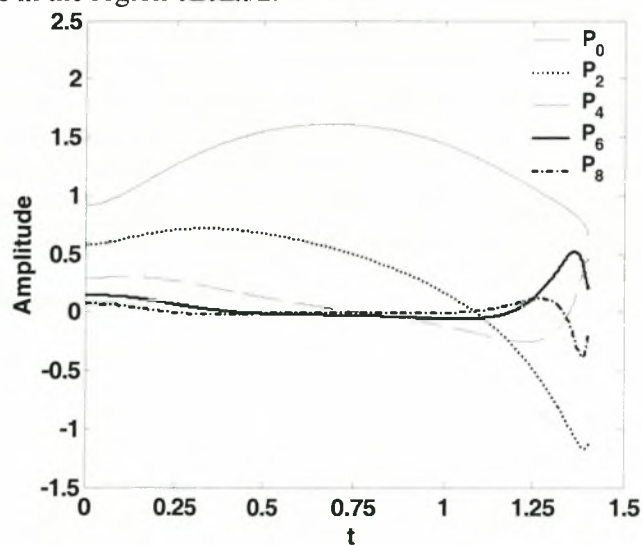


Figure III.5: Time evolution of the numerically obtained shape mode decomposition when $Oh^{-1}=20$, $S=0.7$, $P_{St}=4.1$, $\varepsilon_B=2$.

The evolution of the dimensional speed of the two bubble tips for the case shown in figure III.4 is illustrated in figure III.6 as an indicator of jet velocity. In it as well as in subsequent graphs, negative values of interfacial speed denote inward motion. Initially the bubble tips coincide with the poles. However, during the collapse phase the velocity of the dimple that is formed is shown, hence the slight jump in the curve towards the last stages of jet coalescence. Dimensional quantities are used in this graph in order to indicate the level of severity during impact as well as the appropriate time scale for bubbles of this size. It should be noted that larger jet speeds are developed as Oh^{-1} increases, which, nonetheless, remain of the same order of magnitude.

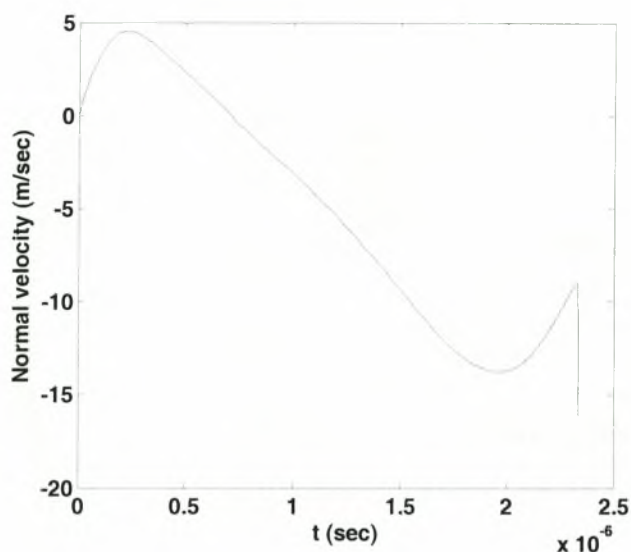


Figure III.6: Time evolution of the dimensional normal velocity of the bubble tip when $Oh^{-1}=20$, $S=0.7$, $P_{St}=4.1$, $\varepsilon_B=2$.

The universal law relating the time from collapse with the $3/2$ power of the minimum distance between the two coalescing jets, reported in section II.3 but also in previous studies of capillary drop pinch-off²⁷ and attributed to the inertia versus capillarity balance, is seen to hold in the case of large overpressures also, figure III.7, especially as Oh^{-1} tends to infinity. It should be noted that, based on the above scaling, during the collapse phase the dimple velocity grows like $(t_0-t)^{-1/3}$, where t_0 denotes the time instant at which the approaching dimples meet at the equatorial plane, irrespective of Oh as long as Oh^{-1} remains large. Hence the steep rise in the absolute value of the calculated velocities exhibited towards the very last moments of the collapse phase. The same pattern is recovered in the case of collapse via sink flow along the equatorial plane.

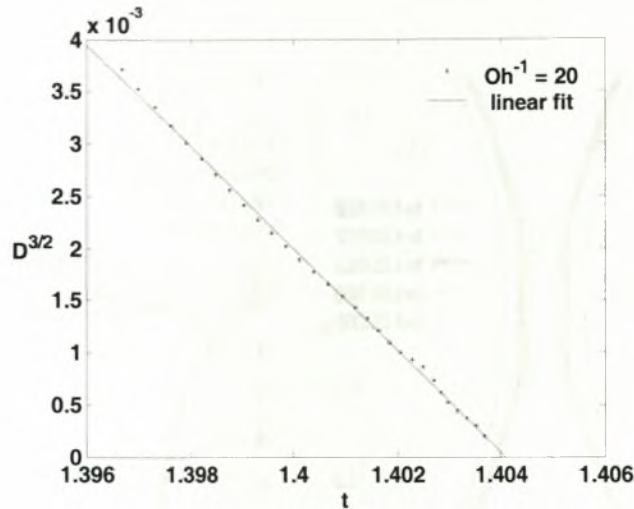
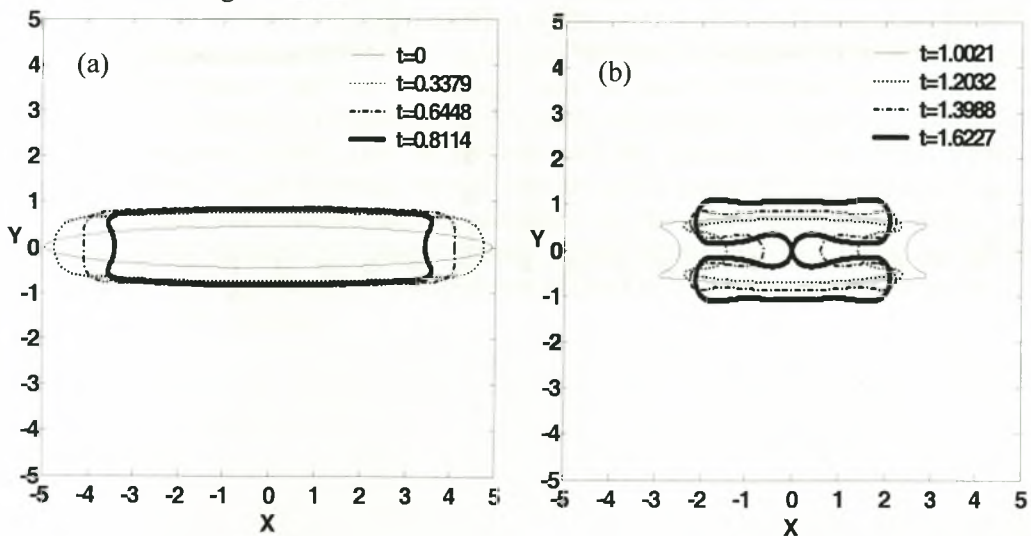


Figure III.7: Time evolution of the distance D , raised to the $3/2$ power, between the dimples that are formed on counter-propagating jets when $Oh^{-1}=20$; $\varepsilon_B=2$ and $S=0.7$.

When S becomes smaller than a threshold value, $S_{Cr} \approx 0.45$ and $\varepsilon_B \geq 2$, an additional break-up mechanism arises that evolves in an off-centered fashion. This is illustrated in figures III.8 and III.9 showing the break-up process of an elongated bubble with Oh^{-1} set to 20 and 1000, respectively. In the former case the centered break-up mechanism reported in section II.3 and recovered here for smaller elongations, i.e. the one leading to a microbubble and a toroidal bubble, is reproduced. On the other hand, as Oh^{-1} increases, the velocity of the two jets is so large that they penetrate well into the bubble interior before the contraction phase is over. In this process the portion of the bubble side-walls that lies closer to the tip that is formed at each one of the two poles approaches the axis of symmetry with a considerable speed. Thus, the bubble side-walls are close enough to interact with the penetrating jet, eventually leading to an off-centered pinching mechanism. Consequently, instead of proceeding along the axis of symmetry each one of the two jets pinches at the bubble side-wall giving rise to two smaller toroidal bubbles located in the vicinity of each one of the poles of the original bubble, and a larger bubble occupying the central region of the original bubble. These mechanisms of collapse were also verified by mesh refinement as it can be seen in figures III.8(d) and III.9(d) where the same results are obtained for 200 and 350 elements in the region $0 \leq \theta \leq \pi/2$.



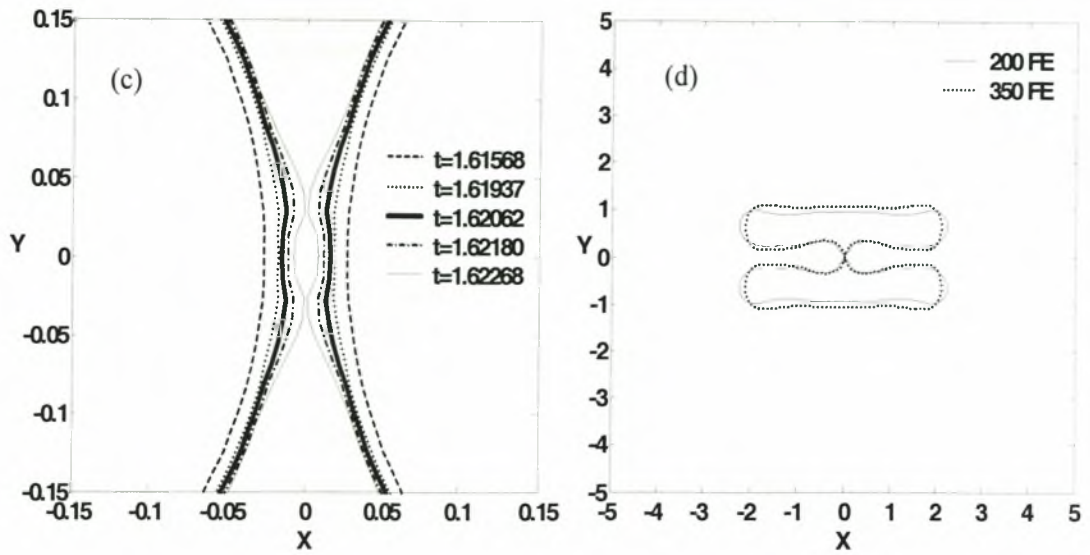
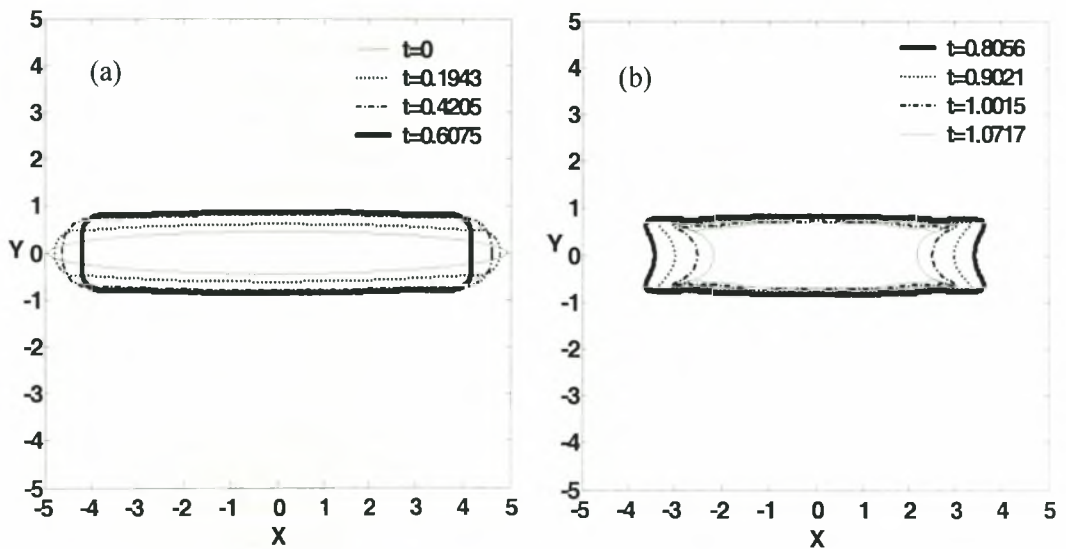


Figure III.8: Time evolution of the shape of the bubble (a) in the beginning of the motion, (b) during jet formation and (c) during collapse; $S=0.45$, $P_{St}=4.1$, $\varepsilon_B=2$, $Oh^l=20$, with 350 elements in the region $0 \leq \theta \leq \pi/2$. (d) mesh refinement with 200 and 350 elements in the region $0 \leq \theta \leq \pi/2$.



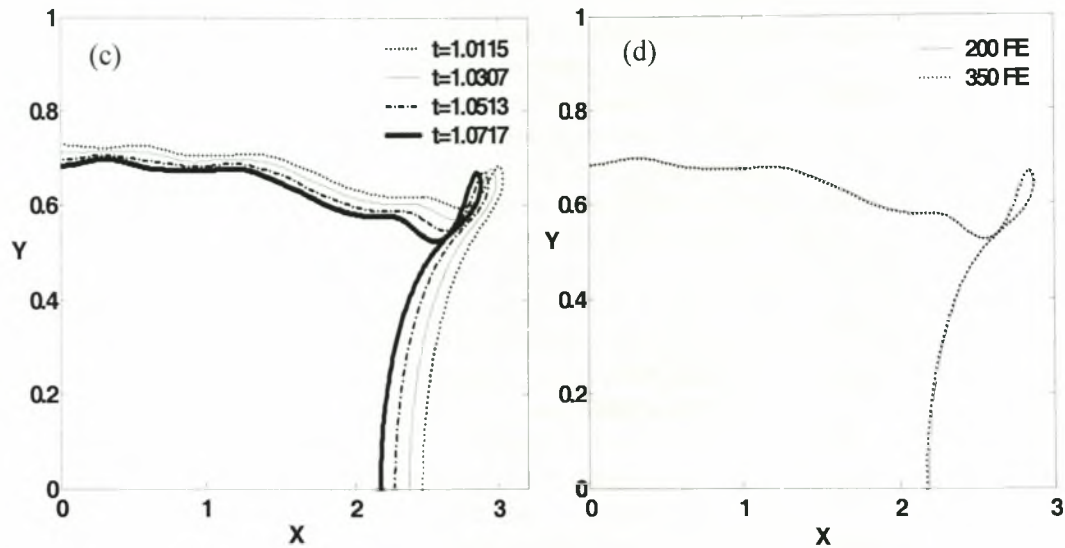


Figure III.9: Time evolution of the shape of the bubble (a) in the beginning of the motion, (b) during jet formation and (c) during collapse; $S=0.45$, $P_{St}=4.1$, $\varepsilon_B=2$, $Oh^{-1}=1000$, with 350 elements in the region $0 \leq \theta \leq \pi/2$. (d) mesh refinement with 200 and 350 elements in the region $0 \leq \theta \leq \pi/2$.

This is a result of the fact that both P_0 and P_2 are present to a large extent in the bubble dynamics for this parameter range, with P_2 more or less following P_0 , see also figure III.10 illustrating the time evolution of the shape mode decomposition for the above two cases. Thus, as P_0 completes one cycle of its pulsation contracting to its minimum size, P_2 completes half of its own oscillation switching from the initial prolate shape to an oblate one. Consequently, as a result of synchronization, the two jets penetrating the bubble from each one of the two poles meet the contracting bubble side-walls. As a result each jet faces an increasing bubble pressure and its front becomes more rounded in order to adjust to changes in the pressure difference across the interface. For bubbles of this size surface tension can accommodate this process and in this fashion the jet front interacts closely with the bubble side walls producing the off-centered collapse mode. When Oh^{-1} decreases the jets are delayed in penetrating the bubble. Consequently there is not enough time for them to interact with the bubble walls, hence the centered collapse mode. Similarly as S decreases further, i.e. the bubble is more elongated initially, the jet is faster and the threshold value Oh^{-1}_{Cr} for the centered mode to occur decreases, as will also be seen in section III.3 where simulations of femto-second laser bubbles will be presented. To the extent that the two modes are not significantly detuned this pattern persists. In fact, increasing ε_B increases the period of P_0 , albeit not significantly, and does not affect Oh^{-1}_{Cr} which remains as predicted when $\varepsilon_B=2$, $Oh^{-1}_{Cr} \approx 200$.

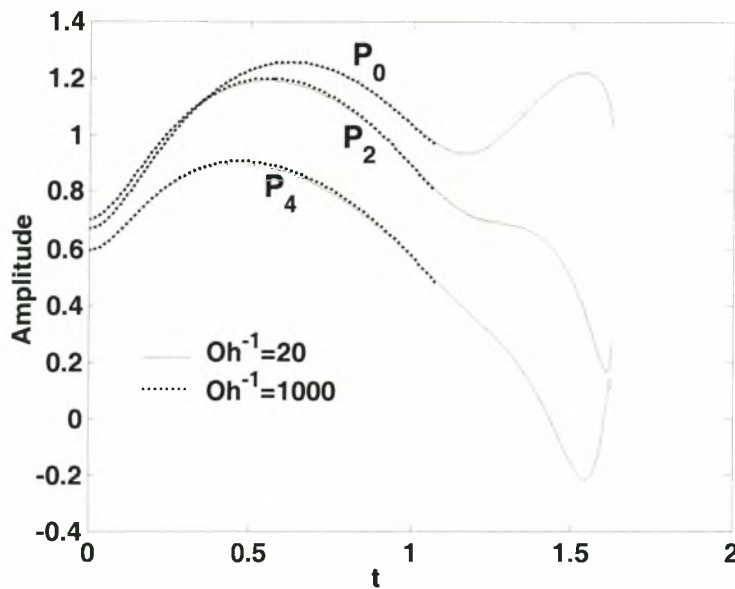


Figure III.10: Time evolution of the numerically obtained shape mode decomposition when $S=0.45$, $P_{St}=4.1$, $\varepsilon_B=2$ and $Oh^{-1}=20$ and 1000 .

Monitoring the minimum distance between the jet tip and the bubble side-wall we can reproduce the universality law mentioned above relating the time from pinch-off with the $3/2$ power of the minimum distance, figure III.11. This result was, to a certain extent, expected since here also the collapsing process involves an inertia versus capillarity balance which is characterized by the above power law.

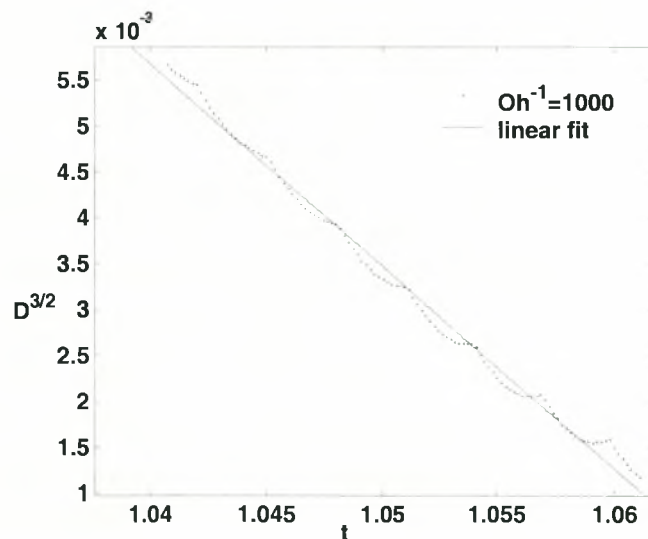
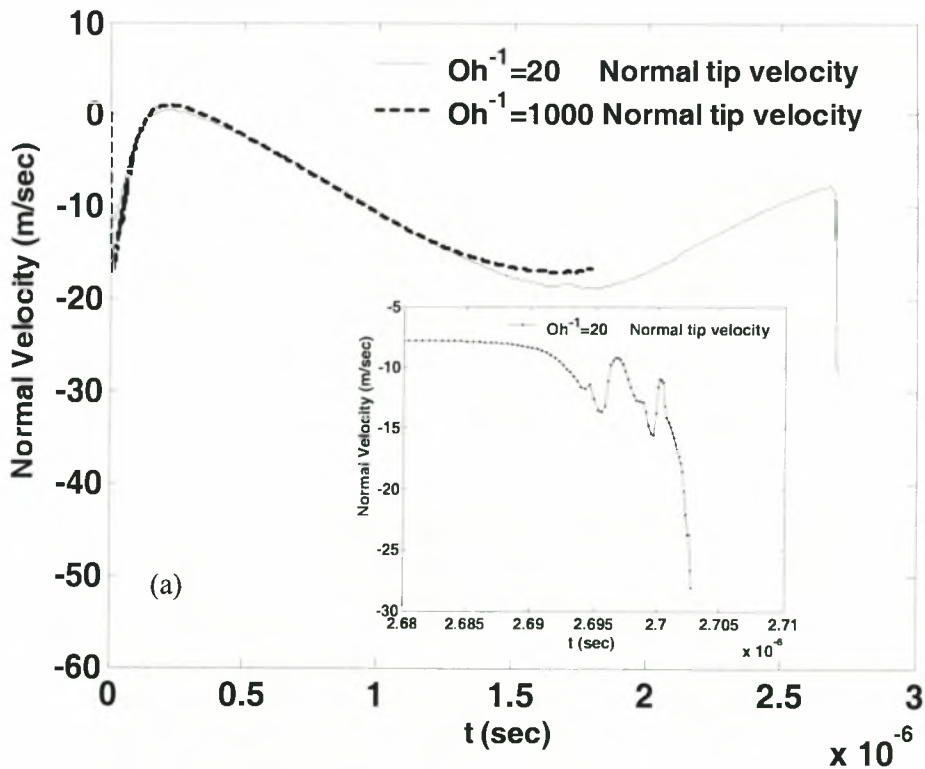


Figure III.11: Time evolution of the distance D , raised to the $3/2$ power, between the dimples that are formed on counter-propagating jets when $Oh^{-1}=1000$; $\varepsilon_B=2$ and $S=0.45$.

Another interesting aspect of the collapse process is the evolution of the jet speed from inception until collapse and it is depicted in figure III.12 when $Oh^{-1}=20$ and 1000. This is a useful quantity if one wants to establish the importance of jet formation in various phenomena such as cavitation damage or even light emission during collapse. As discussed in the introduction, in both phenomena it is believed that shock wave and jet formation play a role the extent of which, however, in different flow arrangements is not always clear and simulations such as the ones presented here can help, along with properly designed experimental investigations, in addressing this issue. The asymptotic increase of jet speed during impact that was discussed in the context of figure III.6 is also illustrated here in the small insert of figure III.12(a). In graph III.12(b) the relative velocity of the two pinching parts of the interface is shown. It exhibits an oscillatory behavior, without the steep increase in absolute value during the collapse phase. This is due to the fact that the normal velocities of the pinching parts of the interface are not aligned with the line connecting them, as was more or less the case with the centered collapse mode. Nevertheless, the universality law still holds during collapse, figure III.11, since this is also determined by the balance between inertia and capillarity. In order to compare jet speed from the above calculations and those presented in the following sections, the speed of the pole at the instant of dimple formation is used as an indicative jet speed. From this point on the universality law takes over leading to increasingly large dimple velocities until collapse.



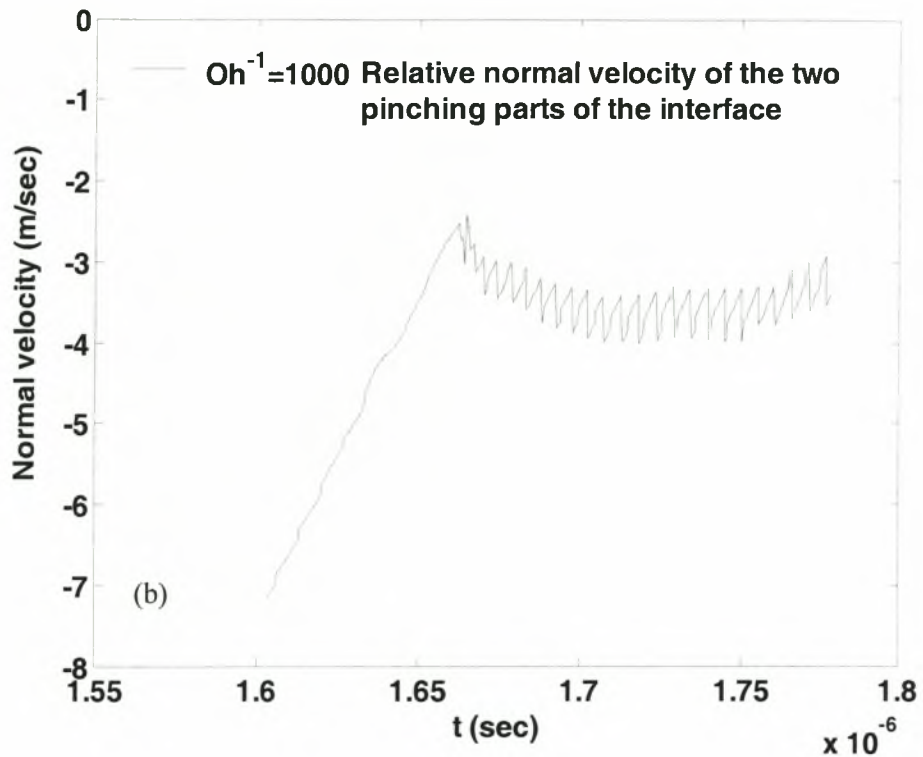


Figure III.12: Time evolution of the dimensional (a) normal velocity of the bubble tip when $Oh^{-1}=20$ and 1000 and (b) relative normal velocity of the pinching parts of the bubble's interface when $Oh^{-1}=1000$; $S=0.45$, $P_{Sr}=4.1$, $\epsilon_B=2$.

Simulations with the bubble oscillations treated as isothermal were also carried out. In this case part of the energy of the system is consumed in order to maintain the bubble at a constant temperature and this has the same effect as a small reduction of Oh^{-1} , favoring the centered collapse mode. In other words, the rest of the problem parameters remaining fixed, the critical Oh^{-1} value for the collapse process to switch from the centered to the off-centered mode increases, with respect to the threshold value for adiabatic oscillations. The rest of the details of collapse do not change significantly when isothermal conditions are assumed, except for the time to collapse, which is longer.

III.2.2 Millimeter sized bubbles, $P_{Sr} \sim 300$, $Oh^{-1} \sim 180$

The collapse mode of bubbles of larger size was also examined, characteristic radius $R=420 \mu\text{m}$, for large initial overpressures and over a range of elongations. Owing to the large size of such bubbles $P_{Sr}=295$ and $Oh^{-1}=174$, for air bubbles oscillating in water at atmospheric pressure, and consequently viscous dissipation does not play as important a role in the system dynamics as was the case with the micron sized bubbles examined in subsection III.2.1. In fact, simulations with Oh^{-1} ranging from 20 to infinity were carried out and no significant effect on the collapse mode was observed. This is a result of the larger size of the bubble and the resulting domination of inertia effects over dissipation. For small initial elongations, $S \approx 0.99$, typically 200 elements were used in the half theta space and the dimensionless time step varied within one calculation between 10^{-4} and 5×10^{-7} in order to accommodate the explosive collapse phase of the

bubble during which $\Delta t \sim \Delta s_{\min}^{5/2}$. For moderate initial elongations, $S \geq 0.7$, larger time steps were used ranging from 10^{-5} to 2×10^{-6} . For large initial elongations, $S \approx 0.45$, the number of elements varied during one calculation from 350 to 600 in the half theta space, in order to properly capture the penetrating jets, while the dimensionless time step varied between 10^{-5} and 10^{-6} .

If a perfectly spherical shape is assumed, $S=1$, while maintaining a large initial overpressure, $\epsilon_B \geq 1$, the bubble performs volume oscillations until it eventually breaks up as a result of an explosive Rayleigh-Taylor instability that is expected to destroy its integrity creating fragments of smaller bubbles. Figures III.13 and III.14 illustrate this behavior in the final bubble shape before collapse and in the time history of the shape mode decomposition as obtained numerically and predicted by linear stability analysis assuming an initial disturbance on the order of the computational accuracy, $a_n(t=0) = 10^{-6}$. As can be gleaned from the final shapes and the shape mode decompositions shown in figures III.13 and III.14, higher modes grow very fast leading to a violent bubble collapse via neck formation characterized by local areas of very low curvature. In fact when $\epsilon_B = 2$ P_{12} grows the fastest leading to the formation of 12 satellite bubbles that are expected to eventually fragment the bubble. It is also interesting to note that P_2 is stable when $\epsilon_B = 2$.

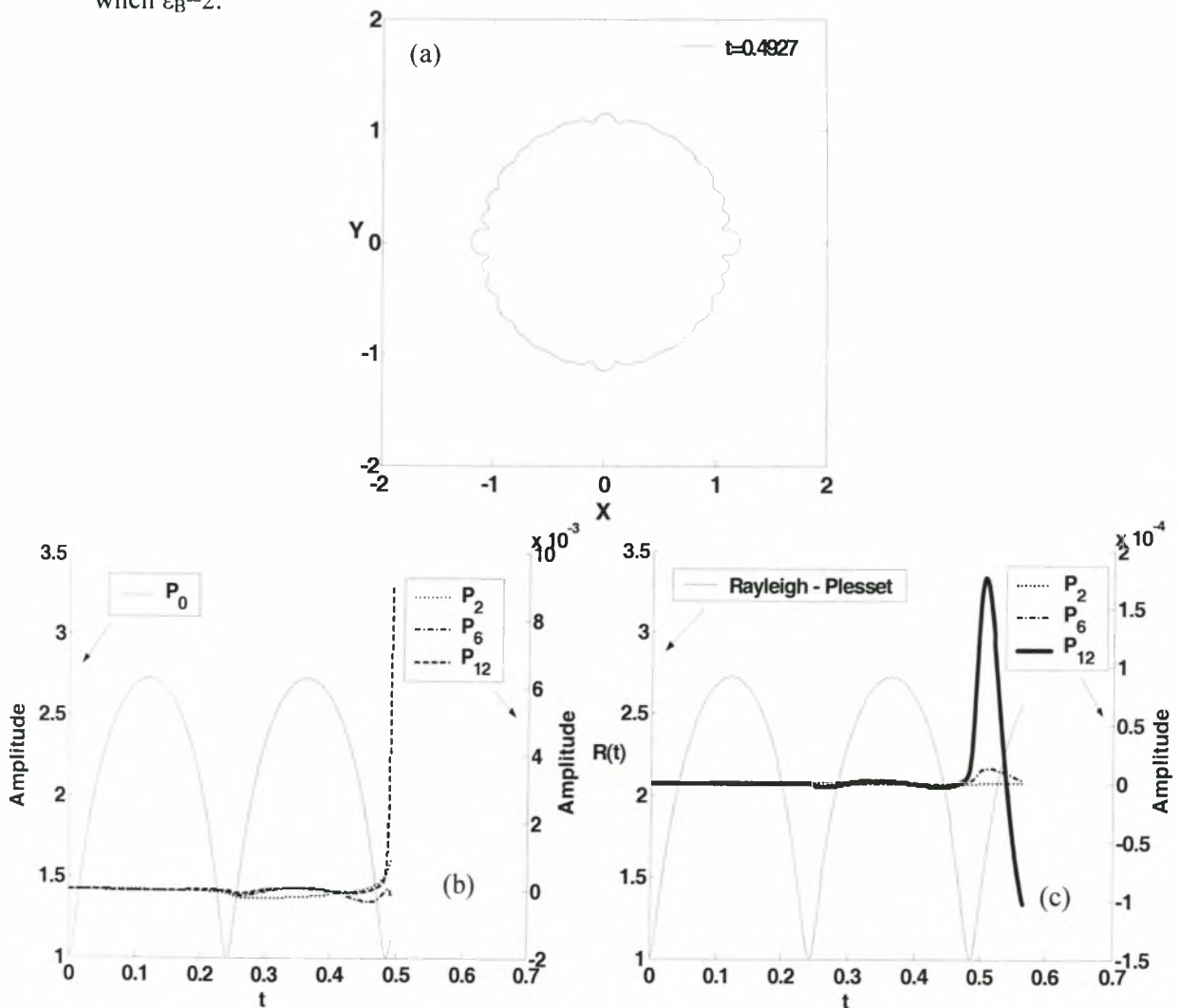


Figure III.13: (a) Bubble shape during collapse, and time evolution of (b) numerically obtained shape mode decomposition and (c) evolution of bubble radius and shape mode decomposition based on stability analysis; $S=1$, $P_{St}=295$, $\varepsilon_B=10$, $Oh^{-1}=174$, with 300 elements in the region $0 \leq \theta \leq \pi/2$.

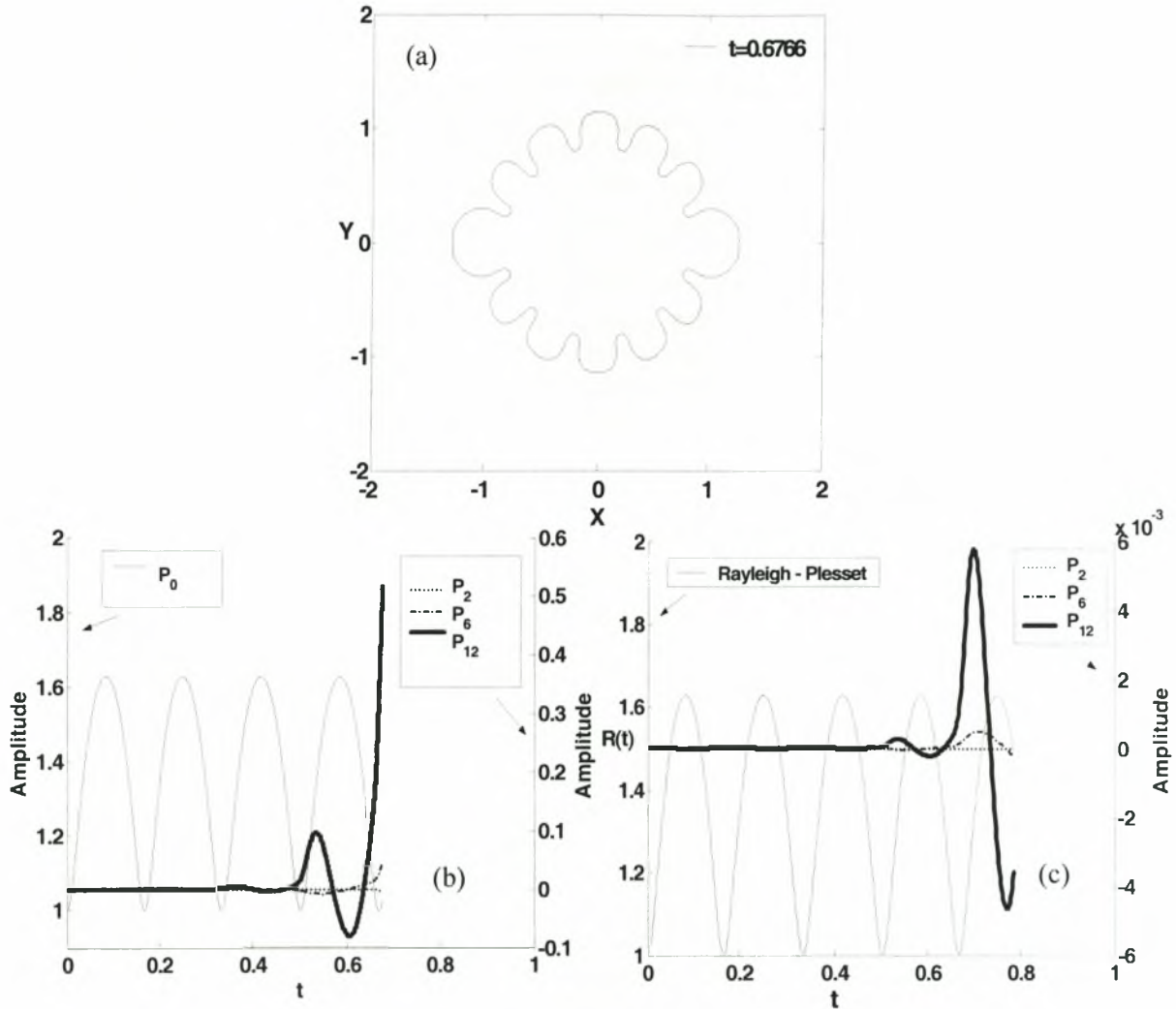


Figure III.14: (a) Bubble shape during collapse, and time evolution of (b) numerically obtained shape mode decomposition and (c) evolution of bubble radius and shape mode decomposition based on stability analysis; $S=1$, $P_{St}=295$, $\varepsilon_B=2$, $Oh^{-1}=174$, with 200 elements in the region $0 \leq \theta \leq \pi/2$.

For very large initial overpressure, $\varepsilon_B \sim 10$, and finite initial elongation, $S < 1$, growth of P_2 is observed in the form of an afterbounce instability that arises during the rebound of the bubble from its minimum volume. The microbubble collapses in a centered fashion, either via a sink flow along the equatorial plane towards the center of the bubble, figure III.15 for $S=0.99$, or along the axis of symmetry, figure III.16 for $S=0.9$, depending on the phase of P_2 growth during collapse, in the manner described in subsection III.2.1 and verified by the shape mode decomposition shown in figures

III.15(c) and III.16(c). The latter type of collapse is recovered for the entire range of initial elongations that was examined, $0.5 \leq S \leq 0.98$. As the initial overpressure increases further, $\varepsilon_B > 10$, the same differentiation in the type of collapse is observed, depending on the initial elongation, with the range in S corresponding to sink flow along the equator increasing. In both cases pinching observes the $3/2$ power law during the break-up process.

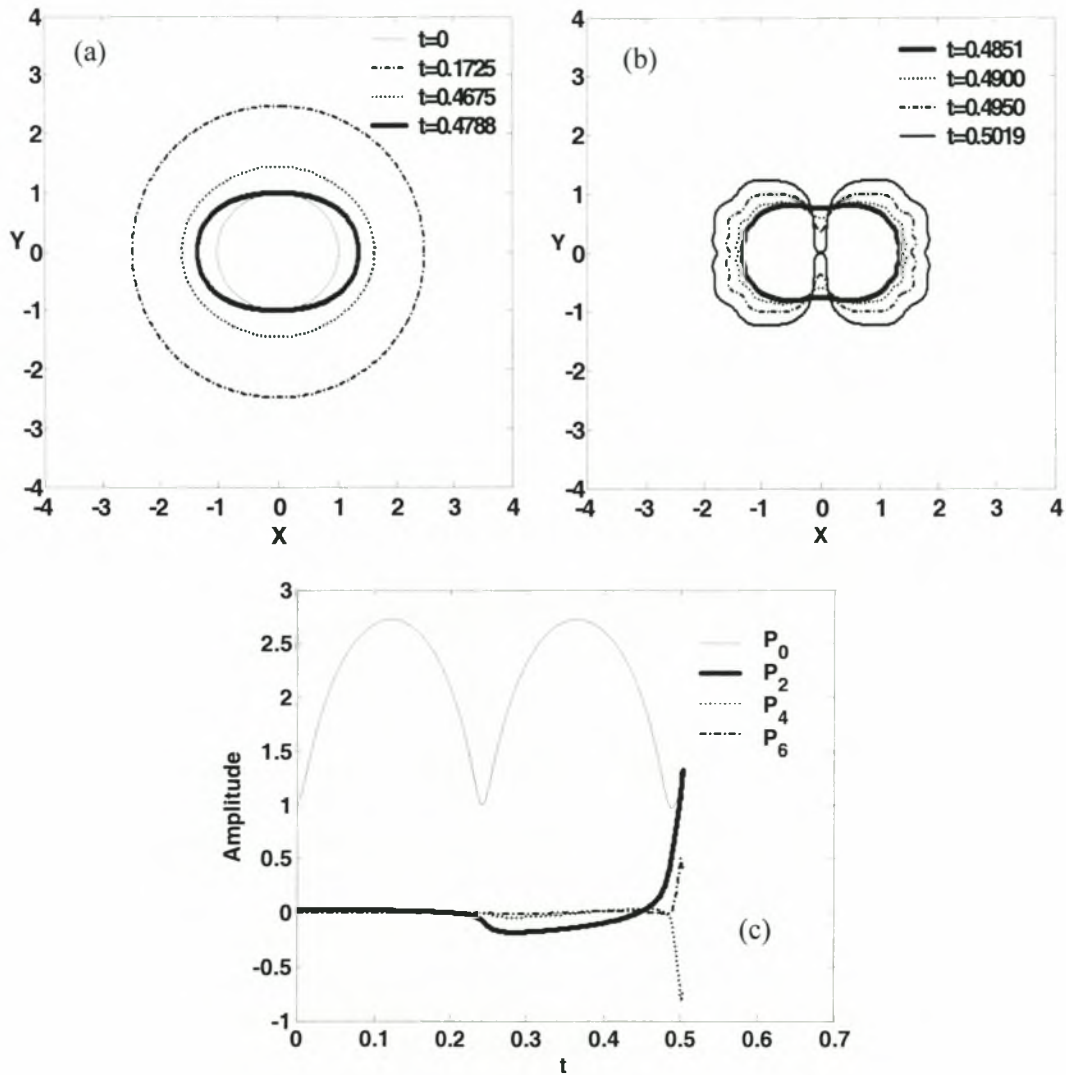


Figure III.15: Time evolution of (a) bubble shapes in the beginning of the motion, (b) bubble shapes during collapse and (c) numerically obtained shape mode decomposition; $S=0.99$, $P_{Si}=295$, $\varepsilon_B=10$, $Oh^{-1}=174$, with 200 elements in the region $0 \leq \theta \leq \pi/2$.

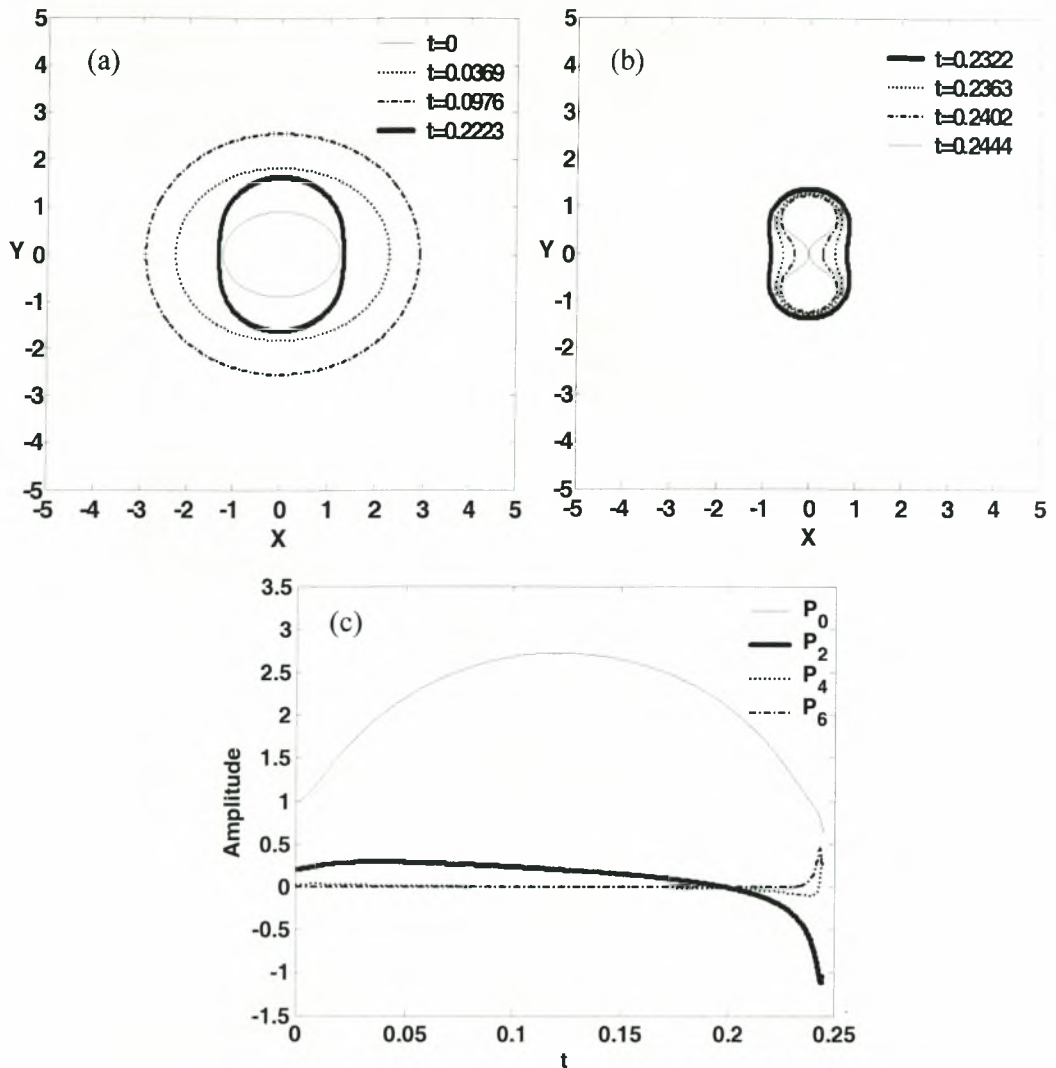


Figure III.16: Time evolution of (a) bubble shapes in the beginning of the motion, (b) bubble shapes during collapse and (c) numerically obtained shape mode decomposition; $S=0.9$, $P_{St}=295$, $\varepsilon_B=10$, $Oh^{-1}=174$, with 200 elements in the region $0 \leq \theta \leq \pi/2$.

A large number of simulations were also conducted with varying Oh number without any effect on the collapse mode. Figure III.17 compares dimensional tip velocities for three different elongations. When $S=0.9$ and 0.7 each tip is located at the poles of the axis of symmetry whereas when $S=0.99$ the tip is located at the equator. Jet speeds at collapse tend to increase with decreasing initial elongation while they are higher than those calculated for micron-sized bubbles, figures III.6 and III.12, indicating the larger effect of jet impact for bubbles of this size. In all the above cases the speed of the approaching tip at the instant of dimple formation was used as an indicative jet speed in the comparison. We use the term jet speed for the case of sink flow as well in order to indicate the localized nature of both types of collapse.

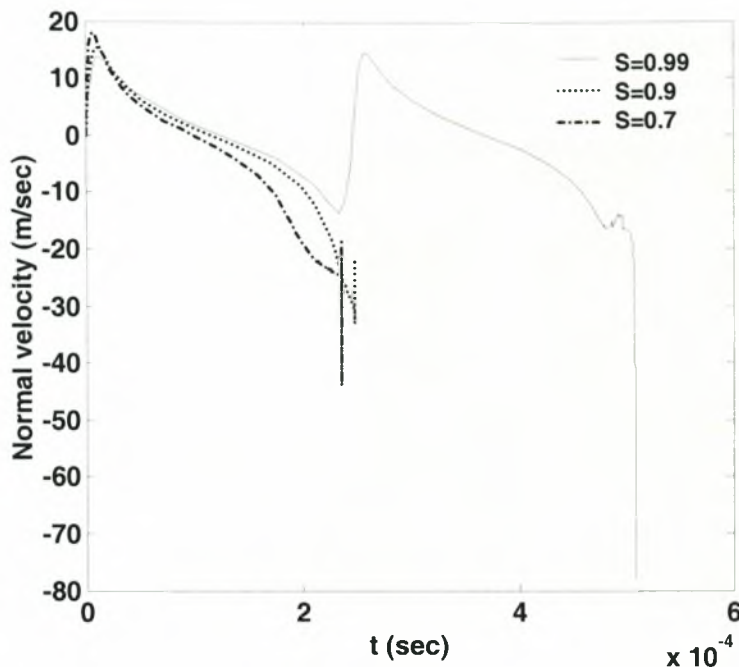


Figure III.17: Time evolution of the dimensional normal velocity of the bubble tip with increasing initial elongation, $S=0.99$, 0.9 and 0.7 ; $P_{St}=295$, $\varepsilon_B=10$ and $Oh^{-1}=174$.

When the bubble is almost spherical, $S \geq 0.95$, and the initial overpressure not very large, $\varepsilon_B=2$, the bubble collapses after a number of periods of oscillations, in a fashion similar to the situation illustrated in figure III.14 leading to fragmentation. This is a result of the stability of P_2 for this parameter range and the growth of higher modes that generate areas of very low radius of curvature where rupture is more likely to happen. For larger elongations, $0.5 \leq S < 0.95$, P_2 exhibits growth and the centered collapse mode is recovered for the entire range of S and ε_B values examined. It should be stressed that for S values below 0.45 the off-centered collapse mode prevails, due to the large jet speed that enhances interaction with the side-walls during the contraction phase. As was explained in the previous subsection this leads to rounding of the jet front and pinching at the side-walls.

III.3 SIMULATIONS OF EXPERIMENTS WITH LASER BUBBLES

We would like to identify the collapse modes that were observed in the above simulations, in the context of the experimental observations reported in [12]. As was mentioned in section III.1, in the latter study nano and femto second laser pulses were employed in order to produce a single millimeter or micron sized bubble, whose collapse was examined for luminescence. The frame sequences that were reported were very useful in understanding the dynamics behind bubble collapse, while careful measurements of light emission showed that only the millimeter sized bubbles were capable of producing it. However, all the available frames were obtained at a certain angle, perpendicular to the bubble axis of symmetry, which, especially in the case of micron sized bubbles, does not allow for ascertaining jet formation. Hence, an effort is made here to simulate, as rigorously as possible, the above experiments and try to shed

light to aspects of the break-up process that are not easily accessible by an experimental study. The simulations are conducted in the manner described in section III.1.

The entire process is more or less isothermal except for the time period between inception of the bubble and the first recorded frame during which liquid evaporation and recondensation takes place under non-isothermal conditions as well as during the collapse phase of the bubble. Nevertheless, based on previous studies in sonoluminescence¹⁸ we do not expect that a varying polytropic constant, γ , will significantly change the results of the simulations. Indeed repeating the simulations setting $\gamma=1.4$ does not provide a different picture from the one with $\gamma=1$, hence we use $\gamma=1$ for the simulations presented throughout this section.

III.3.1 Simulations of femto-second laser bubbles

A characteristic sequence of frames of a collapsing femto-second laser bubble is depicted in figure III.18(a), as recorded with a high-speed camera¹² with frames progressing in time from left to right and from top to bottom. The bubble is severely elongated initially, as illustrated by the first frame obtained 100 ns after the laser pulse. In particular, the initial bubble volume is, roughly, $840 \mu\text{m}^3$, corresponding to an equivalent radius of $5.8 \mu\text{m}$. However, the length of the bubble along its axis of symmetry is, roughly, $100 \mu\text{m}$, which corresponds, assuming an ellipsoidal initial shape, to an elongation parameter $S \approx 0.34$. As can be gleaned from figure III.18(a) the bubble undergoes a first collapse after, roughly, $6.1 \mu\text{s}$ from its inception and then rebounds and oscillates until it eventually settles to its equilibrium radius, $R_{\text{Eq}} \approx 15 \mu\text{m}$.

Following the methodology described section III.1 we first calculate the bubble pressure at equilibrium, based on graphical evaluation of the experimentally obtained volume at equilibrium, and then using the isothermal ideal gas law we obtain the bubble pressure at $t=t_1=100 \text{ ns}$, $P_G(t=t_1)=P_1 \approx 4.5$. The initial bubble pressure is not known but can be estimated so that the maximum volume expansion of the bubble is fitted. In this fashion we obtain $P_G(t=0)=P_0 \approx 50$ which corresponds to $\epsilon_B \approx 9$. Operating in the above parameter range, with $\text{Oh}^{-1} \approx 20$ for bubbles of this size, the collapse of femto-second laser bubbles was simulated. However, the simulations predict break-up via the off-centered mode, figure III.19, which leads to two smaller toroidal bubbles and a larger one occupying the two sides and the central region of the original bubble, respectively, which is in contrast to the experimental observations that show a contracting bubble. Small variation of the initial elongation or the initial overpressure does not change the collapse mode. It must be stressed also that the experimental observations took place at an angle that does not allow for proper observation of jet formation. Consequently, it is not easy to decipher whether it is the centered collapse mode via jet coalescence at the equatorial plane that takes place in the experiments reported in [12]. The simulations do favor the centered collapse mode, albeit for a lower value of Oh^{-1} than that corresponding to the actual bubble size. This result, however, may be an artifact of the weak viscous approach adopted by the present study that is not strictly valid as Oh increases. In fact, it was found by studies²⁵ on bubble stability in the context of sonoluminescence, that boundary layer theory underestimates viscous effects on gas bubbles of μm size. Hence we repeated the simulation setting Oh^{-1} to 3 in an effort to account for this underestimation. Based on the parametric study in subsection III.2.1 we expect that for the severe elongations obtained in the experiments under consideration¹², $S \approx 0.34$, the threshold value of Oh^{-1} for the centered mode to appear would be below the

value 200 that was obtained for $S=0.45$. Indeed setting Oh^{-1} to 3 we obtain the centered collapse mode.

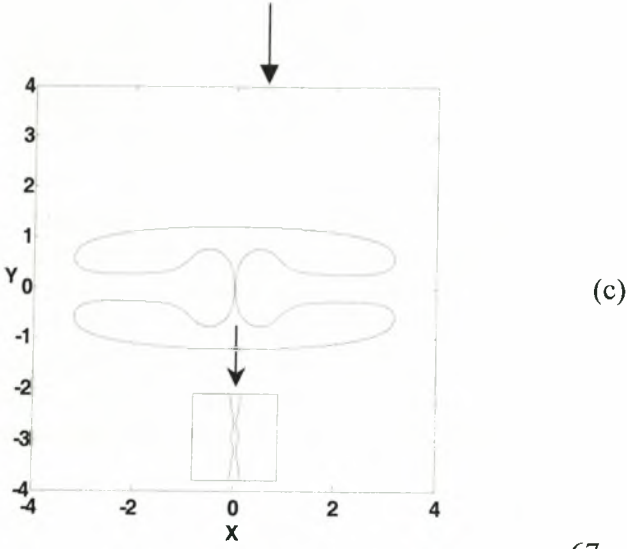
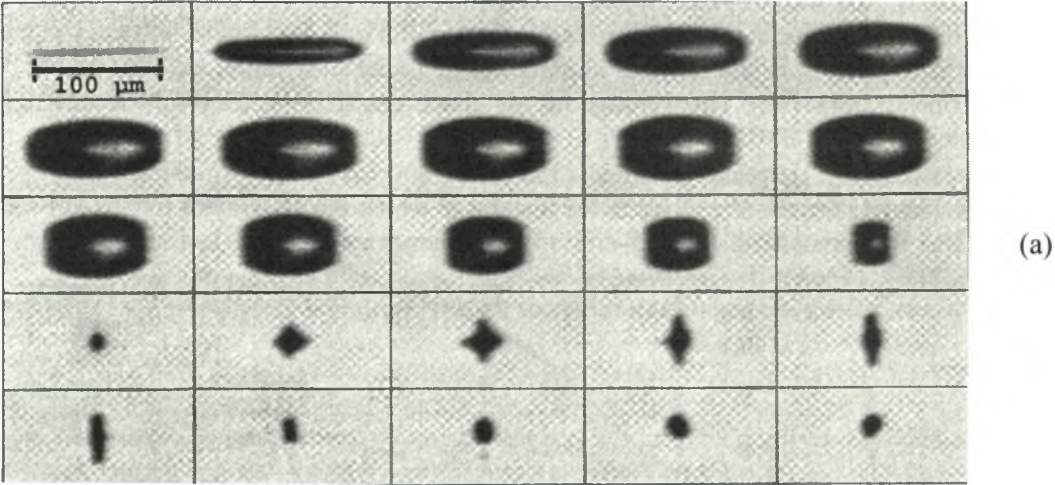


Figure III.18: (a) Frame sequence depicting the collapse of a bubble generated via a femtosecond laser pulse. The host liquid is water at normal pressure and temperature conditions. The width of each frame corresponds to $150\mu\text{m}$. The first frame is captured at $t_1=100\text{ ns}$ while subsequent frames are captured at a time interval of 400 ns . The laser pulse is applied from the left and imparts $0.8\ \mu\text{J}$ to the host liquid. All the frames are reproduced from [12]. (b) Simulations of shape oscillations of femto-second laser bubbles in water; $S=0.34$, $P_{St}=4.1$, $\epsilon_B=9$, $Oh^{-1}=3$, with the number of elements in the region $0\leq\theta\leq\pi/2$ ranging between 350 and 600 as the simulation progresses. Dimensionless times correspond to the instants at which the equivalent frames of Figure III.18(a) were recorded. (c) 5×5 and 45×45 enlargements of the last shape shown in III.18(b).

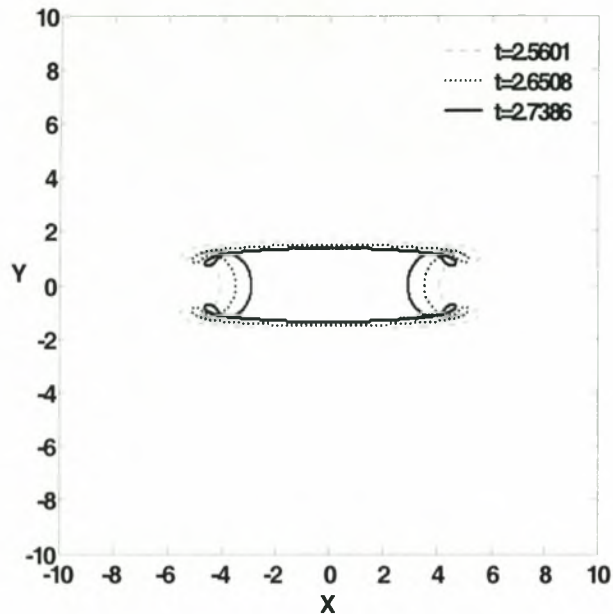


Figure III.19: Simulations of shape oscillations of femto-second laser bubbles in water during collapse; $S=0.34$, $P_{St}=4.1$, $\epsilon_B=9$, $Oh^{-1}=20$, with 500 elements in the region $0\leq\theta\leq\pi/2$.

Figure III.18(b) shows the evolution of bubble shapes following inception, at the time intervals for which bubble shapes were recorded experimentally. During the simulation the number of elements varied between 350 and 600 along the half theta space, $0\leq\theta\leq\pi/2$, in order to properly capture jet formation and propagation, and consequently the time step was varied between 10^{-5} and 10^{-6} using the scaling law $\Delta t \sim \Delta s_{\text{min}}^{3/2}$ governing the process of jet impact. At the dimensionless time instant corresponding to 100 ns the bubble pressure is dropped down to P_1 and then the simulation proceeds until collapse. As illustrated in figure III.18(b) the bubble collapses in a centered fashion and jet impact occurs on the time scale for which the experiments recorded the first bubble collapse, $t=3.037$ or $t' \approx 5.0\ \mu\text{s}$. Consequently, it would be very interesting to conduct similar axisymmetric simulations of bubble collapse employing the full Navier-Stokes equations, in order to verify the collapse mechanism and provide new insight for experimental observations. In addition to that, careful

observations could offer more evidence on jet formation provided the angle of observation is varied so that a closer look is possible on fluid motion along the axis of symmetry. It is worth mentioning that the speed of the bubble tip as calculated from figure III.20 at the moment of jet impact is on the order of 42 m/sec, which is on the same order as the values obtained from the parametric study for cases in which the centered collapse mode prevails.

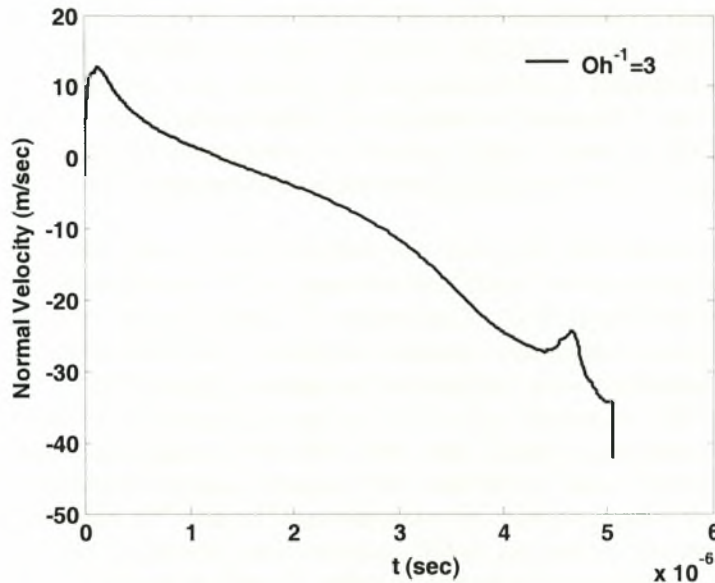


Figure III.20: Time evolution of the dimensional normal velocity of the bubble tip of a femtosecond laser bubble; $S=0.34$, $P_{St}=4.1$, $\varepsilon_B=9$, $Oh^{-1}=3$.

III.3.2 Simulations of nano-second laser bubbles

The collapsing process of nano-second laser bubbles has also been experimentally recorded via high speed camera¹², when water or various mixtures of it with acetone are used as host fluids. In this case due to the relatively long duration of the laser pulse the bubbles are much larger in size, equivalent radius of 0.42 mm, roughly, and their initial elongation much less severe. A characteristic sequences of shapes of nanosecond bubbles recorded experimentally¹² with pure water as host fluid is provided in figure III.21(a). The bubble collapses in a violent and more or less spherosymmetric fashion, before it rebounds and settles to its equilibrium size. As a result of the intensity of collapse significant light emission takes place.

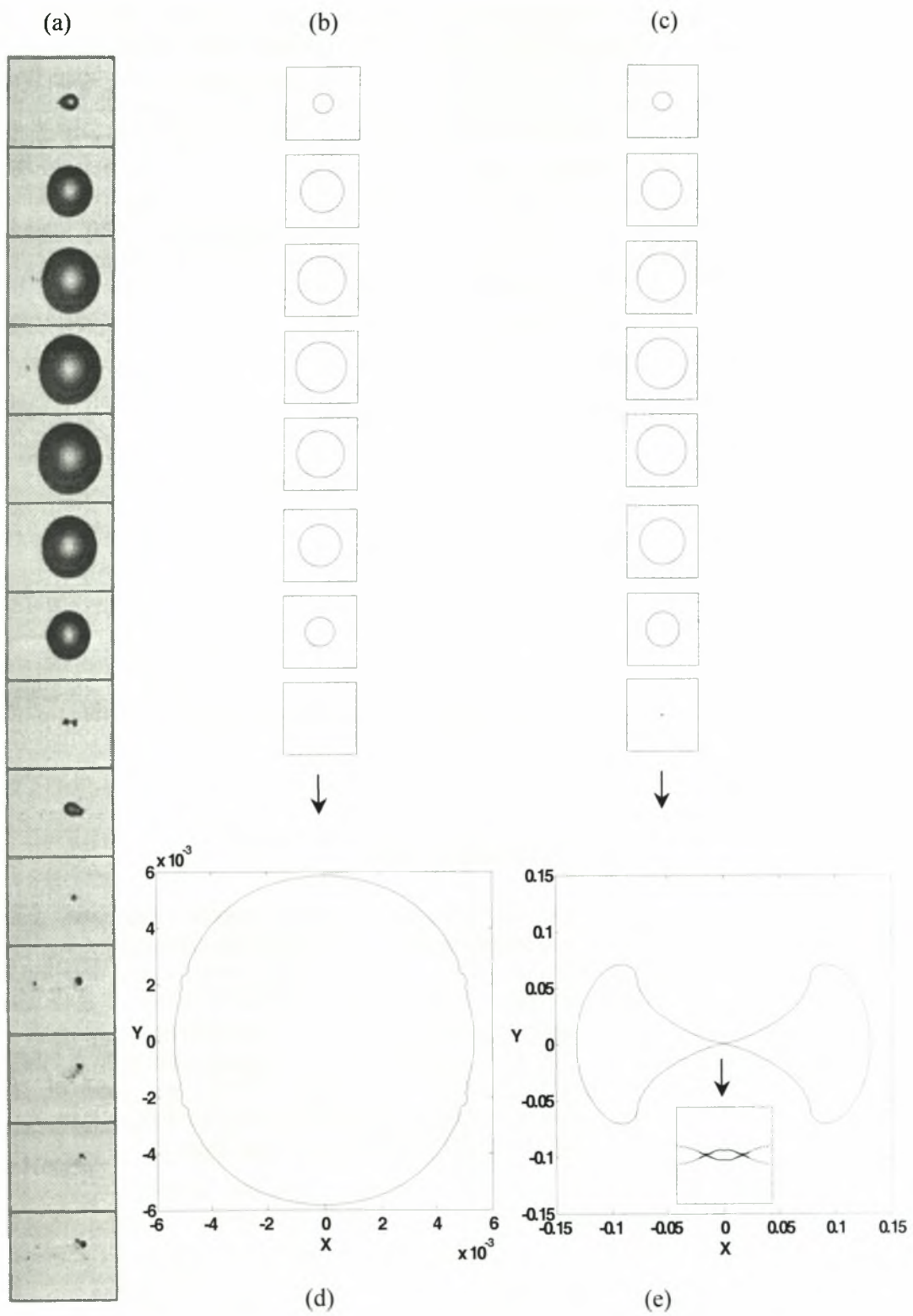


Figure III.21: (a) Frame sequence depicting the collapse of a bubble generated via a nanosecond laser pulse. The host liquid is water at normal pressure and temperature conditions. The width of each frame corresponds to 4mm. The first frame is captured at $t_1=2 \mu\text{s}$ while subsequent frames are captured at a time interval of $30 \mu\text{s}$. The laser pulse is applied from the left and imparts $3.8(4) \text{ mJ}$ to the host liquid. All the frames are reproduced from [12]. (b) Simulations of shape oscillations of nano-second laser bubbles in water; $S=1$, $P_{St}=295$, $\varepsilon_B=81$, $Oh^{-1}=174$. (c) Simulations of shape oscillations of nano-second laser bubbles in water; $S=0.98$, $P_{St}=295$, $\varepsilon_B=81$, $Oh^{-1}=174$. In the simulations 200 elements were used in the region $0 \leq \theta \leq \pi/2$. Indicated dimensionless times correspond to the instants at which the equivalent frames of figure III.21(a) were recorded. (d) 3100×3100 enlargement of the last shape shown in III.21(b) and (e) 125×125 and 1125×1125 enlargements of the last shape shown in III.21(c).

Following the same procedure that was used for femto-second bubbles the pressure at dimensional time $t=2 \mu\text{s}$ when the first frame was recorded as well as the initial overpressure are estimated; $P_1=P_G(t=t_1) \approx 62$, $P_0=P_G(t=0) \approx 24400$. The initial elongation is small but finite and cannot be estimated with great accuracy based on the recorded frames. Consequently a series of simulations were conducted for different initial elongations with S ranging from 1 to 0.8. In the simulations 200 elements were used in the half theta space while the time step varied significantly in order to accommodate the abrupt volume change of the bubble. In fact, a dimensionless time step variation between 10^{-4} and 10^{-9} was necessary in order to capture the dynamics of the bubble from the beginning until collapse. When the bubble assumes a perfectly spherical shape initially it is seen to collapse sphero-symmetrically with maximum violence and on the time scale obtained by the high-speed camera recordings. Figure III.21(b) shows the calculated shapes at the same time interval, $\Delta t=30 \mu\text{s}$, as the recorded frames, as well as the last shape obtained before simulations stopped. The latter is not spherosymmetric any more. Rather, it is deformed in a manner that is relevant to Rayleigh-Taylor instability. Indeed, this is verified by shape mode decomposition performed on the calculated shapes. In addition, growth of shape modes is predicted by linear stability analysis using equation (III.6) with the radial motion provided by the Rayleigh-Plesset equation and the same sequence of pressure change as in the simulations. In this context, however, the bubble is not expected to retract and acquire an equilibrium state, as indicated by the experiments. Instead, it would fragment in several pieces. In fact, the calculated final volume is much smaller than the one measured experimentally, figure III.21(b), indicating that bubble collapses in a less violent fashion. Allowing for a small initial elongation of the bubble leads to a more realistic collapsing process where details of collapse are captured more accurately, such as the bubble volume and jet formation, figure III.21(c). As S decreases the minimum volume increases and for the appropriate range in S values, $0.9 \leq S \leq 0.98$, the experimentally obtained minimum volume is better approximated by the simulations as well as the details of the bubble shape, figure III.22.

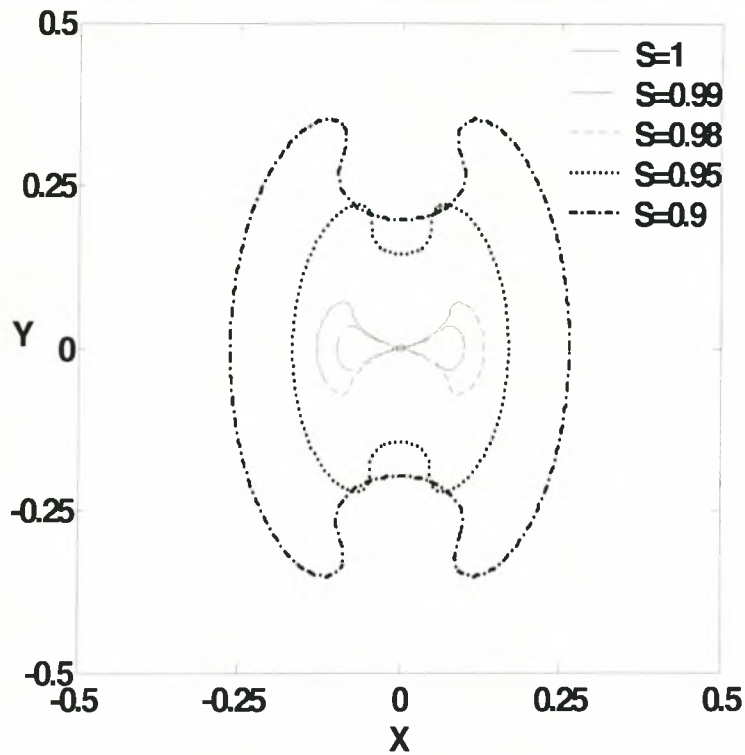
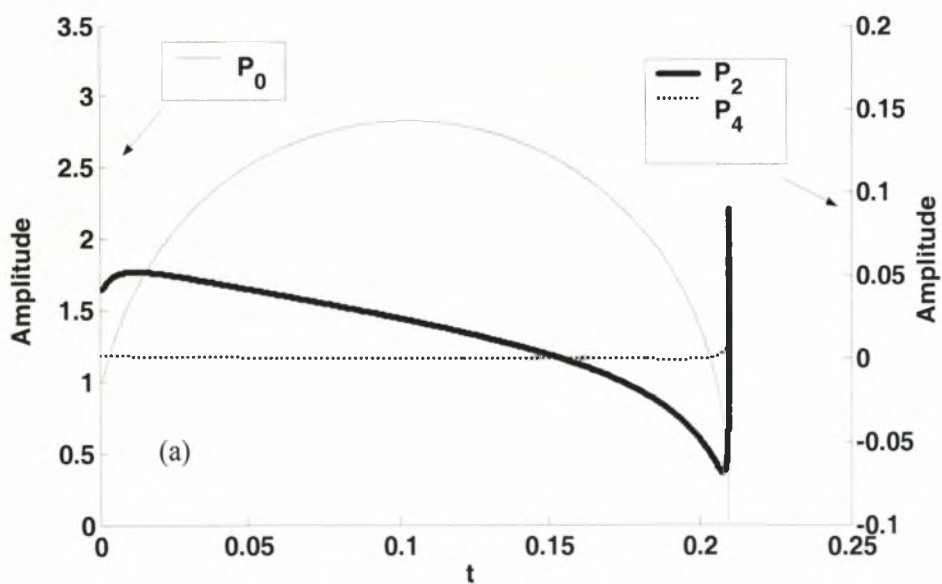


Figure III.22: Last numerically obtained shape when $S=1, 0.99, 0.98, 0.95$ and 0.9 .

Nevertheless, the bubble volume at impact remains below the experimental observation, probably due to the net effect of liquid evaporation due to adiabatic heating during collapse, but also because it is difficult to experimentally capture the absolute volume minimum. In all cases shown in figure III.22 the bubble collapses via a sink flow along the equator. This is a result of P_2 growth that dominates the bubble dynamics as illustrated by the mode decomposition in figure III.23.



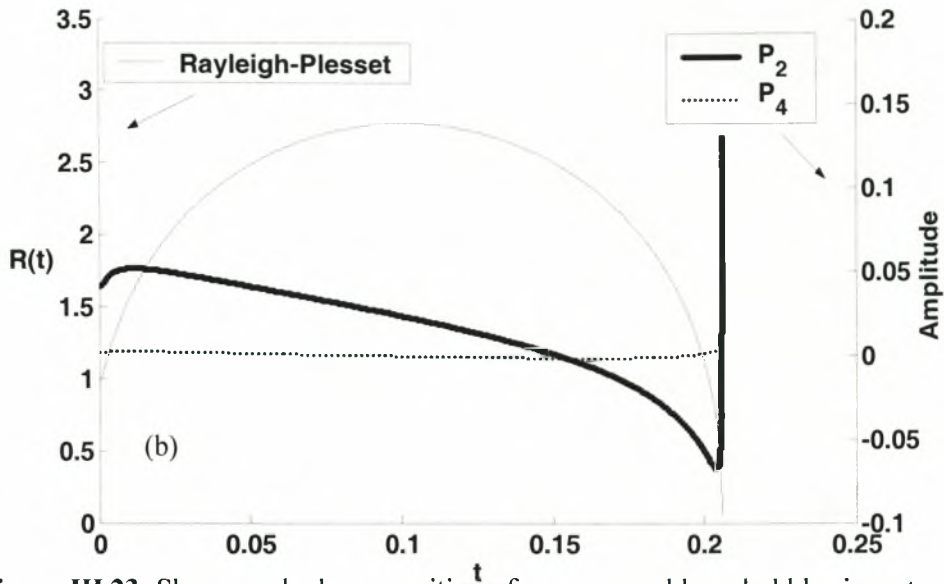
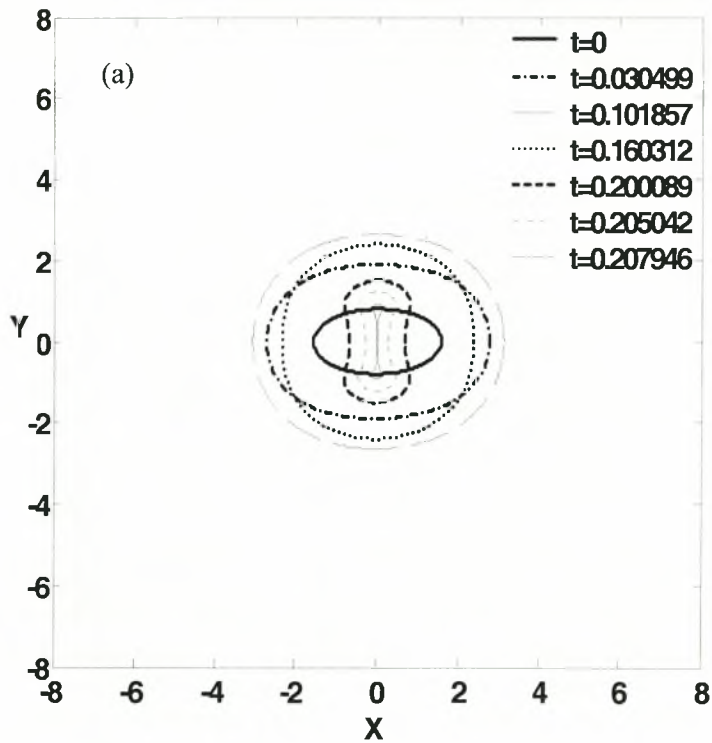


Figure III.23: Shape mode decomposition of nano-second laser bubbles in water, on (a) numerically obtained shapes and (b) evolution of bubble radius and shape mode decomposition based on stability analysis; $S=0.98$, $P_{St}=295$, $\epsilon_B=81$, $Oh^{-1}=174$.

Further reduction of S to 0.8 accelerates jet formation, which now takes place along the axis of symmetry due to the high initial content of P_2 , figure III.24(a), but weakens jet impact owing to lack of sphericity, figure III.24(b).



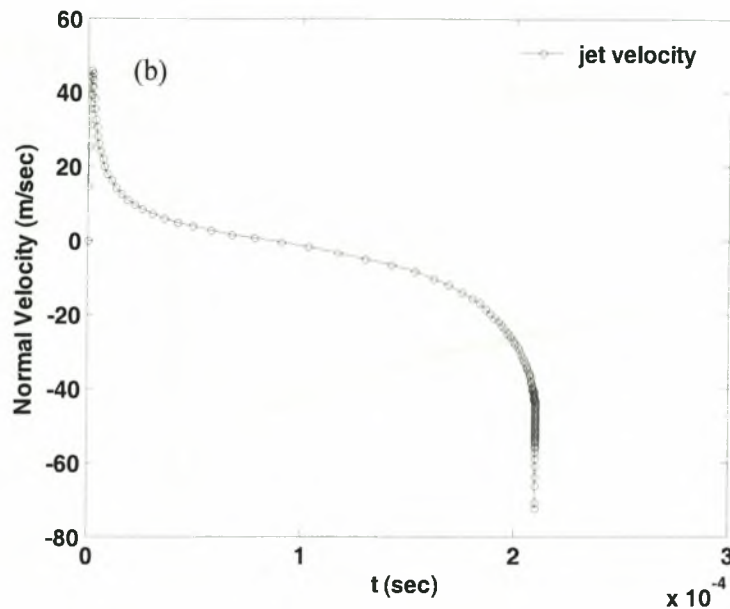


Figure III.24: (a) Simulations of shape oscillations of femto-second laser bubbles in water during collapse, (b) time evolution of the dimensional normal velocity of the bubble tip of a femtosecond laser bubble; $S=0.8$, $P_{St}=295$, $\epsilon_B=81$, $Oh^{-1}=174$.

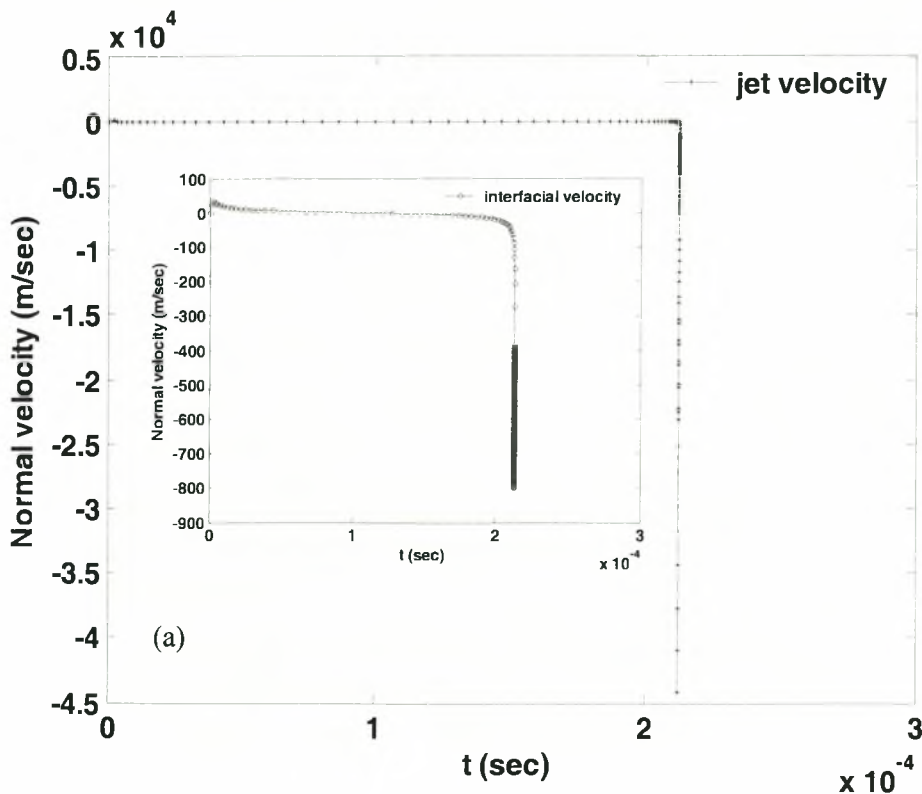
The case with $S=0.95$ seems to be the closest as far as prediction of the bubble minimum volume and jet impact are concerned, figure III.22. The penetrating “jet”, by that we refer to the liquid region around the equator in the interest of brevity even though it is really a sink flow, is quite narrow in this case and capturing the details of impact requires combination of a large number of elements and a very small time step. Thus the simulation was not continued until final impact, as this would be computationally very expensive without adding any insight to our understanding of the phenomenon.

It should also be stressed that towards the final stages of collapse fluid velocities comparable with the speed of sound in water develop and consequently the flow becomes compressible. The effect of compressibility is not captured by the present numerical technique but it is not expected that it will change the details of bubble collapse significantly. If more accurate predictions of the details of bubble collapse are required, such as the speed of the sink flow near the center of the bubble and minimum bubble volume, then adiabatic heating and liquid evaporation that take place during collapse have to be modeled^{88,89}, along with compressibility effects.

Based on the simulations with small initial elongation ($S \sim 1$), the time from collapse scales with the $5/2$ power of the bubble radius, for the period of time over which the bubble shape remains almost spherical, as expected from transient cavitation theory⁸⁹, hence the large speed of collapse. Another important aspect of the break-up process is the formation of the sink flow along the equator. This effect is also observed in the recorded bubble shapes¹²; see also figure III.21(a). Projected on a plane that contains the axis of symmetry the sink flow region takes the form of two “jets” that approach each other and coalesce at the axis of symmetry giving rise to a tiny microbubble in the center along with two bubbles that occupy the two hemispheres of the original bubble. This process takes place in a fashion that is similar to the one

observed in the parametric study for millimeter size bubbles subject to very large internal overpressure, see also figure III.15(b). The time from jet coalescence again scales with the $3/2$ power of the minimum distance between the two jets. The same type of collapse via a sink flow has been observed experimentally and verified numerically when bubbles deform inside a tip vortex^{76,87}.

As illustrated in figure III.21(c), towards the last stages of collapse there are two events that occur co-currently, namely bubble volume contraction and jet formation. The interfacial speed, referring to the speed of the part of the interface that remains nearly spherical, and jet velocities are shown in figure III.25(a) and they are both quite large. In particular, the interfacial velocity is, roughly, 800 m/sec, whereas the jet velocity is on the order of 15000 m/sec. These are quite large speeds but they have to be compared with the speed of sound in the gas that fills the laser bubble, in the heavily compressed state that it acquires during the collapse phase, in order to ascertain whether a shock wave will be detached from the interface and converge towards the bubble interior, in addition to more specific experimental observations. On the other hand it is quite clear that sphericity of the bubble shape for the most part of the collapsing process, along with substantial initial overpressure, are enough to establish a very severe jet impact. It would be very interesting to examine the time instant of photon emission in the experimental observations, in order to decipher exactly when it happens and which effect dominates. These issues have been addressed before in the context of aspherical bubble collapse near rigid boundaries¹¹ and it was seen that when the time interval separating the bubble volume minimum from jet impact is smaller than 50 ns, the framing resolution of the camera, it is impossible to distinguish between the two events. It should also be noted that the life span of the jet, from inception to impact, is on the order of 150 ns, which is within the capacity of modern high-speed cameras. It seems that such measurements are possible in the context of nanosecond laser bubbles and it would be quite useful if this line of research were to be pursued further.



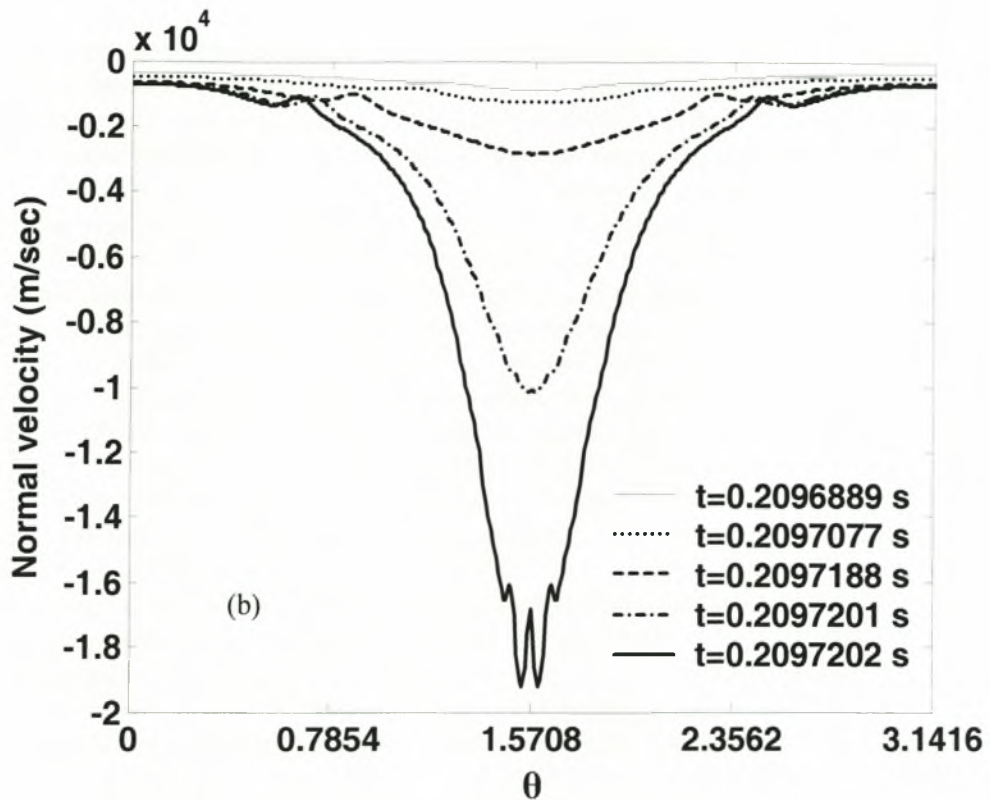


Figure III.25: (a) Interfacial and jet speed during collapse of a nanosecond laser bubble and (b) evolution of the normal velocity distribution along the bubble interface; $S=0.98$, $P_{St}=295$, $\varepsilon_B=81$, $Oh^{-1}=174$.

Similar simulations were conducted based on experimental recordings of nanosecond laser bubbles collapsing in a 5% water solution of acetone, figure III.26(a). In this case the experiments indicate no light emission despite the, more or less, spherically symmetric nature of collapse. The parameter values for this arrangement are nearly the same as in the case with water as the host fluid; $P_{St} \approx 302$, $S \approx 0.98$, $P_G(t=0) = 24400$ or $\varepsilon_B \approx 81$, $Oh^{-1} \approx 176$ and $P_1 = P_G(t=t_1) \approx 304$. As shown from the shapes obtained from the numerical simulations at time intervals based on the experimental recordings, figure III.26(b), the former predict a very similar collapse mode with the case of pure water. Nevertheless the experiments indicate a much less severe collapse. This effect cannot be reproduced by simply employing small perturbations of the simulation parameters. It requires a more drastic change such as that provided by reducing the pressure drop suffered by the bubble at $t=t_1$. Then, as illustrated in figure III.26(c), the speed of collapse is significantly reduced, which conforms with the failure to detect photon emission in the experiments. This improvement may be due to the fact that the reduction in pressure drop better describes the higher tendency of acetone to vaporize that restricts the extent of plasma recondensation. It is the latter effect that is mainly simulated by the sudden pressure drop at $t=t_1$. Clearly then, if proper accounting of the evaporation process is required, the heat and mass transfer phenomena that take place, especially during the early stages of inception of laser bubbles, have to be modeled^{88,89}. In addition, compressibility effects have to be taken into consideration during the collapse phase of the bubble if the exact temperature and pressure conditions at the instant of light emission need to be known.

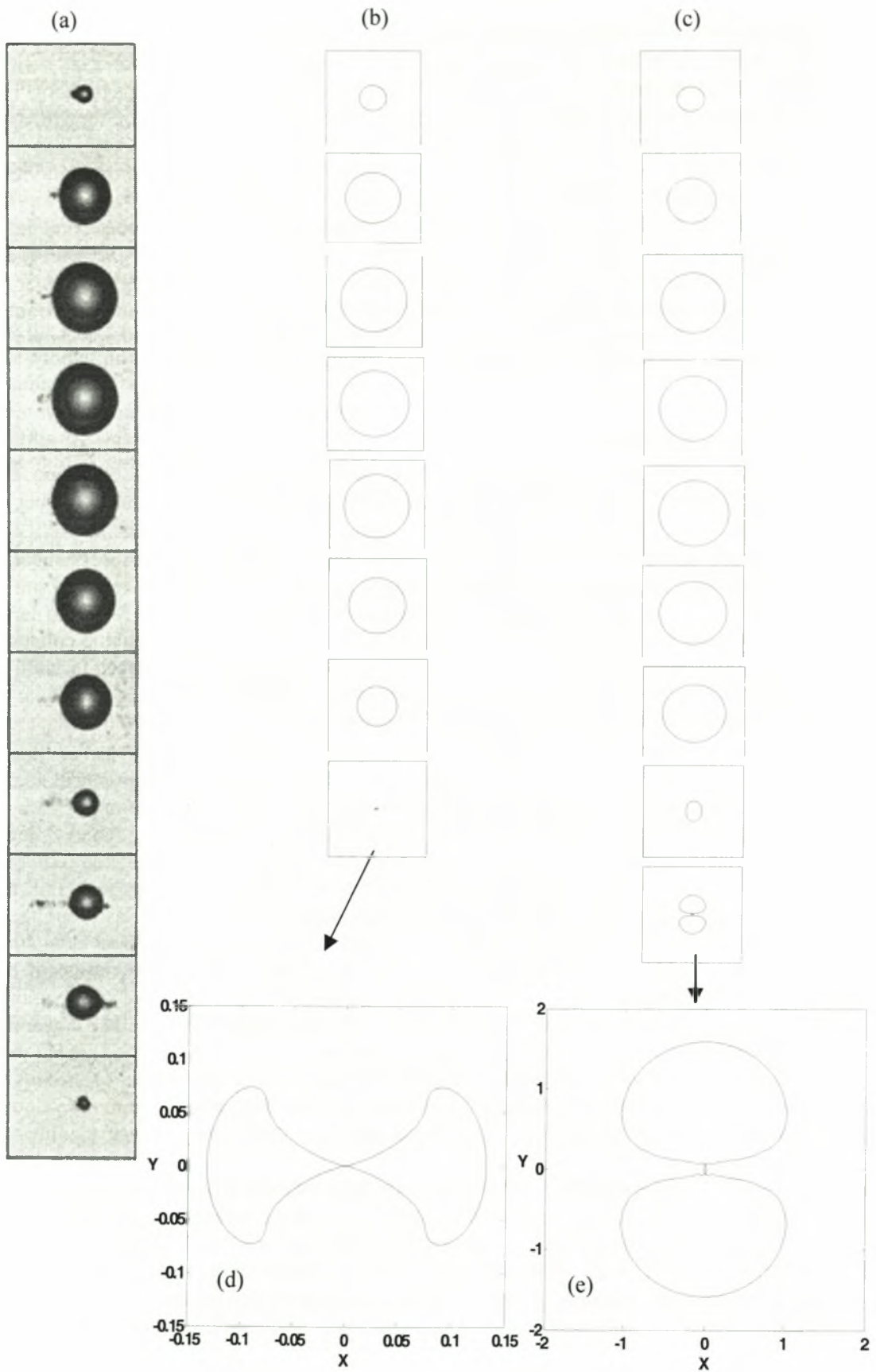


Figure III.26: (a) Frame sequence depicting the collapse of a bubble generated via a nanosecond laser pulse. The host liquid is 5% water solution of acetone at normal pressure and temperature conditions. The width of each frame corresponds to 4mm. The first frame is captured at $t_1=2 \mu\text{s}$ while subsequent frames are captured at a time interval of $30 \mu\text{s}$. The laser pulse is applied from the left and imparts $3.8(4) \text{ mJ}$ to the host liquid. All the frames are reproduced from [12]. (b) Simulations of shape oscillations of nano-second laser bubbles in 5% water solution of acetone; $S=0.98$, $P_{st}=302$, $\varepsilon_B=81$, $Oh^{-1}=176$, $P_G(t=t_1)=304$. (c) Simulations of shape oscillations of nano-second laser bubbles in 5% water solution of acetone; $S=0.98$, $P_{st}=302$, $\varepsilon_B=81$, $Oh^{-1}=176$, $P_G(t=t_1)=1404$. In the simulations 200 elements were used in the region $0 \leq \theta \leq \pi/2$. Indicated dimensionless times correspond to the instants at which the equivalent frames of figure III.26(a) were recorded. (d) 123×123 enlargement of the last shape shown in III.26(b) and (e) 7×7 enlargements of the last shape shown in III.26(c).

III.3. CONCLUSIONS

An extensive parametric study was carried out numerically regarding the collapse mode of small bubbles, initial radius on the order of $6 \mu\text{m}$ corresponding to $P_{st} \approx 4$ and $Oh^{-1} \approx 20$, and large bubbles, initial radius on the order of $400 \mu\text{m}$ corresponding to $P_{st} \approx 300$ and $Oh^{-1} \approx 180$, in water under atmospheric pressure, subject to large internal overpressures with characteristic amplitude ε_B , and a wide range of initial elongations S . For small bubbles it is seen that for small elongations, $S \sim 1$, and large overpressures, $\varepsilon_B \sim 1$, a threshold value exists in Oh^{-1} above which the bubble collapses via jet formation or sink flow as a result of P_2 growth due to an afterbounce instability, whereas below this threshold it eventually settles to its equilibrium state. Increasing ε_B destabilizes the bubble by decreasing the threshold in Oh^{-1} for P_2 growth. For moderate initial elongations, e.g. $0.5 \leq S \leq 0.75$ when $\varepsilon_B = 2$, and the entire range of initial overpressures that was investigated, $2 \leq \varepsilon_B \leq 10$, the collapse mode via jet propagation and impact along the axis of symmetry prevails irrespective of Oh , with the upper limit of the S interval increasing as ε_B increases. This is a combined effect of the initial P_2 level and unstable growth. As S is further reduced, $S < 0.5$, an off centered collapse mechanism arises that involves interaction between the penetrating jets and the contracting bubble side-walls. Simulations of collapsing femtosecond laser bubbles¹² whose size is on the order of several μm 's, operating in the very large initial elongation and initial overpressure parameter range, provide a fairly accurate description of the asymmetric collapse process and in the time scale of the experimental observations, involving jet propagation and impact along the axis of symmetry. It should be noted that the available experimental observations could not resolve jet formation and impact due to the angle of observation. Another important aspect of the experimental recordings of femtosecond bubbles, is that they do not fission after they attain minimum volume. Instead they retract and perform oscillations until they settle down to their equilibrium state.

When the parametric study focuses on large bubbles, $P_{st} \sim 300$ and $Oh^{-1} \sim 200$ the effect of Oh , i.e. viscous dissipation, is minimal. For large internal overpressures, $\varepsilon_B \geq 1$, and very small elongations, $S \sim 1$, the bubble breaks up as a result of Rayleigh-Taylor instability. Shape mode decomposition obtained numerically, and corroborated by stability analysis, captures growth of high axisymmetric modes that leads to satellite bubble formation and break-up in regions of very small radius of curvature. In the

presence of small but finite initial elongation, $S < 1$, impact is observed due to growth of P_2 in the form of an afterbounce instability, as also verified by stability analysis. Jet propagation occurs along the axis of symmetry or sink flow takes place along the equator, depending on the phase in P_2 growth. In fact, for very large initial overpressures and very small elongations, $\varepsilon_B \sim 10$ and $S \geq 0.95$, propagation along the equator prevails. The latter may take longer to be initiated, due to the small initial P_2 content, but leads to a more explosive impact as a result of the increased sphericity of the bubble. For not very small elongations, $S < 0.9$, jet propagation occurs along the axis of symmetry irrespective of ε_B . In fact, this type of behavior persists for quite large elongations, i.e. S values as small as 0.5, below which the off-centered mode prevails. Collapse via sink flow is recovered in the simulations of nanosecond laser bubbles, size on the order of half a millimeter. This seems to agree with the available experimental recordings that indicate a similar mode of impact and on the same time scale as the simulations. The above collapse patterns as obtained via the parametric study, including the simulations of relevant experimental observations, are schematically shown in Tables III.1(a),(b).

Bubbles with initial radius $R_0 \sim 5 \mu\text{m}$ in water at 1 atm; $P_{Sr} \sim 4$, $Oh \sim 20$	
Initial elongation S	Type of collapse
Small elongations, $S \sim 1$, e.g. $0.75 < S \leq 1$ when $\varepsilon_B = 2$	$Oh^{-1} > Oh_{Cr}^{-1}$ collapse via jet impact along the axis of symmetry or the equator due to P_2 growth during the bubble afterbounce, $Oh^{-1} < Oh_{Cr}^{-1}$ damping of oscillations as S decreases or ε_B increases Oh_{Cr}^{-1} decreases
Moderate elongations, e.g. $0.5 < S \leq 0.75$ when $\varepsilon_B = 2$	Collapse via jet impact along the axis of symmetry irrespective of Oh , as ε_B increases the upper limit of the S interval increases
Large elongations, $S < 0.5$	$Oh^{-1} < Oh_{Cr}^{-1}$, collapse via jet impact along the axis of symmetry, $Oh^{-1} > Oh_{Cr}^{-1}$ off centered collapse mode, as S decreases Oh_{Cr}^{-1} decreases (in the case of experiments with femtosecond laser bubbles when $S = 0.35$ $Oh_{Cr}^{-1} \sim 3$), ε_B does not affect Oh_{Cr}^{-1} ($2 \leq \varepsilon_B \leq 10$)

Table III.1(a): Collapse pattern for micrometer size bubbles depending on the parameter range

Bubbles with initial radius $R_0 \sim 400 \mu\text{m}$ in water at 1 atm; $P_{Sr} \sim 300$, $Oh \sim 180$	
Initial elongation S	Type of collapse
Almost spherical bubble, $S \sim 1$, $1 \leq \epsilon_B$	Bubble fissions via Rayleigh-Taylor instability
Very small initial elongation, $0.95 \leq S < 1$ for large $\epsilon_B \geq 10$	Collapse via jet formation along the equator (case of experiments with nanosecond laser bubbles) as ϵ_B increases the intensity of jet impact increases
Large initial elongation $0.5 \leq S \leq 0.95$, $\epsilon_B \geq 2$	Collapse via jet formation along the axis of symmetry
Very large initial elongation, $S \leq 0.45$	Collapse via the off centered mode

Table III.1(b): Collapse pattern for millimeter size bubbles depending on the parameter range

In the literature, bubble pinching in the presence of elongation and overpressure has been obtained in a different context⁷⁶, when spark ignited bubbles are allowed to deform between two vertical plates. Simulations and experiments with bubble sizes on the order of $450 \mu\text{m}$ subject to internal overpressure, the latter was not as large as the one used in the present study, indicate bubble collapse on the axis of symmetry and bubble fission. Simulations also indicate a large pressure signal in the host fluid, at the time that the bubble splits and in the vicinity of the pinching area, which was conjectured to be a numerical artifact. The two bubble fragments are followed after pinching occurs, until reentrant jet formation and impact takes place in the tips corresponding to the north and south poles of the original bubble. An important aspect of the comparison between simulations and experiments in the present study is the fact that, as indicated by the experiments, the bubble does not fission after it attains its minimum volume. As it turns out, both femtosecond and nanosecond laser bubbles survive the impact intact and eventually retract to their equilibrium size. This is quite interesting and indicates that during impact enough amount of kinetic energy is dissipated into the host fluid so that the bubble overcomes the shock of impact intact. It should also be stressed that, as can be surmised by the stability analysis results shown in figure III.23, the Rayleigh-Plesset theory does not predict that the bubble will reach equilibrium so fast. In fact, stability analysis predicts shape instability, which is generally believed to destroy the integrity of the bubble. This, however, is not observed in the experiments shown in figures III.18(a) and III.21(a). Clearly, there is a stabilizing mechanism involved in the collapse process. Diffusion does not have enough time to act in this fashion, as is the case with acoustically trapped bubbles, because here the collapse process occurs within a single volume pulsation, or a few pulsations when acetone-water mixtures are used. It seems that, in the parameter range that is relevant to laser induced bubbles, jet formation and impact is both an energy focusing mechanism. see also figure III.25(b), but also a stabilizing mechanism regarding bubble integrity and this might also bear some significance in the phenomenon of luminescence when laser induced bubbles collapse. It should also be noted that the pressure in the host fluid exhibits a strong peak in the vicinity of the region where impact takes place. Figure III.27(a) shows a blow up of the bubble shape in the region where the sink flow converges, i.e. around the equator. It is near this region that the liquid pressure peaks. figure III.27(b), and is expected to emit a strong pressure signal. The latter follows the

details of the bubble shape. There is uncertainty regarding the accuracy of the actual numbers, since compressibility is expected to decelerate liquid motion, but the strong pressure signal is definitely there. The same was true for small overpressures, as was shown in figure II.11(e), but to a lesser extent. Consequently, the intense pressure signal reported at the moment of bubble fission in [76] is verified. However, there is an issue regarding the post pinching bubble behavior since experiments with laser bubbles do not indicate splitting. This is an issue that warrants further examination, possibly along with more careful accounting of liquid evaporation and compressibility effects during collapse.

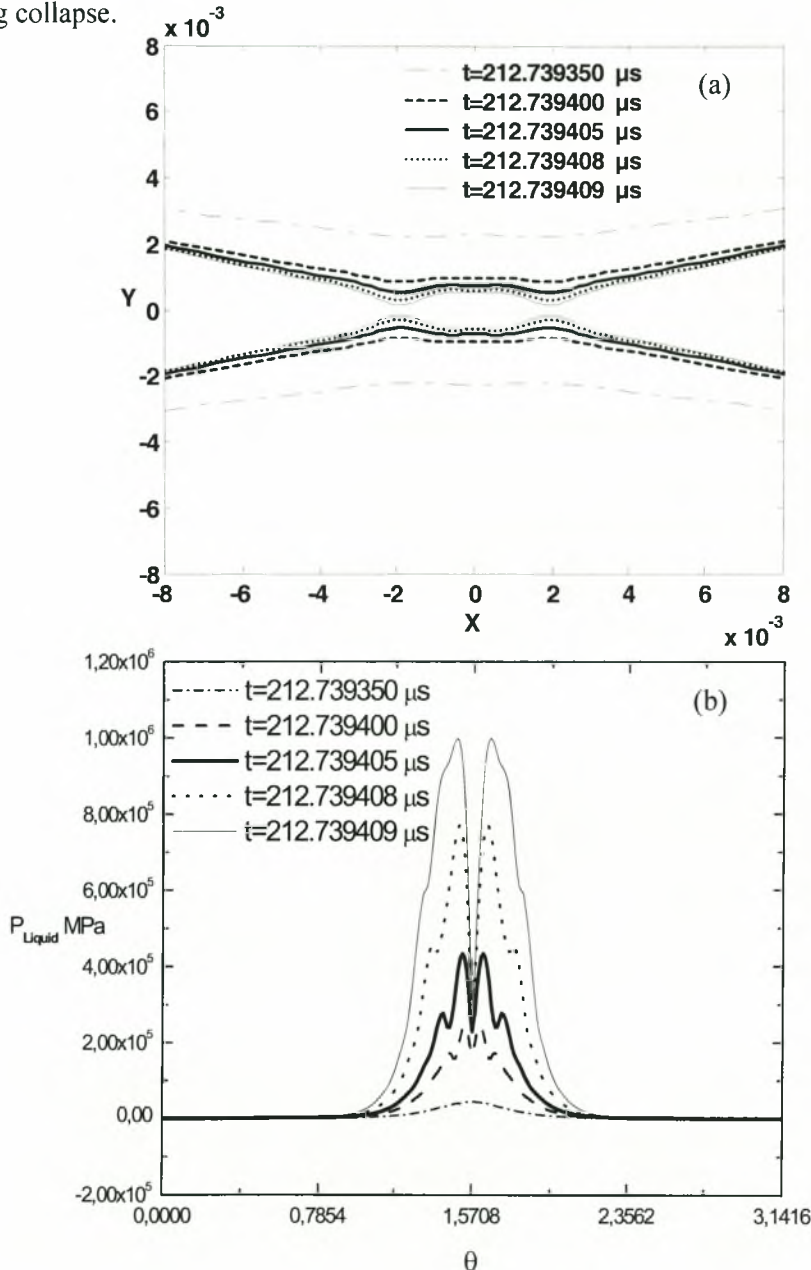


Figure III.27: (a) Blow up on the bubble shape near the equator during collapse and (b) evolution of the pressure distribution on the liquid side along the bubble interface during collapse; $S=0.98$, $P_{St}=295$, $\epsilon_B=81$, $Oh^{-1}=174$.

CHAPTER IV

Numerical Simulations of the Collapse of Acoustically Driven Bubbles

Similar to the case of single-cavitation bubble luminescence (SCBL), simulations show that loss of sphericity accompanied with jet formation and impact during collapse is also possible with acoustically trapped bubbles in a standing pressure wave (SBSL), due to the many afterbounces of the bubble during its collapse phase. Jet impact occurs as a result of P_2 growth in the form of an afterbounce instability. When the sound amplitude is decreased or liquid viscosity is increased the intensity of the afterbounce is decreased and jet impact is suppressed. When the sound amplitude is increased jet formation is superceded by Rayleigh-Taylor instability. In the same context stable luminescence is quenched in experimental observations. In the simulations the severity of jet impact during collapse is quite large, and its local nature quite distinct. This attests to the fact that it is an energy focusing mechanism whose importance in generating the conditions under which a luminescence event is observed should be further investigated.

IV.1 Simulation of single-bubble sonoluminescence (SBSL)

Acoustically levitated bubbles with equilibrium radius on the order of a few micrometers are trapped in the pressure antinode of a standing pressure wave due to the primary Bjerknes forces. Thus, they implement radial oscillations at a more or less fixed position. Extensive experimental investigations have shown that the concentration of the dissolved gas and the temperature of the host liquid significantly affect the intensity of the emitted light, revealing the complexity of the phenomenon²². Furthermore, it has been established experimentally²³ that SBSL occurs under a narrow parameter range, in terms of sound amplitude and equilibrium radius, for given driving frequency and dissolved gas concentration. It is known⁹⁰ that for given dissolved gas concentration, relative to its saturation concentration, there is a threshold sound amplitude above which a bubble will grow due to rectified diffusion, whereas it will eventually dissolve below it. It was shown²³ that there exists a small boundary line in the amplitude equilibrium radius plane (P_{Ac} , R_{Eq}) that separates regions of bubble growth and bubble dissolution as the bubble equilibrium radius R_{Eq} increases. This ensures the possibility for stable bubble pulsations, while shape instabilities and break-up prevail as P_{Ac} or R_{Eq} are further increased. This boundary line exists for parameter values over which sonoluminescence takes place²³. Once rectified diffusion determines the bubble equilibrium size, then sound amplitude will determine the mechanics of collapse and subsequent light emission. Interestingly enough, stability analysis^{24,63} reveals that in a similar parameter range shape instabilities set in and, in particular, transition from stable oscillations to parametric and Rayleigh-Taylor instability occurs. We are interested in simulating bubble collapse within the above parameter range in order to capture potential loss of spherosymmetry as well as the specific pattern of bubble deformation and break-up, in an effort to make some useful associations regarding the mechanism behind luminescence. In the literature of sonoluminescence^{22,24,91} it is known that light emission is very sensitive to the amplitude of sound, dissolved gas concentration and heat capacity ratio, γ , but also to host liquid viscosity. We would like to investigate this

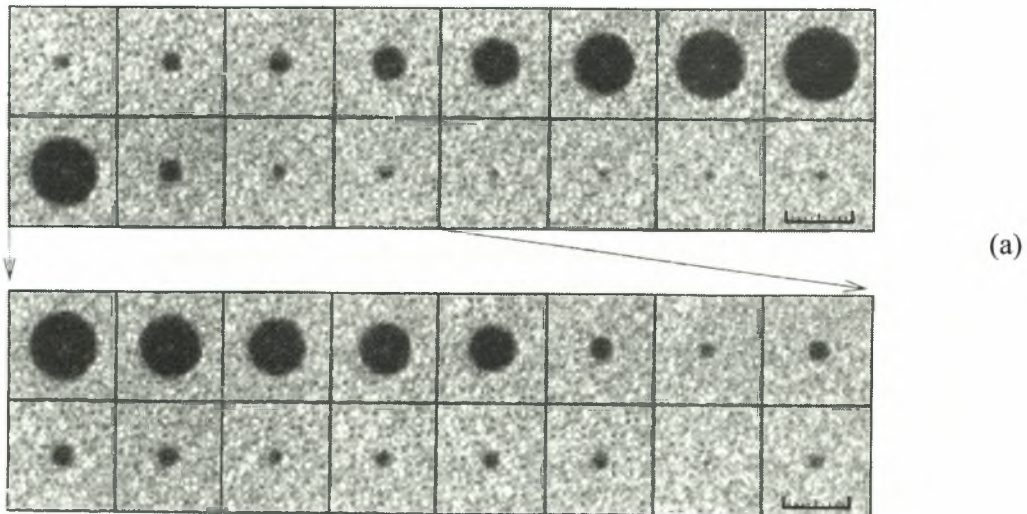
sensitivity and, possibly, associate it with the collapse pattern. To this end, we employ the same numerical approach that was used for SCBL with the difference that in the case of SBSL a sinusoidal pressure wave is imposed on the far field pressure characterized by dimensionless amplitude ε and frequency ν_f ,

$$P_{\infty} = P_{st} (1 + \varepsilon \cos 2\pi\nu_f t) = P_{st} + P_{Ac} \cos 2\pi\nu_f t. \quad (IV.1)$$

In this case the dimensionless frequency constitutes an additional parameter, that is also

$$\text{made dimensionless via surface tension, } \nu_f = \nu'_f \cdot \left(\frac{\rho R_{Eq}^3}{\sigma} \right)^{1/2}. \quad (IV.2)$$

Experimental observations on SBSL in a water-glycerin mixture with high speed photography are available in the literature¹³. The photographic sequence of the experimentally obtained frames is reproduced in figure IV.1(a) and reveals that a trapped bubble of equilibrium radius $R=8 \mu\text{m}$ driven at 21.4 kHz carries out almost radial oscillations and collapses in a more or less spherosymmetric fashion. This is true for all the stages of oscillation except for the very last ones due to the extremely small size of the bubble. The experimental data for the time series of the bubble radius can be fitted to the Rayleigh-Plesset equation, figure IV.1(b). The parameters obtained from the fitting, liquid viscosity in particular, can be also used in the present model in order to simulate bubble oscillation and collapse as close as possible. It must be stressed that due to the high viscosity of glycerin the resultant Reynolds number is $Re=Oh^{-1} \approx 3.9$. The present axisymmetric model only takes into account weak viscous effects within the boundary layer of the bubble and this approach is accurate as long as Re number remains large. In addition, the model does not account for the vapor pressure inside the bubble, which, however, is not expected to result in large discrepancies, and compressibility which is expected to increase the range of sound amplitudes before Rayleigh-Taylor instability destroys the bubble⁹². In order to overcome the above limitations we conducted a parametric study of the effect of different parameters on bubble collapse.



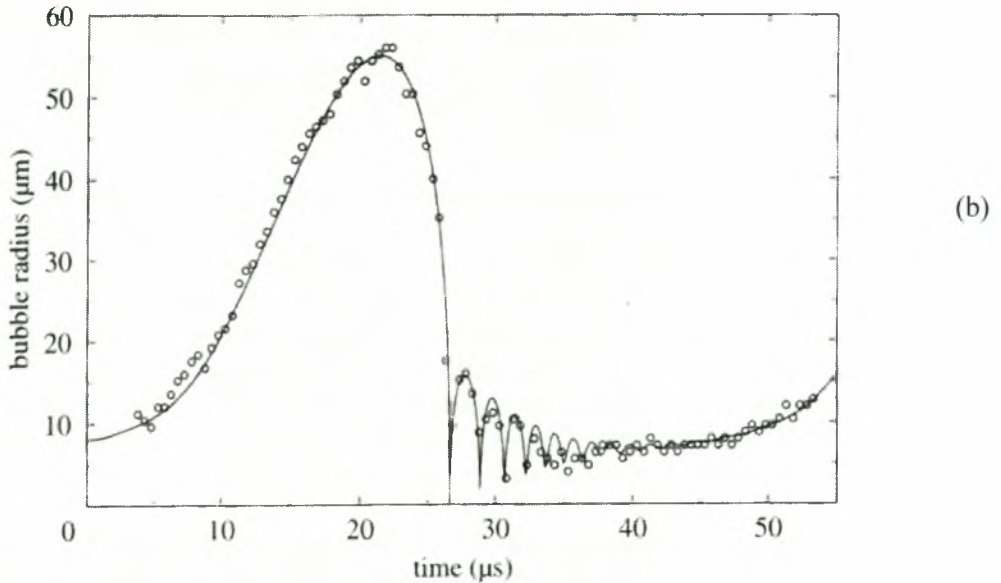


Figure IV.1: (a) Photographic series of a trapped sonoluminescing bubble in a water-glycerin mixture driven at 21.4 kHz. The top row presents the bubble dynamics at an interframe time of ca. 2.5 μs . The bottom row shows the bubble collapse with five-fold temporal resolution (500 ns interframe time). The scale of image is indicated by the ruler (100 μm). (b) Radius-time curve from photographic observations. A numerically calculated curve is superimposed on the experimental data point (open circles). The calculation is based on the following parameters: driving frequency, $f_0=21.4$ kHz; ambient pressure, $p_0=1$ bar; driving pressure, $P_{Ac}=1.32$ bar; vapor pressure, $p_v=25$ mbar; equilibrium radius, $R_{Eq}=8$ μm ; density of the liquid, $\rho=1000$ kg m^{-3} ; viscosity, $\eta=0.006$ N s m^{-2} ; surface tension, $\sigma=0.07$ N m^{-1} . The gas within the bubble is assumed to obey the adiabatic equation of state of an ideal gas with ratio of the specific heats of 1.33. All figures are reproduced from [13].

As a first test we simulated the case shown in figure IV.1 using the above mentioned parameter values, but assuming a small initial elongation characterized by $S=0.96$. As it turns out, at the time instant at which the bubble acquires its minimum volume in the photographic sequence the simulations indicate collapse, figure IV.2(a), along with the onset of jet formation. The signature of the latter effect is identified in figures IV.2(b) and IV.2(c) depicting the time evolution of the Legendre decomposition of the bubble shape throughout the simulation, figure IV.2(b), and during collapse, figure IV.2(c). The last figure shows rapid growth of almost all the harmonic components, P_2 , P_4 , P_6 and P_8 . Linear stability analysis in the manner shown by Hilgenfeldt et al.⁶³ predicts very fast growth rate P_2 pertaining to a Rayleigh-Taylor instability. Towards the final collapse phase nonlinear energy transfer to even higher modes hinders further jet propagation and destroys the integrity of the bubble in regions of the interface where pinching occurs.

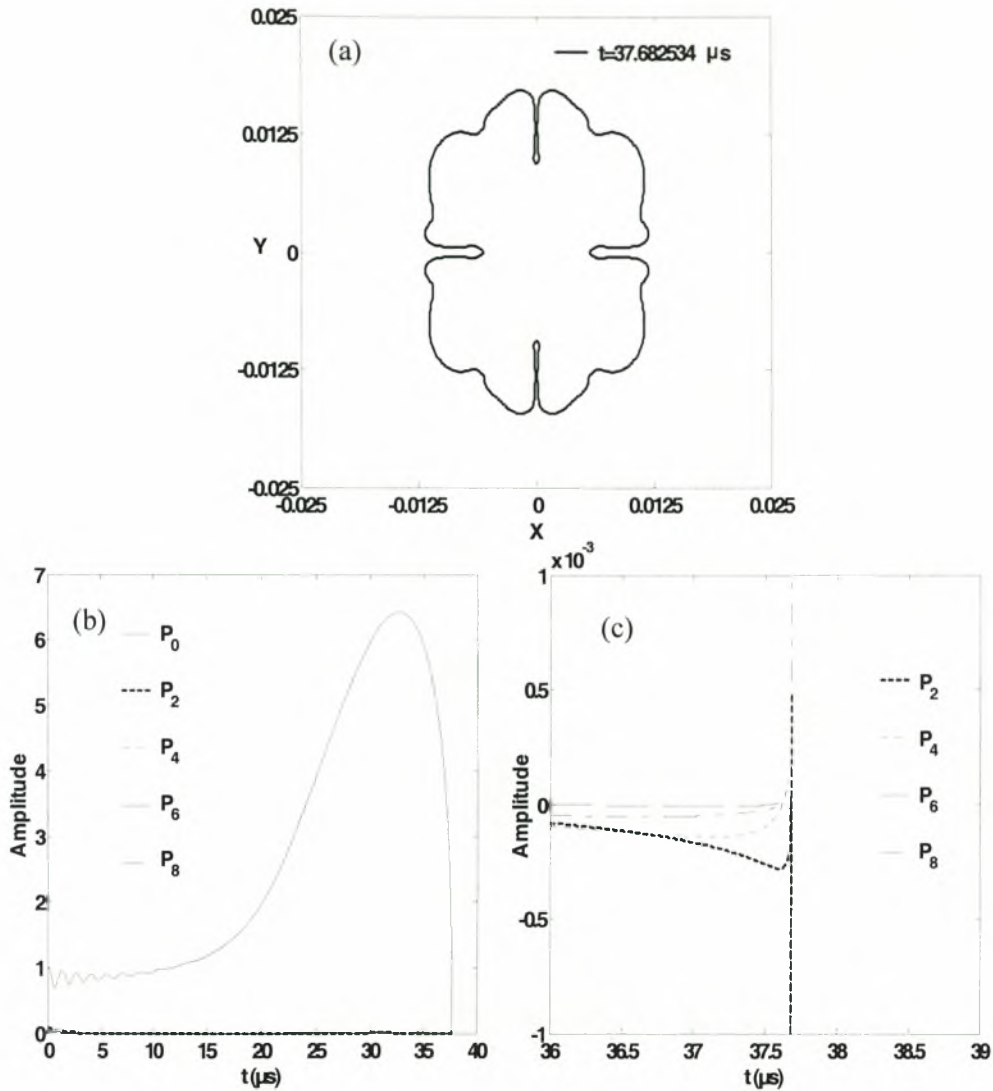


Figure IV.2: (a) Interfacial shape at collapse of a single-bubble in a water-glycerin mixture. (b) Time variation of the first five even Legendre modes of the bubble shape during the entire simulation and (c) during collapse; $S=0.96$, $P_{St}=5.714$, $\varepsilon=1.32$, $\omega_f=0.364$, $Re=3.9$.

Upon decreasing liquid viscosity to 0.001 N s/m^2 , i.e. taking water as the host fluid, during the collapse phase the bubble exhibits jet formation and quick propagation along the axis of symmetry before impact, Figure IV.3(a). As can be gleaned from Figures IV.3(b) and IV.3(c), jet formation and impact is associated with rapid growth of the second Legendre shape mode.

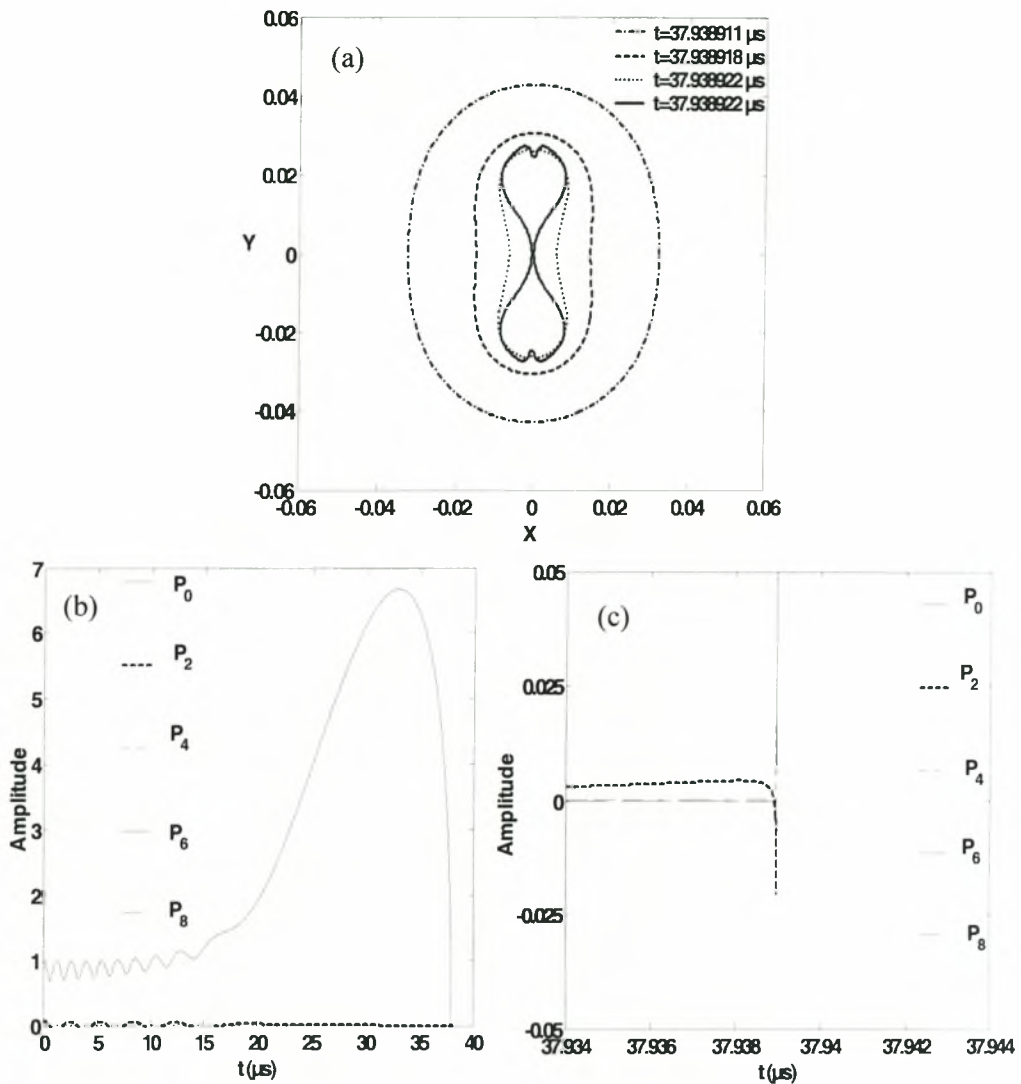


Figure IV.3: (a) Interfacial shape during the collapse phase of a single-bubble in a water-glycerin mixture. (b) Time variation of the first five even Legendre modes of the bubble shape during the entire simulation and (c) during collapse; $S=0.96$, $P_{St}=5.714$, $\varepsilon=1.32$, $\omega_f=0.364$, $Re=23.7$.

On comparing the situations depicted in figures IV.2 and IV.3, it turns out that viscosity does not significantly alter the minimum bubble volume or the Rayleigh-Taylor instability; see also references [24,63]. However, it damps the explosive growth rate of P_2 , which might bear significance on the quenching of light emission in viscous fluids. Consequently, at large amplitudes and relatively small viscosities jet impact may occur before higher modes have the time to grow and pinch the bubble. It should also be noted that jet coalescence is accompanied by very large jet velocities at impact. Figure IV.4(b), attesting to the energy focusing nature of the phenomenon. The interfacial velocity is also shown in figure IV.4(a), for the cases depicted in figures IV.2 and IV.3, corresponding to the radial velocity during the spherosymmetric part of the bubble collapse, which is also quite large and may produce a shock wave. The case with a

higher Re leads to a lower velocity simply because jet impact occurs before Rayleigh-Taylor instability destroys the bubble. Then, the simulations have to stop. However, this is not the case with the bubble motion that may continue and lead to even higher velocities.

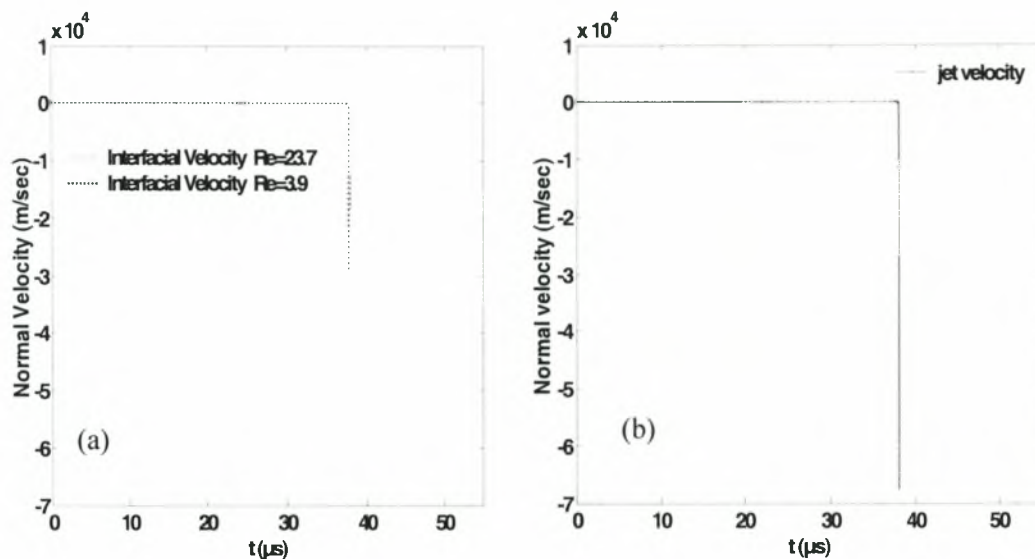


Figure IV.4: (a) Interfacial velocity when $Re=23.7$ and $Re=3.9$ and (b) jet velocity during collapse when $Re=23.7$; $S=0.96$, $P_{Sf}=5.714$, $\epsilon=1.32$, $\omega_f=0.364$.

Jet formation and impact can be viewed as a manifestation of the afterbounce instability, and this is verified independently by linear stability analysis. Repeating the above simulations for a smaller amplitude, $\epsilon=1.1$, and water as the host fluid, jet propagation – sink flow along the equator is obtained, figure IV.5(a). The volume pulsation of the bubble clearly exhibits a sequence of afterbounces, figure IV.5(b), signifying growth of P_2 , figure IV.5(c), and jet formation. The simulations stop due to jet impact while the P_2 content of the normal mode decomposition of the shape is positive, indicating a prolate shape. When the viscosity is increased to that of the water-glycerin mixture the volume afterbounces become weaker while P_2 growth is almost nonexistent. Similarly, further reduction of the disturbance amplitude below a certain threshold value, ϵ_{Cr} , for fixed liquid viscosity, eliminates jet impact; when $Re \approx 23.7$ $\epsilon_{Cr} \approx 0.9$. Repeating the simulations with a smaller initial elongation, e.g. $S=0.99$, does not change the collapse pattern at all except for the actual time of impact, figure IV.6, since anyway the initial P_2 content is damped before the onset of collapse. Even if a small amount of P_3 is introduced initially, still P_2 growth dominates the dynamics of collapse for most cases where an afterbounce instability is present. Jet formation and impact is associated with the major afterbounces following the collapse phase of the bubble. In fact, monitoring the amplitude ratio between the P_2 and P_0 pulsations it turns out that jet impact occurs when the magnitude of this ratio becomes on the order of 1. Performing linear stability analysis in the above parameter range verifies the pattern of P_2 growth or damping mentioned above.

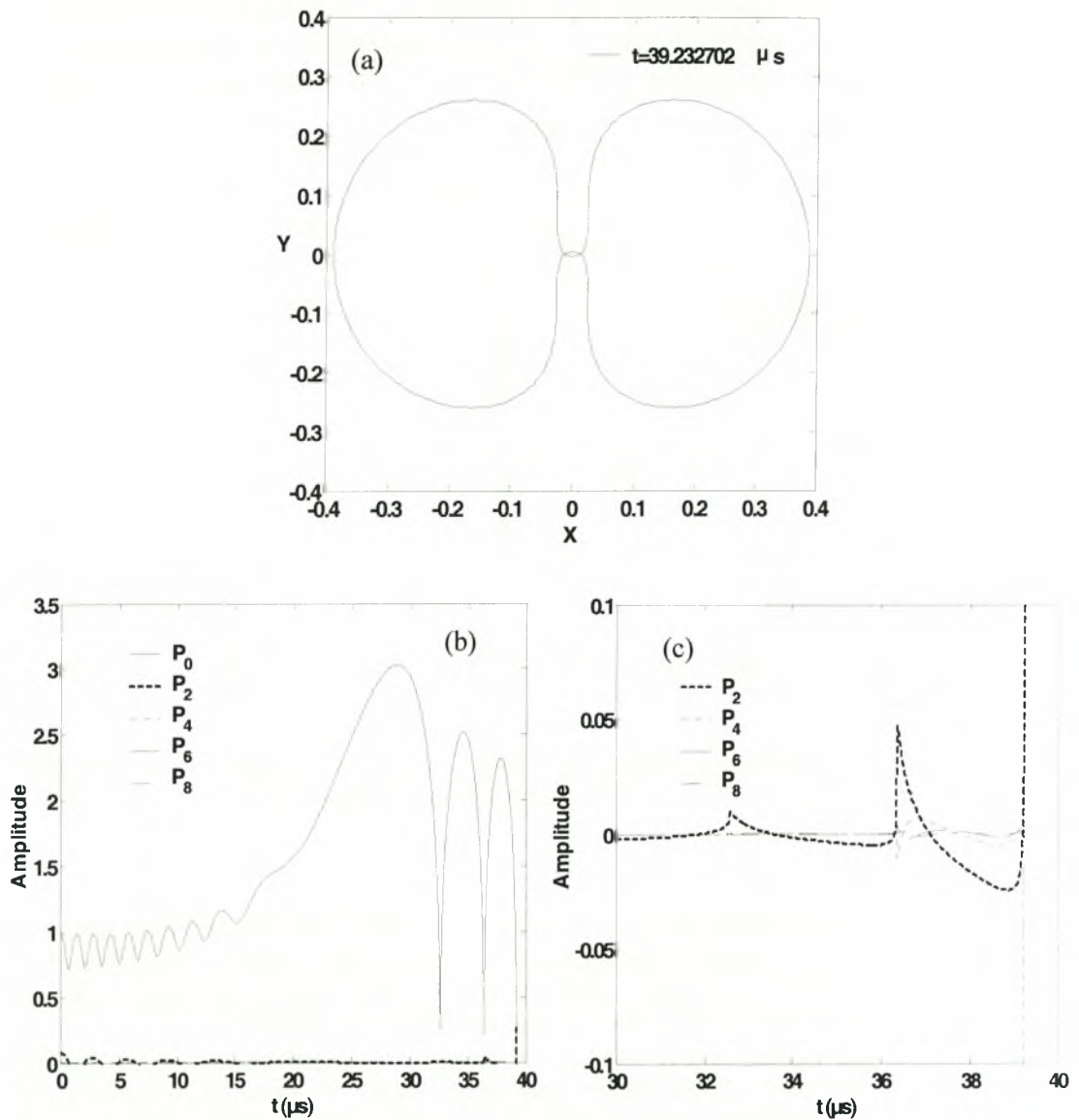


Figure IV.5: (a) Interfacial shape at collapse of a single-bubble in water. (b) Time variation of the first five even Legendre modes of the bubble shape during the entire simulation and (c) during collapse; $S=0.96$, $P_{St}=5.714$, $\varepsilon=1.1$, $\omega_f=0.364$, $Re=23.7$.

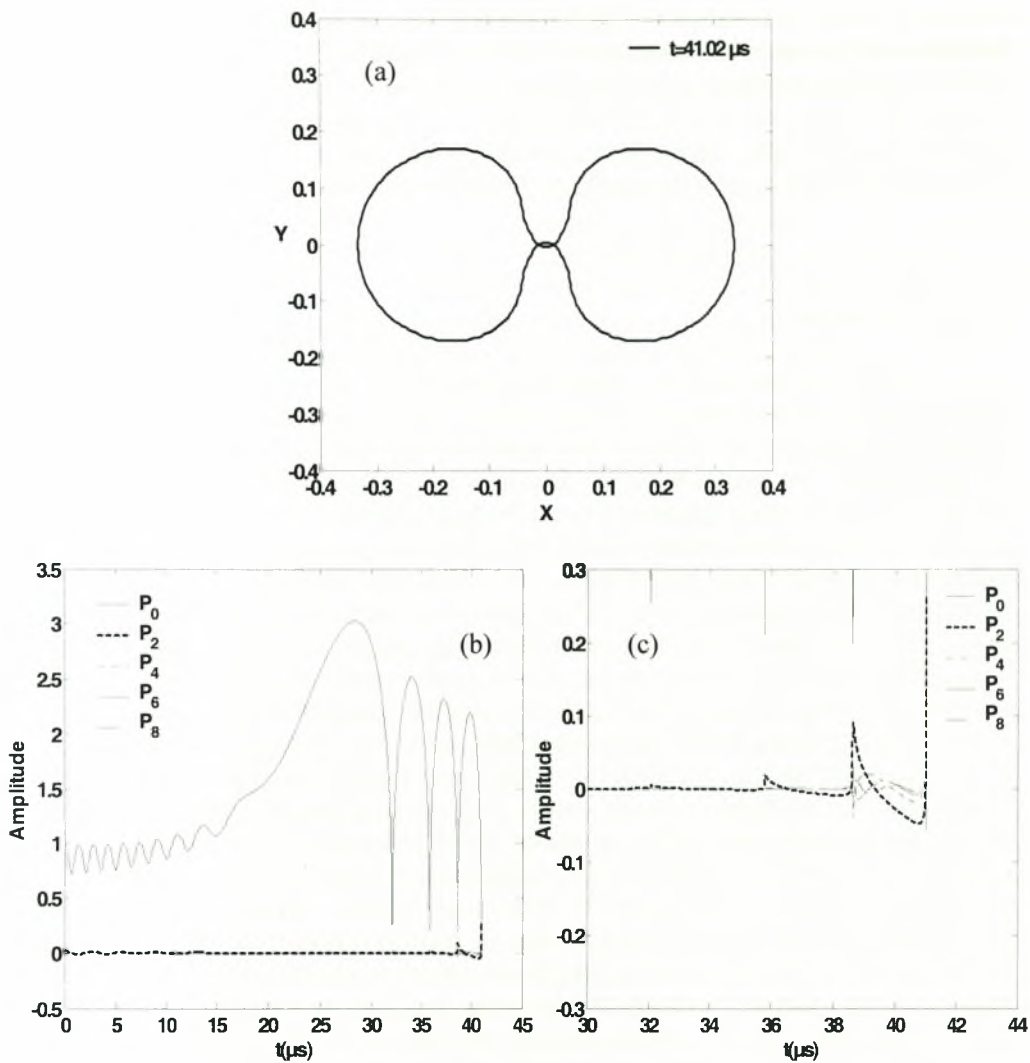


Figure IV.6: (a) Interfacial shape at collapse of a single-bubble in water. (b) Time variation of the first five even Legendre modes of the bubble shape during the entire simulation and (c) during collapse; $S=0.99$, $P_{St}=5.714$, $\varepsilon=1.1$, $\omega_f=0.364$, $Re=23.7$.

It should be stressed that both here as well as with laser-induced bubbles, jet impact does not necessarily destroy the integrity of the bubble. In fact, nanosecond laser bubbles, as illustrated from the experimental observations shown in figure III.21(a), after acquiring their minimum volume they retract and eventually settle to their equilibrium radius. As shown from figure III.21(c), simulations indicate jet impact-sink flow for this particular set of frames. If indeed this is the case, comparison between simulations and experiments with laser bubbles points in this direction, then jet impact may not destroy acoustically trapped bubbles either, but simply act as a dissipation mechanism of the excessive energy contained in the bubble during collapse. Unfortunately, our simulations have to stop once jet impact takes place. This is an

interesting point that warrants further investigation, as it may be the case that jet formation and stable sonoluminescence coexist. Consequently, an acoustically trapped bubble may keep oscillating after impact and periodically exhibit the collapse-jet impact process. The energy associated with the process of jet impact is probably radiated away from the point of impact via secondary shock wave formation, while at the same time it is dissipated in order to heat the nearby gas and liquid masses.

IV.2 Conclusions

In this section we have simulated experiments on SBSL after relaxing the assumption of spherosymmetry. The boundary integral method was used, which is capable of predicting the detailed axisymmetric deformation of the bubble interface during collapse. The initial asphericity is very small and may only be due to very small variations in the primary Bjerknes force. Owing to the very small size of the bubbles, equilibrium radius on the order of $5\mu\text{m}$, loss of sphericity cannot be easily captured by high-speed photography. Nevertheless, in SBSL the volume pulsation is quite asymmetric, in comparison with SCBL, and consequently any initial elongation is mostly dissipated before the afterbounce instability sets in, compare figures III.23 and IV.5, during the many afterbounces of the bubble volume after the major initial collapse. As a result initial elongation does not play a significant role in the simulations of acoustically trapped bubbles conducted here, aside from determining the exact time of impact. According to the simulations there is a narrow parameter window within which final collapse happens via jet impact that occurs, either through its two poles or through the opposite sides of the equatorial plane like a sink flow, with a very large velocity. It is a result of the afterbounce instability that leads to oblate or prolate shapes depending on the phase of P_2 growth that causes impact. As the amplitude further increases the collapse becomes more violent, jet formation is suppressed, and Rayleigh-Taylor instability prevails. As the amplitude decreases or the viscosity increases jet velocity during collapse decreases until jet impact is fully suppressed. It was also shown by the simulations that both the jet velocity, associated with the severity of jet impact, and bubble interfacial velocity, associated with the shock wave strength, are quite severe and may be correlated with light production. However, jet formation and impact was better captured by the simulations presented here, and it was seen in the context of experiments with laser induced bubbles that it does not necessarily lead to bubble fragmentation. It should then be investigated whether it can coexist with the process of continuous bubble pulsation in the context of SBSL, in which case it constitutes a mechanism that may extend the range of light emission predicted by adiabatic collapse.

CHAPTER V

Non-linear Radial Oscillations of Encapsulated Microbubbles subject to Ultrasound: The effect of membrane constitutive law

The nonlinear radial oscillations of bubbles that are encapsulated in an elastic shell, also known as contrast agents in diagnostic echocardiography, are investigated numerically subject to three different constitutive laws describing the viscoelastic properties of the shell: the Mooney-Rivlin (MR), the Skalak (SK) and the Kelvin-Voigt (KV) models are used in order to describe strain-softening, strain-hardening and small displacement (Hookean) behavior of the shell material, respectively. The equations governing liquid motion coupled with the radial micro-bubble pulsations in response to an ultrasonic beam are obtained based on the Keller – Miksis model, which also takes into consideration the compressibility of the external liquid far from the micro-bubble. The resonance frequency and scattering cross section of the fundamental and higher harmonics depend strongly upon the nonlinear material behavior as well as the shell and liquid parameters. In particular, for even moderately nonlinear acoustic disturbances membrane elasticity has a measurable effect on the resonance frequency leading to higher values as it increases. When the membrane is strain-softening (MR) the resonance frequency decreases with increasing sound amplitude whereas the opposite happens when the membrane is strain-hardening (SK). This is an effect of the decrease/increase in the actual membrane elasticity with increasing external strain for the MR and SK membranes, respectively, and the concomitant rise/drop in the displacements. It amounts to increasing/decreasing the effective system inertia and this is reflected in the resonance frequency. These are quite measurable variations that, for an isotropic load such as is the case for spherically symmetric pulsations, are determined by the area dilatation modulus. In addition, as the amplitude of the acoustic disturbance increases the total scattering cross section of a microbubble with an SK membrane tends to decrease whereas, that of a KV or an MR membrane tends to increase. SK membranes are only mildly affected by the sound amplitude, as far as their active scatter is concerned in comparison with the external disturbance, and this reduces their scattering cross section. The importance of this effect in the interpretation of certain features of experimental observations of oscillating micro-bubbles subject to large peak negative pressures is discussed.

V.1 PROBLEM FORMULATION

We consider an encapsulated micro-bubble with initial external and internal radius R'_0, a'_0 , respectively, submerged in a Newtonian liquid of density ρ_l , dynamic viscosity μ_l and static pressure P'_{st} taken to be at 1 bar, figure V.1 (a). The microbubble consists of ideal gas encapsulated in a viscoelastic membrane. The latter is taken to be volume incompressible with shear modulus G_s and dynamic viscosity μ_s . Initially the membrane is at static equilibrium where it may develop uniform residual stresses, assuming a spherosymmetric configuration, so the external and internal radii for which the membrane is free of stresses are:

$$R'_E = R'_0 - u' \Big|_{r'=R'_0}, \quad a'_E = a'_0 - u' \Big|_{r'=a'_0}, \quad (V.1)$$

where $u' \Big|_{r'=R'_0}$, $u' \Big|_{r'=a'_0}$ are the radial displacements that produce these residual stresses, figure V.1(b); throughout this study primed letters denote dimensional variables. The gas inside the micro-bubble exerts on the membrane a pressure $P'_{g,0}$ the variations of which are applied instantaneously and uniformly throughout the gas due to its negligible density. We also assume that the micro-bubble executes adiabatic oscillations. Consequently, each moment the pressure inside the bubble is correlated with the micro-bubble volume as:

$$P'_g V'^{\gamma} = P'_{g,0} V'^{\gamma}_0, \quad (V.2)$$

with V'_0 denoting the initial microbubble volume and $\gamma = 1.4$ the polytropic constant for an adiabatic process.

The bubble is insonated by a sinusoidal pressure disturbance in the far field

$$P'_\infty(t) = P'_{st} + P'_{Ac}(t') = P'_{st} \left[1 + \varepsilon \sin(\omega_f t') \right], \quad (V.3)$$

where $\omega_f = 2\pi\nu_f$, with $\nu_f = 1 - 10$ MHz the forcing frequency lying in the ultrasound range, $P'_{Ac}(t')$ is the far field pressure disturbance, and ε is the amplitude of the acoustic disturbance. The acoustic disturbance is also characterized by a wavelength, ℓ , and wavenumber, $k = 2\pi/\ell$, that is related to the speed of sound, c , in the host fluid in the usual manner, $c = \omega_f/k$. When the micro-bubble radius, R'_0 is much smaller than the sound wavelength, ℓ , or when the velocities that develop in the liquid, as a result of the micro-bubble pulsations, are much smaller than the speed of sound we can neglect compressibility effects, at least near the interface⁶⁰. More details on the treatment of liquid compressibility are given in the subsection where the modeling of the host fluid is presented. The n-harmonic component of the scattering cross section is given by^{34,35}

$$\sigma_{Sc,n} = 4\pi \frac{\int_0^{t'_f} (r'^2 P'^2_{Sc})_n dt'}{\int_0^{t'_f} P'^2_{Ac} dt'} \quad (V.4)$$

where,

$$P'_{Sc}(r', t') = P'_l(r', t') - P'_{st} - P'_{Ac}(t') \quad (V.5)$$

is the scattered pressure from the micro-bubble's interface, registered in the host fluid at a distance r' from the micro-bubble's center of mass and subscript n denotes the n-

harmonic component of the scattering cross section. In the present study σ_{sc} is evaluated at the interface, in which case $r' = R'$ is the instantaneous external micro-bubble radius.

The initial external radius of the micro-bubble, R'_0 , is assigned as the characteristic length of the problem. Since the timescale of micro-bubble oscillations is determined by the external forcing frequency, ω_f , the characteristic time of the problem is $\frac{1}{\omega_f}$ and subsequently the characteristic velocity, $\omega_f R'_0$. Finally, the characteristic pressure is defined via the characteristic velocity as $\rho_l \omega_f^2 R_0'^2$.

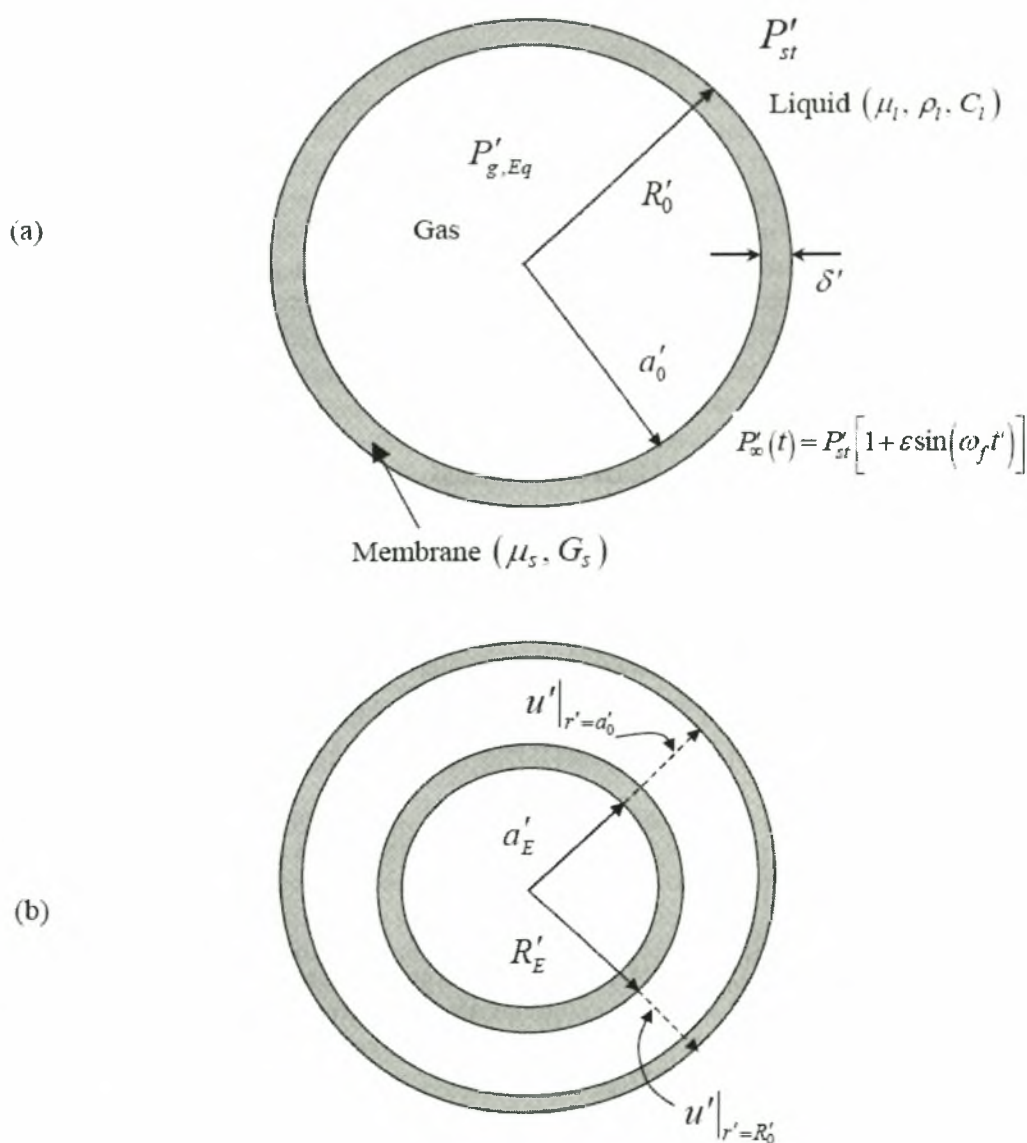


Figure V.1: Schematic diagram of a contrast agent (a) at equilibrium and (b) at the unstressed state and at equilibrium.

V.1.1 Governing equations of the external liquid

The pulsating motion of the micro-bubble may exhibit very large velocities, especially as the amplitude of the acoustic disturbance increases as is the case when high mechanical index, MI, ultrasonic bursts are employed. As a result of its low viscosity viscous effects may be neglected in the bulk of the host fluid, taken to be either water or blood, and a velocity potential, ϕ' , may be introduced which simplifies the analysis significantly. In addition, inclusion of liquid compressibility is required in the model in order to account for fluid motion in the far field. When the Mach number of the flow, based on the radial velocity of the micro-bubble's interface with the host liquid, $\dot{R}' \sim \omega_r R'_0$, is small but not negligible, $M = \frac{\omega_r R'_0}{c} \ll 1$, the far field flow is

compressible and described by the wave equation whereas near the bubble-host fluid interface the flow field can be described by the Laplace equation, to leading order⁹³,

$$M^2 \frac{\partial^2 \phi}{\partial t^2} - \Delta \phi = 0. \quad (\text{V.6})$$

where $\phi = \phi' / (\omega_r R'_0)^2$ is the dimensionless velocity potential. Alternatively, as was mentioned above, for this assumption to be valid the wavelength of the acoustic disturbance has to be much bigger than the micro-bubble radius.

This structure essentially leads to the Keller-Miksis model describing very fast radial oscillations of a bubble, where the pressure inside the liquid in dimensionless form is given by an extended version of the Bernoulli equation that holds when compressibility effects are accounted for to first order. Near the interface the velocity potential assumes the classical form for spherical symmetry,

$$\phi(r, t) = -\frac{\dot{R}R^2}{r} \quad (\text{V.7})$$

In this fashion, and utilizing the known wave form for the pressure disturbance that is applied in the far field in conjunction with (V.6), the non-linear ordinary differential equation describing spherosymmetric oscillations of a micro-bubble in a compressible liquid reads

$$(1 - MR\dot{R})R\ddot{R} + \left(\frac{3}{2} - \frac{MR}{2}\right)\dot{R}^2 = (1 + MR\dot{R})(P_l|_{r=R} - P_{st} - P_{Ac}) + MR\frac{d}{dt}(P_l|_{r=R} - P_{Ac}) \quad (\text{V.8})$$

where R is the dimensionless external micro-bubble radius at time t , $\dot{R} = \frac{dR(t)}{dt}$, $\ddot{R} = \frac{d^2R(t)}{dt^2}$ and $P_l|_{r=R}$ is the dimensionless pressure of the host liquid calculated at the micro-bubble's interface.

Equation (V.8) provides the instantaneous location of the bubble's interface once the liquid pressure is known. Thus, of great importance in modeling the behavior of contrast agents is the evaluation of the stresses that are applied on the membrane from the liquid side of the interface as well as those that are developed on it due to its viscoelastic properties. According to the model adopted here the surrounding liquid is taken to be Newtonian while viscous stresses are only considered near the interface. Consequently, in the context of spherosymmetric oscillations, the radial component,

$$X_{lr}|_{r=R} = -P_l|_{r=R} + \frac{1}{\text{Re}} \left(2 \frac{\partial^2 \phi}{\partial r^2} \Big|_{r=R} - \frac{2}{3} \Delta \phi \right) \quad (\text{V.9})$$

is the only surviving contribution from the liquid stresses on the membrane force balance. The second term inside the parenthesis arises as a result of compressibility. It is not very important when $M \ll 1$ ⁹³, nevertheless it is kept here as it was included in the original Keller-Miksis model. The Keller-Miksis as well as the Herring⁹⁴ and Gilmore⁹⁵ models all belong to the same family of approximations that are first order accurate in the Mach number and are used quite often in order to describe fast bubble oscillations.

V.1.2 Modeling of the Mechanical Behavior of the Membrane - Constitutive Laws

The liquid pressure exerted on the membrane can be calculated via a stress balance that is applied on the membrane itself. In this fashion the micro-bubble model can be completed by correlating the pressure of the external liquid, $P_l|_{r=R}$, calculated on the interface of the bubble, with the instantaneous pressure inside the bubble, P_g , and the normal stresses that develop on the membrane due to its radial deformation and velocity. Subsequent substitution in (V.8) provides a nonlinear ordinary differential equation that can be solved for the radial position and velocity of the interface.

When the membrane thickness is taken to be finite in which case it constitutes a shell that surrounds the bubble, two interfacial force balances can be set up corresponding to the gas-membrane and liquid-membrane interfaces. These are force balances involving stresses that develop in the phase occupying either side of the two interfaces as well as interfacial tensions. The latter may be present because, despite the viscoelastic nature of the shell material, a small amount of contact between the gas inside the bubble and the host liquid is possible due to the very small shell thickness. They are not expected to play a major role in the microbubble dynamics nevertheless they are included for completeness. In this context, i.e. when the shell thickness is infinitesimally small, a single force balance can be written for the gas-liquid interface,

$$\left[P'_g \underline{\underline{I}} - P'_l \underline{\underline{I}} + \underline{\underline{X}}'_l \right] \cdot \underline{\underline{n}} = \sigma \left(\underline{\underline{\nabla}}'_s \cdot \underline{\underline{n}} \right) \cdot \underline{\underline{n}} - \underline{\underline{\nabla}}'_s \cdot \underline{\underline{X}}'_m; \quad (\text{V.10})$$

where $\underline{\underline{I}}$ denotes the unitary stress tensor, $\underline{\underline{n}}$ the normal vector at the interface pointing towards the host fluid, $\underline{\underline{\nabla}}'_s$ the surface gradient operator, σ the interfacial tension between the gas in the microbubble and the host liquid in the presence of the membrane, P'_g , $\underline{\underline{X}}'_l$ the liquid pressure and deviatoric stress tensor, respectively, and $\underline{\underline{X}}'_m$ the two-dimensional stress tensor containing the stresses that develop on the membrane surface as a result of its mechanical properties such as elasticity and viscosity⁹⁶. Owing to the negligible viscosity of the gas filling the volume inside the membrane, only pressure forces are accounted for on the gas side of the stress balance in (V.10). It should also be noted that, as opposed to surface tension that is isotropic, tensions due to elasticity are non-isotropic, vary along the interface and enter not only the normal but also the tangential components of the force balance. A detailed presentation of the stresses that develop on the membrane, depending on the constitutive law that describes the mechanical behavior of the material that forms the membrane, is provided in the following.

V.1.2.1 Kelvin-Voigt Model

One of the earlier used constitutive laws³⁴ governing the mechanical behavior of the membrane is the Kelvin-Voigt law (KV) that relates the viscoelastic stresses to the strain and rate of strain tensors, $\underline{\underline{\gamma}}'$, $\underline{\underline{\dot{\gamma}}}'$, in a linear fashion,

$$\underline{\underline{X}}_s' = 2\left(G_s \underline{\underline{\gamma}}' + \mu_s \underline{\underline{\dot{\gamma}}}'\right), \quad \underline{\underline{\gamma}}' = \frac{1}{2}\left[\underline{\underline{\nabla}}'\underline{\underline{u}}' + (\underline{\underline{\nabla}}'\underline{\underline{u}}')^T\right], \quad \underline{\underline{\dot{\gamma}}}' = \frac{1}{2}\left[\underline{\underline{\nabla}}'\underline{\underline{U}}' + (\underline{\underline{\nabla}}'\underline{\underline{U}}')^T\right], \quad (\text{V.11})$$

where $\underline{\underline{u}}'$ and $\underline{\underline{U}}'$ are ascribed as the dimensional displacement and velocity vectors inside the membrane, respectively and G_s , μ_s the shell shear modulus and viscosity expressed in Nt/m^2 and $\text{kg}/(\text{m s})$, respectively. We consider radial pulsations and neglect inertia effects in, and shape oscillations of, the shell, which is taken to be at equilibrium at all times. It should also be stressed that the above model is essentially Hooke's law, with the addition of a viscous term, and therefore is strictly valid for small membrane displacements. Nevertheless, different variations of it that are valid either for finite^{34,42} or infinitesimal^{35,36,44,47} shell thickness, are extensively used in the literature over a very wide range of pressure amplitudes and viscoelastic parameter values. Consequently, we also make use of it in the present study, for the purpose of comparing its validity range against other more relevant constitutive laws that account for changes in the material properties, such as the shear modulus, with increasing pressure amplitude or frequency of sound.

Following Khismatullin & Nadim⁴² we consider the r-component of the momentum and continuity equations for the shell, integrate in the radial direction across the shell and take the stress equilibrium between the membrane and the external liquid and the internal gas. Thus, we obtain the liquid pressure exerted on the membrane, $P_l|_{r=R}$. Owing to the small membrane thickness, in comparison with the microbubble radius, we proceed by taking the ratio between the shell thickness, δ' , and bubble external radius, R' , to be negligibly small throughout the bubble pulsation. In this fashion the dimensionless liquid pressure $P_l|_{r=R}$ reads in dimensionless form:

$$P_l|_{r=R} = \left[\frac{2}{We} + P_{st}\right] \left(\frac{R_0}{R}\right)^{3\gamma} - \frac{2}{WeR} - \frac{4}{Re_l R} - \frac{4}{Re_l} \frac{3\delta'\mu_s}{R_0\mu} \frac{\dot{R}}{R^2} - 4 \frac{3G_s\delta'}{\rho_l\omega_f^2 R_0^3} \left(\frac{R-1}{R^2}\right) \quad (\text{V.12})$$

where, $We = \frac{\rho_l\omega_f^2 R_0^3}{\sigma}$ denotes the Weber number comparing inertia forces in the liquid

due to the external forcing with surface tension, $Re_l = \frac{\rho_l\omega_f R_0^2}{\mu_l}$ and $m = \frac{3\mu_s\delta'}{\mu R_0}$ the Reynolds number of the external liquid, comparing forces of inertia with viscous dissipation, and the relative fluid to membrane viscosity, respectively, and $G = \frac{3\delta'G_s}{\rho_l\omega_f^2 R_0^3}$

the dimensionless shear stress modulus that compares elastic with inertia forces. The above equation holds when the membrane remains very thin while undergoes small displacements during the microbubble pulsation, and is essentially the Church-Hoff model for viscoelastic membranes^{44,47}. It assumes an incompressible shell with a simplified expression for the shell displacements, $u \approx R^2(R - R_0)/r^2$.

Upon replacing equation (V.12) in (V.8) we obtain the following ordinary non-linear ordinary differential equation (ODE) with dimensionless time t as the only independent variable, and the external microbubble radius, R , as the only unknown:

$$\begin{aligned}
 & -\left(\frac{3}{2} - \frac{M\dot{R}}{2}\right)\dot{R}^2 + (1 + M\dot{R}) \left[\frac{2}{WeR} + P_{st} \left(\frac{R_0}{R}\right)^{3\gamma} - \frac{4}{Re_l R} \frac{\dot{R}}{R} - \frac{4}{Re_l} m \frac{\dot{R}}{R^2} + \right. \\
 & \left. -4G \left(\frac{R-1}{R^2}\right) - P_{st} - \varepsilon P_{st} \sin(t) \right] \\
 & + RM \left[\frac{2}{We R^2} \frac{\dot{R}}{R} + \frac{4}{Re_l R^2} \frac{\dot{R}^2}{R} - \frac{4}{Re_l} m \frac{2\dot{R}^2}{R^3} + \right. \\
 & \left. -4G \frac{\dot{R}(2-R)}{R^3} - \varepsilon P_{st} \cos(t) \right] = \left[(1 - M\dot{R})R + \frac{4M}{Re_l} + \frac{4Mm}{Re_l R} \right] \ddot{R}
 \end{aligned} \tag{V.13}$$

The above equation can be solved with the appropriate initial conditions in order to provide the radial position and the velocity of the membrane, and through them the rest of the important dependent variables of the flow. By construction the above model cannot account for the effect of prestress. Hence, we initially impose equilibrium conditions:

$$R(t=0) = 1, \quad \dot{R}(t=0) = 0, \quad u|_{r=1} = u(r=1, t=0) = 0. \tag{V.14}$$

V.1.2.2 Strain Hardening and Strain Softening Materials

Most materials do not respond to external forces through a constant elasticity modulus. Rather, they exhibit a varying stress strain relation at large deformations or at very abrupt changes of pressure, as is the case with ultrasound. Two very common families of materials characterized by this kind of response are strain softening and strain hardening materials. In the former case the membrane material is such that its shear modulus is reduced as strain grows whereas the opposite is true for the latter type of membrane materials. Both types of materials are used in the manufacturing of contrast agents, e.g. lipid bi-layers are strain hardening whereas most polymer shelled air filled particles are strain softening. Consequently, taking into consideration the specific material behavior will enhance the predictive capabilities of the model. In the following we present the governing equations for the mechanical behavior of a viscoelastic membrane at equilibrium, taken to be infinitesimally thin in comparison with the radius as is normally the case with contrast agents used in ultrasound diagnostic imaging, for different types of nonlinear response.

Following Barthes & Rallison⁹⁷ we associate the elastic tension tensor, \underline{X}_M' , on a deformed two-dimensional surface with the Green-Lagrange surface deformation tensor, \underline{e} , via the strain energy function $w(I_1, I_2)$, where I_1, I_2 denote the 2D strain invariants:

$$\underline{\underline{X}}_M' = \frac{2}{J_s} \left[\frac{\partial w}{\partial I_1} \underline{\underline{A}} \cdot \underline{\underline{A}}^T + \frac{\partial w}{\partial I_2} J_s^2 (\underline{\underline{I}} - \bar{\underline{\underline{N}}}\bar{\underline{\underline{N}}}) \right]. \quad (\text{V.15})$$

$$\underline{\underline{e}} = \frac{1}{2} \left[\underline{\underline{A}}^T \cdot \underline{\underline{A}} - (\underline{\underline{I}} - \bar{\underline{\underline{N}}}\bar{\underline{\underline{N}}}) \right] \quad (\text{V.16})$$

$$J_s = \lambda_1 \lambda_2 = \sqrt{\det(\underline{\underline{A}}^T \cdot \underline{\underline{A}} + \bar{\underline{\underline{N}}}\bar{\underline{\underline{N}}})}, \quad (\text{V.17})$$

$$I_1 = 2\text{tr}(\underline{\underline{e}}) = \lambda_1^2 + \lambda_2^2 - 2, \quad I_2 = J_s^2 - 1 = \lambda_1^2 \lambda_2^2 - 1$$

In the above $\underline{\underline{A}}$ denotes the surface displacement gradient, $\bar{\underline{\underline{N}}}$ the normal vector at a reference unstressed state and λ_1^2, λ_2^2 the two non-zero eigenvalues of $\underline{\underline{A}}^T \cdot \underline{\underline{A}}$ that correspond to local principal axes of deformation in the tangential membrane plane and represent the principal extension ratios along the same axes. The two invariants, I_1, I_2 , denote the elongation of a local line element and the local area dilatation, respectively. The above formulation does not account for the membrane bending resistance, which, however, is not needed as long as the shape of the micro-bubble remains spherical. More details on the theory of elasticity in the presence of large displacements can be found in Green & Zerna⁹⁸, as well as in the literature of capsule mechanics^{50,61,96}.

The strain energy $w(I_1, I_2)$ depends on the nature of the membrane material and assumes different forms as the mechanical behavior of the membrane changes. A typical strain energy describing a very thin sheet of an isotropic, volume-incompressible, rubber-like material with strain softening behavior, is the one provided by the two-dimensional Mooney-Rivlin (MR) law⁹⁸,

$$w^{\text{MR}} = \frac{G_{\text{MR}}}{2} \left[(1-b) \left(I_1 + 2 + \frac{1}{I_2 + 1} \right) + b \left(\frac{I_1 + 2}{I_2 + 1} + I_2 + 1 \right) \right] \quad (\text{V.18a})$$

$$X_{\text{MII}}^{\text{MR}} = \frac{G_{\text{MR}}}{\lambda_1 \lambda_2} \left(\lambda_1^2 - \frac{1}{(\lambda_1 \lambda_2)^2} \right) [1 + b(\lambda_2^2 - 1)], \quad (\text{V.18b})$$

with G_{MR} the Mooney-Rivlin surface shear modulus expressed in Nt/m; when the indices are exchanged in (V.18b) the stress component along principal direction 2 is obtained. The case with $b=0$ corresponds to a neo-Hookean membrane whereas as b , which ranges between 0 and 1, tends to zero the membrane becomes softer. It should also be noted that the Mooney-Rivlin constitutive law allows for unrestricted area dilatation that is compensated by progressive thinning of the membrane, whereas the case with $b=0$ (neo-Hookean membrane) represents the appropriate linear stress strain relationship that accounts for the change in metric properties during deformation. Emelianov et al⁵³ examined the dynamics of a bubble surrounded by a Mooney material that extends to infinity in order to assess the importance of external shear.

One of the most widely used constitutive laws pertaining to strain hardening membranes is the one developed by Skalak et al.⁴⁸ in order to model the lipid bi-layer structure surrounding the red blood-cell,

$$w^{\text{SK}} = \frac{G_{\text{SK}}}{2} (I_1^2 + 2I_1 - 2I_2 + CI_2^3), \quad (\text{V.19a})$$

$$X_{\text{MII}}^{\text{SK}} = \frac{G_{\text{SK}}}{\lambda_1 \lambda_2} \left\{ \lambda_1^2 (\lambda_1^2 - 1) + C (\lambda_1 \lambda_2)^2 [(\lambda_1 \lambda_2)^2 - 1] \right\}. \quad (\text{V.19b})$$

with G_{SK} denoting the Skalak (SK) surface shear modulus expressed in Nt/m. The parameter C in the above equations is always positive and controls the extend of area incompressibility of the membrane. In the case of red blood-cells $C \gg 1$ in order to accommodate the almost incompressible nature of the membrane area. Nevertheless, this is a quite general law that is used for strain hardening membranes whether they are area incompressible or not. Membrane viscosity can also be accounted for via a linear Newtonian term that is added to the elastic stresses and involves the membrane velocity, $\mu_{2d} \frac{2}{\lambda_1} \frac{\partial \lambda_1}{\partial t'}; \frac{1}{\lambda_1} \frac{\partial \lambda_1}{\partial t'}$ is the first principal component of the surface rate of strain tensor⁵⁰ and μ_{2d} the 2d membrane viscosity expressed in Kg/s.

For a two-dimensional membrane the viscoelastic contributions to the force balance equation (V.10) enter through the surface divergence of the surface stress tensor. In the context of spherosymmetric oscillations only the radial component of the divergence has a nonzero contribution, while the membrane principal extension ratio due to its radial displacement reads

$$\lambda(t') = \lambda_1 = \lambda_2 = \frac{R'(t')}{R'_E} = \frac{R'(t')}{R'_0 - u^r|_{r=R'_0}}; \quad (V.20)$$

R'_E is the membrane radial position in the absence of strain. For better illustration of the above concepts, figure V.2 shows the variation of principal tension $X_1=X_2=T$ when a membrane sample is subject to isotropic strain along the principal directions 1 and 2, as is the case with radial pulsations that are examined in the present study, as a function of membrane relative area change for different types of membranes. Clearly, as $b=1-\Psi$ approaches zero the membrane softness increases whereas as C deviates from unity even the linear behavior of an SK membrane deviates from the predictions of the KV law. In addition, as C increases beyond 10 it has essentially achieved its asymptotic behavior of an area incompressible membrane at infinity. It should be noted that, in view of the isotropy in the deformation that is assumed in the present study, the main elastic effect that is assessed here is that of area dilatation due to pulsation. This is reflected in the area dilatation modulus K that is defined as the ratio between the isotropic elastic tension and the relative area change (λ^2-1) for small deformations. It turns out that a Hookean material with Poisson ratio $\nu_s=1/2$, a MR material and a SK material with $C=1$ all are characterized by area dilatation modulus K equal to $3G_{2d}$, where G_{2d} denotes the 2d shear modulus of the membrane. In the case of a KV membrane $G_{2d}=G_s\delta'$. In the following we will use this parameter in order to compare the behavior of membranes with the same area dilatation modulus that obey different constitutive laws. Thus, for a MR membrane we will use $G_{MR}=G_s\delta'$, and similarly for an SK membrane with $C=1$ we will use $G_{SK}=G_s\delta'$. In the latter type of membrane it can be seen that when $C=1$, $K=G_{2d}(2C+1)$. Consequently, in the following we will ensure that the area dilatation modulus is the same when we compare strain hardening with strain softening and Hookean (i.e. KV) membranes. In addition we will present a separate set of results in order to assess the effect of parameter C on SK membranes, which essentially represents the effect of increasing the area dilatation modulus for a given SK membrane.

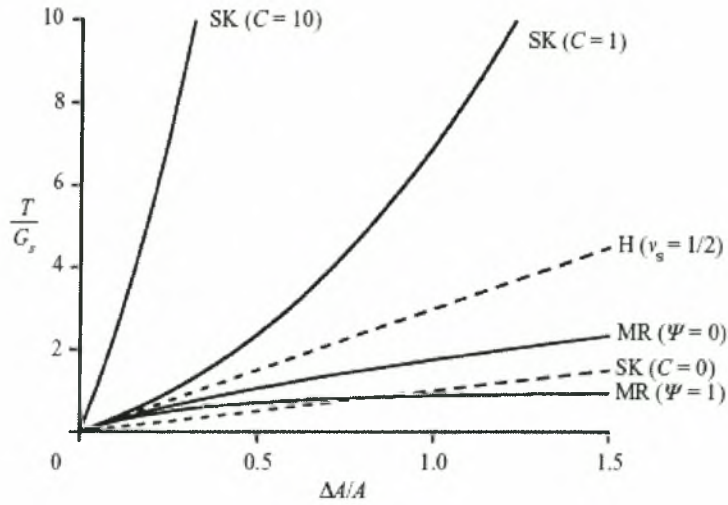


Figure V.2: Isotropic tension: principal tension T/G_s as a function of relative area change. Comparison of the linear Hooke (H) law and the nonlinear Mooney-Rivlin (MR) and Skalak (SK) laws (adapted from Barthes et al.⁵⁰); $\nu_s=1/2$ denotes the 2d surface Poisson ratio.

Upon introduction into the stress equilibrium equation that holds on the membrane, eq. (V.10), of the MR constitutive law and reverting to dimensionless formulation in a manner analogous to the Kelvin-Voigt model, we obtain the following expression for the liquid pressure on the membrane:

$$P_l|_{r=R} = \left(\frac{1}{R}\right)^{3\gamma} \left[P_s + \frac{2}{We} + 2G \left[1 - (1-u|_{r=1})^6 \right] \left[1 + b \left[\left(\frac{1}{1-u|_{r=1}} \right)^2 - 1 \right] \right] \right] + \quad (V.21)$$

$$-\frac{2}{WeR} - \frac{4\dot{R}}{Re_r R} - \frac{2G}{R} \left[1 - \left(\frac{1-u|_{r=1}}{R} \right)^6 \right] \left[1 + b \left[\left(\frac{R}{1-u|_{r=1}} \right)^2 - 1 \right] \right] - \frac{4\dot{R}}{Re_r R^2} m$$

where $G = \frac{G_{MR}}{\rho_l \omega_f^2 R_0^3}$, $m = \frac{\mu_{MR}}{\mu R_0}$, are the dimensionless numbers that arise and

$u|_{r=1} = u(r=1, t=0) = u_0$ the initial membrane displacement that determines the residual stresses inside the membrane. Note the slightly different definition of these numbers from the situation with a KV membrane owing to the two-dimensional geometry of the interface. Finally, substituting the above expression in (V.8) we obtain a nonlinear ODE describing the time variation of the radial position and velocity of an MR membrane, that is equivalent to (V.13) for the Kelvin-Voigt model:

$$\begin{aligned}
& -\left(\frac{3}{2}-\frac{M\dot{R}}{2}\right)\dot{R}^2 + (1+M\dot{R}) \left[\frac{2}{We} + P_{st} + 2G \left[1 - (1-u_0)^6 \right] \left[1 + b \left[\left(\frac{1}{1-u_0} \right)^2 - 1 \right] \right] \left(\frac{1}{R} \right)^{3\gamma} + \right. \\
& \left. \frac{2}{WeR} - \frac{4\dot{R}}{Re_t R} - \frac{4m\dot{R}}{Re_t R^2} - P_{st} - \varepsilon P_{st} \sin(t) + \right. \\
& \left. - \frac{2G}{R} \left[1 - \left(\frac{1-u_0}{R} \right)^6 \right] \left[1 + b \left[\left(\frac{R}{1-u_0} \right)^2 - 1 \right] \right] \right] + \\
& + RM \left[\begin{aligned} & -3\gamma R^{-3\gamma-1} \dot{R} \left[\frac{2}{We} + P_{st} + 2G \left[1 - (1-u_0)^6 \right] \left[1 + b \left[\left(\frac{1}{1-u_0} \right)^2 - 1 \right] \right] \right] + \\ & \frac{2\dot{R}}{We R^2} + \frac{4\dot{R}^2}{Re_t R^2} + \frac{8m\dot{R}^2}{Re_t R^3} - \varepsilon P_{st} \cos(t) + \\ & -2G \left[-(1-b) \frac{\dot{R}}{R^2} + \frac{b\dot{R}}{(1-u_0)^2} + (1-b) \frac{7(1-u_0)^6 \dot{R}}{R^8} + \frac{5b(1-u_0)^4 \dot{R}}{R^6} \right] \end{aligned} \right] = \\
& = \left[(1-M\dot{R})R + \frac{4M}{Re_t} + \frac{4mM}{Re_t} \frac{1}{R} \right] \ddot{R}
\end{aligned} \tag{V.22}$$

In a similar fashion, for an SK membrane, as parameter C grows the stresses developed on the membrane also increase for the same deformation. Following a similar procedure as with the MR membrane the following expression for the dimensionless liquid pressure, $P_l|_{r=R}$, on an SK membrane is derived,

$$\begin{aligned}
P_l|_{r=R} &= \left(\frac{1}{R} \right)^{3\gamma} \left[P_{st} + \frac{2}{We} + 2G \left[\left(\frac{1}{1-u_0} \right)^2 (1-C) + C \left(\frac{1}{1-u_0} \right)^6 - 1 \right] \right] + \\
& - \frac{2}{WeR} - \frac{4\dot{R}}{Re_t R} - \frac{2G}{R} \left[\left(\frac{R}{1-u_0} \right)^2 (1-C) + C \left(\frac{R}{1-u_0} \right)^6 - 1 \right] - \frac{4\dot{R}}{Re_t R^2} m
\end{aligned} \tag{V.23}$$

where $G = \frac{G_{SK}}{\rho_l \omega_f^2 R_0^3}$, $m = \frac{\mu_{SK}}{\mu R_0}$, are the dimensionless numbers that arise. Substituting equation (V.23) in (V.8) the equation governing the radial motion of an SK membrane

$$\begin{aligned}
& -\left(\frac{3}{2} - \frac{M\dot{R}}{2}\right)\dot{R}^2 + (1+M\dot{R}) \left[\frac{2}{WeR} + P_{st} + 2G \left[\left(\frac{1}{1-u_0}\right)^2 (1-C) + C \left(\frac{1}{1-u_0}\right)^6 - 1 \right] \left(\frac{1}{R}\right)^{3\gamma} + \right. \\
& \left. \frac{4}{Re_l R} - \frac{4m}{Re_l R^2} - P_{st} - \varepsilon P_{st} \sin(t) + \right. \\
& \left. - \frac{2G}{R} \left[\left(\frac{R}{1-u_0}\right)^2 (1-C) + C \left(\frac{R}{1-u_0}\right)^6 - 1 \right] \right] + \\
& + RM \left[\frac{-3\gamma R^{-3\gamma-1} \dot{R} \left[\frac{2}{We} + P_{st} + 2G \left[\left(\frac{1}{1-u_0}\right)^2 (1-C) + C \left(\frac{1}{1-u_0}\right)^6 - 1 \right] \right]}{We R^2} + \frac{4}{Re_l R^2} + \frac{8m}{Re_l R^3} - \varepsilon P_{st} \cos(t) + \right. \\
& \left. - 2G \left[\frac{2(1-C)\dot{R}}{(1-u_0)^2} + \frac{6CR^4 \dot{R}}{(1-u_0)^6} \right] \right] = \\
& \left[(1-M\dot{R})R + \frac{4M}{Re_l} + \frac{4mM}{Re_l R} \right] \ddot{R}
\end{aligned} \tag{V.24}$$

is obtained. The dimensionless numbers in the above equation bear the same significance with equivalent ones appearing in (V.22) for the MR membrane. Equations (V.22) and (V.24) can be solved for the radial position and the velocity of the interface with the appropriate initial conditions,

$$R(t=0) = 1, \quad \dot{R}(t=0) = 0, \quad u|_{r=1} = u(r=1, t=0) = u_0. \tag{V.25}$$

V.1.3 Linear theory

Linearization of the governing equations is a useful tool in order to obtain the resonance frequency of the micro-bubble as a function of its size and mechanical properties, but also in order to interrelate the viscoelastic parameters that are involved in different constitutive laws⁵⁰. Starting with the Kelvin-Voigt model we apply infinitesimal perturbations to the basic solution, which is the micro-bubble equilibrium. To simplify the analysis we assume that the membrane is free of residual stresses at $t=0$, i.e. $u_0 = 0$. Applying small disturbances on the external radius as well as the far field pressure,

$$R = 1 + \varepsilon R_d, \quad P_\infty = P_{st} + \varepsilon P_{st} \sin(t), \quad \varepsilon \ll 1, \tag{V.26}$$

introducing the above expansions in the governing equations and retaining terms of order ε only, we obtain

$$\begin{aligned}
& \left[1 + \frac{4M}{Re_l} + \frac{4Mm}{Re_l} \right] \ddot{R}_d + \left[\frac{2M}{We} + \frac{4}{Re_l} + \frac{4m}{Re_l} + \right. \\
& \left. + 3\gamma M \left(\frac{2}{We} + P_{st} \right) + 4GM \right] \dot{R}_d + \\
& + \left[3\gamma \left(\frac{2}{We} + P_{st} \right) - \frac{2}{We} + 4G \right] R_d = -\varepsilon P_{st} \sin(t) - \varepsilon P_{st} M \cos(t)
\end{aligned} \tag{V.27}$$

The above equation is of the type

$$F_1 \ddot{R}_d + F_2 \dot{R}_d + F_3 R_d = -\varepsilon P_{st} \sin(t) - \varepsilon P_{st} M \cos(t) \quad (V.28)$$

which admits an analytical solution of the form,

$$R_d(t) = -B e^{\omega_R t} \cos(\omega_I t) + \frac{B \omega_R - A}{\omega_I} e^{\omega_I t} \sin(\omega_I t) + A \sin(t) + B \cos(t) \quad (V.29)$$

with

$$A = -\varepsilon P_{st} \frac{-F_1 + F_2 M + F_3}{F_2^2 + F_1^2 - 2F_1 F_3 + F_3^2}, \quad B = \varepsilon P_{st} \frac{F_1 M - F_3 M + F_2}{F_2^2 + F_1^2 - 2F_1 F_3 + F_3^2}, \quad (V.30)$$

and $\omega = \omega_R + i\omega_I$ the roots of the characteristic polynomial. ω_R is normally negative and acts as a measure of the system damping whereas ω_I is the dimensionless natural frequency of the micro-bubble.

Following the same procedure on equations (V.22) and (V.24) governing the dynamics of MR and SK membranes and taking $u_0 = 0$, for simplicity, we obtain again eq. (V.27) for a membrane obeying the MR constitutive law, provided $\mu_{MR} = 3\delta' \mu_s$, $G_{MR} = G_s \delta'$, and

$$\left[1 + \frac{4M}{Re_l} + \frac{4Mm}{Re_l} \right] \ddot{R}_d + \left[\frac{2M}{We} + \frac{4}{Re_l} + \frac{4m}{Re_l} + 3\gamma M \left(\frac{2}{We} + P_{st} \right) + 4GM(1+2C) \right] \dot{R}_d + \left[3\gamma \left(\frac{2}{We} + P_{st} \right) - \frac{2}{We} + 2G(2+4C) \right] R_d = -\varepsilon P_{st} \sin(t) - \varepsilon P_{st} M \cos(t) \quad (V.31)$$

for the Skalak law, provided $\mu_{SK} = 3\delta' \mu_s$, $G_{SK} = G_s \delta'$. For the SK membrane in addition to the above conditions it is required that $C = 1$. We conclude that the micro-bubble behavior is independent of the membrane constitutive law if the membrane deformation is small, for an MR membrane, whereas for an SK membrane parameter C , pertaining to the material it is made of, should become unity. In all other cases the micro-bubble behavior is heavily dependent on the constitutive law and this is an effect that will be demonstrated in the following sections of the present article. In the same manner, the effect of the initial residual stresses of the membrane on the micro-bubble scattering cross section is an additional issue that must be investigated in connection with the membrane material law.

For small external perturbations and when the micro-bubble has reached the phase of steady oscillations, we can neglect any transient effects and calculate the scattering cross section from equations (V.4-V.5) by employing the solution of the linearized problem given in (V.29)

$$\sigma_{Sc} = \frac{4\pi R_0^2}{[\omega_I^2 - 1]^2 + \delta_t^2} \sqrt{\frac{1+M^2}{F_1^2}}, \quad \omega_I^2 = \frac{\omega_0^2}{\omega_t^2} = \frac{F_3}{F_1}, \quad \delta_t = \frac{F_2}{F_1}, \quad (V.32)$$

where ω_0 is the dimensional micro-bubble natural frequency and δ_t the total damping coefficient. In equation (V.32) the dimensional scattering cross section is evaluated on the undisturbed micro-bubble interface, $R(t=0)=1$. It is important to note that the pressure signal attenuates as the distance, r' , from the interface increases⁹⁹. Nevertheless, the effect of different parameters on the scattering cross section as it is evaluated on the interface, will be examined in the present study since it focuses on the effect of membrane mechanical behavior.

V.2 NUMERICAL IMPLEMENTATION

We use the 4th order Runge-Kutta (RK) integrator in order to solve the 2nd order non-linear ordinary differential equation, eq. (V.13), (V.22) or (V.24) depending on the membrane model employed, governing the motion of the membrane. The time step of the numerical integration is fixed and is selected so that enough time steps are afforded within one period of the forced or the natural radial pulsations. Eventually results are tested for convergence and agreement with linear theory, whenever the latter is possible. The same approach has been successfully employed in the past for simulating large amplitude oscillations of free bubbles⁶⁸ near the Blake threshold. In order to compute

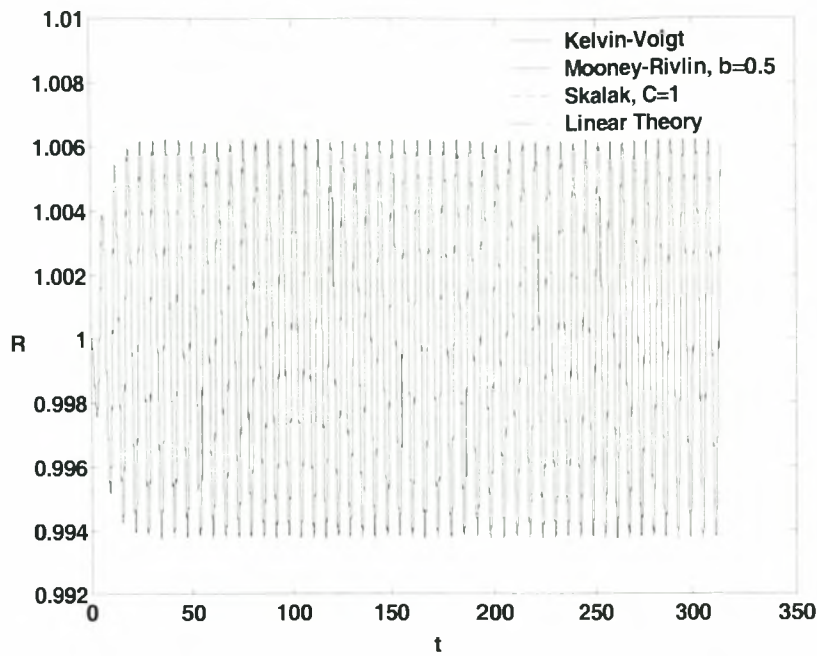
the integral $\int_0^{t_f} (R P_{sc})^2_n dt$ in equation (V.4) we implement the Parseval's identity

$$\int_0^{t_f} f(t)^2 dt = \frac{t_f}{2} \sum_{n=1}^{\infty} (a_n^2 + b_n^2) \quad (V.33)$$

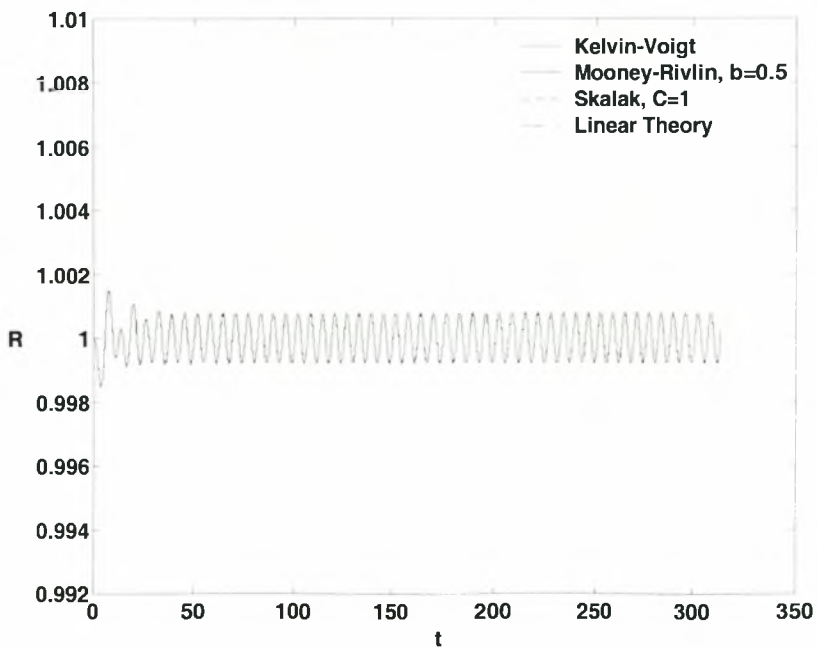
where t_f is the duration of the time integration and $a_n, b_n, n=1,2,\dots,\infty$ are the Fourier coefficients of $f(t)$ which are calculated through the Fast Fourier Transformation(FFT) algorithm. The zeroth order coefficient is not included in the right hand side of (V.33) since it corresponds to the time average of $f(t)$, which will be zero in view of (V.5).

V.2.1 Validation of the numerical scheme

The validity of the above numerical implementation was investigated in the case of small pressure disturbances, where numerical results are compared against the predictions of linear theory. For more severe pressure perturbations direct comparison with experimental results is the ultimate way to ascertain the applicability of the model. In figure V.3 the time evolution of the external micro-bubble radius on- and off-resonance is shown, when a sinusoidal disturbance is imposed, while in figure V.4 the scattering cross section versus the external forcing frequency is plotted for the same set of parameter values. Agreement between the computations and linear theory, equation (V.32), is obvious. It is also illustrated that when $\delta' \ll R'_0$ and $C=1$ the three constitutive laws predict the same dynamic behavior for the micro-bubble. However, when non-linear perturbations are applied the three constitutive laws can exhibit quite different dynamic behavior as will be seen in the following.



(a)



(b)

Figure V.3: Evolution of the external microbubble radius with time for a sinusoidal pressure disturbance with amplitude $\varepsilon = 0.05$, (a) on-resonance with $\nu_f = 2.8 \text{ MHz}$ and (b) off-resonance with $\nu_f = 5 \text{ MHz}$, as obtained from linear theory and from simulations with the three different types of membranes; $\mu_s = 0.6 \text{ kgm}^{-1}\text{s}^{-1}$, $G_s = 35 \text{ MPa}$, $R_0' = 3 \text{ }\mu\text{m}$, $\delta' = 15 \text{ nm}$, $b=0.5$ and $C=1$.

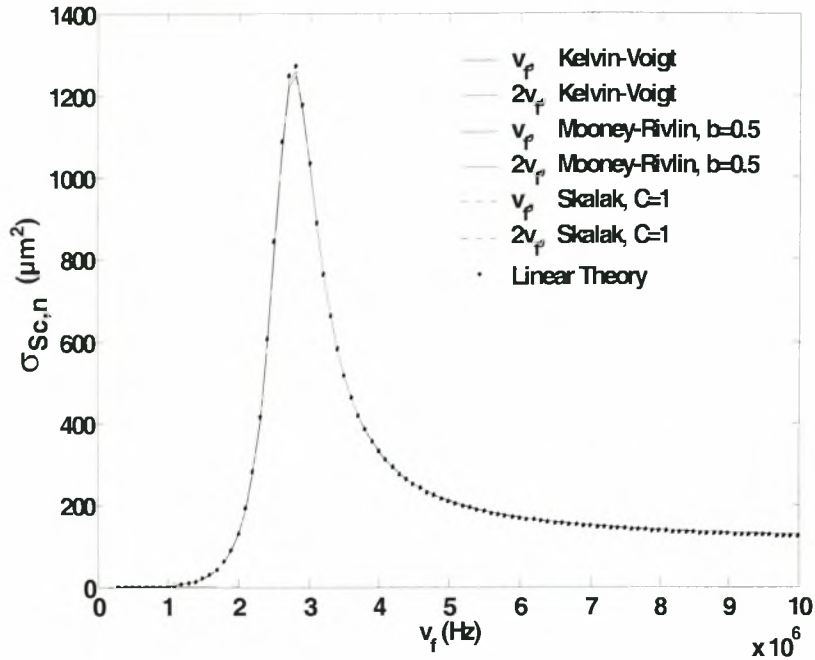


Figure V.4: Scattering cross section vs external forcing frequency as obtained from linear theory and from simulations with the three different types of membranes; $\mu_s = 0.6 \text{ kgm}^{-1}\text{s}^{-1}$, $G_s = 35 \text{ MPa}$, $R'_0 = 3 \text{ }\mu\text{m}$, $\delta' = 15 \text{ nm}$, $b=0.5$ and $C=1$.

It should also be stressed that estimating the resonance frequency, ω_{Res} , from the peak in the first harmonic component of the scattering cross section and evaluating it analytically from the characteristic polynomial of (V.28) gives the same result for bubbles of this size, $R'_0 = 3 \text{ }\mu\text{m}$. In the next section it will be seen that this agreement gradually loses validity as the bubble size decreases, or, equivalently, as viscous damping becomes more important. In order to extract ω_{Res} from (V.28) ω_f should be removed from it since dimensional $\omega' = \omega \cdot \omega_f$ does not depend on the forcing frequency. Indeed this is possible because, by inspecting equations (V.27) or (V.31), one notices that F_1 is independent of ω_f whereas $F_2 = \frac{\bar{F}_2}{\omega_f}$, $F_3 = \frac{\bar{F}_3}{\omega_f^2}$. Thus, in dimensional form,

$$\omega' = \frac{-\bar{F}_2 \pm \sqrt{\bar{F}_2^2 - 4\bar{F}_1\bar{F}_3}}{2\bar{F}_1}, \quad (\text{V.34})$$

where \bar{F}_2, \bar{F}_3 , have dimensions of $1/\text{s}$ and $1/\text{s}^2$, respectively, and ω_{Res} is the real part of ω' . An alternative estimate of resonance frequency can be obtained through the peak in scattering cross-section provided either analytically from (V.32) by finding the value of ω_f for which $\partial\sigma_{\text{sc}} / \partial\omega_f = 0$, or numerically by plotting the graph of scattering cross section as a function of ω_f .

V.3 RESULTS AND DISCUSSION

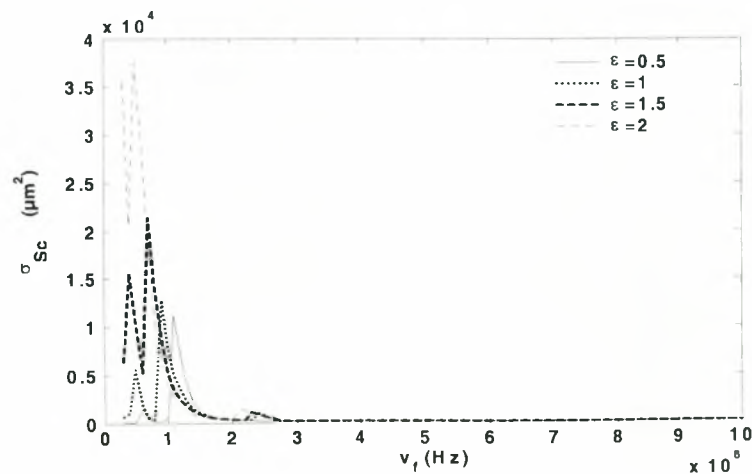
In this section a detailed parametric study is presented on the effect of the micro-bubble properties, size and mechanical properties of the membrane, and the ultrasound characteristics, amplitude and frequency, on the response of an insonated contrast agent. The effect of the host fluid properties is also examined, albeit to a lesser extent. The resonance frequency as well as the scattering cross section of the fundamental and higher harmonics, are monitored primarily when moderate to large acoustic disturbances are applied. The parametric study is conducted for the Kelvin-Voigt, the Mooney-Rivlin and the Skalak membrane constitutive laws while the effect of residual stresses in the onset of insonation is also investigated. The problem parameters are based on those provided from experimental and theoretical studies available in the literature of contrast agent research. In particular, an estimate for the membrane stiffness and friction was obtained for SonovueTM 47,100,101 and different polymer encapsulated air bubbles⁴⁴ by fitting the Church-Hoff model to their experimental recordings of scattering cross section and sound attenuation. Based on the same set of experimental data we use $\delta' \approx 15$ nm as a characteristic membrane thickness and take $R'_0 \approx 3$ μ m as an indicative micro-bubble radius. In this fashion and in order to conduct a parametric study we allow for variation of G_s between 30 and 105 MPa and μ_s between 0.6 and 1.6 kg/(m·s), based on the above studies as well as on the parameter range considered by similar theoretical studies⁴². We also set parameters b and C to 0 and 1 for the MR and the SK constitutive laws, respectively, unless stated otherwise. These two parameters are not easily estimated as they require extensive and very careful stress strain measurements. Nevertheless, as will be seen in the following, the area elasticity modulus, K , is the determining factor in the case of spherically symmetric bubble pulsations and, consequently, fitting data obtained in the regime of low acoustic disturbances can provide $K=3G_s$ for MR membranes or $G_s(1+2C)$ for SK membranes which can then be used for modeling the contrast agent under consideration.

The physical properties of water and blood are used for the host liquid; $\rho_l=998$ kg/m³ for both water and blood, $\mu_l=0.001$ and 0.004 kg/(m·s), $C_l=1550$ and 500 m/s, for water and blood respectively. Finally, the average interfacial tension σ is set to 0.072 and 0.045 kg/s² for water and blood, respectively. It is almost the same as the gas-host fluid interfacial tension, for the case of a shell with very small thickness. In any case it is not one of the primary variables of this study. Unless otherwise specified the physical constants of water are used in the simulations. The bulk of the results from the simulations are presented in the form of graphs of scattering cross section as a function of forcing frequency $\nu_f=\omega_f/(2\pi)$ when the latter varies in the MHz regime, which is also the frequency range of diagnostic imaging. This mode of presentation is preferred over one using dimensionless parameters, in order to accommodate comparison in performance between different membrane materials as the forcing frequency changes, as well as comparison with similar studies available in the literature of contrast agent dynamics.

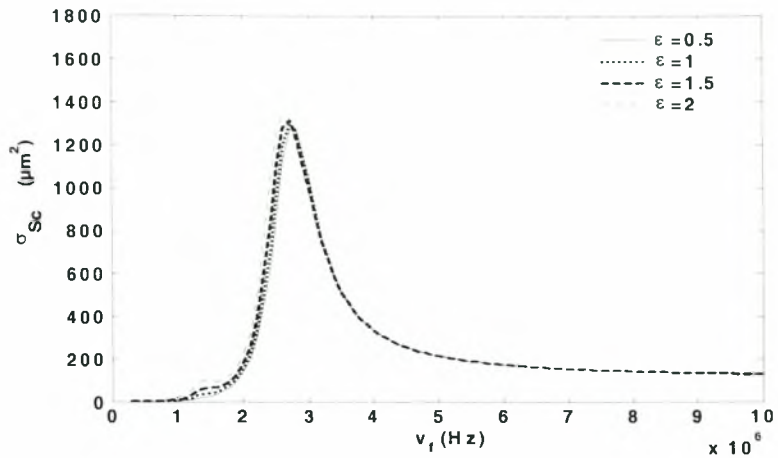
Experimental measurements^{106,44} indicate that the scattering cross section from encapsulated bubbles is weaker than the one obtained from free bubbles. It was argued by Khismatullin & Nadim⁴² that this is basically due to membrane viscosity rather than elasticity. Even though this is a valid argument it will be seen in the following that if the proper constitutive law for the membrane is not known, predictions of the resonance frequency based on simplified models may be in significant error. Resonance frequency is heavily dependent on the membrane area dilatation modulus and it could be the case

that the scattered signal from a micro-bubble is relatively weak simply because the ultrasonic beam is out of resonance. The total scattering cross section as a function of acoustic amplitude for the four types of bubble behavior examined in the present study, i.e. a free bubble and a microbubble with a KV, an MR or an SK membrane, is presented in figure V.5. Figures V.6 and V.7 show the harmonic components of the scattering cross section from a free bubble, a KV, an MR and an SK membrane, in response to an acoustic disturbance of increasing amplitude. In each graph the effect of increasing G_s is depicted on the different harmonic components of the scattering cross section for given amplitude. The response refers to the state of pulsation at which the micro-bubble performs steady oscillations, i.e. after the initial transient period has elapsed. The resonance frequency for a given set of parameters corresponds to the maximum in the different harmonic components of the scattering cross section over the range of applied forcing frequencies.

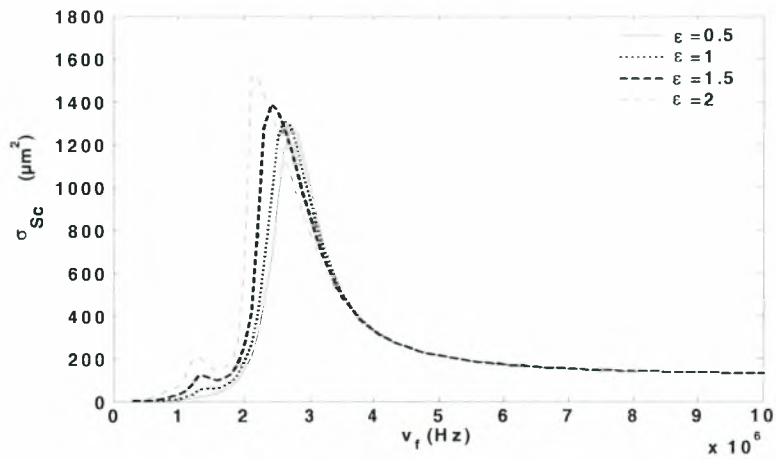
Overall, as the shear modulus G_s increases the resonance frequency, as was already known from previous studies^{34,35,42}, for all three constitutive laws as shown in Table V.1. As the amplitude of the acoustic disturbance increases, increasing ϵ , the extent of nonlinearity increases and as a first effect one notices the decrease in the resonance frequency, slight for KV and more intense for MR membranes, corresponding to an increase in the period of the steady bubble pulsation. This is a well-known result from weakly nonlinear theory of free bubble dynamics¹⁰³, it is most clearly manifested for small to moderate amplitudes and signifies the increase of effective system inertia with nonlinearity. However, when the SK constitutive law is used the resonance frequency exhibits a slow increase, indicating a progressive stiffening of the membrane and a concomitant loss of effective system inertia. These effects can also be gleaned from the evolution of total scattering cross section for different values of ϵ , shown in figure V.5. The deviation in resonance frequency between the predictions of Hooke's law, as manifested in the KV model, and those from the MR and SK constitutive laws is on the order of a few tenths of a MHz which is not trivial, given the sensitivity of modern imaging techniques, and keeps increasing with increasing amplitude of sound. It should also be stressed that it is the area dilatation modulus that determines the microbubble response. As shown from Table V.1, setting C to 2 but varying G_s so that the product $G_s(2C+1)$ is equal to $3G_s$, where G_s is now taken from the values shown in Table V.1 with $C=1$, reproduces very closely the values for resonance frequency.



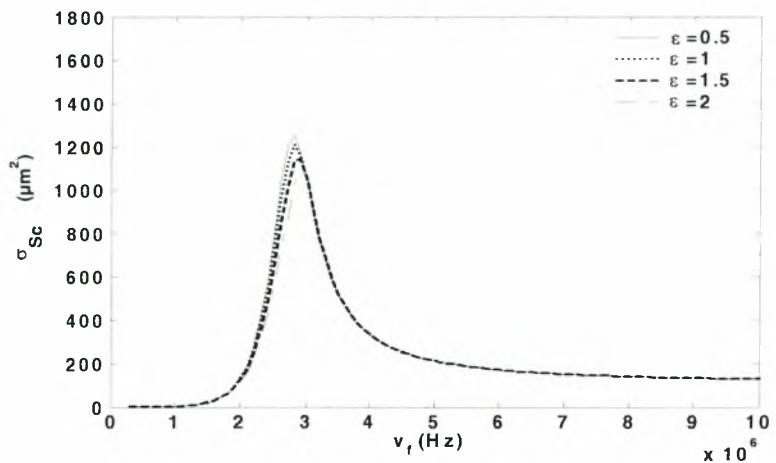
(a)



(b)

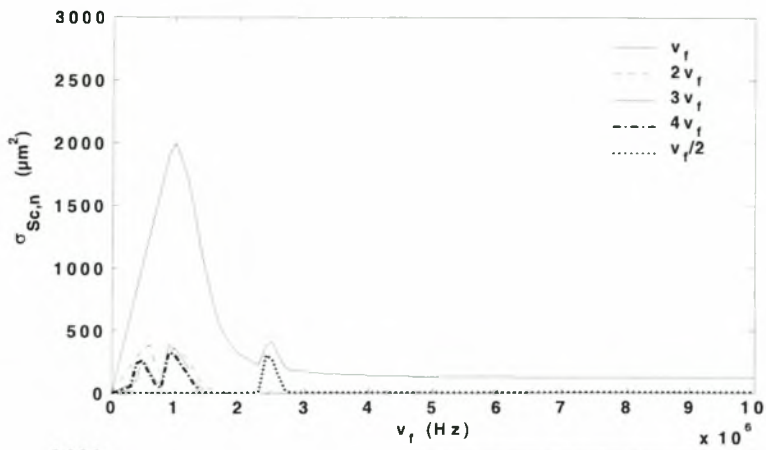


(c)

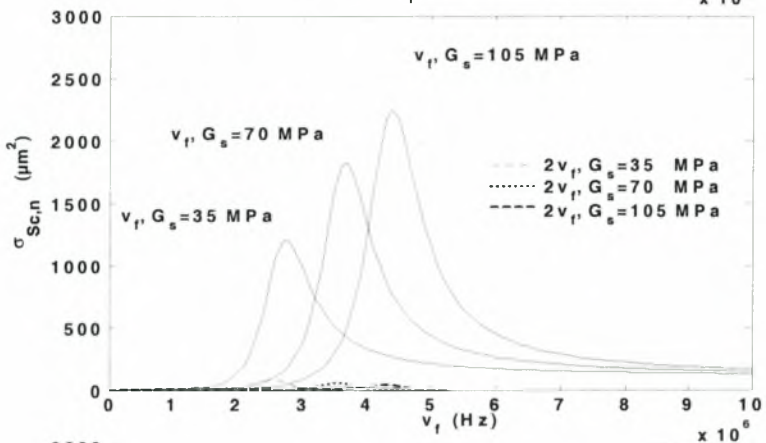


(d)

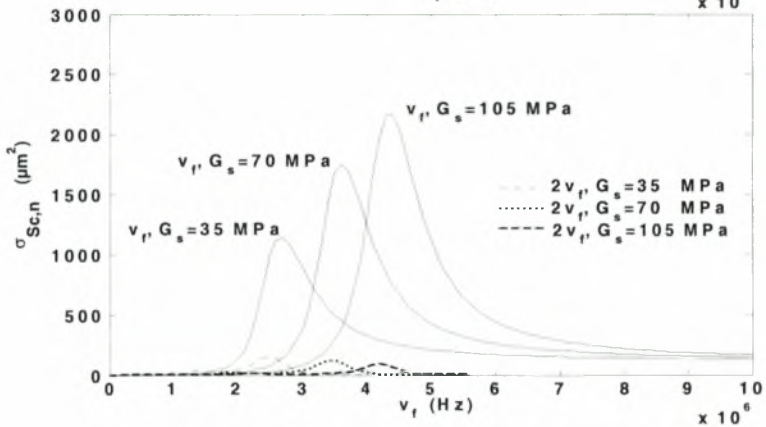
Figure V.5: Total scattering cross section vs external forcing frequency, when $\varepsilon = 0.5, 1, 1.5$ and 2 , for (a) a free bubble, (b) a KV, (c) an MR ($b = 0$) and (d) an SK ($C = 1$) membrane; $\mu_s = 0.6 \text{ kgm}^{-1}\text{s}^{-1}$, $G_s = 35 \text{ MPa}$, $R'_0 = 3 \text{ }\mu\text{m}$, $\delta' = 15 \text{ nm}$.



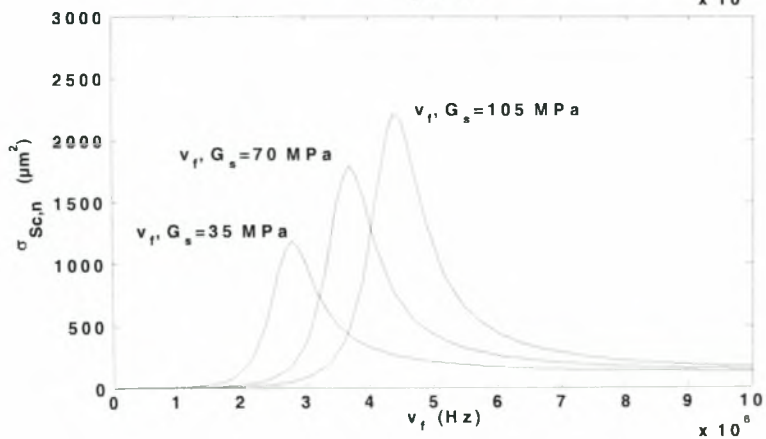
(a)



(b)

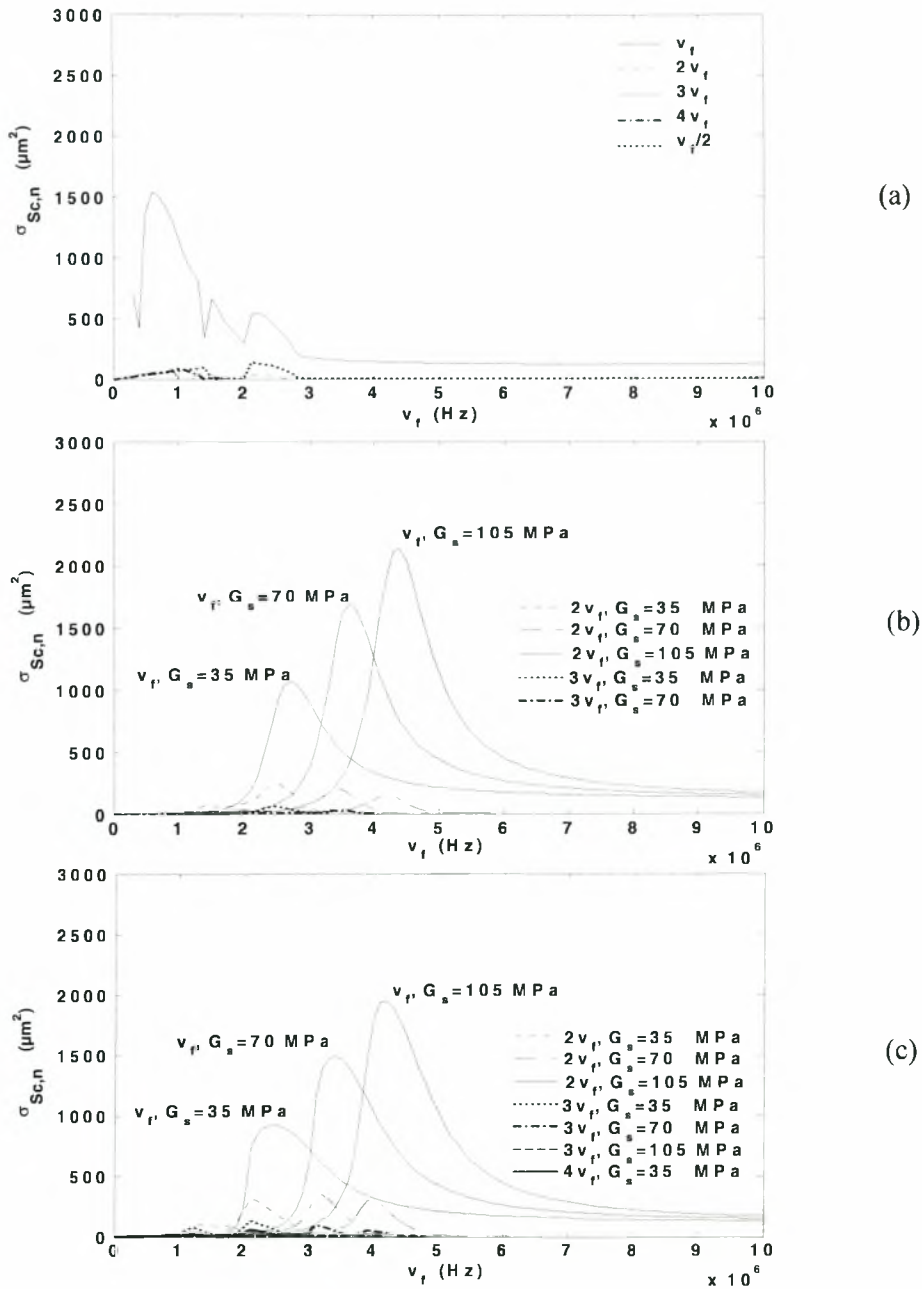


(c)



(d)

Figure V.6: Harmonic components of the scattering cross section vs. forcing frequency for (a) a free bubble, and (b) a KV, (c) an MR ($b = 0$) and (d) an SK ($C = 1$) membrane, when $G_s = 35, 70$ and 105 MPa; $\mu_s = 0.6 \text{ kgm}^{-1}\text{s}^{-1}$, $R'_0 = 3 \text{ }\mu\text{m}$, $\delta' = 15 \text{ nm}$, $\varepsilon = 1$.



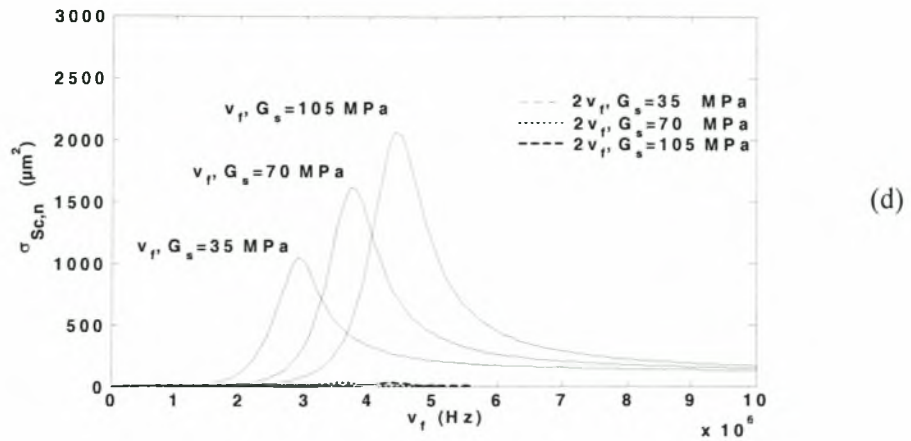


Figure V.7: Harmonic components of the scattering cross section vs. forcing frequency for (a) a free bubble, and (b) a KV, (c) an MR ($b = 0$) and (d) an SK ($C = 1$) membrane, when $G_s = 35, 70$ and 105 MPa; $\mu_s = 0.6 \text{ kgm}^{-1} \text{ s}^{-1}$, $R_0 = 3 \text{ }\mu\text{m}$, $\delta' = 15 \text{ nm}$, $\varepsilon = 2$.

Free bubble	
ε	ν_{res} (MHz)
0.5	1.1
1	1
1.5	0.8
2	0.6

Kelvin - Voigt – ν_{res} (MHz)			
G_s (MPa)	35	70	105
ε			
0.5	2.8	3.7	4.4
1	2.7	3.7	4.4
1.5	2.7	3.6	4.4
2	2.7	3.6	4.4

Mooney - Rivlin – ν_{res} (MHz)			
G_s (MPa)	35	70	105
ε			
0.5	2.7	3.7	4.4
1	2.7	3.6	4.4
1.5	2.6	3.5	4.3
2	2.4	3.4	4.2

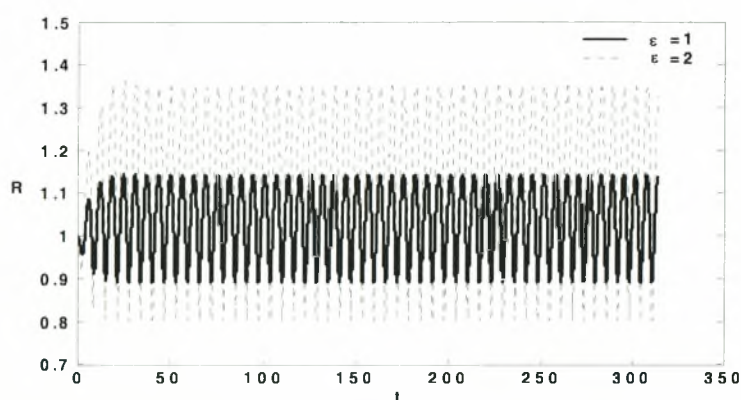
Skalak – v_{res} (MHz) (C=1)			
G_s (MPa)	35	70	105
ε			
0.5	2.8	3.7	4.4
1	2.8	3.7	4.4
1.5	2.9	3.7	4.4
2	2.9	3.7	4.4
5	3.4	4.1	4.6

Skalak – v_{res} (MHz) (C=2)			
G_s (MPa)	21	42	63
ε			
0.5	2.8	3.7	4.4
1	2.8	3.7	4.4
1.5	2.8	3.7	4.4
2	2.9	3.7	4.4
5	3.4	4	4.5

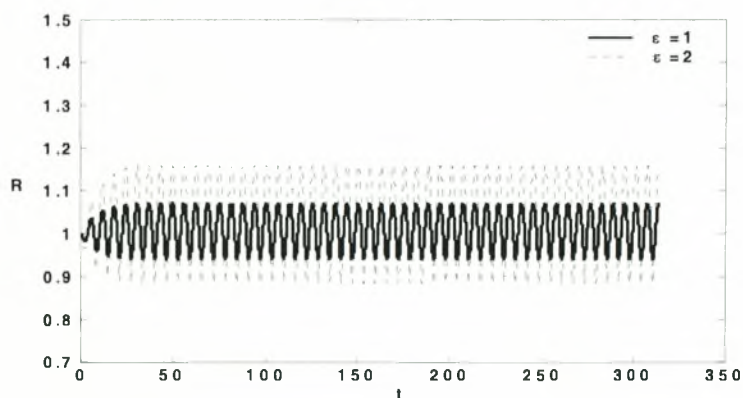
Table V.1: Resonance frequency of the first harmonic component as a function of area dilatation modulus and acoustic amplitude, recovered from numerical simulations. The rest of the problem parameters are provided in Figures V.5 –V.7.

Nonlinearity, however, has an additional effect on encapsulated bubbles by varying the effective area dilatation modulus of their membranes, in an average sense over one period of volume pulsation after initial transients have elapsed, for those that obey the MR or SK constitutive laws. This, owing to the decrease or increase of the effective shear modulus, results in an increase in the total scattering cross section for MR membranes and a corresponding decrease for SK membranes for reasons to be explained in detail in the following. Encapsulated bubbles tend to scatter a smaller amount of radiated energy due to the additional damping of the shell, as indicated by comparing peaks among graphs corresponding to free and encapsulated bubbles in figure V.5. On the other hand they can store more energy, which they then scatter back to the surrounding fluid, due to the elastic memory of the encapsulating shell. At the same time, however, also due to their elasticity, membranes exhibit smaller velocities at resonance in comparison with free bubbles and this decreases active scatter¹⁰⁴ caused by the volume change of the microbubble, while reducing viscous damping both in the surrounding fluid as well as the membrane. Nevertheless, especially for larger bubbles, viscous damping is not as important compared to that due to the encapsulating shell; hence the decreased scatter from encapsulated micro-bubbles. The combined result of these effects is clearly illustrated in figure V.5, based on which it can be surmised that the attenuation or intensification of volume oscillations, that is mostly evident in high acoustic amplitudes, determines the energy scatter from the microbubble. This is corroborated by Figures V.8 and V.9 where the radial displacement and velocity for

encapsulated bubbles for the two characteristic nonlinear constitutive laws employed in the present study and for two different values of the area dilatation modulus and the acoustic amplitude, are plotted at resonance. Due to the effective hardening of SK materials the membrane displacement and velocity at resonance increases very mildly as the amplitude of the disturbance or the area dilatation modulus increases, figure V.9. Consequently, when the sound amplitude increases the total scattering cross section decreases due to the disproportionately small increase of the microbubble's active scatter in comparison with the external disturbance. When MR membranes are subject to a sound field of increasing amplitude their effective elasticity decreases, which leads to additional enhancement of radial displacement and velocity, figure V.8, than expected based solely on the amplitude of the acoustic disturbance and this is reflected in the amplified scattering cross section. Comparing the level of total scatter between the three constitutive laws under examination, a material obeying the KV law is only moderately affected by the amplitude of sound exhibiting a slight increase in the total scatter. Overall it can be argued that MR membranes permit larger deformations than SK membranes and consequently tend to scatter more echo, through changes in the micro-bubble volume (active scatter).



(a)



(b)

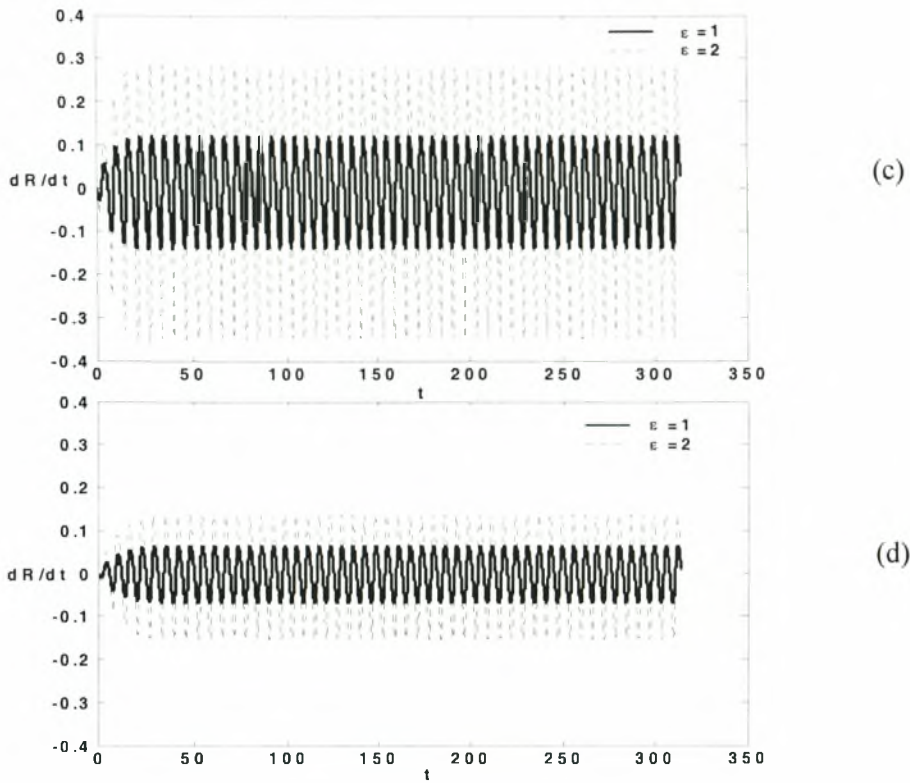
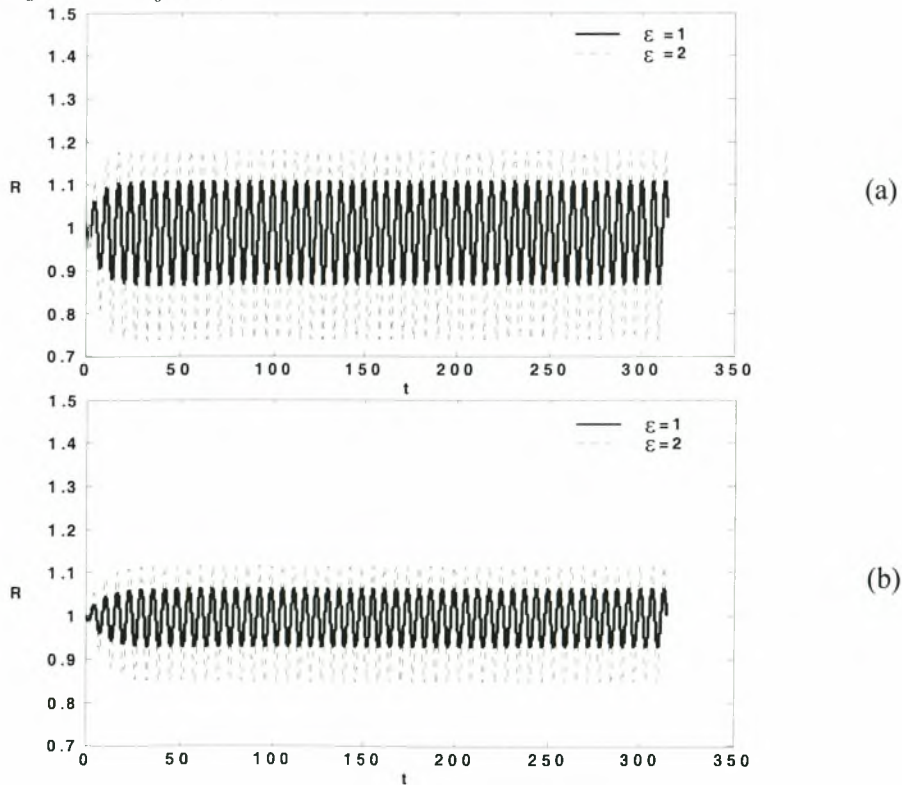


Figure V.8: Time evolution of the (a), (b) external microbubble radius and (c), (d) interfacial velocity when $G_s=35$ and 105 MPa, respectively, and $\epsilon=1$ and 2 , for an MR membrane ($b=0$) on-resonance, $v_f=2.7$ and 4.4 MHz, respectively; $\mu_s=0.6 \text{ kgm}^{-1} \text{ s}^{-1}$, $R'_0=3 \text{ }\mu\text{m}$, $\delta'=15 \text{ nm}$.



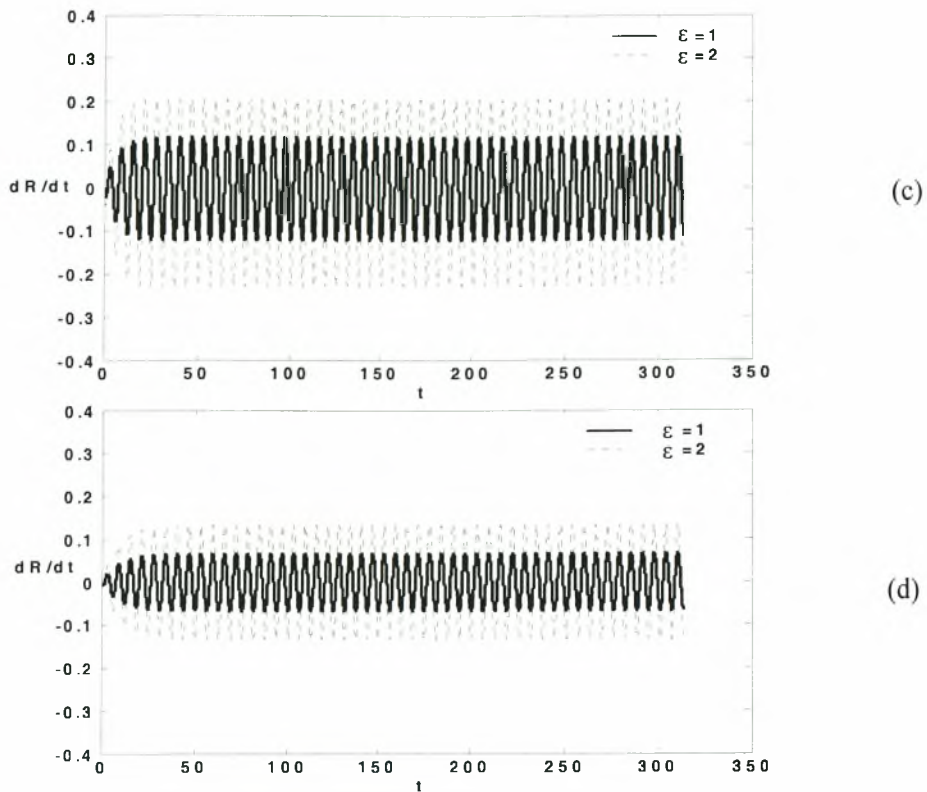


Figure V.9: Time evolution of the (a), (b) external microbubble radius and (c), (d) interfacial velocity when $G_s=35$ and 105 MPa, respectively, and $\epsilon=1$ and 2 , for an SK membrane ($C=1$) on-resonance, $\nu_f=3.4$ and 5.6 MHz, respectively; $\mu_s=0.6$ kgm⁻¹s⁻¹, $R'_0=3$ μ m, $\delta'=15$ nm.

Emphasis should also be placed on the harmonic content of the scattered signal since this finds extensive use in modern techniques of nonlinear signal processing^{105,47}. As it turns out, figure V.8, soft membranes exhibit larger displacements and velocities in comparison with hard membranes. As a result of the larger amplitude of membrane motion the amount of energy that is returned to the host fluid is scattered at lower frequencies with respect to KV and SK membranes. In addition, the content of the scattered signal in harmonic components, for given amplitude of the acoustic disturbance, is also increased which makes strain-softening membranes exceptionally useful for diagnostic tools where harmonic imaging is a preferred modality. In fact, as the amplitude of sound increases the scattered signal from the fundamental harmonic becomes weaker at resonance, compared to that from a strain hardening membrane, due to the appearance of higher harmonics. Another important aspect of the microbubble response at large amplitudes is the appearance of a subharmonic, $\omega_f/2$, signal in the back-scatter that is especially evident for MR membranes and that can be quite useful for nonlinear image processing⁴⁷; see also figures V.17 and V.18. In general, a rich harmonic content from a certain contrast agent is a clear indication of a strain-softening membrane.

Establishing the constitutive law requires prior knowledge of parameter b for MR membranes, i.e. determining the membrane softness, or parameter C for SK membranes, i.e. determining the membrane hardness. Figure V.10 shows the effect of parameter b on the micro-bubble response. As it approaches zero the membrane becomes softer and consequently scatters less energy in the fundamental harmonic whose resonance frequency tends to decrease, while the total scattering cross section increases in a manner similar to the situation observed when the amplitude of the acoustic disturbance was increased. On the other hand the harmonic content increases which makes the micro-bubble more amenable to nonlinear harmonic image processing. The effect of the residual stresses on the scattering cross section is almost non-existent for MR or KV membranes hence it is not shown in figure V.10. This is not the case when the membrane material obeys the Skalak law. The more strain hardening is the material the more intense is the shift of the resonance frequency to higher values as well as the scatter of the fundamental harmonic, figure V.11. For the same reason the residual stresses play an increasingly important role in the micro-bubble response, altering both the resonance frequency and the scattering cross section. The compressive or expansive nature of initial displacements that cause the residual stresses plays a pivotal role in determining these aspects of micro-bubble behavior. In particular, compressive initial stresses tend to decrease the micro-bubble resonance frequency while decreasing the amount of scatter at resonance. The opposite is true for positive initial displacements corresponding to volume expansion. In the latter situation the relative increase in the contrast agent's area, figure V.2, amounts to increasing its effective shear modulus as well. Thus a positive/negative initial displacement at equilibrium amounts to an increase/decrease in the shear modulus. As a result the membrane's ability to store and subsequently scatter energy is accentuated/weakened and its resonance frequency is increased/decreased, figure V.11. In the same figure the effect of increasing parameter C is also illustrated. Essentially, the effective shear modulus of the membrane increases and the micro-bubble exhibits more intense scatter and larger resonance frequencies for a given amount of residual stresses at $t=0$. It should also be noted that the harmonic content from a microbubble with a strain hardening membrane changes marginally as C varies provided the area dilatation modulus remains the same, i.e. G_s also varies in order to fix the K value.

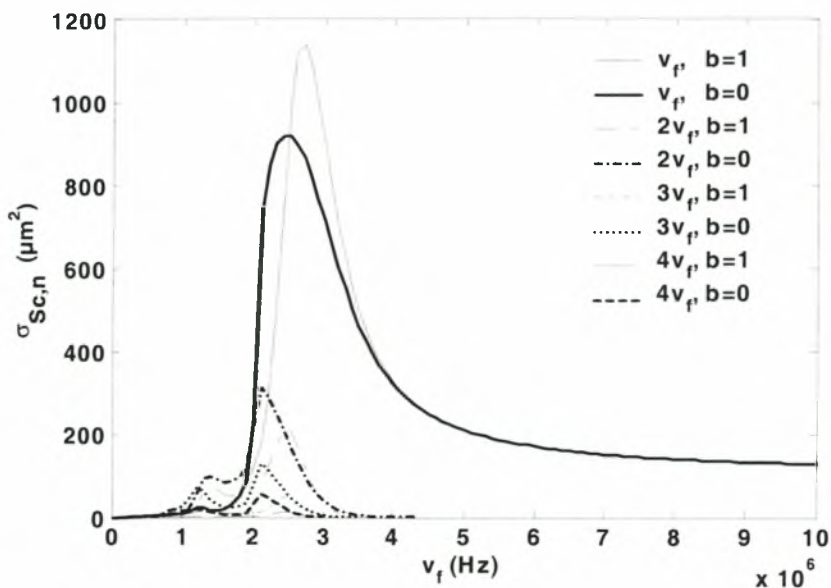


Figure V.10: Harmonic components of the scattering cross section vs. forcing frequency for an MR membrane with $b=0$ and 1; $\mu_s = 0.6 \text{ kgm}^{-1}\text{s}^{-1}$, $G_s = 35 \text{ MPa}$, $R'_0 = 3 \text{ }\mu\text{m}$, $\delta' = 15 \text{ nm}$, $\varepsilon = 2$.

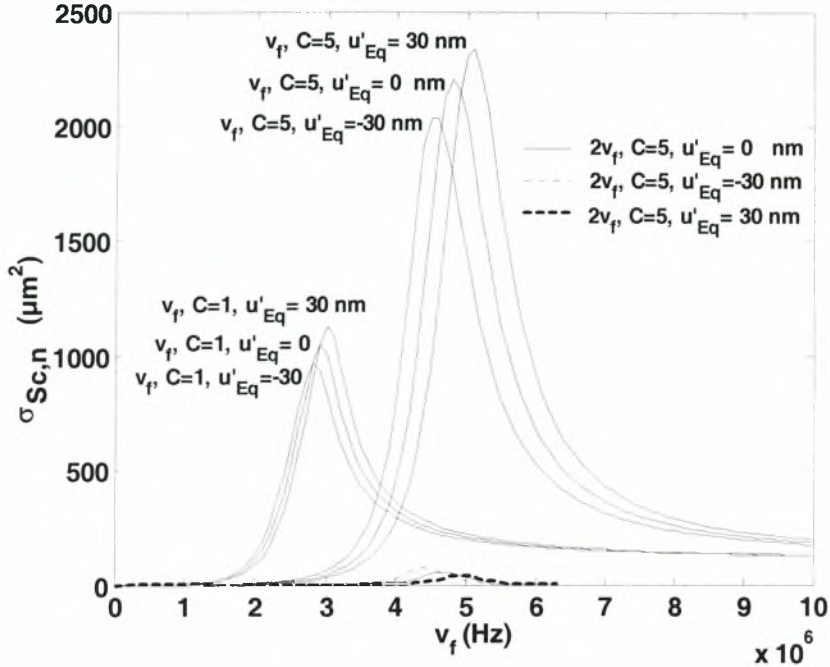
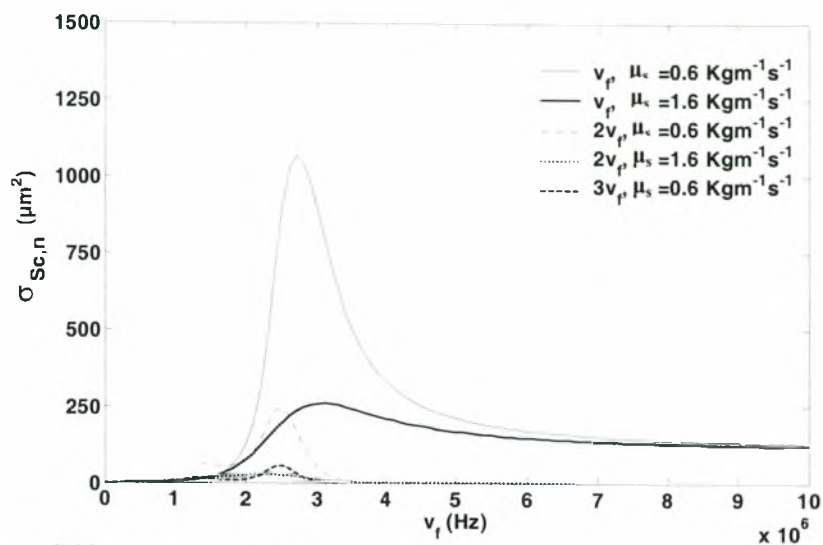
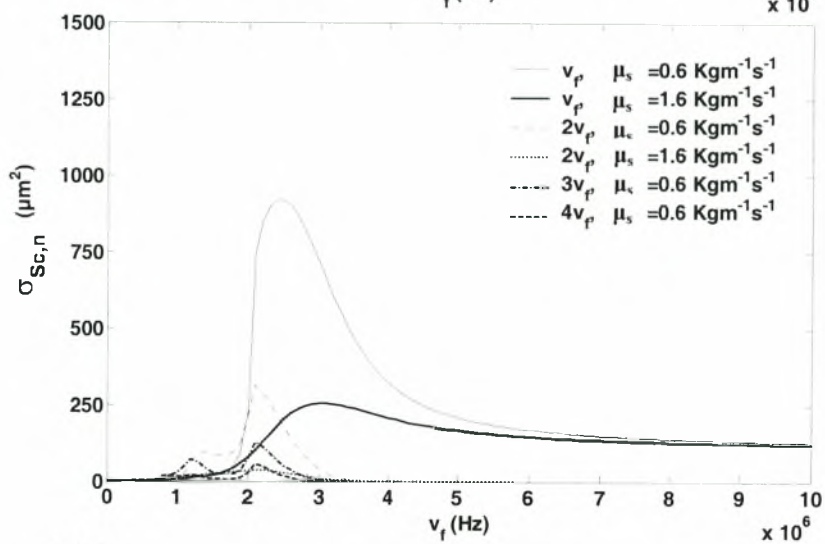


Figure V.11: Harmonic components of the scattering cross section vs. forcing frequency for an SK membrane with $C=1$ and 5 and nonzero residual stresses at $t=0$, $u'_{Eq} = u'(t'=0) = -30, 0$ and 30 nm ; $\mu_s = 0.6 \text{ kgm}^{-1}\text{s}^{-1}$, $G_s = 35 \text{ MPa}$, $R'_0 = 3 \text{ }\mu\text{m}$, $\delta' = 15 \text{ nm}$, $\varepsilon = 2$.

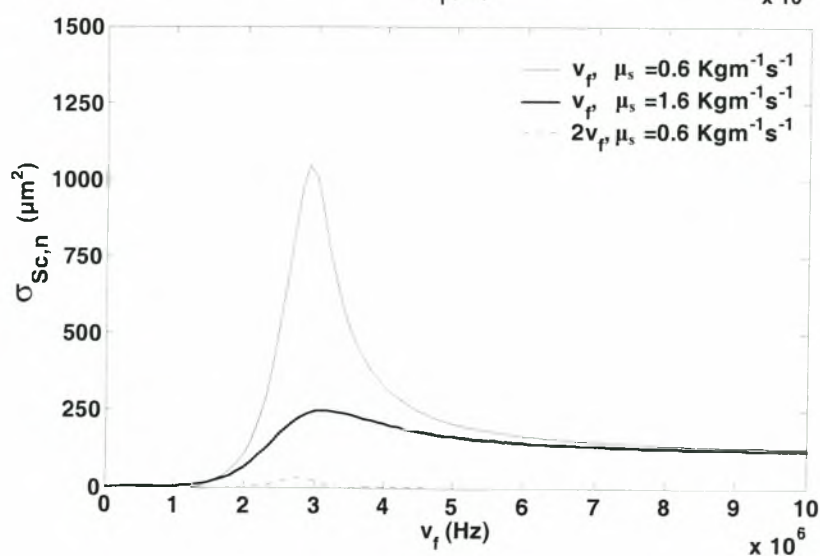
The effect of damping due to the viscosity of the membrane is illustrated in figure V.12 for the three constitutive laws and it is seen to significantly reduce the amount of scatter in all cases. This result is in accord with previous findings⁴² where the weak backscatter signal from encapsulated bubbles, in comparison with free ones, is attributed to membrane viscosity. In addition, damping due to membrane viscosity essentially eliminates the effect of higher harmonics. Of course, as was discussed above, when elasticity increases the scatter can be quite significant at resonance. In particular, for strain hardening membranes a strong first harmonic scattered signal can be obtained as the area dilatation modulus increases. A combined effect on the membrane elasticity and viscosity is observed when the membrane thickness is varied. Provided it remains much smaller than the bubble radius, increasing δ' amounts to increasing the effective membrane elasticity and viscosity, by increasing the two dimensional shear modulus and viscosity, μ_{MR} or $\mu_{SK} = 3\delta'\mu_s$, G_{MR} or $G_{SK} = G_s\delta'$. This behavior was shown, section V.1.3, to be the case for small amplitude disturbances and it persists for large amplitude acoustic disturbances. Indeed, increasing membrane thickness results in the combined effect of increasing the resonance frequency, in the manner expected for each constitutive law, while decreasing the amplitude of scatter at resonance due to the accentuated effect of membrane viscosity.



(a)



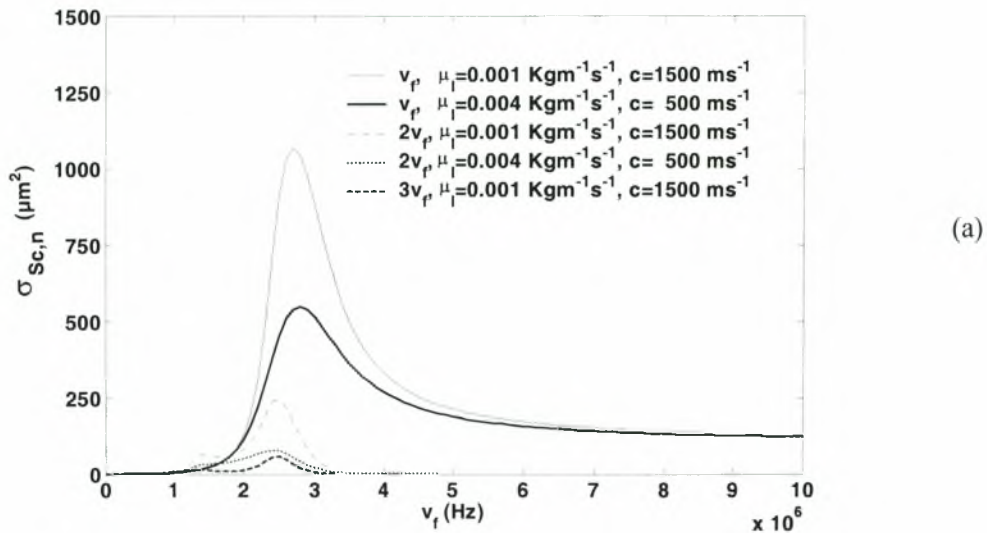
(b)



(c)

Figure V.12: Effect of membrane viscosity on the harmonic components of the scattering cross section vs. forcing frequency for (a) a KV, (b) an MR ($b = 0$) and (c) an SK ($C = 1$) membrane, with $\mu_s = 0.6$ and $1.6 \text{ kgm}^{-1}\text{s}^{-1}$; $G_s = 35 \text{ MPa}$, $R'_0 = 3 \text{ }\mu\text{m}$, $\delta' = 15 \text{ nm}$, $\varepsilon = 2$.

The host fluid also contributes to the damping of micro-bubble pulsations due to its viscosity and compressibility. Viscous damping is known to dominate³⁷ over thermal and acoustic damping for bubbles whose radius lies in the micrometer range, however for forcing frequencies in the MHz range acoustic damping becomes increasingly important. Performing the simulation presented in figure V.12 using blood as the host liquid amounts to quadrupling its viscosity. This results in minimal changes in the scatter and forcing frequency, especially for bubbles with equilibrium radius $R'_0 \geq 3 \text{ }\mu\text{m}$, which corroborates the fact that membrane viscosity constitutes the dominant damping mechanism for contrast agents. However, when the effect of sound attenuation is taken into consideration and the concomitant reduction in the speed of sound in the presence of a bubble population^{34,106} e.g. for a suspension of bubbles with volume fraction on the order of 5×10^{-4} the speed of sound becomes roughly 500 m/s, acoustic damping becomes a major component of total damping, figure V.13. At the same time a small but noticeable shift to higher resonance frequencies is exhibited as a result of increased liquid compressibility.



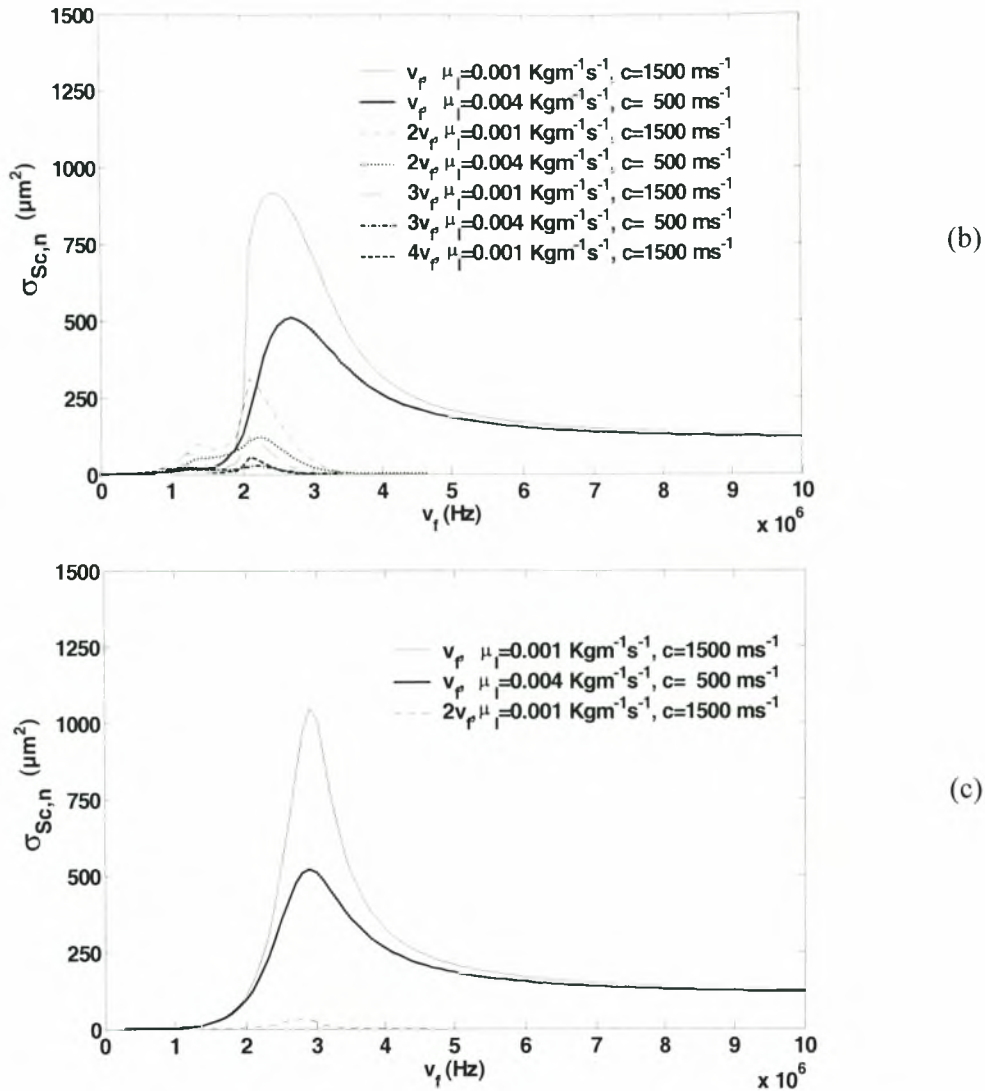


Figure V.13: Effect of the surrounding fluid on the harmonic components of the scattering cross section vs. forcing frequency for (a) a KV, (b) an MR ($b = 0$) and (c) an SK ($C = 1$) membrane. $\mu_l = 0.001 \text{ kgm}^{-1}\text{s}^{-1}$ and $c = 1500 \text{ m/s}$ for water whereas $\mu_l = 0.004 \text{ kgm}^{-1}\text{s}^{-1}$ and $c = 500 \text{ m/s}$ for blood with a 5×10^{-4} microbubble volume fraction; $\mu_s = 0.6 \text{ kgm}^{-1}\text{s}^{-1}$, $G_s = 35 \text{ MPa}$, $R_0' = 3 \text{ }\mu\text{m}$, $\delta' = 15 \text{ nm}$, $\varepsilon = 2$.

The effect of bubble size on the scattering cross section is also examined for the different types of membrane. In general, larger micro-bubbles scatter more echo than smaller ones and their spectrum is enriched with higher harmonics and sub harmonics, figures V.14-V.17. The latter arise especially for free bubbles or encapsulated bubbles with a soft membrane at large acoustic disturbances. Note, for instance, the large subharmonic signal for a MR membrane exhibited by microbubbles with an initial radius $R_0' \approx 5 \text{ }\mu\text{m}$, figure V.17(b). This is particularly useful for imaging purposes while also serving as a means to identify a strain softening membrane. On the other hand,

when the material is strain hardening the harmonic content of the scattered signal is almost negligible. The ability of micro-bubbles to scatter more echo as their size gets larger, figures V.16 and V.17, is attributed to the fact that they can store more energy in the form of volume pulsations for given membrane displacement. In addition, their resonance frequency acquires smaller values as their radius grows, irrespective of the membrane constitutive law. Another important aspect of the simulations presented in figures V.14-V.17 is that the value of external forcing frequency for which maximum scatter is registered coincides with the value predicted from the characteristic polynomial, eq. (V.34), of the linearized equation describing micro-bubble pulsations, eq. (V.28), for bubble equilibrium radii as small as $R'_0 = 2.5 \mu\text{m}$. This is contrary to the findings reported by Khismatullin & Nadim⁴² and is probably attributed to the Newtonian nature of the host liquid in the present study. However, as the bubble size decreases, $R'_0 \leq 2 \mu\text{m}$, the values predicted for ω_{Res} from the peak in scatter, as this is provided by maximizing (V.32) or by identifying the maximum in the numerical evaluation of the scattering cross-section versus forcing frequency, and from equation (V.34) start deviate, Table V.2. This may be attributed to the increased importance of viscous damping at such small bubble sizes. In fact, in this range of bubble radii the effect of resonance tends to disappear, figures V.14 and V.15, in agreement with previous studies. Indeed, the dominance of intermediate size micro-bubbles, $R'_0 = 3 \mu\text{m}$, in the scattered signal has been observed in experimental measurements of echo¹⁰⁰ with commercial contrast agents containing a distribution of bubble sizes. This is a combined result of the fact that smaller micro-bubbles do not scatter significantly while the percentage of larger ones in the bubble size distribution is quite small, since bubbles larger than, roughly, $10 \mu\text{m}$ cannot pass through pulmonary circulation¹⁰².

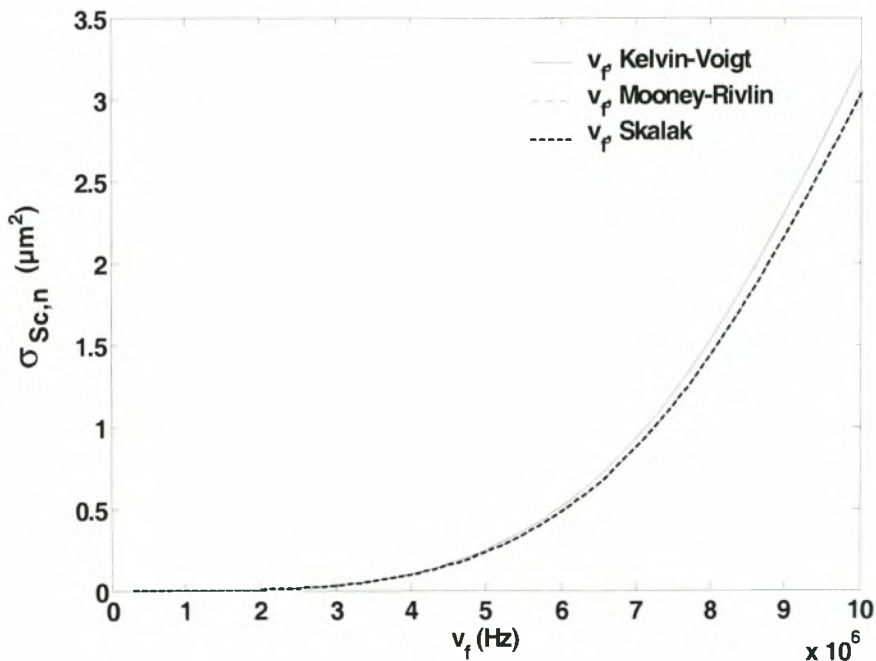


Figure V.14: First harmonic component of the scattering cross section vs. forcing frequency for (a) a KV, (b) an MR ($b = 0$) and (c) an SK ($C = 1$) membrane: $\mu_s = 0.6 \text{ kgm}^{-1}\text{s}^{-1}$, $G_s = 35 \text{ MPa}$, $R'_0 = 1 \mu\text{m}$, $\delta' = 15 \text{ nm}$, $\varepsilon = 0.5$.

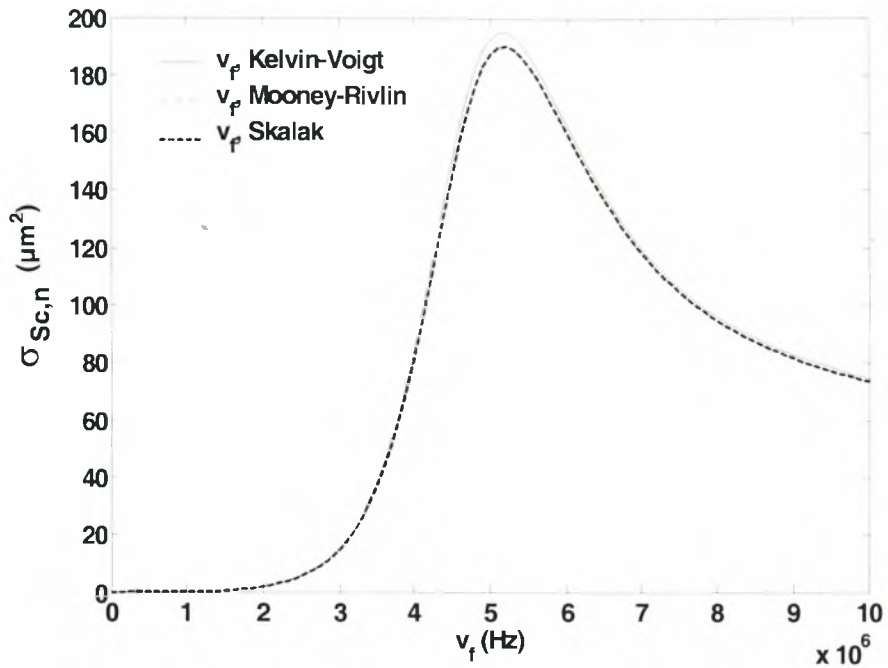
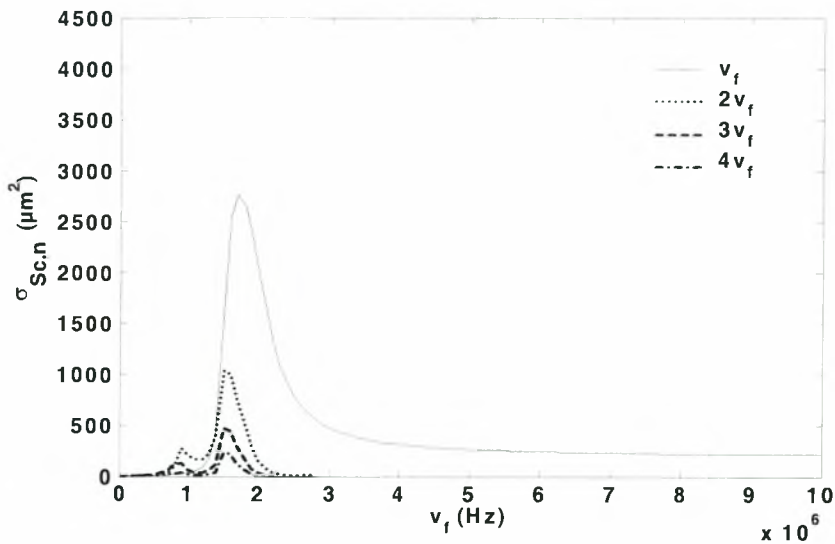
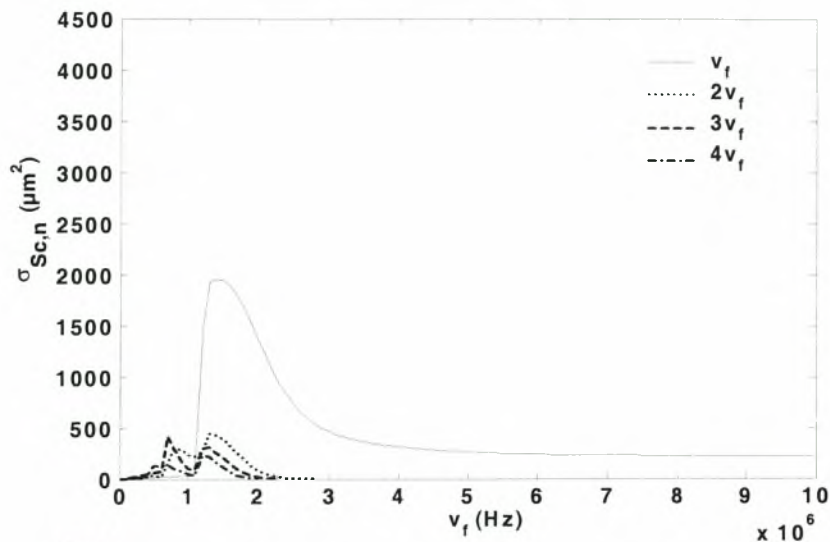


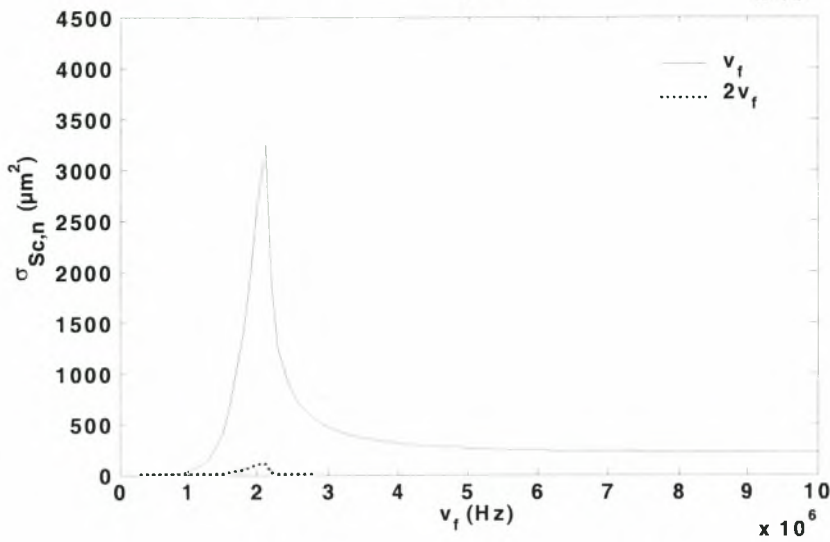
Figure V.15: First harmonic component of the scattering cross section vs. forcing frequency for (a) a KV, (b) an MR ($b=0$) and (c) an SK ($C=1$) membrane; $\mu_s = 0.6 \text{ kgm}^{-1}\text{s}^{-1}$, $G_s = 35 \text{ MPa}$, $R'_0 = 2 \text{ }\mu\text{m}$, $\delta' = 15 \text{ nm}$, $\varepsilon = 0.5$.



(a)

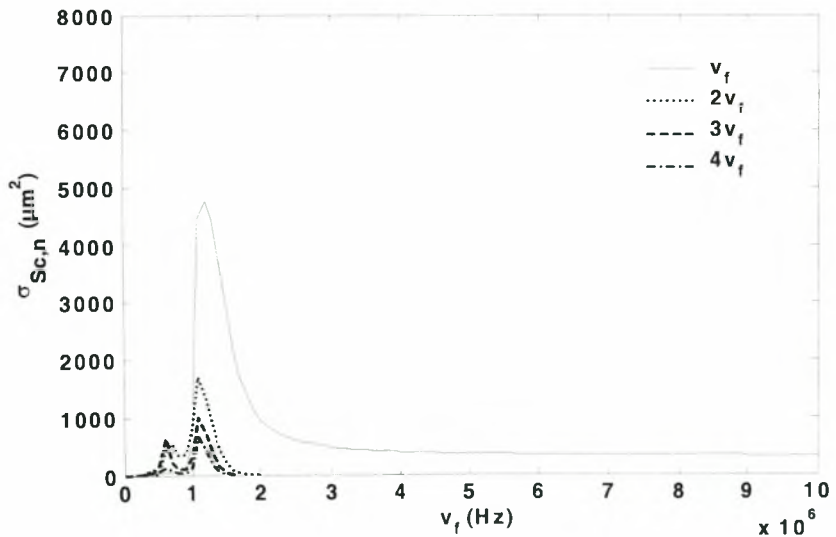


(b)

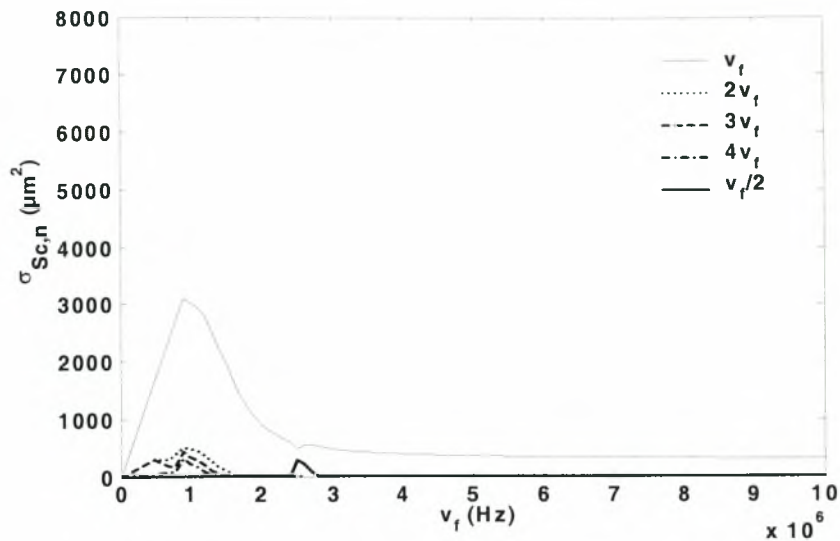


(c)

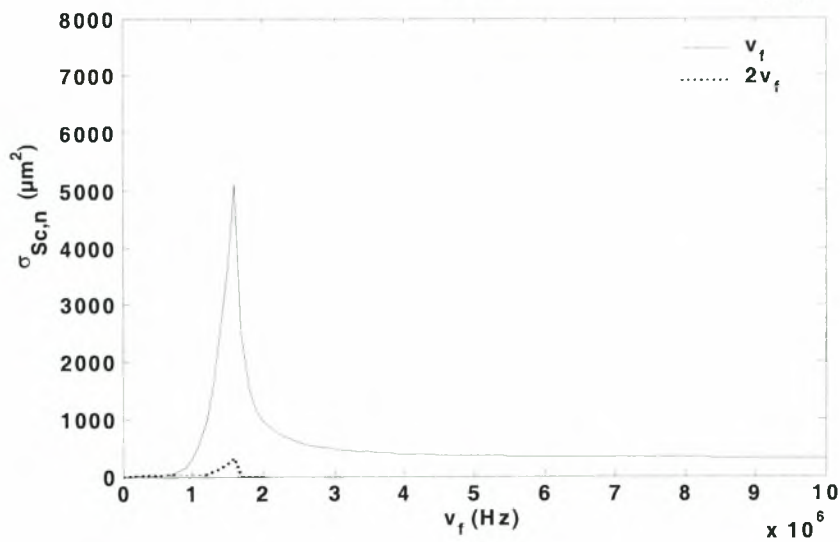
Figure V.16: Harmonic components of the scattering cross section vs. forcing frequency for (a) a KV, (b) an MR ($b=0$) and (c) an SK ($C=1$) membrane; $\mu_s = 0.6 \text{ kgm}^{-1}\text{s}^{-1}$, $G_s = 35 \text{ MPa}$, $R'_0 = 4 \text{ }\mu\text{m}$, $\delta' = 15 \text{ nm}$, $\varepsilon = 2$.



(a)



(b)



(c)

Figure V.17: Harmonic components of the scattering cross section vs. forcing frequency for (a) a KV, (b) an MR ($b=0$) and (c) an SK ($C=1$) membrane; $\mu_s = 0.6 \text{ kgm}^{-1}\text{s}^{-1}$, $G_s = 35 \text{ MPa}$, $R'_0 = 5 \text{ }\mu\text{m}$, $\delta' = 15 \text{ nm}$, $\varepsilon = 2$.

R'_0 (μm)	ν_{res} (MHz) Equation (V.34)	$\nu_{\text{res.}}$ (MHz) Equation (V.32)
1	9.5	-
1.5	6.7	8.6
2	4.6	5.2
2.5	3.4	3.6
3	2.7	2.8
3.5	2.2	2.2
4	1.8	1.8
4.5	1.5	1.5
5	1.3	1.3

Table V.2: Comparison of the resonance frequency as obtained via equations (V.32) and (V.34), for different equilibrium radii; $G_s=35$ MPa, $\mu_s = 0.6 \text{ kgm}^{-1}\text{s}^{-1}$ and $\delta' = 15 \text{ nm}$.

V.4 CONCLUSIONS

The effect of membrane constitutive law on the response of a micro-bubble subject to ultrasonic disturbances was investigated. Emphasis was placed on the combined effect of increasing amplitude of sound and the mechanical behavior of the membrane on the microbubble response. The behavior of strain softening and strain hardening membranes as this is incorporated in two widely used constitutive laws for this type of material, namely the Mooney-Rivlin and the Skalak laws, respectively, was contrasted to that of a membrane obeying a Hookean type constitutive law, namely the Kelvin-Voigt law, and to that of free bubbles. It was shown that, for acoustic disturbances with amplitudes ϵ as low as 0.5, membranes can behave in a quite different fashion than expected on the basis of a Hookean type law. In particular, strain-softening membranes produce an increasing scattering cross section, figure V.5(c), as the amplitude of acoustic disturbance increases while exhibiting a lower resonance frequency. This is a result of their increased active scatter at large deviations from equilibrium, which is a side effect of the reduction in their effective area dilatation modulus at large external stresses, that allows for larger membrane displacements than expected based on a Hookean type behavior. Thus, as the amplitude of sound increases MR membranes scatter significantly more echo than KV membranes due to the intensification of their active scatter, figures V.5(c) vs. V.5(b). In addition, such membranes are characterized by higher harmonic content in their scatter, which makes them more amenable to nonlinear imaging techniques. This may entail the onset of shape oscillations, which will also enrich the frequency spectrum. In order for effects of this nature to be captured the assumption of spherosymmetric oscillations should be relaxed.

On the contrary membranes consisting of strain hardening material produce more intense echo than KV membranes at moderate amplitudes and at a larger resonance frequency, which may be quite significant as the degree of hardness

increases. However, as the amplitude of sound increases the scattering cross section from SK membranes decreases and may even become comparable with that from KV membranes, which exhibit a slight increase in their back-scatter with increasing amplitude of sound at very large amplitudes, figure V.5(d) vs. V.5(b). This is again a result of the interplay between the change in active scatter and effective area dilatation modulus, in comparison with the effect of the external disturbance. Again the reduced deviation from equilibrium, due to the massive increase in elastic modulus at large amplitudes, dominates the microbubble dynamics leading to a significant reduction in active scatter despite the more efficient storage of elastic energy. Such membranes basically scatter on the fundamental frequency only, owing to their relatively smaller deformation and velocity compared to Hookean or strain softening membranes.

It should also be stressed that for spherically symmetric pulsations it is the area dilatation modulus that determines microbubble dynamics, i.e. parameter $K=G_s(2C+1)$ for SK membranes, which deviates from the value obtained for a Hookean or a MR membrane at small acoustic disturbances, i.e. $K=3G_s$, when $C \neq 1$. Nevertheless, in the absence of shear, the set of measurements that is typically carried out in order to estimate G_s and μ_s , i.e. sound attenuation and scattering cross section measurements, is enough to fit K for either type of membrane under isotropic tension, as long as it is made at the appropriate range of low sound amplitudes. Parameter b is not expected to change things dramatically for MR membranes whereas parameter C is incorporated in K for SK membranes.

This behavior may explain certain findings of experimental investigations³⁸ with contrast agents encapsulated by a membrane consisting of a lipid bi-layer, e.g. Definity, where a reduction in the backscatter was recorded with increasing peak negative pressure before it turned and started increasing at very large amplitudes, probably due to membrane rupture and formation of a free bubble. The membrane surrounding red blood-cells also consists of a lipid bi-layer and is known to be strain hardening by nature. Consequently, incorporating a strain hardening constitutive law in the microbubble model, when the pulsations of Definity are studied, may better explain the dependence of its scattering cross section on peak negative pressure at moderately large amplitudes. In a different context Sarkar et al.⁴⁷ employed a number of the available contrast agent models in order to match experimental measurements of the fundamental and the subharmonic scatter from a Sonazoid solution. In that study the constant elasticity model fails to capture the plateau in the subharmonic scatter exhibited by the measurements at very large sound amplitudes, $\epsilon \sim 10$, whereas the Church-Hoff model underpredicts the subharmonic measurements and cannot satisfactorily capture the plateau in the two signals. The authors attribute part of the failure to the softening of the membrane leading to higher amounts of scatter than expected based on the Church-Hoff model, which is not strictly valid when large membrane displacements are present. We carried out a number of scattering calculations using the values for $G_s \approx 52$ MPa and $\mu_s \approx 0.99$ Pa s obtained in the above study for Sonazoid by fitting the Church-Hoff model to low amplitude sound attenuation data; $R_0 = 1.6$ μm . Figures 7a,d and 8a,d from the above study are reproduced, Figures V.18a,b,c,d in the present study, with the addition of the curve corresponding to the strain softening membrane model presented here with $b=0$. The latter model predicts the fundamental and subharmonic signals quite well and for the entire range of sound amplitudes, for relatively large forcing frequencies, $\omega_f \geq 2\pi$ 4.4 MHz which is also the resonance frequency for the bubble size used in the sample under examination; see also Figs V.18c,d. For lower values of the forcing

frequency the model with the strain softening membrane is qualitatively correct but tends to over-predict the two signals; see Figs V.18a,b. This failure may be attributed to errors in the estimation of G_s , perhaps due to the fact that the attenuation data were not acquired at low enough amplitudes for the fitting to be valid, to bubble size distribution effects or, more importantly to variations in membrane viscosity as a result of the high frequency of the acoustic disturbance. Namely, a large number of polymeric materials exhibit a shear thinning behavior when subjected to high frequency disturbances due to disentanglement of the polymer chains. Consequently, the membrane material is expected to exhibit a higher viscosity as low frequencies, which may account for the systematic over-prediction of the two signals at low frequencies by the model presented here.

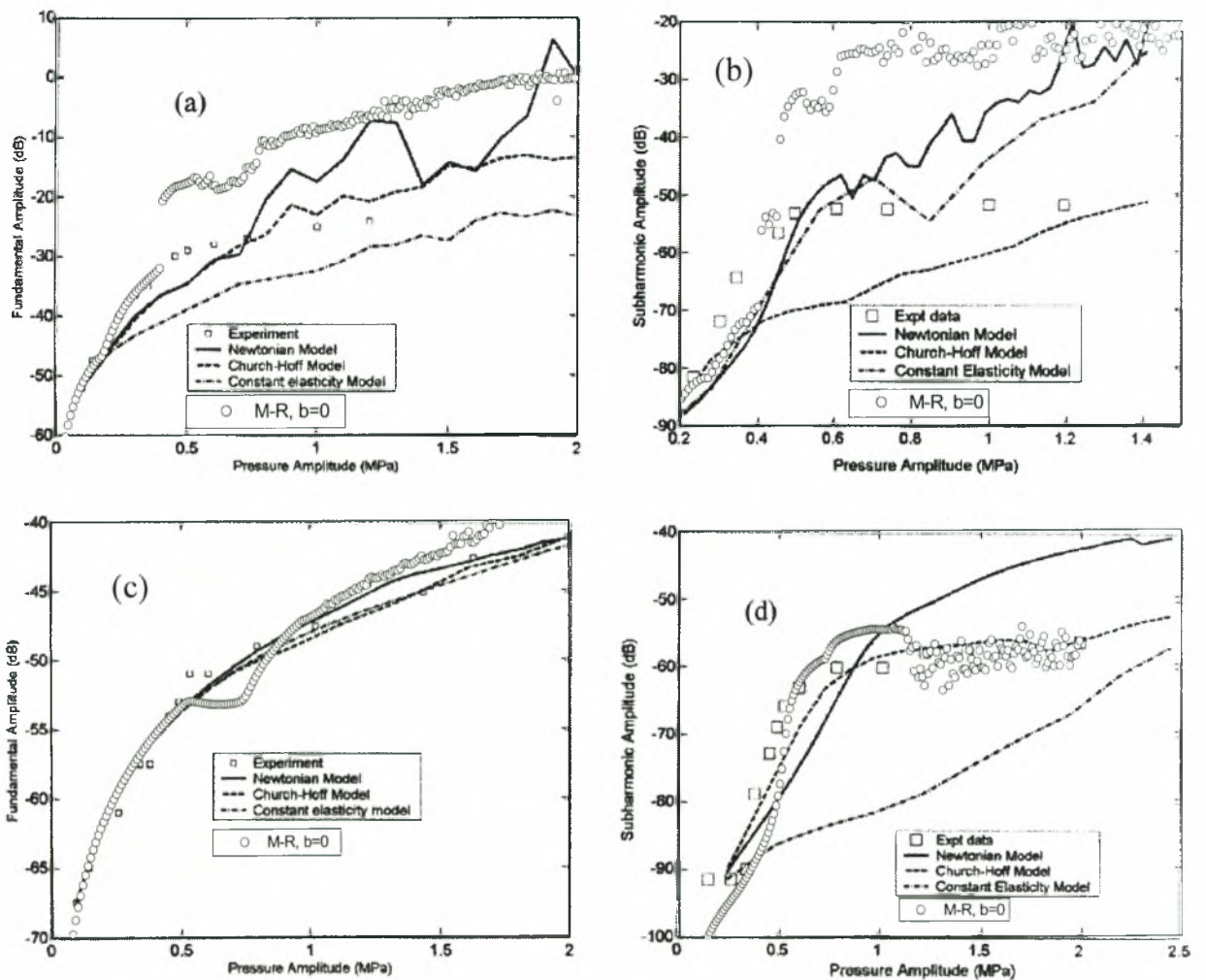


Figure V.18. Comparison between experimental measurements and predictions based on the Church-Hoff, the constant elasticity, the Newtonian and the strain softening model, of the fundamental and subharmonic signals when (a), (b) $\omega_f=2\pi 2$ MHz and (b), (d) $\omega_f=2\pi 4.4$ MHz, for Sonazoid microbubbles. The data from experimental measurements as well as the predictions from the Church-Hoff, the constant elasticity and the Newtonian models are reproduced from Sarkar et al.⁴⁷

In certain low MI perfusion imaging techniques a single harmonic component signal is preferred. Of course this is the case provided that the membrane stays in tact and does not rupture as the amplitude of the acoustic disturbance increases. Membrane rupture does happen, either due to buckling⁵² during compression or due to excessive tensile stress³³ during expansion; hence establishing the range of cohesion for such pulsating micro-bubbles is a prerequisite for possible applications. This process is bound to destroy spherosymmetry, which becomes too severe an assumption in understanding micro-bubble break-up. As a first step in this direction as well as to describe shape oscillations a model of axisymmetric oscillations should be employed, including the effect of bending resistance in order to properly capture membrane buckling, and it will be the subject of a future study.

Based on the above, it should also be stressed that, apart from the effect of damping due to membrane viscosity, the weak scatter that is sometimes registered from encapsulated bubbles may also be attributed to the fact that the acoustic disturbance is out of resonance with the micro-bubbles, based on their size distribution. A reliable prediction of resonance frequency and scattered echo requires proper understanding of the membrane material mechanical properties. Failure to properly characterize the membrane material may lead to severe errors in the estimation of the resonance frequency as well as the rest of the important parameters of the micro-bubble response. The combined fluid-membrane interaction model presented here is a relatively simple extension of the models used in the literature, that requires estimation of only one additional parameter provided the strain hardening or strain softening nature of the membrane material is established. As discussed in the penultimate paragraph a similar approach for the membrane viscosity may also be needed in order to fully account for material degradation under the severe external disturbances present in modern applications involving microbubbles. Measurement of such material properties, as well as characterization studies of the viscoelastic properties of general complex fluids, are possible nowadays in surface science¹⁰⁷ and present a meaningful direction for future research in the field of contrast agents that may ultimately lead to optimal design of the micro-bubble encapsulating material.

CHAPTER VI

Axisymmetric oscillations and collapse of an encapsulated microbubble subject to acoustic disturbances

Controlling the cohesion of contrast agents is important in optimizing perfusion imaging but also drug delivery techniques. In order to gain understanding regarding its cohesion range, the large-amplitude axisymmetric oscillations and collapse of an encapsulated microbubble is examined theoretically and numerically. Thus, the stability of spherosymmetric pulsations to infinitesimal axisymmetric shape deformations is examined, in a manner similar to that previously employed for free bubbles⁶³. The elastic stresses that develop on the membrane due to the bending moments are accounted for, based on shell stability theory⁶⁴, and are determined by the scalar bending modulus, $k_{b, \text{dim}}$. This is a measure of the shell resistance to bending and is introduced as an additional parameter, due to the anisotropy of the membrane elasticity along the interface and perpendicular to it⁶⁵. Once this parameter is known the resonance frequencies for shape oscillations of the microbubble are predicted as well as conditions for break-up. The two constitutive laws that were employed in the spherosymmetric model are implemented here also.

Conditions for buckling are recovered using static considerations and are seen to be relevant only for slow compression studies or when the forcing frequency is much smaller than the eigenfrequency for volume pulsations of the micro-bubble. Dynamic considerations reveal two major instabilities in a manner analogous to the case with free bubbles. For given equilibrium radius the parametric instability is first obtained as the amplitude of acoustic disturbance crosses a certain threshold. It corresponds to subharmonic resonance between the forcing frequency and the resonance frequencies of shape harmonics. As the amplitude of sound is further increased dynamic buckling occurs, evolving in a much shorter time scale. It can be viewed as the equivalent of Rayleigh-Taylor instability discussed in the case of free bubbles. In this fashion it is possible to construct phase diagrams for an encapsulated microbubble that define the regions marking the onset of instability.

A numerical model was also developed, implementing a hybrid boundary-finite element method, in order to solve for the velocity potential and shape deformation of an axisymmetric encapsulated microbubble. Thus, the above instability modes were verified and interesting dynamic phenomena such as jet formation and break-up were captured. The jet formation is associated with P_2 growth via parametric instability. The details of the final stages of collapse during the jetting phenomenon could not be captured because of the appearance of an instability that is associated with growth of short waves due to the large shear tension q . Instability of higher modes leads to formation of multilobed structures. Such bubbles will probably break up as a result of excessive tensile strength at regions of high curvature.

VI.1 PROBLEM FORMULATION

We consider an encapsulated microbubble with mean equilibrium radius R_{eq} submerged in a Newtonian liquid of density ρ_l , dynamic viscosity μ_l and static pressure P'_s . The microbubble consists of ideal gas encapsulated in a viscoelastic membrane with infinitesimal thickness δ , in comparison with the radius, shear modulus G_s and dynamic viscosity μ_s , while it has no residual stresses at static equilibrium. The membrane material can be either strain softening or strain hardening. In the former case the membrane material is such that the effective elastic modulus decreases as strain deformation grows whereas the opposite is true for the latter type of membrane material. It is also assumed that the membrane has negligible density due to its small thickness and consequently inertia effects in the shell can be neglected. Thus the shell is taken to be at equilibrium at all times. It should be noted that throughout this study primed letters denote dimensional variables.

A sinusoidal pressure wave is imposed on the far field pressure characterized by an amplitude ε and a forcing frequency ω_f ,

$$P'_x = P'_s (1 + \varepsilon \cos \omega_f t') \quad (VI.1)$$

At equilibrium the fluid surrounding the microbubble is quiescent and the pressure inside the bubble is connected to that in the far field via the equation,

$$P'_G(t=0_-) - P'_s = \frac{2\sigma}{R} \quad (VI.2)$$

where σ the mean surface tension between internal gas-membrane and membrane-external liquid; σ will be very small for a viscoelastic membrane.

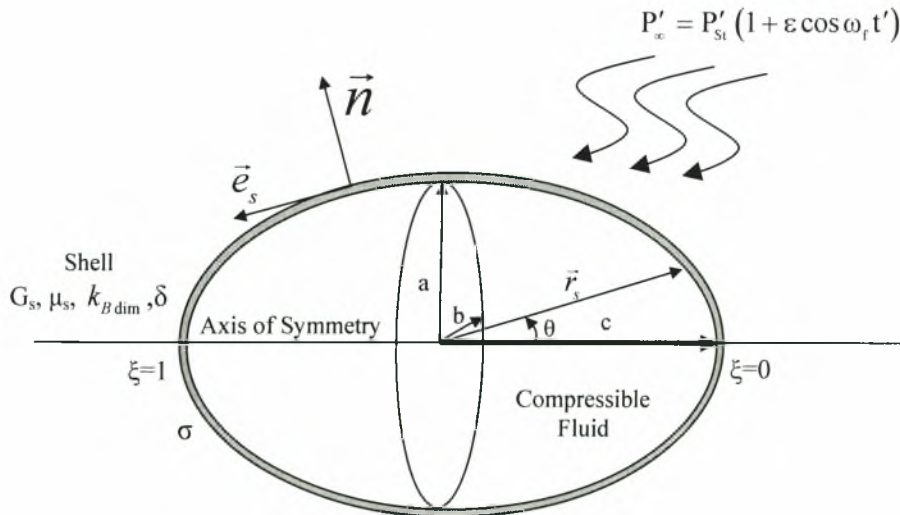


Figure VI.1: Geometrical configuration of an encapsulated microbubble in the context of the present study.

The shape of the bubble is assumed to be axisymmetric at all times, while the initial shape is that of an ellipsoid as the one considered in chapter II.1, figure VI.1. When $S=1$, the spherical shape is recovered whereas as S decreases the imposed elongation along the axis of symmetry becomes stronger. In the present analysis we will assume that the microbubble is of spherical shape initially, $S=1$. The external radius of the micro-bubble at equilibrium, R_{Eq} , is considered as the characteristic length of the problem. Since the timescale of micro-bubble oscillations is determined by the external forcing frequency, ω_f , the characteristic time of the problem is $\frac{1}{\omega_f}$ and subsequently the characteristic velocity, $\omega_f R_{Eq}$. Finally, the characteristic pressure is defined via the characteristic velocity as $\rho_l \omega_f^2 R_{Eq}^2$.

Considering incompressible flow the dimensionless equations governing the motion in the ambient fluid read as follows:

Continuity equation expressing the differential mass balance,

$$\vec{\nabla} \cdot \vec{V} = 0; \quad (VI.3)$$

Navier Stokes equations expressing the differential momentum balance

$$\frac{\partial \vec{V}}{\partial t} + \vec{V} \cdot \vec{\nabla} \vec{V} = -\vec{\nabla} P + \frac{1}{\text{Re}_l} \nabla^2 \vec{V}, \quad (VI.4)$$

where the effect of gravity is dropped due to the small size of the bubbles.

Quiescent flow conditions in the far field,

$$\vec{r} \rightarrow \infty: \quad \vec{V} \rightarrow 0, \quad P \rightarrow P_\infty = P_{St}. \quad (VI.5a,b)$$

Due to negligible density and kinematic viscosity of the gas inside the bubble we take the bubble pressure to be uniform and drop the deviatoric part of the stress tensor on the side of the gas inside the bubble. In addition, owing to the very short time frame over which the phenomena that are investigated in the present study evolve, we can neglect heat transfer to and from the surrounding liquid, to a first approximation, and consider adiabatic or isothermal oscillations. Consequently the variation of the bubble pressure with time is given by

$$P_G(t=0) \left(\frac{4}{3} \pi \right)^\gamma = P_G(t) V_G^\gamma(t), \quad (VI.6)$$

where γ denotes the polytropic constant, $1 \leq \gamma \leq 1.4$, and V_G the dimensionless instantaneous volume of the bubble; for an adiabatic process $\gamma=1.4$.

VI.1.1 The Lagrangian representation of the microbubble interface

In an effort to capture more complicated bubble shapes for which Eulerian description would be multi-valued, we adopt the Lagrangian formulation for the description of the motion of particles occupying the bubble's interface. ξ is a Lagrangian coordinate that identifies particles on the interface and is related to the arclength, s , of the interface by

$$\frac{\partial s}{\partial \xi} = (r_\xi^2 + r^2 \theta_\xi^2)^{1/2}, \quad 0 \leq \xi \leq 1; \quad (VI.7)$$

ξ as a subscript denotes partial differentiation. The kinematic condition forcing points on the surface to move with the fluid velocity is given by

$$\dot{\vec{r}} = \dot{\vec{r}}_d : \frac{d\vec{r}_d}{dt} = \vec{V}, \quad (\text{VI.8})$$

where \vec{r}_d denotes the position vector of a material point on the surface of the bubble;

Taking into account the definition of the position vector, $\vec{r}_d = r \vec{e}_r$, (VI.9)

and the normal and tangential vector to the interface,

$$\vec{n} = \frac{r\theta_s}{\sqrt{r_s^2 + r^2\theta_s^2}} \vec{e}_r - \frac{r_s}{\sqrt{r_s^2 + r^2\theta_s^2}} \vec{e}_\theta \quad (\text{VI.10a,b})$$

$$\vec{e}_s = \frac{r_s}{\sqrt{r_s^2 + r^2\theta_s^2}} \vec{e}_r + \frac{r \cdot \theta_s}{\sqrt{r_s^2 + r^2\theta_s^2}} \vec{e}_\theta$$

we obtain the two kinematic conditions to the interface

$$\left. \frac{dr}{dt} \right|_{r_0, \theta_0} = \frac{\Phi_\xi r_\xi + \frac{\partial \Phi}{\partial n} r \theta_\xi \sqrt{r_\xi^2 + r^2 \theta_\xi^2}}{r_\xi^2 + r^2 \theta_\xi^2}, \quad \left. \frac{d\theta}{dt} \right|_{r_0, \theta_0} = \frac{\Phi_\xi \theta_\xi r - \frac{\partial \Phi}{\partial n} r_\xi \sqrt{r_\xi^2 + r^2 \theta_\xi^2}}{r(r_\xi^2 + r^2 \theta_\xi^2)}; \quad (\text{VI.11a,b})$$

subscripts s and ξ denote differentiation along the interface and $\Phi, \frac{\partial \Phi}{\partial n}$ are the scalar potential and the normal velocity on the interface, respectively. The above two equations ensure continuity of velocities at the interface with $r_0(\xi, 0), \theta_0(\xi, 0)$ and $r(\xi, t), \theta(\xi, t)$ denoting spherical coordinates of the particles initially and after time t has elapsed, respectively; $\xi = \theta_0/\pi$ is a Lagrangian variable that identifies different particles.

VI.1.2 Interfacial Force Balance: Coupling of Hydrodynamic and Elastic forces

The force balance on the interface reads as:

$$\vec{r} = \vec{r}_s : \left(-PI + \frac{1}{\text{Re}_l} \underline{\underline{\tau}} \right) \cdot \vec{n} + P_G \vec{n} = \frac{2k_m}{We} \vec{n} + \overline{\Delta F} = \frac{(\vec{\nabla}_s \cdot \vec{n}) \vec{n}}{We} + \overline{\Delta F}, \quad (\text{VI.12})$$

where \vec{n} denotes the inwards pointing unit normal vector with respect to the fluid surrounding the bubble, figure VI.1, $\vec{\nabla}_s, k_m$, denote the surface gradient and mean curvature on the bubble's interface, respectively, and $\underline{\underline{\tau}} = \frac{\partial V_i}{\partial x_j} + \frac{\partial V_j}{\partial x_i}$, the unit and

deviatoric stress tensor, respectively; $\overline{\Delta F}$ denotes the resultant force due to the elastic stresses on the membrane, $We = \frac{\rho_l \omega_f^2 R_{Eq}^3}{\sigma}$ is the Wember number which compares

inertia with capillarity and $\text{Re}_l = \frac{\rho \omega_f R_{Eq}^2}{\mu_l}$ is the Reynolds number which compares inertia with viscous forces of the external liquid.

If we consider a microbubble with radius as small as $R_{eq} \approx 1.5 \mu\text{m}$, water as the host liquid, density $\rho=1000 \text{ kg/m}^3$ and dynamic viscosity $\mu_l \approx 0.001 \text{ kg/(m}\cdot\text{s)}$, which is insonated by a pressure wave with forcing frequency $\nu_f=2.4 \text{ MHz}$, then the resultant $\text{Re}_l \approx 34$. This means that we can neglect viscous effects to a first approximation, especially since it has been shown (see previous chapter but also reference [42]) that shell viscosity represents the dominant damping mechanism for pulsating microbubbles. To this end we consider that $\text{Re}_l \rightarrow \infty$ and that the external flow field is irrotational, in which case we can employ potential theory,

$$\vec{V} = \vec{\nabla}\Phi. \quad (\text{VI.13})$$

Combining the above equation with continuity we recover the well-known result that the scalar velocity potential satisfies the Laplace equation,

$$\nabla^2\Phi = 0 \quad (\text{VI.14})$$

Following Pelekasis & Tsamopoulos⁶⁶, we recast the Laplace equation in an integral form involving quantities evaluated at the interface, i.e. we introduce the boundary integral formulation of the Laplace equation:

$$-\Phi(\hat{r}, \hat{\theta}, t) + \int_0^1 \left[\Phi(r, \theta, t) - \Phi(\hat{r}, \hat{\theta}, t) \right] \frac{\partial G}{\partial n}(\hat{r}, \hat{\theta}, r, \theta) r \sin \theta (r_\xi^2 + r^2 \theta_\xi^2)^{1/2} d\xi = \int_0^1 \frac{\partial \Phi}{\partial n}(r, \theta, t) G(\hat{r}, \hat{\theta}, r, \theta) r \sin \theta (r_\xi^2 + r^2 \theta_\xi^2)^{1/2} d\xi \quad (\text{VI.15})$$

where hatted coordinates, \hat{r} , $\hat{\theta}$, depend on the location of the field point $\hat{\xi}$ and are not subject to integration. The above equation relates the scalar velocity potential to its normal derivative at the interface and can be obtained by applying Green's third identity on the Laplace equation and allowing the field point, where the potential is evaluated, to approach the interface. G and $\partial G/\partial n$ denote the axisymmetric free space singular kernel of the Laplace equation and its normal derivative, respectively. The latter possesses a non-integrable $1/p$ singularity, with p denoting the distance between the source and field points on the bubble's interface. The difference between the values of the potential at the field and source points has been introduced in equation (VI.15) in order to circumvent this singularity⁷². It should also be pointed out that the integrals in equation (VI.15) are line integrals along the instantaneous generating curve of the axisymmetric interface between the bubble and the surrounding fluid.

As $\text{Re}_l \rightarrow \infty$ the normal and tangential force balance on the interface are derived by equation (VI.12),

$$\text{Normal force balance: } P_G - P = \frac{2k_m}{We} + \Delta F_n \quad (\text{VI.16})$$

$$\text{Tangential force balance: } \vec{e}_s \cdot \frac{1}{\text{Re}_l} \underline{\underline{\tau}} \cdot \vec{n} = \Delta F_t \approx 0 \quad (\text{VI.17})$$

$$\text{where } \overline{\Delta F} = \Delta F_n \vec{n} + \Delta F_t \vec{e}_s = -\vec{\nabla}_s \cdot \underline{\underline{T}} \quad (\text{VI.18})$$

Equations (VI.16) and (VI.17) ensure continuity of forces that are applied on the interface. In equation (VI.18)

$\vec{\nabla}_s = \sum_{i=1}^2 \vec{a}'^i \frac{\partial}{\partial u_i}$ $i=1,2$ denotes the surface gradient operator⁹², $\vec{a}_i = \frac{\partial \vec{r}_s}{\partial u_i}$, $i=1,2$ and

$\vec{a}'^i = \frac{(-1)^i (\vec{a}_j \times \vec{n})}{|\vec{a}_1 \cdot \vec{a}_2 \times \vec{n}|}$, $i, j=1,2$ $i \neq j$ are the covariant and contravariant basis vectors,

respectively, while

$$\underline{\underline{T}} = \underline{\underline{\tau}} + \vec{q}\vec{n} \quad (\text{VI.19})$$

denotes the complete interface tension tensor; $\underline{\underline{\tau}}$ denotes the in-plane visco-elastic tension tensor and $\vec{q}\vec{n}$ the transverse shear tensor which gives the shear tensions due to the developed bending moments⁶¹.

The shear tension vector \vec{q} is related with the tensor of bending moments $\underline{\underline{m}}$,

$$\vec{q} = \vec{\nabla}_s \cdot \underline{\underline{m}} \cdot (\underline{\underline{I}} - \vec{n}\vec{n}) \quad (\text{VI.20a})$$

while for the antisymmetric part of the in-plane tension tensor

$$\underline{\underline{\tau}} - \underline{\underline{\tau}}^T = (\vec{\nabla}_s \vec{n}) \cdot \underline{\underline{m}} - \underline{\underline{m}}^T \cdot (\vec{\nabla}_s \vec{n}) \quad (\text{VI.20b})$$

Equations (VI.20a,b) represent the torque balance in a differential element of the membrane⁶¹.

The pressure and velocity fields satisfy Bernoulli's equation,

$$\frac{\partial \Phi}{\partial t} + \frac{1}{2} |\nabla \Phi|^2 + P = P_\infty, \quad (\text{VI.21})$$

which in conjunction with the normal force balance at the interface, equation (VI.16), provide the dynamic condition describing the evolution of the velocity potential on the bubble surface,

$$\frac{D\Phi}{Dt} = \frac{1}{2} \left[\left(\frac{\partial \Phi}{\partial n} \right)^2 + \frac{\Phi_\xi^2}{r_\xi^2 + r^2 \theta_\xi^2} \right] + P_\infty - P_G + \frac{2k_m}{We} + \Delta F_n \quad (\text{VI.22})$$

In the above equation

$$\frac{D\Phi}{Dt} = \frac{\partial \Phi}{\partial t} + \vec{u} \cdot \vec{\nabla} \Phi = \frac{\partial \Phi}{\partial t} + |\vec{u}|^2 \quad (\text{VI.23})$$

Owing to axisymmetry the derivatives with respect to ξ should satisfy the following conditions:

$$\frac{\partial r}{\partial \xi} = \frac{\partial \Phi}{\partial \xi} = \frac{\partial^2 \Phi}{\partial \xi \partial n} = \frac{\partial^2 \theta}{\partial \xi^2} = 0, \quad \text{at } \xi = 0,1 \quad (\text{VI.24})$$

corresponding to the two poles of the coordinate system.

VI.1.3 Interfacial tensions and bending moments

The Cartesian curvature tensor is defined⁶¹ as $\underline{\underline{B}} \equiv \bar{\nabla}_s \bar{\mathbf{n}}$, the components of which are $b_{ij} = \bar{\mathbf{a}}_i \cdot \underline{\underline{B}} \cdot \bar{\mathbf{a}}_j$, $i, j = 1, 2$ represented to the basis $[\bar{\mathbf{a}}_1, \bar{\mathbf{a}}_2, \bar{\mathbf{n}}]$. Tensor $\underline{\underline{B}}$ is 2x2 symmetric matrix. To diagonalize and find the principal curvatures, the following eigenproblem must be solved,

$$\underline{\underline{B}} \cdot \bar{\mathbf{t}}_i = k_i \cdot \bar{\mathbf{t}}_i, i = 1, 2 \quad (\text{VI.25})$$

where k_i are the principal curvatures and $\bar{\mathbf{t}}_i$ the corresponding eigenvectors represented in the $\bar{\mathbf{a}}$ system. When the shape of the interface, the elastic tensions and the bending moments are axisymmetric, this results in $\bar{\mathbf{t}}_1 = \bar{\mathbf{e}}_s, \bar{\mathbf{t}}_2 = \bar{\mathbf{e}}_\varphi$, where

$$k_1 = k_s = \frac{r_\xi^2 \theta_\xi}{\left((r\theta_\xi)^2 + r_\xi^2 \right)^{3/2}} + \frac{rr_\xi \theta_{\xi\xi} - rr_{\xi\xi} \theta_\xi}{\left((r\theta_\xi)^2 + r_\xi^2 \right)^{3/2}} + \frac{\theta_\xi}{\left((r\theta_\xi)^2 + r_\xi^2 \right)^{1/2}} \quad (\text{VI.26a,b})$$

$$k_2 = k_\varphi = \frac{\theta_\xi}{\left((r\theta_\xi)^2 + r_\xi^2 \right)^{1/2}} - \frac{r_\xi \cot(\theta)}{r \left((r\theta_\xi)^2 + r_\xi^2 \right)^{1/2}}$$

while the mean curvature is simply $k_m = \frac{k_1 + k_2}{2}$. Thus, the principal directions of $\underline{\underline{\tau}}$ and $\underline{\underline{m}}$ coincide⁶¹ with the axisymmetric unit vectors,

$$\underline{\underline{\tau}} = \tau_{ss} \bar{\mathbf{e}}_s \bar{\mathbf{e}}_s + \tau_{\varphi\varphi} \bar{\mathbf{e}}_\varphi \bar{\mathbf{e}}_\varphi, \underline{\underline{m}} = m_s \bar{\mathbf{e}}_s \bar{\mathbf{e}}_s + m_\varphi \bar{\mathbf{e}}_\varphi \bar{\mathbf{e}}_\varphi \quad (\text{VI.27a,b})$$

while the vectorial transverse shear tension lies in the meridional plane⁶¹ and is given by $\bar{\mathbf{q}} = q \bar{\mathbf{e}}_s$.

Substituting the expressions (VI.27a,b), (VI.28) and (VI.19) into (VI.18),(VI.20) we find

$$\begin{aligned} \bar{\Delta F} &= \Delta F_N \bar{\mathbf{n}} + \Delta F_t \bar{\mathbf{e}}_s = \\ &= \left[k_s \tau_{ss} + k_\varphi \tau_{\varphi\varphi} - \frac{1}{\sigma} \frac{\partial}{\partial s} (\sigma q) \right] \bar{\mathbf{n}} - \left[\frac{\partial \tau_{ss}}{\partial s} + \frac{1}{\sigma} \frac{\partial \sigma}{\partial s} (\tau_{ss} - \tau_{\varphi\varphi}) + k_s q \right] \bar{\mathbf{e}}_s \end{aligned} \quad (\text{VI.29})$$

$$q = \frac{1}{\sigma} \frac{\partial \sigma}{\partial s} \left[\frac{\partial}{\partial \sigma} (\sigma m_s) - m_\varphi \right] \quad (\text{VI.30})$$

with $\sigma = r \sin \theta$. Equations (VI.29) and (VI.30) are in agreement with the classical equations of axisymmetric membrane theory derived in surface curvilinear coordinates⁶⁴. From equation (VI.29) it can be deduced that

$$\Delta F_N = k_s \tau_{ss} + k_\varphi \tau_{\varphi\varphi} - \frac{1}{\sigma} \frac{\partial}{\partial s} (\sigma q) \quad (\text{VI.31a,b})$$

$$\Delta F_t = -\frac{\partial \tau_{ss}}{\partial s} - \frac{1}{\sigma} \frac{\partial \sigma}{\partial s} (\tau_{ss} - \tau_{\varphi\varphi}) - k_s q$$

VI.1.4 Constitutive Equations for elastic tensions

Most materials do not respond to external forces in a linear fashion. Rather, they exhibit a non-linear stress strain relation at large deformations. Two very common families of materials characterized by nonlinear response are strain softening and strain hardening materials. In the former case the membrane material is such that the effective elastic modulus decreases as strain deformation grows whereas the opposite is true for the latter type of membrane materials. In the following we present the governing equations for the mechanical behavior of a viscoelastic membrane at equilibrium, taken to be infinitesimally thin in comparison with the radius as is normally the case with contrast agents used in ultrasound diagnostic imaging, for different types of nonlinear response. Following [93] we use general Cartesian co-ordinates for the representation of the surface displacement gradient, $\underline{\underline{A}}$,

$$\underline{\underline{A}} = (\underline{\underline{I}} - \bar{n}\bar{n}) \cdot \frac{\partial \bar{\mathbf{x}}}{\partial \bar{\mathbf{X}}} \cdot (\underline{\underline{I}} - \bar{\mathbf{N}}\bar{\mathbf{N}}) \quad (\text{VI.32})$$

where $\bar{\mathbf{x}}$, $\bar{\mathbf{X}}$ denote the position vector of a membrane point in the deformed and a reference unstressed state and similarly for the normal vectors $\bar{\mathbf{n}}$, $\bar{\mathbf{N}}$. The tensor $\underline{\underline{A}}^T \cdot \underline{\underline{A}}$ has two non zero eigenvalues, λ_1^2, λ_2^2 , that correspond to local principal axes of deformation in the tangential membrane plane and represent the principal extension ratios along the same axes,

$$\lambda_i = \frac{ds_i}{dS_i}, \quad \text{indices are not summed,} \quad (\text{VI.33})$$

where ds_i and dS_i indicate lengths of line elements in each one of the principal directions in the deformed and the referenced state. In the case of axisymmetry

$$\lambda_1 = \lambda_s = \frac{S_\xi(t)}{S_\xi(t=0)}, \quad \lambda_2 = \lambda_\varphi = \frac{\sigma(t)}{\sigma(t=0)} \quad (\text{VI.34a,b})$$

Upon introduction of the Green-Lagrange surface deformation tensor, $\underline{\underline{e}}$, defined as

$$\underline{\underline{e}} = \frac{1}{2} \left[\underline{\underline{A}}^T \cdot \underline{\underline{A}} - (\underline{\underline{I}} - \bar{\mathbf{N}}\bar{\mathbf{N}}) \right], \quad (\text{VI.35})$$

the ratio J_s between the deformed and undeformed local surface area, and the 2d strain invariants⁴⁸ can also be defined as,

$$J_s = \lambda_1 \lambda_2 = \sqrt{\det(\underline{\underline{A}}^T \cdot \underline{\underline{A}} + \bar{N}\bar{N})}, \quad (\text{VI.136})$$

$$I_1 = 2\text{tr}(\underline{\underline{e}}) = \lambda_1^2 + \lambda_2^2 - 2, \quad I_2 = J_s^2 - 1 = \lambda_1^2 \lambda_2^2 - 1.$$

The two invariants, I_1 , I_2 , denote the elongation of a local line element and the local area dilatation, respectively. Once the above quantities are known the principal components of the elastic tension tensor on a deformed two-dimensional membrane can be related to the deformation tensor via the strain energy function $w(I_1, I_2)^{50}$,

$$\underline{\underline{\tau}} = \frac{2}{J_s} \left[\frac{\partial w}{\partial I_1} \underline{\underline{A}} \cdot \underline{\underline{A}}^T + \frac{\partial w}{\partial I_2} J_s^2 (\underline{\underline{I}} - \bar{N}\bar{N}) \right]. \quad (\text{VI.137})$$

The strain energy $w(I_1, I_2)$ depends on the nature of the membrane material and assumes different forms as the mechanical behavior of the membrane changes. A typical strain energy describing a very thin sheet of an isotropic volume incompressible rubber-like material with strain softening behavior, is the one provided by the two-dimensional Mooney-Rivlin (MR) law⁹⁴,

$$w^{\text{MR}} = \frac{E}{6} \left[(1-b) \left(I_1 + 2 + \frac{1}{I_2 + 1} \right) + b \left(\frac{I_1 + 2}{I_2 + 1} + I_2 + 1 \right) \right] \quad (\text{VI.138a})$$

$$\tau_{ss}^{\text{MR}} = \frac{E}{3\lambda_s \lambda_\varphi} \left(\lambda_s^2 - \frac{1}{(\lambda_s \lambda_\varphi)^2} \right) \left[1 + b(\lambda_s^2 - 1) \right] \quad (\text{VI.138b})$$

$$\tau_{\varphi\varphi}^{\text{MR}} = \frac{E}{3\lambda_s \lambda_\varphi} \left(\lambda_\varphi^2 - \frac{1}{(\lambda_s \lambda_\varphi)^2} \right) \left[1 + b(\lambda_s^2 - 1) \right]$$

with E the dimensionless parameter which is defined by $E = \frac{3G_s \delta}{\rho \omega_f^2 R_{Eq}^3}$; The case with

$b=0$ corresponds to a neo-Hookean membrane whereas as b , which ranges between 0 and 1, tends to zero the membrane becomes softer. It should also be noted that the Mooney-Rivlin constitutive law allows for unrestricted area dilatation that is compensated by progressive thinning of the membrane.

One of the most widely used constitutive laws pertaining to strain hardening membranes is the one developed by Skalak et al.⁴⁸ in order to model the lipid bi-layer structure surrounding the red blood-cell,

$$w^{\text{SK}} = \frac{E}{6} (I_1^2 + 2I_1 - 2I_2 + CI_2^3), \quad (\text{VI.139a})$$

$$\tau_{ss}^{\text{SK}} = \frac{E}{3\lambda_s \lambda_\varphi} \left\{ \lambda_s^2 (\lambda_s^2 - 1) + C (\lambda_s \lambda_\varphi)^2 \left[(\lambda_s \lambda_\varphi)^2 - 1 \right] \right\} \quad (\text{VI.139b})$$

$$\tau_{\varphi\varphi}^{\text{SK}} = \frac{E}{3\lambda_s \lambda_\varphi} \left\{ \lambda_\varphi^2 (\lambda_\varphi^2 - 1) + C (\lambda_s \lambda_\varphi)^2 \left[(\lambda_s \lambda_\varphi)^2 - 1 \right] \right\}$$

Parameter C in the above equations is always positive and controls the extent of area incompressibility of the membrane. In the case of red blood-cells $C \gg 1$ in order to accommodate the almost incompressible nature of the membrane area. Nevertheless, this is a quite general law that is used for strain hardening membranes whether they are

area incompressible or not. Membrane viscosity can also be accounted for via a linear Newtonian term that is added to the elastic stresses and involves the membrane velocity. Thus, for the case of an MR membrane we obtain

$$\tau_{ss}^{\text{MR}} = \frac{E}{3\lambda_s\lambda_\varphi} \left(\lambda_s^2 - \frac{1}{(\lambda_s\lambda_\varphi)^2} \right) \left[1 + b(\lambda_\varphi^2 - 1) \right] + \frac{2}{\text{Re}_s} \frac{1}{\lambda_s} \frac{\partial \lambda_s}{\partial t} \quad (\text{VI.40})$$

$$\tau_{\varphi\varphi}^{\text{MR}} = \frac{E}{3\lambda_s\lambda_\varphi} \left(\lambda_\varphi^2 - \frac{1}{(\lambda_s\lambda_\varphi)^2} \right) \left[1 + b(\lambda_s^2 - 1) \right] + \frac{2}{\text{Re}_s} \frac{1}{\lambda_\varphi} \frac{\partial \lambda_\varphi}{\partial t}$$

where $\frac{1}{\lambda_s} \frac{\partial \lambda_s}{\partial t}$, $\frac{1}{\lambda_\varphi} \frac{\partial \lambda_\varphi}{\partial t}$ are the first principal components of the surface rate of strain tensor⁵⁰ and Re_s the Reynolds number of the membrane which is defined by

$$\text{Re}_s = \frac{\rho\omega_j R_{Lq}^3}{\mu_{\text{MR}}}, \text{ with } \mu_{\text{MR}} = 3\delta\mu_s. \text{ A similar expression is obtained for a SK material.}$$

VI.1.5 Constitutive equations for bending moments

Constitutive equations for bending moments have been derived by previous authors working in curvilinear coordinates^{65,108}. One common assumption also adopted in the present study is that the bending moments have a negligible effect on the symmetric part of the elastic tensions given in (VI.37). This is correct for isotropic interfaces and small bending deformations (small changes of the cartesian curvature tensor \underline{B}), because then the bending moment tensor \underline{m} is symmetric and from equation (VI.20b), it comes that the antisymmetric part of $\underline{\tau}$ vanishes⁶¹. In the case of axisymmetry, Zarda et al⁶⁵ introduced the bending measures of strain

$$K_s \equiv \lambda_s k_s - k_s^R, K_\varphi \equiv \lambda_\varphi k_\varphi - k_\varphi^R \quad (\text{VI.41})$$

and invoked an analogy with the linear theory of bending of thin plates to derive the following expression for bending moments which in dimensionless form is written,

$$m_s = \frac{k_B}{\lambda_\varphi} (K_s + \nu K_\varphi), m_\varphi = \frac{k_B}{\lambda_s} (K_\varphi + \nu K_s) \quad (\text{VI.42})$$

where k_s^R, k_φ^R are the dimensionless reference curvatures in the principal directions

where the membrane is free of bending moments, $k_B = \frac{k_{B \text{ dim}}}{\rho\omega_j^2 R_{Lq}^5}$ is a dimensionless

parameter with $k_{B \text{ dim}}$ the scalar bending modulus in (Nm) and ν the Poisson ration; for a sphere $k_s^R = k_\varphi^R = 1$ and for an incompressible material $\nu=0.5$. If the membrane consists of a thin layer of a three dimensional elastic solid of thickness δ , then

$$k_{B \text{ dim}} = \frac{3G_s \delta^3}{12(1-\nu^2)} \quad (\text{VI.43})$$

When membranes that consist of inherently two-dimensional networks of polymers are considered $k_{B, \text{dim}}$ can be treated as an independent physical constant⁶¹.

VI.1.6 Energy variation

Following a similar procedure to that presented in section II.1.3, with the exception that now we use the dynamic boundary condition (VI.22), we obtain the energy balance for the dynamics of the microbubble

$$\frac{1}{2} \frac{d}{dt} \iint_A \Phi \frac{\partial \Phi}{\partial n} dA + \iint_A \frac{\partial \Phi}{\partial n} \left(P_\infty - P_G + \frac{2k_m}{We} + \Delta F_n \right) dA = 0 \quad (\text{VI.44})$$

The first integral signifies variations in the total kinetic energy while the second one represents variations of the energy due to pressure change inside the bubble, due to the elastic membrane energy and due to variations in the membrane area.

VI.2 NUMERICAL SOLUTION

Due to the use of potential theory in the present study the continuity of the velocities that are tangential to the interface is not satisfied. Therefore, we solve only equation (VI.11a) in order to calculate the new radius of the interfacial particles. On the other hand, we satisfy the continuity of the forces at the interface by solving both equations (VI.16) and (VI.17). In fact, we use equation (VI.17) in order to update the angle θ of the interfacial particles.

When shell viscosity is taken into account the terms $\left. \frac{dr_s}{dt} \right|_{r, \theta}$ and $\left. \frac{d\theta_s}{dt} \right|_{r, \theta}$ must be

calculated at each time-step. The first term is calculated directly through equation (VI.11a), in which case only first order spatial derivatives have to be calculated. The second term is calculated via backward differencing on the θ values obtained for each interface particle at each sub-step of the Runge-Kutta, by numerically solving (VI.17). This involves evaluation of spatial derivatives of third order, which has as consequence that as the simulation proceeds short wave instabilities arise, whose wavelength is on the order of minimum element size in a manner analogous to simulations of free bubbles when weak viscous effects are taken into account. Such short wave instabilities cannot be eliminated by mesh refinement alone. The standard procedure in order to circumvent this problem is to implement filtering of the higher modes while monitoring the energy of the system so that it is dissipated appropriately. Inviscid calculations do not exhibit such instabilities hence filtering is avoided. However, in all the simulations to be presented in the following with finite Re_s , after each time-step the term, $A = \left. \frac{d\theta_s}{dt} \right|_{r, \theta}$ is

filtered by introducing the fourth order derivative with respect to ξ ,

$$\frac{\partial A}{\partial t} = \lambda \frac{\partial^4 A}{\partial \xi^4}. \quad (\text{VI.45})$$

The above equation is discretized with the second order accurate fully implicit scheme,

$$A'_j = A_j + \frac{\lambda \Delta t}{\Delta \xi^4} (A'_{j+2} - 4A'_{j+1} + 6A'_j - 4A'_{j-1} + A'_{j-2}), \quad (\text{VI.46})$$

which possesses improved stability characteristics; $\lambda\Delta t / \Delta\xi^4$ was set to a large value, typically between 1 and 1000, for stability reasons.

The above notions were implemented via the following numerical algorithm. At a certain time instant the position of the interface is known, so the radius and the angle of each interfacial particle are known. From the constitutive equations for elastic tensions (VI.38b) or (VI.39b) and the constitutive equations for bending moments (VI.41) and (VI.42), we calculate the developed elastic tensions and bending moments on the membrane. Then taking into account the torque balance, equation (VI.30), the transverse shear tensions due to the bending moments are calculated. The pressure inside the bubble can be calculated through the microbubble volume at that moment and the adiabatic law, equation (VI.6). Then with the use of equation (VI.31a) we calculate the normal component of the forces on the membrane due to the developed tensions and bending moments. From the dynamic condition (VI.22) and the kinematic condition (VI.11a), using the finite element method for spatial discretization and the fourth order explicit Runge-Kutta method⁷² for integration in time, we calculate the new velocity potential and radial position of the interfacial particles. Then, from integral equation (VI.15), using the boundary element method, we calculate the new normal velocity on the interface, $\frac{\partial\Phi}{\partial n}$, while from the tangential force balance (VI.17) in conjunction with

equation (VI.31b) we find the new angle θ of the particles. In this fashion the location and velocity of the interface are updated and the procedure is repeated in time. At the end of each time-step of Runge-Kutta the term $A = \left. \frac{d\theta_s}{dt} \right|_{r,\theta}$ is filtered via equation

(VI.45). The time step is fixed and depends on the number of elements as well as the velocity of the interface. Actually, the time step varied from 10^{-4} till $5 \cdot 10^{-7}$. Typically, 60–200 elements are used for the discretization of the interface in the region $0 \leq \theta \leq \pi$. The entire method is similar to the one used for free bubbles in chapters II, III and IV, with the difference that here viscous effects in the host liquid are not accounted for, whereas emphasis is placed on the flow structure interaction aspect of the problem through the interfacial force balance where hydrodynamic forces from the surrounding fluid and viscoelastic forces due to the shell balance each other.

As the number of elements increases construction of the system matrix, which is full as is normally the case with the boundary integral methodology, becomes the most time consuming part of the computation taking up more than 80 % of the CPU time^{66,72}. In order to optimize computational speed we resort to parallel strategies. In particular, the system matrix is constructed in a parallel fashion with different processors dedicated to different rows of the matrix. The above numerical implementation is validated against mesh refinement and by monitoring the variation of the total energy of the system, equation (VI.44). Finally, the comparison with results of the linear theory of dynamic stability to axisymmetric disturbances constitutes an additional check for our calculations.

VI.3 STABILITY TO NONSPHERICAL DISTURBANCES

We consider a small initial deformation of the microbubble interface that is represented in spherical coordinates,

$$r_d = R(t) + \varepsilon w(\theta, t), \quad \theta_d = \theta + \varepsilon u(\theta, t) / R(t) + O(\varepsilon^2) \quad (\text{VI.47})$$

with $\varepsilon \ll 1$, $w(\theta, t)$ the dimensionless displacement in the radial direction towards the external liquid and $u(\theta, t)$ the dimensionless displacement to the azimuthal direction. r , θ denote the initial radial and azimuthal coordinates of the particles where subscript 0 has been dropped for simplicity.

The form of the asymptotic solution that we seek is

$$\vec{V} = \vec{V}^0 + \varepsilon \vec{V}^1 + O(\varepsilon^2) \quad (\text{VI.48a,b})$$

$$P = P^0 + \varepsilon P^1 + O(\varepsilon^2)$$

Substituting the above equations in the inviscid equations of motion (VI.3) and (VI.4), we obtain the equations of motion of the $O(1)$ problem,

$$\vec{\nabla} \cdot \vec{V}^0 = 0 \quad (\text{VI.49a,b})$$

$$\frac{\partial \vec{V}^0}{\partial t} + \vec{V}^0 \cdot \vec{\nabla} \vec{V}^0 = -\vec{\nabla} P^0$$

and the equations of motion of the $O(\varepsilon)$ problem,

$$\vec{\nabla} \cdot \vec{V}^1 = 0 \quad (\text{VI.50a,b})$$

$$\frac{\partial \vec{V}^1}{\partial t} + \vec{V}^0 \cdot \vec{\nabla} \vec{V}^1 + \vec{V}^1 \cdot \vec{\nabla} \vec{V}^0 = -\vec{\nabla} P^1$$

If we apply the expansion (VI.47) to the kinematic condition of the deformed interface

$$\vec{V} \cdot \vec{n} = -\frac{1}{|\nabla F|} \frac{\partial F}{\partial t}, \quad F \equiv r_d(\theta, t) - (R(t) + \varepsilon w(\theta, t) + O(\varepsilon^2)) \quad (\text{VI.51a,b})$$

and use domain perturbation¹¹¹ in order to expand the radial velocity of the interface

$$V_r|_{r=r_d} = V_r|_{r=R} + \frac{\partial V_r}{\partial r} \Big|_{r=R} \varepsilon w + O(\varepsilon^2) \quad (\text{VI.52})$$

we obtain the kinematic condition of the $O(1)$ problem

$$V_r^0 \Big|_{r=R(t)} = \frac{dR}{dt} \quad (\text{VI.53})$$

and the kinematic condition of the $O(\varepsilon)$ problem in the radial direction

$$\frac{\partial w}{\partial t} = V_r^1 \Big|_{r=R} + \frac{\partial V_r^0}{\partial r} \Big|_{r=R} w - \frac{1}{r} \frac{\partial w}{\partial \theta} V_\theta^0 \Big|_{r=R} + O(\varepsilon^2) \quad (\text{VI.54})$$

It should be emphasized that we don't have to satisfy the kinematic condition in the tangential direction because we employ potential flow on the liquid side. Upon applying expansion (VI.47) on the normal force balance of the deformed interface, equation (VI.16), and on equations (VI.26), (VI.30), (VI.31a), (VI.40), (VI.41), (VI.42), and taking into account that

$$P|_{r=r_d} = P|_{r=R} + \frac{\partial P}{\partial r} \Big|_{r=R} \varepsilon w + O(\varepsilon^2), \quad (\text{VI.55})$$

$$\lambda_s = R + \varepsilon \frac{\partial u}{\partial \theta} + \varepsilon w \quad (\text{VI.56})$$

$$\lambda_\varphi = R + \varepsilon u \cot(\theta) + \varepsilon w$$

we obtain the normal force balance of the $O(1)$ problem,

$$P_G^0 - P^0 \Big|_{r=R} = \frac{2k_m^0}{We} + \Delta F_N^0 = -P_{\text{Overpressure}} \quad (\text{VI.57})$$

$$\text{with } k_m^0 = \frac{1}{R} \quad (\text{VI.58})$$

$$\Delta F_N^{0,MR} = \frac{2E(R^6 - 1)(1 + bR^2 - b)}{3R^7} + \frac{4}{\text{Re}_s} \frac{\dot{R}}{R^2} \quad (\text{VI.59a,b})$$

$$\Delta F_N^{0,SK} = \frac{2E(R^2 - 1 + CR^6 - CR^2)}{3R} + \frac{4}{\text{Re}_s} \frac{\dot{R}}{R^2}$$

and the normal force balance of the $O(\varepsilon)$ problem

$$-P^1 \Big|_{r=R} - \frac{\partial P^0}{\partial r} \Big|_{r=R} w = \frac{2k_m^1}{We} + \Delta F_N^1 + O(\varepsilon^2) \quad (\text{VI.60})$$

$$\text{with } k_m^1 = -\frac{H(w) + 2w}{2R^2} \quad (\text{VI.61})$$

$$\begin{aligned} \Delta F_N^{1,MR} = & -\frac{E}{3R^8} \left\{ \begin{aligned} & H(w) [bR^8 + (1-b)R^6 - bR^2 + (b-1)] + \\ & H(\psi) [-2bR^8 - 4bR^2 + 6(b-1)] + \\ & w [-2bR^8 + 2R^6(1-b) - 10bR^2 + 14(a-1)] \end{aligned} \right\} + \\ & + \frac{2}{\text{Re}_s R^3} [RH(\dot{\psi}) - \dot{R}[H(\psi) + H(w)] + 2R\dot{w} - 4\dot{R}w] + \\ & + \frac{k_B}{R^4} [HH(w - \psi) + (1 - \nu)H(w - \psi)] \end{aligned} \quad (\text{VI.62a})$$

$$\begin{aligned} \Delta F_N^{1,SK} = & -\frac{E}{3R^2} \left\{ \begin{aligned} & H(w) [CR^6 - CR^2 + R^2 - 1] + \\ & H(\psi) [-6CR^6 + 2CR^2 - 2R^2] + \\ & w [2CR^2 - 10CR^6 - 2R^2 - 2] \end{aligned} \right\} + \\ & + \frac{2}{\text{Re}_s R^3} [RH(\dot{\psi}) - \dot{R}[H(\psi) + H(w)] + 2R\dot{w} - 4\dot{R}w] + \\ & + \frac{k_B}{R^4} [HH(w - \psi) + (1 - \nu)H(w - \psi)] \end{aligned} \quad (\text{VI.62b})$$

$$\text{with } u = \frac{\partial \psi}{\partial \theta} \text{ and}$$

$$\begin{aligned}
H(\cdot) &= \frac{\partial^2}{\partial \theta^2}(\cdot) + \cot(\theta) \frac{\partial}{\partial \theta}(\cdot) \\
HH(\cdot) &= \frac{\partial^2}{\partial \theta^2} \left(\frac{\partial^2}{\partial \theta^2}(\cdot) + \cot(\theta) \frac{\partial}{\partial \theta}(\cdot) \right) + \\
&+ \cot(\theta) \frac{\partial}{\partial \theta} \left(\frac{\partial^2}{\partial \theta^2}(\cdot) + \cot(\theta) \frac{\partial}{\partial \theta}(\cdot) \right)
\end{aligned} \tag{VI.63}$$

The last two operators are typically employed in classical axisymmetric shell theory⁶⁴ in order to simplify the algebra by utilizing the useful properties of the Legendre polynomials P_n ,

$$H(P_n) = -\lambda_n P_n, \quad HH(P_n) = \lambda_n^2 P_n, \quad \lambda_n = n(n+1) \tag{VI.64}$$

Finally, the tangential force balance, equation (VI.17), gives the tangential force balance of the $O(\varepsilon)$ problem. It must be stressed that the tangential force balance does not participate in the $O(1)$ problem because its terms are $O(\varepsilon)$ and above.

$$\Delta F_i^1 + O(\varepsilon^2) = 0 \tag{VI.65}$$

with

$$\begin{aligned}
\Delta F_i^{1,MR} &= -\frac{E}{3R^8} \left\{ \begin{aligned} &w_\theta [6 - 6b + 4bR^2 + 2bR^8] + \\ &\psi_\theta [-2bR^6 + 2R^6 - 3\lambda_n + 2bR^2 + bR^6 \lambda_n + \\ &3b\lambda_n - 3bR^2 \lambda_n - R^8 b \lambda_n - R^6 \lambda_n] \end{aligned} \right\} + \\
&+ \frac{2}{\text{Re}_s R^5} [-R(1 - \lambda_n) \dot{\psi}_\theta + \dot{R}(1 - \lambda_n) \psi_\theta - R \dot{w}_\theta + \dot{R} w_\theta] + \\
&+ \frac{k_B}{R^4} (w_\theta - \psi_\theta) (-\lambda_n + 1 - \nu)
\end{aligned} \tag{VI.66a}$$

$$\begin{aligned}
\Delta F_i^{1,SK} &= -\frac{E}{3R^2} \left\{ \begin{aligned} &w_\theta [2R^2 - 2CR^2 + 6CR^6] + \\ &\psi_\theta [\lambda_n - 2 - 3C\lambda_n R^6 + CR^2 \lambda_n + 4R^2 - 3R^2 \lambda_n] \end{aligned} \right\} + \\
&+ \frac{2}{\text{Re}_s R^3} [-R(1 - \lambda_n) \dot{\psi}_\theta + \dot{R}(1 - \lambda_n) \psi_\theta - R \dot{w}_\theta + \dot{R} w_\theta] + \\
&+ \frac{k_B}{R^4} (w_\theta - \psi_\theta) (-\lambda_n + 1 - \nu)
\end{aligned} \tag{VI.66b}$$

where the following identity has been used,

$$\frac{\partial^3}{\partial \theta^3}(\cdot) - (1 + \cot^2 \theta) \frac{\partial}{\partial \theta}(\cdot) + \cot(\theta) \frac{\partial^2}{\partial \theta^2}(\cdot) = -\lambda_n \frac{\partial}{\partial \theta}(\cdot) \tag{VI.67}$$

The $O(1)$ problem, (VI.49a,b), along with the kinematic condition (VI.53), the dynamic condition (VI.57), the far field condition $\vec{v}^0 = 0$, as $r \rightarrow \infty$ and the introduction of the scalar velocity potential $\vec{v}^0 = \nabla \Phi^0$ can be solved analytically. The

equation $\vec{V}^0 = \nabla\Phi^0$ in conjunction with the (VI.49a), the kinematic condition (VI.53) and $\vec{V}^0 = 0$, as $r \rightarrow \infty$ gives

$$V_\theta^0 = 0, \quad V_r^0 = \frac{R^2 \dot{R}}{r^2} \quad (\text{VI.68})$$

while (VI.49b) gives

$$P^0(r,t) = P_\infty(t) + \left[\frac{2R\dot{R}^2 + R^2\ddot{R}}{r} - \frac{R^4\dot{R}^2}{2r^4} \right], \quad R \leq r \leq \infty \quad (\text{VI.69})$$

Evaluation at $r=R$ and use of (VI.57) gives

$$R\ddot{R} + \frac{3}{2}\dot{R}^2 = P_G(t) - \frac{2k_m^0}{We} - \Delta F_N^0 - P_\infty(t) \quad (\text{VI.70})$$

with $P_G(t)$ given from (VI.6). Equation (VI.70) is a variation of the Rayleigh-Plesset equation and collapses on equations (V.22) or (V.24) for MR or SK membranes, respectively, if we set $M = 0$, $Re_i \rightarrow \infty$ and $u_0 = 0$.

The equations of the $O(\varepsilon)$ problem, (VI.50a,b), along with the kinematic condition (VI.54), the dynamic condition (VI.60), the tangential force balance (VI.65), the far field condition $\vec{V}^1 = 0$, as $r \rightarrow \infty$ and the introduction of the scalar potential $\vec{V}^1 = \nabla\Phi^1$, constitute a linear system in \vec{V}^1 , P^1 , w , ψ . To solve this system we consider that

$$\Phi^1 = \sum_{n=0}^{\infty} \frac{\Phi_n(t)}{r^{n+1}} P_n(\theta) \quad (\text{VI.71})$$

from the solution of the Laplace equation in spherical coordinates. so that $\vec{V}^1 = 0$, as $r \rightarrow \infty$

and

$$w = \sum_{n=0}^{\infty} w_n(t) P_n(\theta), \quad \psi = \sum_{n=0}^{\infty} \psi_n(t) P_n(\theta) \quad (\text{VI.72a,b})$$

Substituting in $\vec{V}^1 = \nabla\Phi^1$, using (VI.50a) and the kinematic condition (VI.54), we obtain a relation between $\Phi_n(t)$ and $w_n(t)$. Then, equation (VI.50b) and the dynamic condition (VI.60), provide the following equation for $w_n(t)$, $\psi_n(t)$.

$$\ddot{w}_n + \frac{3\dot{R}}{R} \dot{w}_n + \left[\frac{(1-n)\ddot{R}}{R} + \frac{(n+1)(n-1)(n+2)}{WeR^3} \right] w_n + \frac{n+1}{R} \Delta F_N^1(\dot{w}_n, \dot{\psi}_n, w_n, \psi_n, E, k_B, Re_s, R, \dot{R}, n) = 0 \quad (\text{VI.73a})$$

Finally, the system closes with the tangential force balance (VI.65),

$$\Delta F_t^1(\dot{w}_n, \dot{\psi}_n, w_n, \psi_n, E, k_B, Re_s, R, \dot{R}, n) = 0 \quad (\text{VI.73b})$$

For a microbubble of constant volume, $\dot{R} = \ddot{R} = 0$, (VI.73a,b) yield

$$\ddot{w}_n + \left[\frac{(n+1)(n-1)(n+2)}{WeR^3} \right] w_n + \frac{n+1}{R} \Delta F_N^1(\dot{w}_n, \dot{\psi}_n, w_n, \psi_n, E, k_B, Re_s, R, n) = 0$$

(VI.74a,b)

$$\Delta F_t^1(\dot{w}_n, \dot{\psi}_n, w_n, \psi_n, E, k_B, Re_s, R, n) = 0$$

Considering that w_n, ψ_n assume a solution of the form,

$$w_n(t) = \alpha_n e^{\omega_n t}, \quad \psi_n(t) = \beta_n e^{\omega_n t} \quad (VI.75a,b)$$

and substituting in (VI.74a,b), we obtain a system of the form

$$\underline{A}(E, k_B, Re_s, R, n, \omega_n) \cdot \begin{bmatrix} \alpha_n \\ \beta_n \end{bmatrix} = 0 \quad (VI.76)$$

In order for the system (VI.76) to have a non zero solution its determinant must vanish:

$$\det[\underline{A}(E, k_B, Re_s, R, n, \omega_n)] = 0 \quad (VI.77)$$

The above equation has 3 roots with respect to ω_n , at least one of which is real. If their real part is negative for given n , then the microbubble is stable with respect to axisymmetric disturbances characterized by the n^{th} eigenmode. The imaginary part of the complex pair of eigenvalues provides the cyclic oscillation frequency for the n^{th} mode.

From equation (V.27) we obtain the resonance frequency for volume pulsations for a microbubble consisting of a Mooney-Rivlin membrane,

$$\omega_0^2 = 3\gamma \left(\frac{2}{We} + P_{st} \right) - \frac{2}{We} + 4E \quad (VI.78a)$$

while for a Skalak membrane equation (V.31) gives

$$\omega_0^2 = 3\gamma \left(\frac{2}{We} + P_{st} \right) - \frac{2}{We} + \frac{2E}{3} (2 + 4C) . \quad (VI.78b)$$

In order to determine whether the spherical surface is stable or we should expect deviations from sphericity as the microbubble pulsates, we solve for the time variation of the microbubble radius, equation (VI.70), or equations (V.22), (V.24) for a more accurate description of the radial dynamics. Then we solve (VI.73a,b) for given history of the bubble radius, $R(t)$. If $|w_n(t)|$ or $|\psi_n(t)|$ grow with time then the n^{th} mode is unstable. For the time integration the fourth order Runge-Kutta method is used, while the time step is constant. For the solution of (VI.70) we consider as initial conditions that, $R(t=0) = R_{lq}, \dot{R}(t=0) = 0$, while perturbing the far field pressure.

VI.4 STABILITY OF PERIODIC SOLUTIONS

The general theory for the stability of linear differential equations with periodic coefficients is known as Floquet theory. It is applied in order to determine whether a periodic solution is stable or not, as well as the fashion by which stability is lost. In the particular case where the amplitude of the periodic solution is small, a Mathieu type equation is obtained. More specifically, it can be seen by transforming equations (VI.73a,b) in a standard fashion^{110,111} and assuming relatively small amplitude radial pulsations, that the following Mathieu equation is obtained,

$$v_k'' + \left[\frac{\omega_k^2}{\omega^2} + \left[\left(k + \frac{1}{2} \right) - 3 \frac{\omega_k^2}{\omega^2} \right] \varepsilon \cos \tau \right] v_k = 0, \quad (VI.79)$$

$$\tau = \omega t, \quad \omega_k = \frac{v_k}{R_0^{3/2}}, \quad R = R_0 (1 + \varepsilon \cos(\omega t))$$

In the above equation primes indicate differentiation with respect to τ instead of t , ω_k is given by eq. (VI.77) while ε and ω denote the amplitude and the frequency of the external disturbance. For given ω and $\varepsilon \ll 1$, a number of resonances are possible for each deformation mode k when

$$\frac{\omega}{\omega_k} = \frac{2}{n}, \quad n = 1, 2, 3, \dots \quad (VI.80)$$

provided that

$$2|b_k| = 2 \left| \left[\left(k + \frac{1}{2} \right) - 3 \frac{\omega_k^2}{\omega^2} \right] \frac{\varepsilon}{2} \right| > \frac{\omega_k^2}{\omega^2} = a_k \quad (VI.81)$$

The above criterion leads to the well-known diagram with the Mathieu tongues indicating the stability limits of Mathieu's equation in the a_k, b_k plane (see also figure 6.14 in [111]), that is valid in the limit $\varepsilon \ll 1$. In order to determine the stability boundaries of a pulsating microbubble taking into account large membrane radial displacements, $\varepsilon \sim 1$, a numerical analysis based on the general Floquet theory is necessary and is outlined in the following.

VI.4.1 Periodic Solutions of Autonomous Systems

This case concerns the stability of periodic of solutions of systems⁶⁹ of ODEs. The theory was originally developed for autonomous systems (recall that "autonomous" means that \vec{f} does not depend on t) but it can be applied in our case as well.

$$\dot{\vec{y}} = \vec{f}(\vec{y}; t) \quad (VI.82)$$

For time-periodic solutions, there is a time interval T (the "period") after which the system returns to its original state:

$$\vec{y}(t+T) = \vec{y}(t) \quad (VI.83)$$

Therefore one is free to impose the phase condition, posing a value for y at $t=0$:

$$y_k(t=0) = c \quad (VI.84a)$$

or imposing that $t=0$ be a critical point of y_k :

$$f_k(\bar{y}(t=0); t=0) = 0 \quad (\text{VI.84b})$$

The period T of a particular periodic solution $\bar{y}(t)$ is usually not known beforehand and it must be calculated together with $\bar{y}(t)$. Periodic solutions \bar{y} with periods T can be calculated by solving the following boundary-value problem as

$$\begin{pmatrix} \dot{\bar{y}} \\ \dot{T} \end{pmatrix} = \begin{pmatrix} \bar{f}(\bar{y}; t) \\ 0 \end{pmatrix}, \quad \begin{pmatrix} \bar{y}(0) - \bar{y}(T) \\ f_k(\bar{y}(0); t=0) \end{pmatrix} = 0 \quad (\text{VI.85})$$

For technical reasons it is advisable to normalize the interval to have unit length. Hence we rewrite the above boundary-value problem as

$$\begin{pmatrix} \bar{y}' \\ T \end{pmatrix} = \begin{pmatrix} T\bar{f}(\bar{y}; \tau T) \\ 0 \end{pmatrix}, \quad \begin{pmatrix} \bar{y}(\tau=0) - \bar{y}(\tau=1) \\ f_k(\bar{y}(\tau=0); \tau=0) \end{pmatrix} = 0 \quad (\text{VI.86})$$

where $\tau = \frac{t}{T}$ and $0 \leq \tau \leq 1$.

In our case, the period T of the periodic solution is known due to the external imposing frequency. Equations (VI.73a,b) can be written again in the form of the system (VI.82),

$$\begin{aligned} \frac{d}{dt} \begin{pmatrix} y_1 \\ y_2 \\ y_3 \end{pmatrix} &= \begin{pmatrix} f_1 \\ f_2 \\ f_3 \end{pmatrix} = \\ &= \begin{pmatrix} y_2 \\ - \left[3 \frac{\dot{R}}{R} y_2 + \left[\frac{(1-n)\ddot{R}}{R} + \frac{(n+1)(n-1)(n+2)}{WeR^3} \right] y_1 + \right. \\ &\quad \left. + \frac{n+1}{R} \Delta F_n^1(y_1, y_2, y_3, Q, R, \dot{R}) \right. \\ &\quad \left. Q(y_1, y_2, y_3, R, \dot{R}) \right] \end{pmatrix} \end{aligned} \quad (\text{VI.87})$$

with $y_1 = w_n$, $y_2 = \dot{w}_n$, $y_3 = \psi_n$ as unknowns and \ddot{R}, \dot{R}, R known throughout the period T . Actually, \ddot{R}, \dot{R}, R are calculated by solving equation (VI.70), or equations (V.22) and (V.24).

VI.4.2 The Monodromy Matrix

When tracing a branch of periodic solutions, the question arises as to whether the periodic solutions are stable, for which parameter range, and in which way stability is lost. To analyze stability of periodic solutions, one needs the monodromy matrix⁶⁹

which will be defined subsequently. In what follows, we investigate stability of one particular periodic solution $\bar{y}^*(t)$ with period T .

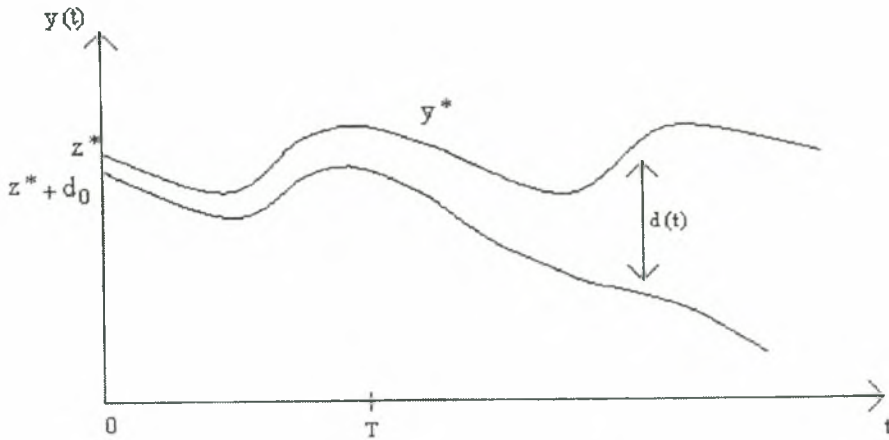


Figure VI.2: Time evolution of the periodic solution $\bar{y}^*(t)$ whose the initial vector \bar{z}^* is perturbed with \bar{d}_0

Stability of \bar{y}^* manifests itself in the way neighboring trajectories behave, figure VI.2. Trajectories of the differential equation are denoted by $\bar{\varphi}$,

$$\bar{\varphi}(t; \bar{z}) \text{ solves } \dot{\bar{y}} = \bar{f}(\bar{y}; t) \text{ with } \bar{y}(t=0) = \bar{z} \quad (\text{VI.88})$$

A trajectory that starts from the perturbed initial vector $\bar{z}^* + \bar{d}_0$, progresses with the distance

$$\bar{d}(t) = \bar{\varphi}(t; \bar{z}^* + \bar{d}_0) - \bar{\varphi}(t; \bar{z}^*) \text{ to the periodic orbit } \bar{y}^* . \text{ Here } \bar{z}^* = \bar{y}^*(t=0) \text{ is taken.}$$

Measuring the distance after one period T gives $\bar{d}(T) = \bar{\varphi}(T; \bar{z}^* + \bar{d}_0) - \bar{\varphi}(T; \bar{z}^*)$.

Taylor expansion yields $\bar{d}(T) = \frac{\partial \bar{\varphi}(T; \bar{z}^*)}{\partial \bar{z}} \bar{d}_0 + \text{terms of higher order}$. The matrix

$$\underline{M} \equiv \frac{\partial \bar{\varphi}(T; \bar{z}^*)}{\partial \bar{z}} \text{ plays a role in deciding whether the initial perturbation } \bar{d}_0 \text{ decays or}$$

grows and is called the monodromy matrix or Floquet transition matrix.

Some properties of φ help to find another representation of the monodromy matrix.

Note that $\bar{\varphi}$ from Eq. (VI.88) obeys the differential equation (VI.82),

$$\frac{d\bar{\varphi}(t; \bar{z})}{dt} = \bar{f}(\bar{\varphi}(t; \bar{z}); t), \quad \forall t \quad (\text{VI.89})$$

Differentiating this identity with respect to \bar{z} yields

$$\frac{d}{dt} \frac{\partial \bar{\varphi}(t; \bar{z})}{\partial \bar{z}} = \frac{\partial \bar{f}(\bar{\varphi}; t)}{\partial \bar{\varphi}} \frac{\partial \bar{\varphi}(t; \bar{z})}{\partial \bar{z}} \quad (\text{VI.90})$$

From $\varphi(0; \bar{z}) = \bar{z}$ we infer

$$\frac{\partial \bar{\varphi}(0; \bar{z})}{\partial \bar{z}} = \underline{\underline{I}} \quad (\text{VI.91})$$

Consequently, the monodromy matrix $\underline{\underline{M}}$ is identical to $\underline{\underline{\Phi}}(T)$, when $\underline{\underline{\Phi}}(T)$ solves the matrix initial-value problem

$$\underline{\underline{\dot{\Phi}}} = \frac{\partial \bar{f}}{\partial \bar{y}}(\bar{y}^*; t) \underline{\underline{\Phi}}, \quad \underline{\underline{\Phi}}(0) = \underline{\underline{I}} \quad (\text{VI.92})$$

So, the n^2 monodromy matrix $\underline{\underline{M}}$ -of the periodic solution $\bar{y}^*(t)$ with period T and

$$\text{initial vector } \bar{z}^* \text{ is defined by } \underline{\underline{M}} = \underline{\underline{\Phi}}(T) = \frac{\partial \bar{\varphi}(T; \bar{z}^*)}{\partial \bar{z}}, \quad (\text{VI.93})$$

where $\bar{\varphi}$ and $\underline{\underline{\Phi}}$ are defined in Eqs.(VI.88) and (VI.92).

VI.4.3 Discretization of the Equations: Derivation of the Residual Vector and the Jacobian Matrix

The discretization of the equations (VI.87) is accomplished with the trapezoidal rule,

$$\frac{\bar{y}^{n+1} - \bar{y}^n}{\Delta t} = \frac{\bar{f}(\bar{y}^{n+1}; t^{n+1}) + \bar{f}(\bar{y}^n; t^n)}{2} \quad (\text{VI.94})$$

where $n+1$ denotes the new time instant. So the residual vector is written at the l iteration of the Newton-Raphson method

$$\underline{\underline{R}}^{n+1,l} = \begin{pmatrix} R_1^{n+1,l} \\ R_2^{n+1,l} \\ R_3^{n+1,l} \end{pmatrix} = \begin{pmatrix} \left(y_1^{n+1,l} - y_1^n \right) - \frac{\Delta t}{2} (f_1^{n+1,l} + f_1^n) \\ \left(y_2^{n+1,l} - y_2^n \right) - \frac{\Delta t}{2} (f_2^{n+1,l} + f_2^n) \\ \left(y_3^{n+1,l} - y_3^n \right) - \frac{\Delta t}{2} (f_3^{n+1,l} + f_3^n) \end{pmatrix} = 0 \quad (\text{VI.95})$$

with Jacobian matrix

$$\underline{\underline{J}}^{n+1,l} = \frac{\partial R_i^{n+1,l}}{\partial y_j^{n+1,l}} = \begin{pmatrix} \frac{\partial R_1^{n+1,l}}{\partial y_1^{n+1,l}} & \frac{\partial R_1^{n+1,l}}{\partial y_2^{n+1,l}} & \frac{\partial R_1^{n+1,l}}{\partial y_3^{n+1,l}} \\ \frac{\partial R_2^{n+1,l}}{\partial y_1^{n+1,l}} & \frac{\partial R_2^{n+1,l}}{\partial y_2^{n+1,l}} & \frac{\partial R_2^{n+1,l}}{\partial y_3^{n+1,l}} \\ \frac{\partial R_3^{n+1,l}}{\partial y_1^{n+1,l}} & \frac{\partial R_3^{n+1,l}}{\partial y_2^{n+1,l}} & \frac{\partial R_3^{n+1,l}}{\partial y_3^{n+1,l}} \end{pmatrix} = \begin{pmatrix} 1 - \frac{\Delta t}{2} \frac{\partial f_1^{n+1,l}}{\partial y_1^{n+1,l}} & -\frac{\Delta t}{2} \frac{\partial f_1^{n+1,l}}{\partial y_2^{n+1,l}} & -\frac{\Delta t}{2} \frac{\partial f_1^{n+1,l}}{\partial y_3^{n+1,l}} \\ -\frac{\Delta t}{2} \frac{\partial f_2^{n+1,l}}{\partial y_1^{n+1,l}} & 1 - \frac{\Delta t}{2} \frac{\partial f_2^{n+1,l}}{\partial y_2^{n+1,l}} & -\frac{\Delta t}{2} \frac{\partial f_2^{n+1,l}}{\partial y_3^{n+1,l}} \\ -\frac{\Delta t}{2} \frac{\partial f_3^{n+1,l}}{\partial y_1^{n+1,l}} & -\frac{\Delta t}{2} \frac{\partial f_3^{n+1,l}}{\partial y_2^{n+1,l}} & 1 - \frac{\Delta t}{2} \frac{\partial f_3^{n+1,l}}{\partial y_3^{n+1,l}} \end{pmatrix} \quad (\text{VI.96})$$

The solution in the new iteration $l + 1$ is calculated as,

$$y_i^{n+1,l+1} = y_i^{n+1,l} + \left(\underline{\underline{J}}^{n+1,l} \right)^{-1} R_i^{n+1,l}, \quad i = 1, 2, 3. \quad (\text{VI.97})$$

The solution at the $n+1$ time instant is found when the following criterion is satisfied:

$$\sqrt{\sum_{i=1}^3 \left(y_i^{n+1,l+1} - y_i^{n+1,l} \right)^2} < 10^{-9} \quad (\text{VI.98})$$

The jacobian matrix $\underline{\underline{J}}$ calculated at the last iteration is used to calculate the monodromy matrix $\underline{\underline{M}}$, as it will be shown in the next session.

VI.4.4 Calculating the Monodromy Matrix

Discretizing equation (VI.92), we obtain $\underline{\underline{\Phi}}^{n+1} = \underline{\underline{\Phi}}^n \left[\underline{\underline{I}} + \Delta t \cdot \underline{\underline{J}}^{n+1} \right] = \underline{\underline{\Phi}}^n \cdot \underline{\underline{G}}^{n+1}$ (VI.99)

$$\text{with } \underline{\underline{J}}^{n+1} = \frac{\partial f_i}{\partial y_j^{n+1}} = \begin{pmatrix} \frac{\partial f_1^{n+1}}{\partial y_1^{n+1}} & \frac{\partial f_1^{n+1}}{\partial y_2^{n+1}} & \frac{\partial f_1^{n+1}}{\partial y_3^{n+1}} \\ \frac{\partial f_2^{n+1}}{\partial y_1^{n+1}} & \frac{\partial f_2^{n+1}}{\partial y_2^{n+1}} & \frac{\partial f_2^{n+1}}{\partial y_3^{n+1}} \\ \frac{\partial f_3^{n+1}}{\partial y_1^{n+1}} & \frac{\partial f_3^{n+1}}{\partial y_2^{n+1}} & \frac{\partial f_3^{n+1}}{\partial y_3^{n+1}} \end{pmatrix} = \frac{2}{\Delta t} \underline{\underline{I}} - \frac{2}{\Delta t} \underline{\underline{J}}^{n+1} \quad (\text{VI.100})$$

It is the case that $\underline{\underline{\Phi}}^0 = \underline{\underline{\Phi}}(t=0) = \underline{\underline{I}}$ and, consequently, using equation (VI.99) we obtain

$$\underline{\underline{M}} = \underline{\underline{\Phi}}(t=T) = \underline{\underline{\Phi}}^N = \underline{\underline{G}}^1 \cdot \underline{\underline{G}}^2 \dots \underline{\underline{G}}^N \quad (\text{VI.101})$$

So, the matrix $\underline{\underline{M}}$ is found at the end of the period T , and the jacobian matrix $\underline{\underline{J}}$ at each time instant is used for the calculation. In our case $M = M(w_n, \dot{w}_n, \psi_n; R, \dot{R})$ is a function of the periodic solution for given external forcing frequency, the stability of which we want to investigate.

VI.4.5 Mechanisms of Losing Stability

Matrix $\underline{\underline{M}}$ has n eigenvalues. One of them is equal to unity and the other $n-1$ determine the stability in the following manner:

$\bar{y}(t)$ is stable if $|\mu_j| < 1$ for $j = 1, \dots, n-1$

$\bar{y}(t)$ is unstable if $|\mu_j| > 1$ for some j

- If $\text{Im}(\mu_j) = 0$ and $\text{Re}(\mu_j) < -1$ then the unstable solution $\bar{y}(t)$ is periodic with twice the period of the radial pulsation.

- If $\text{Im}(\mu_j) = 0$ and $\text{Re}(\mu_j) > 1$ then the unstable solution $\bar{y}(t)$ is periodic with the same period with that of the radial pulsation.

- If $\text{Im}(\mu_j) \neq 0$ and $|\mu_j| > 1$ then the unstable solution $\bar{y}(t)$ is not exactly periodic.

VI.5 RESULTS AND DISCUSSION

VI.5.1 STATIC BUCKLING INSTABILITY: COMPARISON WITH SHELL THEORY

VI.5.1.1 STABILITY ANALYSIS

Static Stability

The present section is intended to compare results of stability analysis with known results of shell theory, in order to validate the present approach. For this reason as a first step we will consider that the shell consists of a thin layer of three-dimensional elastic solid of thickness δ , so that the scalar bending modulus $k_{B\text{dim}}$ is related with the shear stress modulus through the equation (VI.43) with $\delta \ll R_{Eq}$. In this fashion the following formula provides a minimum overpressure above which static buckling instability occurs¹⁰⁹

$$P'_{crit,Th} = \frac{2E_v}{\sqrt{3(1-\nu^2)}} \left(\frac{\delta}{R_{Eq}} \right)^2 = \frac{2(3G_s)}{\sqrt{3(1-\nu^2)}} \left(\frac{\delta}{R_{Eq}} \right)^2, \quad (VI.102)$$

This is a well-known result from shell theory^{64,109}, based on static considerations, which is valid when the shell consists of a three dimensional elastic isotropic material following Hooke's law, i.e. the base spherical configuration undergoes small displacements.

We select typical values from the bibliography for the microbubble parameters (size, thickness and viscoelastic properties). Thus, we set the microbubble equilibrium radius to $R_{Eq} = 1.5 \mu m$, the membrane thickness to $\delta = 15 nm$, the membrane viscosity to $\mu_s = 0.3 Pa \cdot s$, the shear stress modulus to $G_s = 133 MPa$, the Poisson ratio to $\nu=0.5$, while the scalar bending modulus, given by the equation (VI.43), to $k_{B\text{dim}} = 1.496 \cdot 10^{-16} Nm$. Throughout this study we assume that the membrane material follows either the Mooney-Rivlin law with constant $b=0$ or $b=1$, or the Skalak law with constant $C=1$.

As it has been shown in section V.2.1, when the deformations are small the Mooney-Rivlin law, the Skalak law for $C=1$ and Hooke's law coincide. To calculate the critical overpressure $P'_{crit,M}$ above which static buckling occurs we first evaluate ω_n , through eq. (VI.77), as a function of the bubble radius R and mode number n and then, from the normal force balance (VI.57), we recover the corresponding overpressure, $P'_{overpressure}$. Next we plot contours of ω in the $(P'_{overpressure}, n)$ plane and estimate the minimum overpressure, $P'_{crit,M}$, for $Re(\omega_n)=0$. For example, if we consider the microbubble with the above characteristics, then equation (VI.102) predicts $P'_{crit,Th} = 53200 Pa$, while the present theoretical model predicts $P'_{crit,M} \approx 53750 Pa$ for a material following the Mooney-Rivlin law with $b=1$ and $P'_{crit,M} \approx 53100 Pa$ for a material following the Skalak law with $C=1$, figures VI.3 (a),(b). Both laws predict that the most dangerous mode is $n=17$, while the dimensionless radius where static buckling occurs is $R_{crit}=0.9967$.

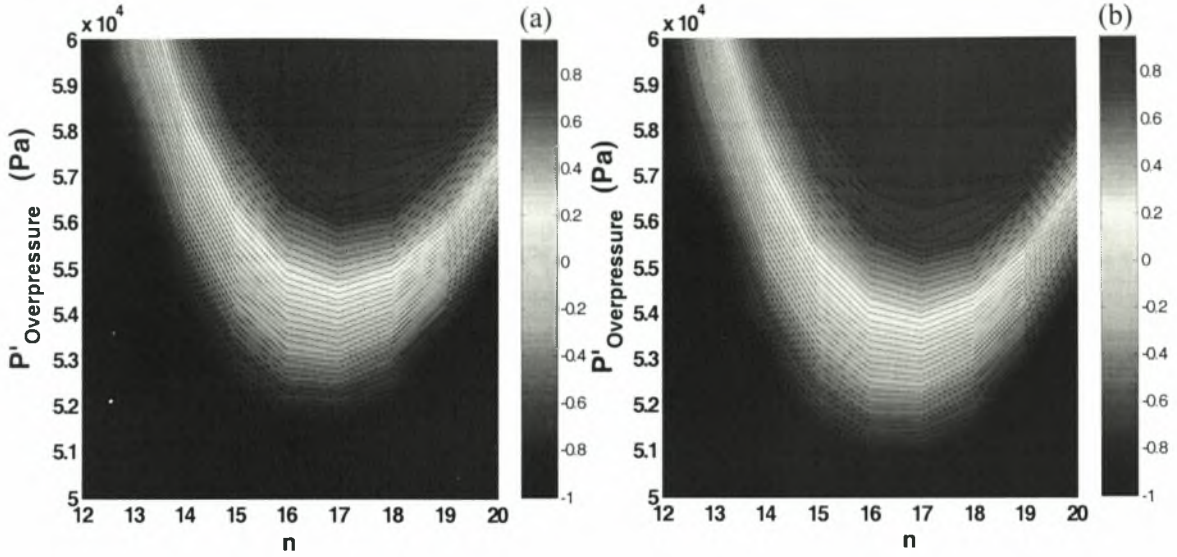


Figure VI.3: Contours of eigenvalues ω in the $(P'_{\text{overpressure}}, n)$ plane for a) the Mooney-Rivlin law ($b=1$) and b) the Skalak law ($C=1$); $R_{\text{Eq}} = 1.5 \mu\text{m}$, $G_s = 133 \text{ MPa}$, $\delta = 15 \text{ nm}$, $\mu_s = 0.3 \text{ Pa}\cdot\text{s}$, $k_{\text{Bdim}} = 1.496 \cdot 10^{-16} \text{ Nm}$, $\nu=0.5$

Dynamic Stability

Next we consider a microbubble with the above characteristics and a membrane following the Mooney-Rivlin law ($b=1$), that is immersed inside a liquid of static pressure $P'_{st} = 101325 \text{ Pa}$, density $\rho_l = 998 \frac{\text{kg}}{\text{m}^3}$, sound velocity $C_l = 1540 \frac{\text{m}}{\text{s}}$ and dynamic viscosity $\mu_l = 0.001 \text{ Pa}\cdot\text{s}$. It must be noted that the sound velocity and the dynamic viscosity of the external fluid are not accounted for in this case, since shell viscosity is the controlling damping mechanism of the oscillations. Thus, we take $C_l \rightarrow \infty$ and $\mu_l = 0$. At $t=0$, a step change in the far field pressure is imposed, $P'_\infty = P'_{st}(1 + \varepsilon)$, characterized by an amplitude $\varepsilon=0.547$ such that the overpressure that the membrane feels is $P'_{\text{overpressure}} \geq P'_{\text{crit},M}$ at steady state. Figure VI.4(a) shows the evolution of dimensionless radius $R(t)$ as predicted by eq. (VI.70). Figure VI.4(b) shows the time evolution of the dimensional overpressure that the membrane feels at each moment, the theoretical prediction for the threshold in overpressure, $P'_{\text{crit,Th}} = 53200 \text{ Pa}$, for static buckling to take place based on equation (VI.102), and the threshold value provided by the static analysis presented here, $P'_{\text{crit},M} \approx 53750 \text{ Pa}$, obtained from figure VI.3(a). In figure VI.4(c), the time evolution of w_{16}, w_{17}, w_{18} is shown where it can be seen that the 17th is the only unstable mode. It must be pointed that while $P'_{\text{overpressure}} \geq P'_{\text{crit},M}$ for the first time when $t' \approx 0.02 \mu\text{s}$, the mode starts to actually grow when $t' \approx 8 \mu\text{s}$. This must be a characteristic of dynamic buckling instability, indicating that a time interval of the order of some μs is required for the growth of the unstable modes. If the amplitude is reduced to $\varepsilon=0.537$ so that $P'_{\text{overpressure}} < P'_{\text{crit},M}$ in the steady

state, all modes are stable as it can be seen in figures VI.4(d),(e). Even if $P'_{overpressure} \geq P'_{crit,M}$ in the transition state, this seems that cannot instigate growth of unstable modes.

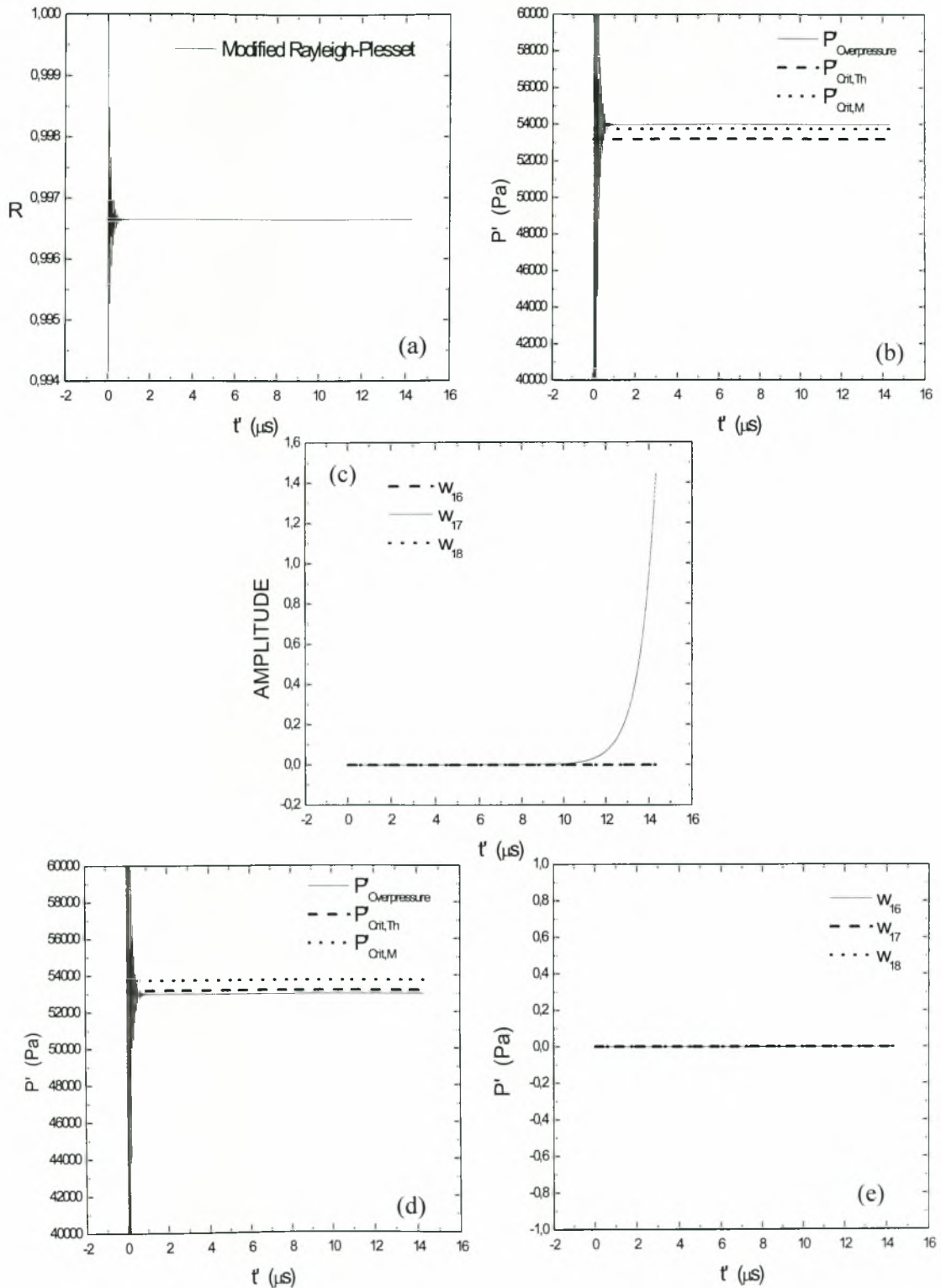


Figure VI.4: Time evolution of the (a) microbubble radius, (b) dimensional overpressure, (c) shape mode decomposition based on dynamic stability analysis for a Mooney-Rivlin membrane with $b=1$ and $\varepsilon=0.547$. Time evolution of the (d) dimensional overpressure and (e) shape mode decomposition based on dynamic stability analysis for a Mooney-Rivlin membrane with $b=1$, $\varepsilon=0.537$; $R_{Eq} = 1.5 \mu m$, $G_s = 133 MPa$, $\delta = 15 nm$, $\mu_s = 0.3 Pa \cdot s$, $k_{Bdim} = 1.496 \cdot 10^{-16} Nm$, $\nu=0.5$, $\rho_l = 998 \frac{kg}{m^3}$, $P_{st} = 101325 Pa$, $\mu_l = 0$, $C_l \rightarrow \infty$, $\gamma=1.4$, type of pressure perturbation in the far field: $P'_\infty = P'_{st}(1 + \varepsilon)$

VI.5.1.2 NUMERICAL SIMULATIONS

Static Problem

We also solved the non-linear formulation of the static problem numerically using the B-cubic splines as basis functions and performing simple continuation on the dimensionless load;

$$\Delta F_N = k_s \tau_{ss} + k_\varphi \tau_{\varphi\varphi} - \frac{1}{\sigma} \frac{\partial}{\partial s} (\sigma q) = -(P_\infty - P_G) = -P_{Overpressure} \quad (VI.103a,b)$$

$$\Delta F_t = -\frac{\partial \tau_{ss}}{\partial s} - \frac{1}{\sigma} \frac{\partial \sigma}{\partial s} (\tau_{ss} - \tau_{\varphi\varphi}) - k_s q = 0$$

Thus, we calculated the critical overpressure, $P'_{crit,M} \approx P'_{Overpressure} = 53800 Pa$, for the case already considered analytically in section VI.5.1.1. The eigenvector that corresponds to the first unstable eigenvalue was calculated by numerically evaluating the eigenvalues of the Jacobian matrix that was obtained at the bifurcation point, i.e. the critical load. It is shown in figures VI.5(a),(b). The mode very closely resembles the 17th Legendre mode as predicted by stability analysis.

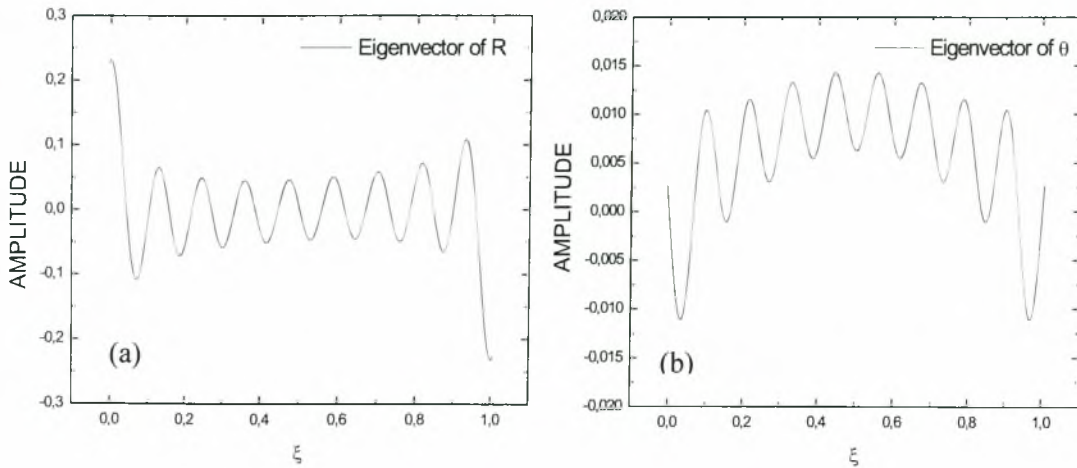
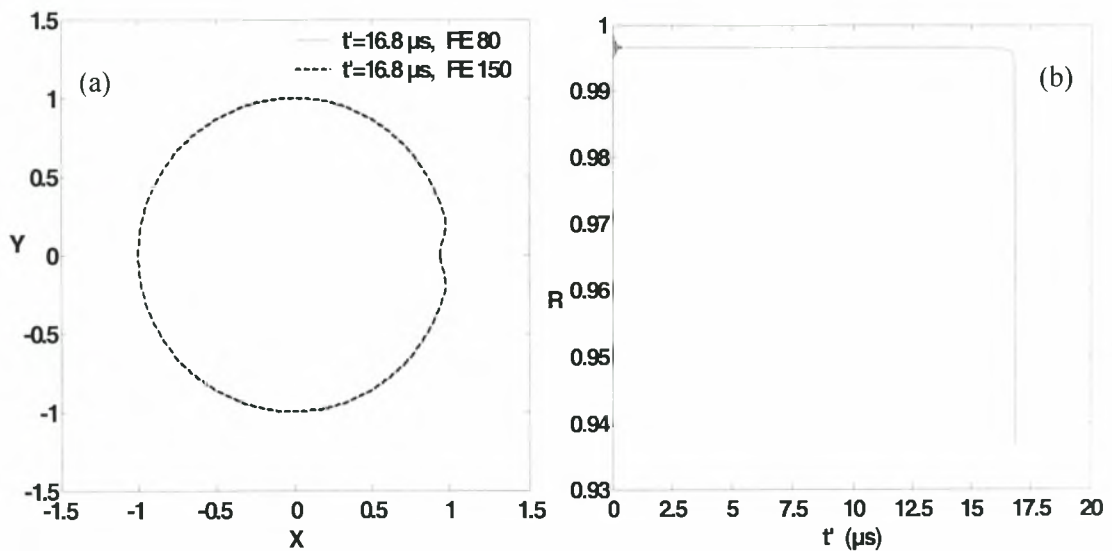


Figure VI.5: (a) Radius and (b) azimuthal angle θ of the interface particles, for the eigenvector corresponding to the first negative eigenvalue; $S=1$, $R_{Eq} = 1.5 \mu m$, $G_s = 133 MPa$, $\delta = 15 nm$, $k_{Bdim} = 1.496 \cdot 10^{-16} Nm$, $\nu=0.5$, $P'_{Overpressure} = 53800 Pa$ for a Mooney-Rivlin membrane, $b = 1$, 200 elements in the region $0 \leq \theta \leq \pi$.

Dynamic Problem

Finally, we solved the non-linear formulation of the dynamic problem numerically using the B-cubic splines as basis functions and applying a pressure perturbation in the far field of the type, $P'_{\infty} = P'_{st}(1 + \varepsilon)$. The microbubble shape just before simulations had to stop due to excessive growth of the unstable mode, P_{17} , and the time evolution of the microbubble radius as it is calculated for the first particle of the region $0 \leq \theta \leq \pi$, i.e the one with $\theta=0$ constantly, are shown in figures VI.6(a,b). The shape corresponds to the post buckling state of the microbubble. It is a result that has been verified by mesh refinement as it can be seen from figure VI.6(a). It isn't obvious that the prevailing mode is the 17th. However, in figure VI.6(c,d) we plot the shape mode decomposition where it can be seen that the most unstable mode is the 17th.



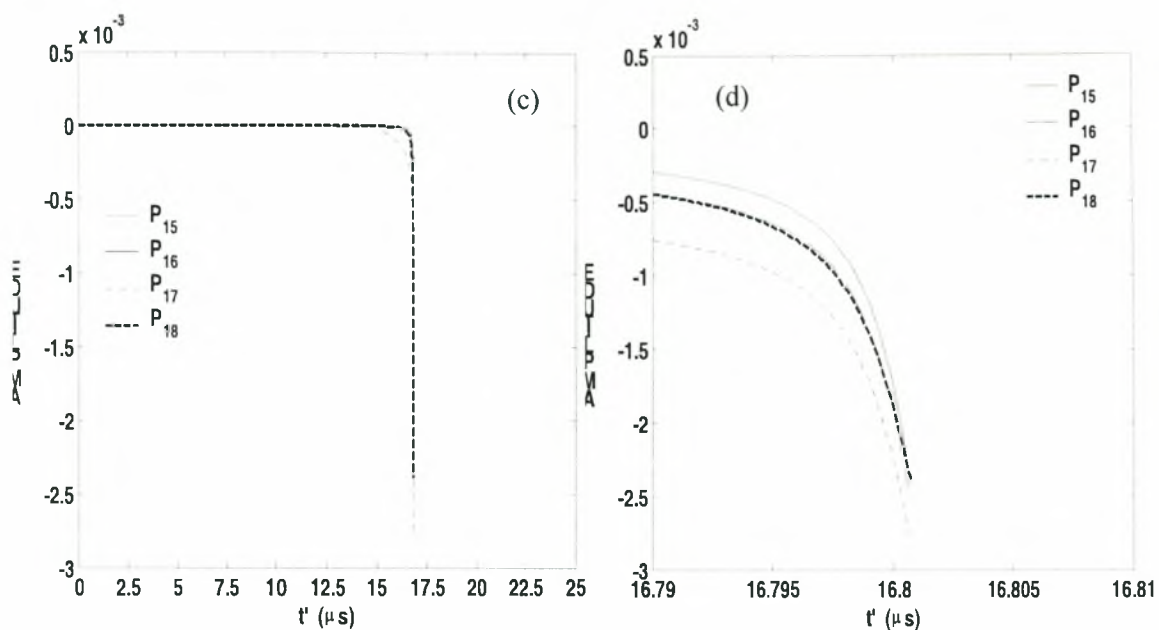


Figure VI.6: Simulation of the oscillations of a contrast agent whose shell obeys the Mooney-Rivlin constitutive law with $b=1$. (a) Microbubble shape during collapse, (b) time evolution of the radial position of the interfacial particle with $\theta=0$, (c) numerically obtained shape mode decomposition during the entire simulation and (d) during collapse; $S=1$, $R_{\mu q} = 1.5 \mu m$, $G_s = 133 MPa$, $\delta = 15 nm$, $\mu_s = 0.3 Pa \cdot s$, $\nu=0.5$, $k_{Bdim} = 1.496 \cdot 10^{-16} Nm$, $\rho_l = 998 \frac{kg}{m^3}$, $P'_{st} = 101325 Pa$, $\mu_l = 0$, $C_l \rightarrow \infty$, $\varepsilon=0.547$, $\gamma=1.4$, type of pressure perturbation in the far field: $P'_\infty = P'_{st}(1 + \varepsilon)$

VI.5.2 DYNAMIC BUCKLING AND PARAMETRIC INSTABILITY: COMPARISON WITH EXPERIMENTS AND THE DETERMINATION OF THE SCALAR BENDING MODULUS k_{Bdim}

Thus far we have assumed that the shell consists of a thin layer of three-dimensional elastic solid of thickness, δ , considered to be isotropic in all directions and consequently it can be shown that the scalar bending modulus k_{Bdim} is related with the shear stress modulus through (VI.43). However, a microbubble shell is not isotropic in the transverse direction. This is a similar case to that of a red blood cell, whose membrane consists of a lipid bilayer. The latter is strain hardening and non-isotropic in the direction perpendicular to the long chains of molecules forming the lipid. As a result, besides the membrane elasticity which pertains to deformations along the interface, the scalar bending modulus k_{Bdim} must be introduced as an independent parameter, called bending elasticity⁴⁸, which must be specified for each membrane material.

Estimating bending resistance of the shell is a difficult task as it may require use of Atomic Force Measurement on an isolated contrast agent. An alternative approach could be based on the static buckling instability that appears when a contrast agent

experiences slow compression. For given equilibrium radius, shear modulus and shell viscosity, observation of the microbubble radius for which buckling occurs under slow compression (the microbubble starts losing the initial spherical configuration) can be used in conjunction with static stability analysis to provide the scalar bending modulus $k_{B \text{ dim}}$.

Alternatively, another procedure could be applied for the estimation of this parameter. It entails optical observation of contrast agent destruction or even the observation of microbubble shape oscillations to known conditions in conjunction with numerical simulations or dynamic stability analysis. As it will be shown in the following sections, shape oscillations and destruction of a microbubble, when the latter is insonated by a sinusoid pressure perturbation with frequency near or above the resonance frequency, are attributed either to parametric instability or to dynamic buckling. We use the term ‘dynamic buckling’ versus ‘static buckling’ because there are differences between these two instabilities, in the conditions under which they appear, in the unstable mode as well as the critical overpressure above which the instability occurs. As will be seen in the following, dynamic buckling appears when the external forcing has frequency near or above the microbubble resonance while static buckling occurs when the external frequency is fairly below resonance. Due to the geometrical (thickness, equilibrium radius) as well as the physical (shear modulus, membrane viscosity) properties of the contrast agents, the resonance frequency is on the order of MHz. This, along with the fact that the microbubble is insonated with frequency on the order of MHz in medical applications, leads to the conclusion that a microbubble mainly experiences the dynamic buckling instability. However, both instabilities evolve on a very fast time scale when the overpressure exerted on the membrane exceeds a critical value, the latter is higher for dynamic buckling and is normally associated with a higher unstable mode, that depends on the scalar bending modulus $k_{B \text{ dim}}$.

Besides dynamic buckling instability, the microbubble may experience parametric instability^{112,113} in a fashion similar to free bubbles albeit to significantly lower external loads. This process can also destroy the microbubble cohesion even though it evolves on a much slower time scale. Microbubble destruction depends on the severity of the membrane shape deformation that this type of instability causes or equivalently on the tensions that will be developed inside the membrane. This instability is excited when the forcing frequency resonates with one of the eigenfrequencies for shape oscillations of the microbubble. These eigenfrequencies depend on the scalar bending modulus $k_{B \text{ dim}}$, among other parameters of the shell. Determining the amplitude of the external disturbance above which a mode becomes unstable, one could not only control the frequency of shape oscillations but also predict the parameter range for microbubble cohesion and the onset of interesting flow configurations, such as jetting^{114,115,116}, that are potentially useful in medical applications as for example in directing the action of the microbubble towards nearby cells.

The second aforementioned procedure for the estimation of the scalar bending modulus $k_{B \text{ dim}}$ will be applied to a MP1950 microbubble. The microbubble shell consists of phospholipid molecules and exhibits a rather strain-softening behavior. This can be concluded from experimental measurements with this kind of microbubble¹¹⁷. Once $k_{B \text{ dim}}$ has been specified for a given type of contrast agent by reproducing its response to a specific external disturbance, one can predict the minimum pressure amplitude for a given forcing frequency where dynamic buckling or parametric

instability occurs for different equilibrium microbubble radii, in the form of a phase diagram. In this fashion it is possible to determine the boundary separating fragmentation due to dynamic buckling from parametric instability and recover other dynamic effects reported in experimental observations¹¹⁵ such as jetting.

VI.5.2.1 DYNAMIC BUCKLING INSTABILITY - THE CASE OF MP1950 MICROBUBBLE

We would like to simulate specific optical observations of contrast agent destruction in order to specify a) the mechanism behind microbubble collapse and b) the scalar bending modulus $k_{B \text{ dim}}$. We simulate experimental observations by Chomas et al.⁷⁰ where an experimental contrast agent, MP1950 with a phospholipid membrane, with equilibrium radius $R_{eq} = 1.5 \mu\text{m}$ and decafluorobutane C_4F_{10} as the internal gas, balances inside water with static pressure $P_{st}' = 1 \text{ bar}$. The microbubble is insonated with a two-cycle sinusoid with peak negative pressure of 1.2 MPa and a center forcing frequency $\nu_f = 2.4 \text{ MHz}$. The optical frame images are shown in figures VI.7 (a)-(g), while in figure VI.7(h) the time evolution of the microbubble diameter is monitored. As can be seen from the latter figure the microbubble contracts initially, then expands and then again contracts until near the minimum radius the membrane breaks up giving 5 free bubbles. The collapse mechanism was originally attributed to Rayleigh-Taylor instability due to the very large velocity of the microbubble interface during the last stage of collapse.

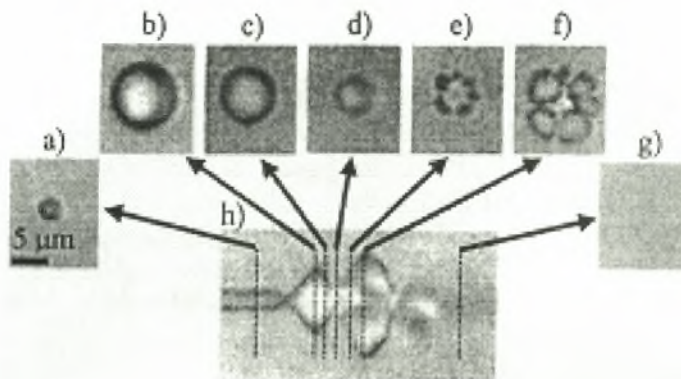


Figure VI.7: Optical frame images and evolution of the diameter of the oscillation and fragmentation of a contrast agent microbubble (MP1950). The bubble has an initial diameter of $3 \mu\text{m}$, shown in (a). The image in (h) shows the diameter of the bubble as a function of time, and dashed lines indicate the times at which the two-dimensional frame images in (a)-(g) were acquired relative to the (h) image. The time interval between Figs. VI.5(b) and VI.5(f) is 80 ns while the shutter duration used in Figs. VI.5(b)-VI.5(f) is 50 ns. All the frames are reproduced from [70].

Firstly, we would like to check the assertion that the mechanism behind microbubble collapse is the Rayleigh-Taylor instability. A useful piece of information that we employ in order to obtain the membrane elasticity and the surface tension is the fact that the maximum radius of the microbubble when the membrane is in tact (figure VI.7 (b)), is three times the microbubble equilibrium radius.

Numerical Simulation Considering the Shell as a Free Surface

The Rayleigh-Taylor instability appears usually for large acceleration of a free surface and this occurs normally at the beginning of an expansion or near the minimum radius when the bubble is collapsing^{23, 24,25,63}. Based on this, we initially simulate the above case as a free surface with surface tension $\sigma = 0.677 \text{ N/m}$ and taking into account weak viscous effects, such that the maximum expansion is recovered. Figure VI.8(a) shows the last shape obtained from the simulation, while in figure VI.8(b) the time evolution of the microbubble diameter is presented. It is obvious that the microbubble does not collapse in the time scale of the above experimental observations, indicating that the instability is most likely not of the classic Rayleigh-Taylor type observed in free bubbles.

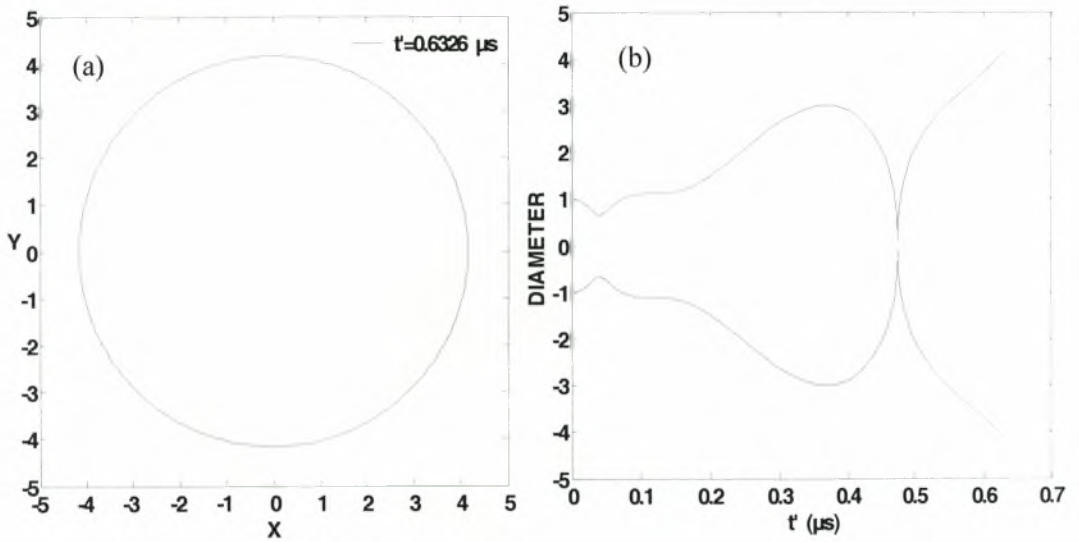


Figure VI.8: Simulation of the oscillations of a contrast agent with its membrane treated as a free surface. (a) Last microbubble shape before the simulation stops, (b) time evolution of the microbubble diameter; $S=1$, $R_{i,q} = 1.5 \mu\text{m}$, $\rho_l = 998 \text{ kg/m}^3$, $\mu_l = 0.001 \text{ Pa}\cdot\text{s}$, $C_l \rightarrow \infty$, $\sigma = 0.677 \text{ N/m}$, $P'_{st} = 101325 \text{ Pa}$, $\gamma=1.07$, $\varepsilon=12$, $v_f = 2.4 \text{ MHz}$, type of pressure perturbation in the far field: $P'_\infty = P'_{st} [1 + \varepsilon \cos(2\pi v_f t')]$, 100 elements in the region $0 \leq \theta \leq \pi/2$.

Dynamic Stability and Numerical Simulation Considering the Shell as a Material Following Mooney-Rivlin Constitutive Law

Next, we consider that the microbubble consists of a shell following the Mooney-Rivlin constitutive law. It is known from experimental observations¹¹⁸ regarding the same type of microbubble that the shell thickness is $\delta \approx 1 \text{ nm}$ while its viscosity depends on the equilibrium radius, $\mu_s (\text{sPa}) \cdot \delta (\text{nm}) = 1.34 R_{Eq} (\mu\text{m}) - 0.69$. This relation has been produced by employing linear regression on experimental results. If we set the membrane thickness to $\delta = 1 \text{ nm}$, then from the above equation $\mu_s = 1.32 \text{ Pa} \cdot \text{s}$. The microbubble expansion measured from the experiment by Chomas et al.⁷⁰ is achieved if we set $G_s = 520 \text{ MPa}$ with $b=0$. This value of shear stress modulus is obtained by solving the spherosymmetric model, equation (V.22), considering that $\mu_l = 0.001 \text{ Pa} \cdot \text{s}$, $C_l = 1540 \text{ m/s}$, $\rho_l = 998 \text{ kg/m}^3$, $\gamma = 1.07$ and surface tension $\sigma = 0.051 \text{ N/m}$. The above values for the properties of the host liquid have also been used in [118] in order to simulate this contrast agent. If we consider that $C_l \rightarrow \infty$, $\mu_l = 0$, then $G_s = 590 \text{ MPa}$ for $b=0$. This value for elasticity is in the range reported in [118]. The resonance frequency of this contrast agent is calculated from equation VI.78(a), $v_{res} = 7.23 \text{ MHz}$ for $G_s = 520 \text{ MPa}$ and $v_{res} = 7.65 \text{ MHz}$ for $G_s = 590 \text{ MPa}$. The only parameter that remains to be specified is the scalar bending modulus $k_{B \text{ dim}}$.

We tune the scalar bending modulus $k_{B \text{ dim}}$ so that the microbubble collapses in the right time scale and as close to that experimentally observed as possible. This adaptation predicts a range of acceptable values for the scalar bending modulus because we are not certain as to which modes appear. The range for $G_s = 590 \text{ MPa}$, $C_l \rightarrow \infty$, $\mu_l = 0$ is $5 \cdot 10^{-14} \leq k_{B \text{ dim}} \leq 4 \cdot 10^{-13} \text{ Nm}$ with most possible value $k_{B \text{ dim}} \approx 3.45 \cdot 10^{-13} \text{ Nm}$, almost 10^6 times greater than the prediction of (VI.43).

The degree of softness of the shell material is fixed by setting b to zero, so that the above contrast agent exhibits shape oscillations of the 4th mode at a transmit frequency of 19MHz and a reasonable amplitude of the external disturbance, $\varepsilon=5$, in accordance with the experimental observations¹¹² shown in figure VI.9. This is found by conducting stability analysis on the periodic pulsation of a microbubble of diameter 1.4 μm , with the above viscoelastic characteristics and bending modulus $k_{B \text{ dim}} = 3 \cdot 10^{-14} \text{ Nm}$, that is insonated with a sinusoidal pressure perturbation in the far field, $P'_\infty = P'_{st} [1 + \varepsilon \cos(2\pi v_f t')]$ with $\varepsilon=5$. The Monodromy matrix for the 4th mode possesses one unstable eigenvalue with $\text{Im}(\mu) = 0$ and $\text{Re}(\mu) = -1.53 < -1$. This is an indication of subharmonic resonance where the 4th shape mode oscillates with twice the period of the imposed forcing frequency. If the external amplitude is increased to $\varepsilon=12$, then the 5th mode appears in harmonic resonance with the imposed forcing frequency, $\text{Im}(\mu) = 0$ and $\text{Re}(\mu) = 1.08 > 1$. It should be stressed that if $k_{B \text{ dim}}$ is increased beyond $3.45 \cdot 10^{-13} \text{ Nm}$ stability analysis does not predict shape oscillations of the contrast agent.

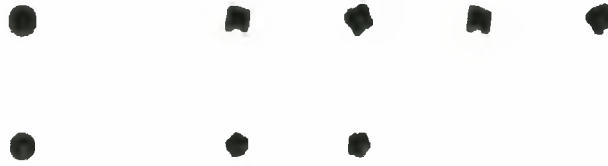
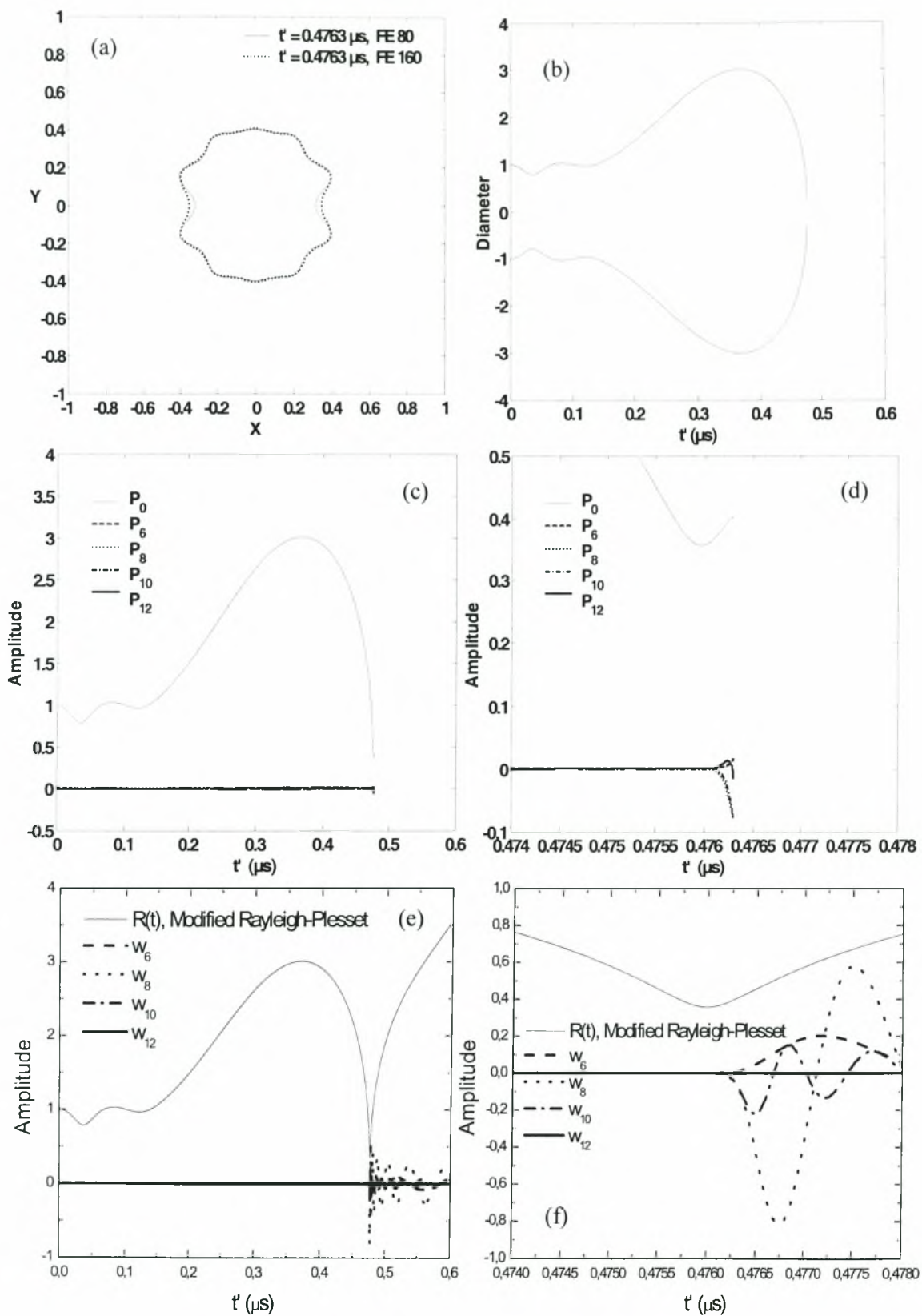


Figure VI.9: Mode $n=4$ (top) and mode $n=5$ (bottom) vibrations for small microbubbles of $1.4 \mu\text{m}$ diameter. The transmit frequency is 19 MHz. All the frames are reproduced from [112].

In figure VI.10(a),(b) the microbubble shape during collapse as well as the evolution of the microbubble diameter are shown, as they are obtained from a dynamic simulation of the optical observations shown in Fig. VI.7, treating the membrane as a MR material with $b=0$, $G_s = 590 \text{ MPa}$, and scalar bending modulus $k_{b \text{ dim}} \approx 3.45 \cdot 10^{-13} \text{ Nm}$ with $C_l \rightarrow \infty$, $\mu_l = 0$. The membrane seems to digress from the initial spherical configuration in the time scale obtained from the experiments. The validity of the simulation was checked against mesh refinement as well as by monitoring the variation of the energy given by equation (VI.44), figures VI.10(a),(g). The total energy is conserved throughout the simulation. The most unstable mode that emerges in the simulation of the full problem seems to be the 8th Legendre mode. This can be gleaned from the evolution of the Legendre mode decomposition of the shape shown in figures VI.10(c),(d). The numerical result was verified by dynamic stability analysis with respect to non spherical disturbances, figures VI.10(e),(f). In figure VI.10(h) the evolution of the $P'_{\text{Overpressure}}$ exerted on the shell is plotted, as predicted by the dynamic stability analysis. The maximum value is $P'_{\text{Overpressure,Max}} \approx 1.05 \cdot 10^9 \text{ Pa}$ while static stability predicts $P'_{\text{Crit,M}} \approx 2.07 \cdot 10^6 \text{ Pa}$ and $R_{\text{Crit}} \approx 0.825$ with P_2 as the most unstable mode. Consequently static buckling cannot describe the process shown in figure VI.7. The behavior shown in figure VI.7 and reproduced in figures VI.10a,h corresponds to the dynamic buckling instability and this is manifested by the fact that the unstable modes appear within a very short time frame and during the compression phase of the microbubble oscillation. The instability appears during the first or the second period of the forcing frequency and therefore it cannot be a parametric instability which requires a large number of oscillations in order to appear. It is also worthwhile to mention that the modes start to develop near the minimum or during the expansion phase of the microbubble oscillation. This has to do with the dynamic nature of the instability that requires a time interval for the unstable modes to appear.



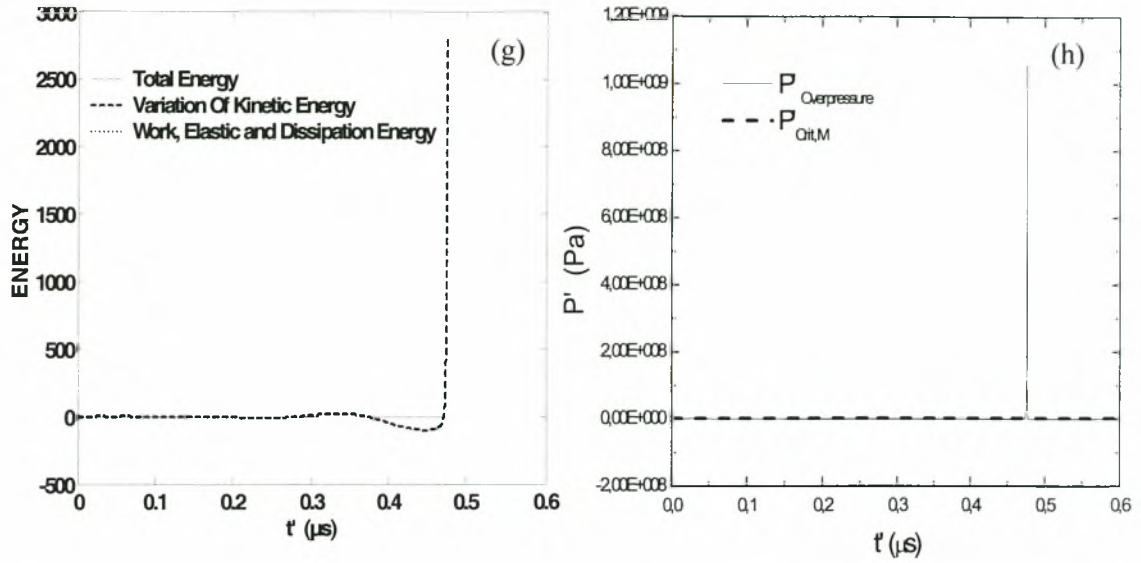


Figure VI.10: Simulation of the oscillation and collapse of the contrast agent considering it as a shell following Mooney-Rivlin constitutive law $b=1$, (a) Microbubble shape during collapse, (b) time evolution of the microbubble diameter, (c)-(d) numerically obtained shape mode decomposition, (e)-(f) evolution of bubble radius and shape mode decomposition based on stability analysis, (g) comparison between time variation of the kinetic energy, work, membrane elastic energy, surface energy and dissipation due to the membrane viscosity, (h) time evolution of the $P'_{Overpressure}$ exerted on the shell; $S=1$, $R_{Eq} = 1.5 \mu m$, $G_s = 590 MPa$, $\delta = 1 nm$, $\mu_s = 1.32 Pa \cdot s$, $k_{\beta dim} = 3.45 \cdot 10^{-13} Nm$, $b=0, v=0.5$, $\rho_l = 998 \frac{kg}{m^3}$, $\mu_l = 0$, $C_l \rightarrow \infty$, $P'_{st} = 101325 Pa$, $\sigma = 0.051 \frac{N}{m}$, $\gamma=1.07$, $\varepsilon=12$, $v_f = 2.4 MHz$, far field disturbance: $P'_{\infty} = P'_{st} [1 + \varepsilon \cos(2\pi v_f t')]$

The dynamic buckling instability is strongly dependent on the scalar bending modulus $k_{\beta dim}$. Indeed, if the bending modulus is increased to $k_{\beta dim} = 6.89 \cdot 10^{-13} Nm$, then the microbubble surpasses the second compression phase without losing its integrity. This can be seen from figures VI.11 (a) and (b) where the last shape of the simulation and the time evolution of the microbubble diameter, are monitored. The same result is derived by dynamic stability analysis. However, $P'_{Overpressure,Max} \approx 1.05 \cdot 10^9 Pa$ while static stability predicts $P'_{Crit,M} \approx 4.1 \cdot 10^6 Pa$. This is a significant difference between dynamic and static buckling. It seems that the overpressure above the critical limit acts for a very small time interval so that the modes don't have the time to be excited. The membrane viscosity may also contribute to the damping of the excited modes, stabilizing the microbubble shell.

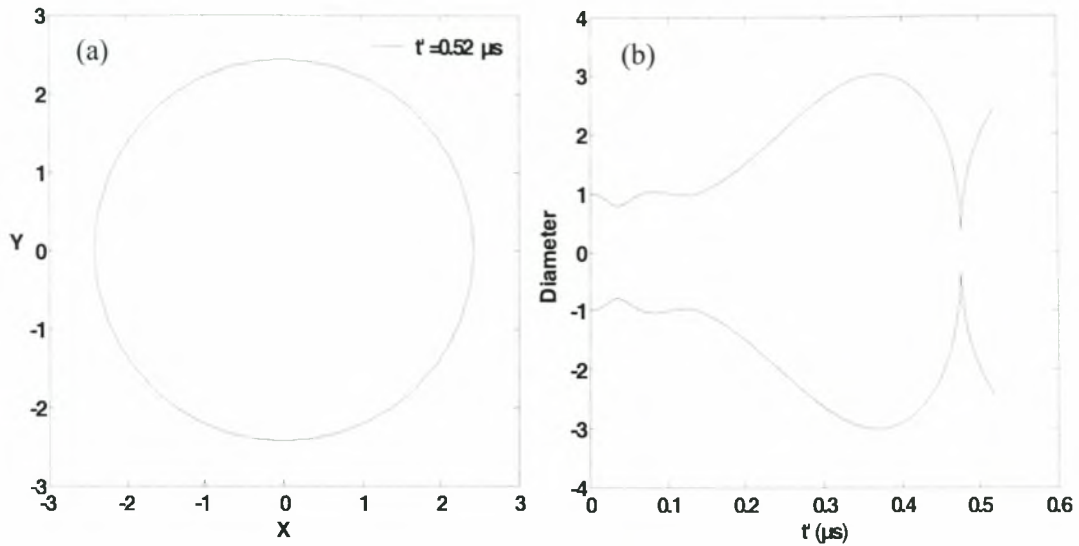
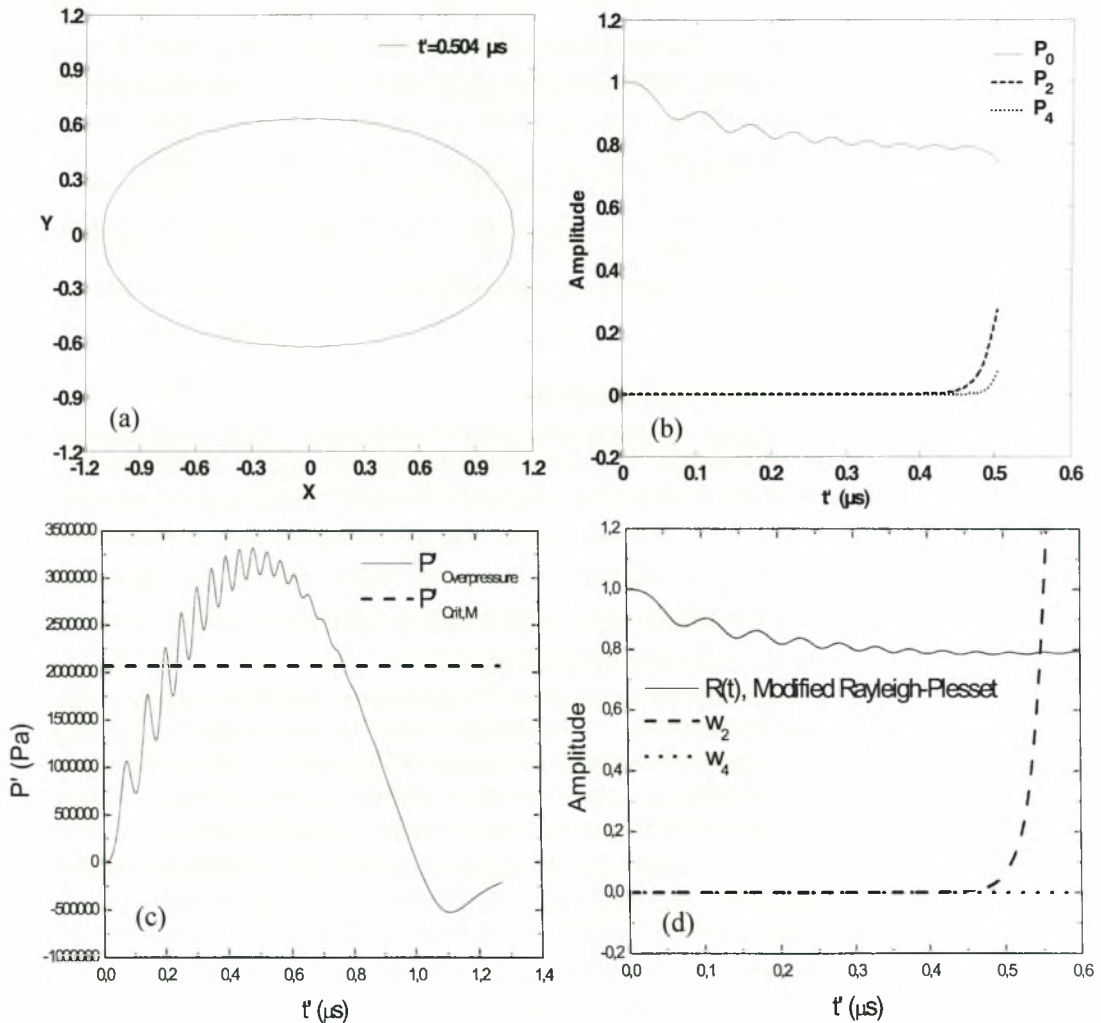


Figure VI.11: Simulation of the oscillation of the contrast agent considering it as a shell. (a) Last microbubble shape from the simulation, (b) time evolution of the microbubble diameter; $S=1$, $R_{liq} = 1.5 \mu m$, $G_s = 590 MPa$, $\delta = 1 nm$, $\mu_s = 1.32 Pa \cdot s$, $k_{Bdim} = 6.89 \cdot 10^{-13} Nm$, $b=0$, $\nu=0.5$, $\rho_l = 998 \frac{kg}{m^3}$, $\mu_l = 0$, $C_l \rightarrow \infty$, $P'_{st} = 101325 Pa$, $\sigma = 0.051 \frac{N}{m}$, $\gamma=1.07$, $\epsilon=12$, $\nu_f = 2.4 MHz$, type of pressure perturbation in the far field: $P'_\infty = P'_{st} \left[1 + \epsilon \cos(2\pi\nu_f t') \right]$

The Effect of the Forcing Frequency

The difference between the static and dynamic buckling as regards the unstable mode and the critical overpressure has to do with the dynamic nature of the external load with frequency near the microbubble resonance frequency. Indeed, if we consider the case with $k_{Bdim} = 3.45 \cdot 10^{-13} Nm$ but with an external frequency that is well below the resonance frequency $\nu_{res} = 7.65 MHz$, i.e. $\nu_f = 500 kHz$ and $\epsilon=33$, such that $P'_{Overpressure,Max} \geq P'_{Crit,M} \approx 2.07 \cdot 10^6 Pa$ then static buckling instability occurs with the second Legendre mode as the dominant emerging unstable mode. This can be seen in figures VI.12 (a),(b), where the last shape from the simulation and the evolution of the shape modes are plotted, respectively. The numerical result was recovered by applying dynamic stability analysis, as can be seen from figures VI.12 (c),(d) where the evolution of the overpressure that is exerted on the membrane and of the second and fourth modes are shown, respectively. However, dynamic stability cannot predict the energy transfer to the fourth mode, as this is captured by the numerical simulation. It must be noticed that as the imposed frequency decreases the critical overpressure above which static buckling occurs tends to coincide with the $P'_{Crit,M}$. It must be stressed that the simulation stopped because a certain type of instability appeared near the equatorial plane. This was a recurring theme in the dynamic simulations of contrast agents conducted in the present study. It is always accompanied by an increase in the transverse shear tension q and growth of short waves, figure VI.12(e). Simulations have to stop because of

increased stiffness of the problem that would require an excessively small time step⁶¹ in order to capture further shell deformation. Besides the numerical aspect, growth of the transverse shear q results in break-up of the membrane beyond a certain limit that is normally a physical constant of the material known from material testing experiments¹¹⁹ and is incorporated in certain criteria predicting material failure. In that sense the very large values predicted for transverse shear, q , indicate break-up of the membrane as a result of increased deformation. As was mentioned above, this type of behavior is systematically captured by the simulations conducted here. However, its predictive validity is limited by the choice constitutive law for bending moments and the bending measures for strain. The latter is only valid for small deviations from the initial curvature. Incorporating a more realistic measure of bending strain might alleviate the stiffness of the problem and allow for more deformed shapes to be obtained by the simulations, as is often the case with experimental observations of oscillating contrast agents.



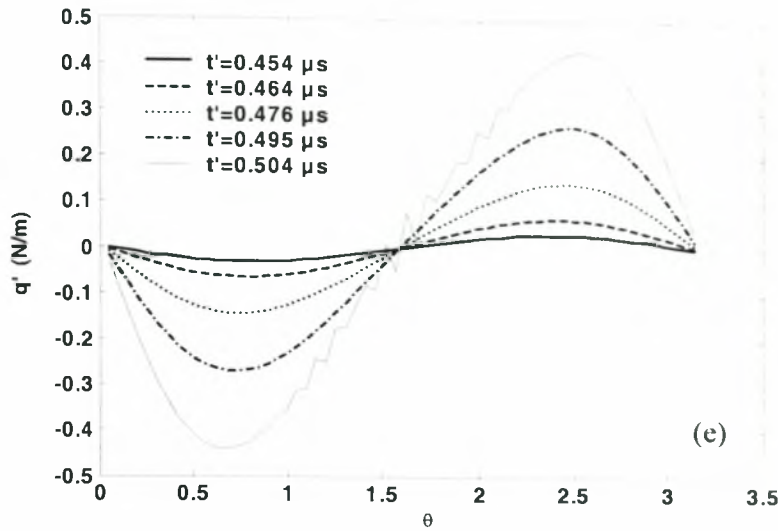


Figure VI.12: The effect of the forcing frequency on the buckling instability. (a) Last microbubble shape from the simulation, (b) numerically obtained shape mode decomposition, (c) time evolution of the $P'_{Overpressure}$ that the shell feels, (d) evolution of bubble radius and shape mode decomposition based on stability analysis, (e) time evolution of the distribution of transverse shear tension q' ; $S=1$, $R_{Eq} = 1.5 \mu m$, $G_s = 590 MPa$, $\delta = 1 nm$, $\mu_s = 1.32 Pa \cdot s$, $k_{Bdim} = 3.45 \cdot 10^{-13} Nm$, $b=0$, $\nu=0.5$, $\rho_l = 998 \frac{kg}{m^3}$, $\mu_l = 0$, $C_i \rightarrow \infty$, $P'_{st} = 101325 Pa$, $\sigma = 0.051 \frac{N}{m}$, $\gamma=1.07$, $\epsilon=33$, $\nu_f = 500 kHz$, far field pressure disturbance: $P'_\infty = P'_{st} [1 + \epsilon \sin(2\pi\nu_f t')]$

VI.5.2.2 PARAMETRIC INSTABILITY

Subharmonic Resonance

If we ignore the experiments shown in figure VI.9 based on reference [112], we can reproduce the optical observations shown in figure VI.7 considering a microbubble with the characteristics of MP1950 but with $G_s = 174 MPa$, $b=1$ and $k_{Bdim} = 1.25 \cdot 10^{-13} Nm$. The cyclic oscillation frequency for the n th mode can then be calculated from equation (VI.77). Thus, the eigenfrequency of the 2nd mode is $\nu_2 = 5.83 MHz$. We impose a sinusoidal pressure perturbation in the far field with $\nu_f = 2\nu_2 = 11.66 MHz$ and amplitude $\epsilon=12$. Figure VI.13(a) shows the evolution of the $P'_{Overpressure}$ exerted on the shell and the static limit for buckling for this microbubble, $P'_{Crit,M} \approx 4.4 \cdot 10^6 Pa$. The evolution of the 2nd mode is also presented, as predicted from dynamic stability analysis, figure VI.13 (b). It can be seen that even though $P'_{Overpressure} < P'_{Crit,M}$ there is a subharmonic parametric instability that appears roughly after 70 periods of oscillation. This is manifested by the fact that a) the instability grows period after period of the oscillation and b) the period of the unstable mode is twice the period of the spherosymmetric pulsation. An other proof of this fact is that the stability of the

periodic solution provides an eigenvalue, μ , with $\text{Im}(\mu) = 0$ and $\text{Re}(\mu) = -1.401 < -1$. Finally, we solved the non-linear dynamic problem and we reasserted this type of instability. This can be seen in figures VI.13(c),(d) where the last shape from the simulation and the shape mode decomposition are presented, respectively. It should also be noted that the simulation had to stop due to the appearance of the type of instability discussed before in relation with the case shown in figure VI.12. In both cases the instability appears, when transverse shear q acquires very large values. Consequently, it must be pointed out that parametric instability can also destroy the microbubble through the development of regions of very high transverse shear that can tear the membrane apart. The latter effect depends on the resistance of the membrane material to the developed internal shear during the deformation.

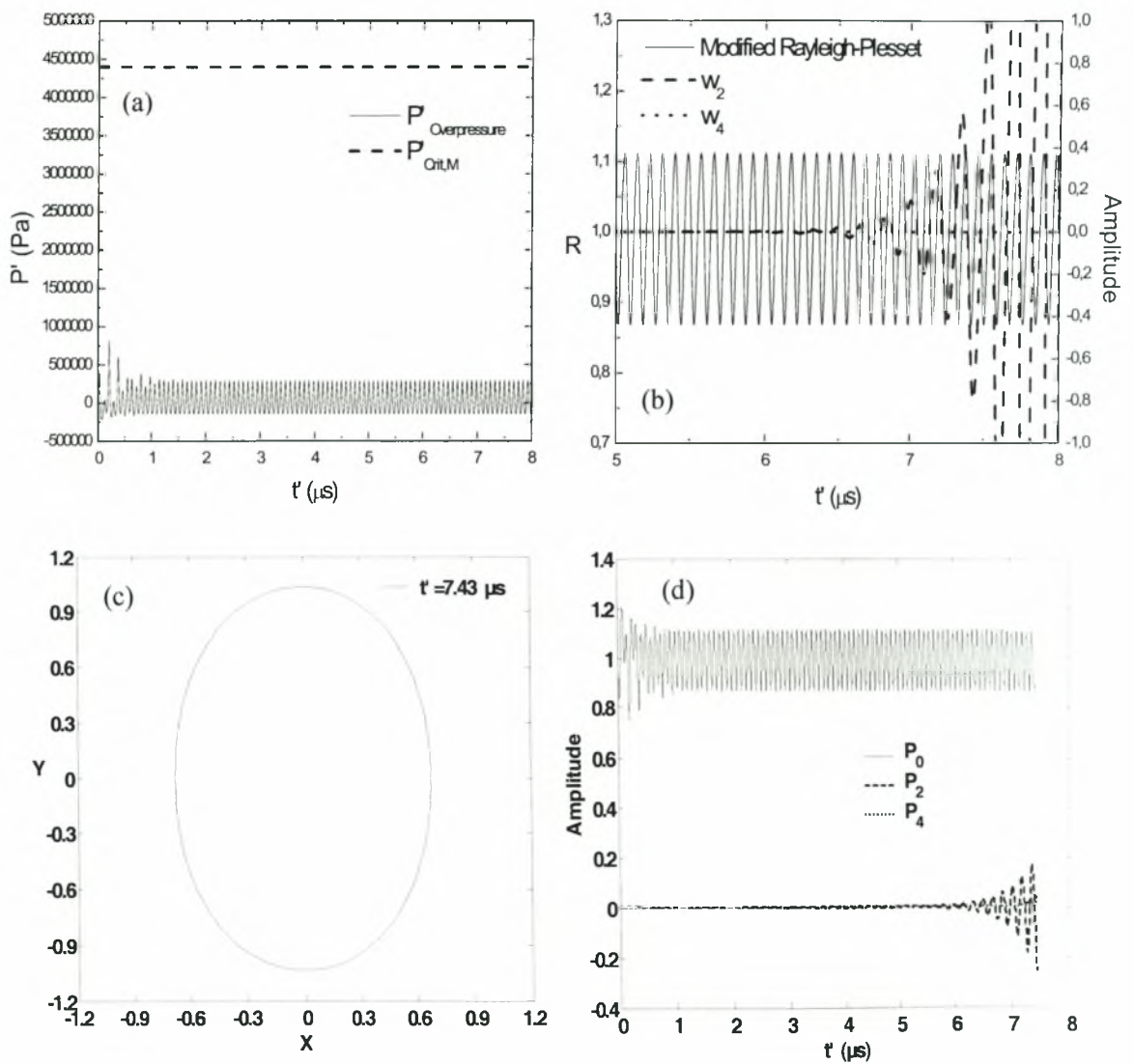


Figure VI.13: Parametric Instability – Subharmonic Resonance during the oscillation of an encapsulated microbubble. (a) Time evolution of the $P'_{Overpressure}$ that the shell feels, (b) evolution of bubble radius and shape mode decomposition based on stability analysis, (c) Last microbubble shape from the simulation, (d) numerically obtained shape mode decomposition; $S=1$, $R_{liq} = 1.5 \mu m$, $G_s = 174 MPa$, $\delta = 1 nm$, $\mu_s = 1.32 Pa \cdot s$, $k_{b, dim} = 1.25 \cdot 10^{-13} Nm$, $b=1$, $\nu=0.5$, $\rho_l = 998 \frac{kg}{m^3}$, $\mu_l = 0$, $C_l \rightarrow \infty$, $P'_{st} = 101325 Pa$, $\sigma = 0.051 \frac{N}{m}$, $\gamma=1.07$, $\varepsilon=12$, $\nu_f = 11.66 MHz$, type of pressure perturbation in the far field: $P'_\infty = P'_{st} [1 + \varepsilon \cos(2\pi\nu_f t')]$

Harmonic Resonance

We consider the microbubble of the previous case and a sinusoidal pressure perturbation in the far field with $\nu_f = \nu_2 = 5.83 MHz$ and amplitude $\varepsilon=6.5$. The $P'_{Overpressure}$ that the shell feels and the static buckling limit are monitored in figure VI.14(a), while the evolution of the microbubble radius and the second mode as predicted by dynamic stability are presented in figure VI.14(b). As can be seen from the latter figure the second mode oscillates with the same period as the forcing frequency. This is a harmonic resonance between the second mode and the forcing frequency. This parametric instability appears after almost 120 periods of microbubble oscillation and it is usually more difficult to be observed experimentally relative to the sub harmonic resonance, since the former evolves on a much longer time scale. Dynamic stability of the periodic solution provides an eigenvalue, $Im(\mu) = 0$ and $Re(\mu) = 1.145 > 1$, corroborating the fact that this is a case of harmonic resonance.

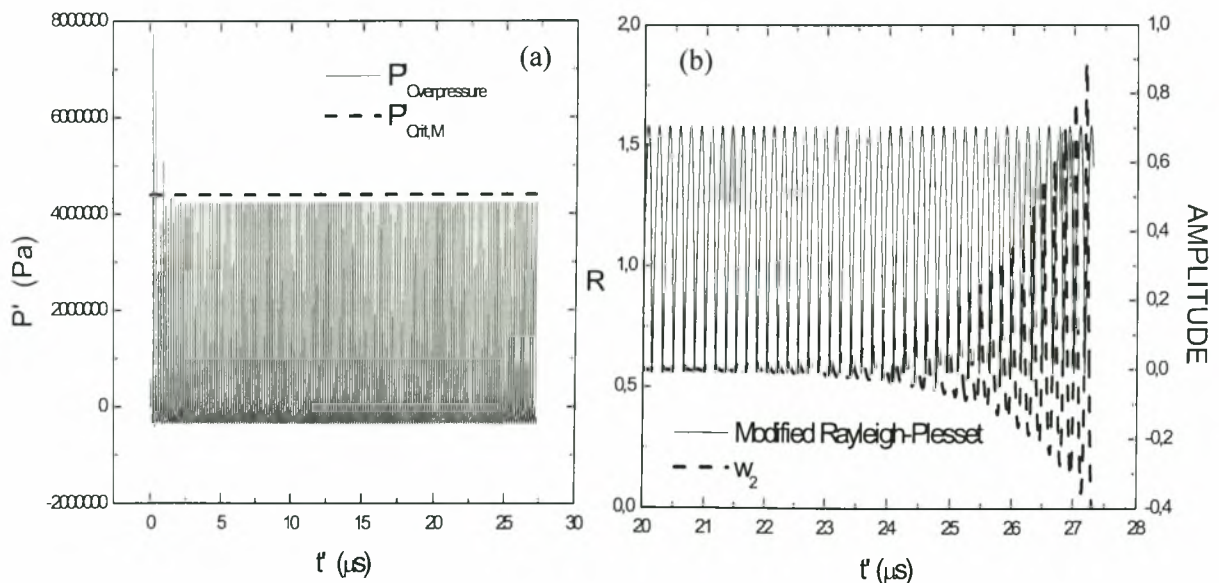
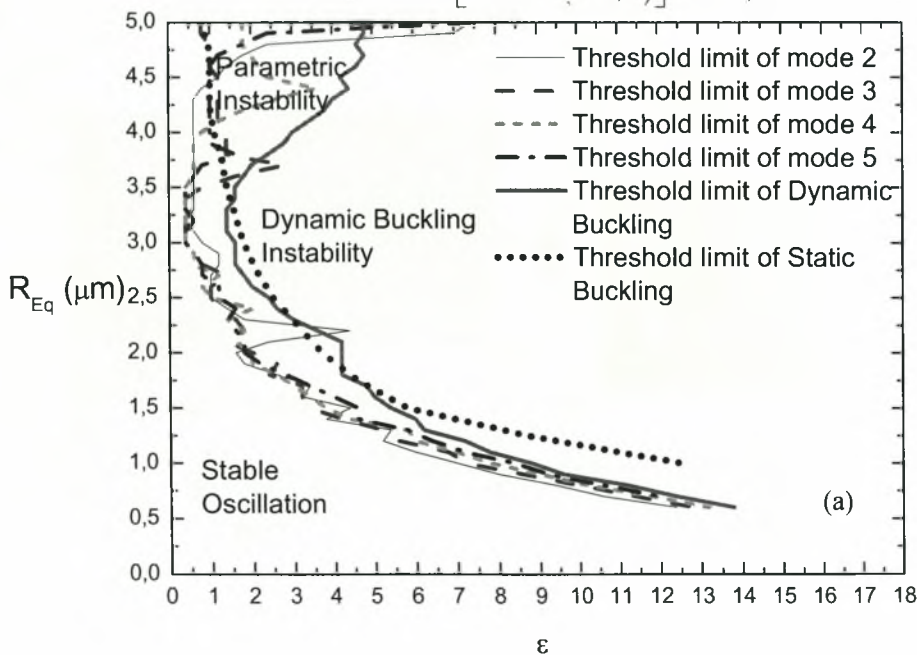


Figure VI.14: Parametric Instability – Harmonic Resonance during the oscillation of an encapsulated microbubble. (a) Time evolution of the $P'_{\text{overpressure}}$ that the shell feels, (b) evolution of bubble radius and shape mode decomposition based on stability analysis; $S=1, R_{\text{Eq}} = 1.5 \mu\text{m}, G_s = 174 \text{ MPa}, \delta = 1 \text{ nm}, \mu_s = 1.32 \text{ Pa}\cdot\text{s}, k_{\text{Bdim}} = 1.25 \cdot 10^{-13} \text{ Nm}, b=1$, $v=0.5, \rho_l = 998 \frac{\text{kg}}{\text{m}^3}, \mu_l = 0, C_l \rightarrow \infty, P'_{st} = 101325 \text{ Pa}, \sigma = 0.051 \frac{\text{N}}{\text{m}}, \gamma=1.07, \varepsilon=6.5, v_f = 5.83 \text{ MHz}$, type of pressure perturbation in the far field: $P'_\infty = P'_{st} [1 + \varepsilon \cos(2\pi v_f t')]$

VI.5.3 PHASE DIAGRAM FOR AN ENCAPSULATED MICROBUBBLE AND THE ONSET OF THE JETTING PHENOMENON

In a manner analogous to the case with free bubbles⁶³, it is possible to construct phase diagrams in the $\varepsilon - R_{\text{Eq}}$ plane for an encapsulated microbubble, and define the regions marking the onset of instability. The criterion for the onset of parametric instability is based on the most unstable eigenvalue, μ , that is provided by the Floquet analysis. If $\text{Im}(\mu) = 0$ and $\text{abs}[\text{Re}(\mu)] > 1$, then the specific mode is parametrically unstable. The criterion that was chosen for the onset of dynamic buckling instability is based on the growth rate of a specific mode during the first two cycles of the imposed frequency. It is adopted based on studies with free bubbles where a mode is expected to dominate the microbubble shape when it reaches the same order of magnitude as the current bubble radius. In figures VI.15 (a),(b) phase diagrams are shown for the MP1950 microbubble with scalar bending modulus $k_{\text{Bdim}} = 3 \cdot 10^{-14} \text{ Nm}$ and $k_{\text{Bdim}} = 1 \cdot 10^{-13} \text{ Nm}$, respectively, when it is insonated with a sinusoidal pressure perturbation in the far field, $P'_\infty = P'_{st} [1 + \varepsilon \cos(2\pi v_f t')]$ with $v_f = 2.4 \text{ MHz}$.



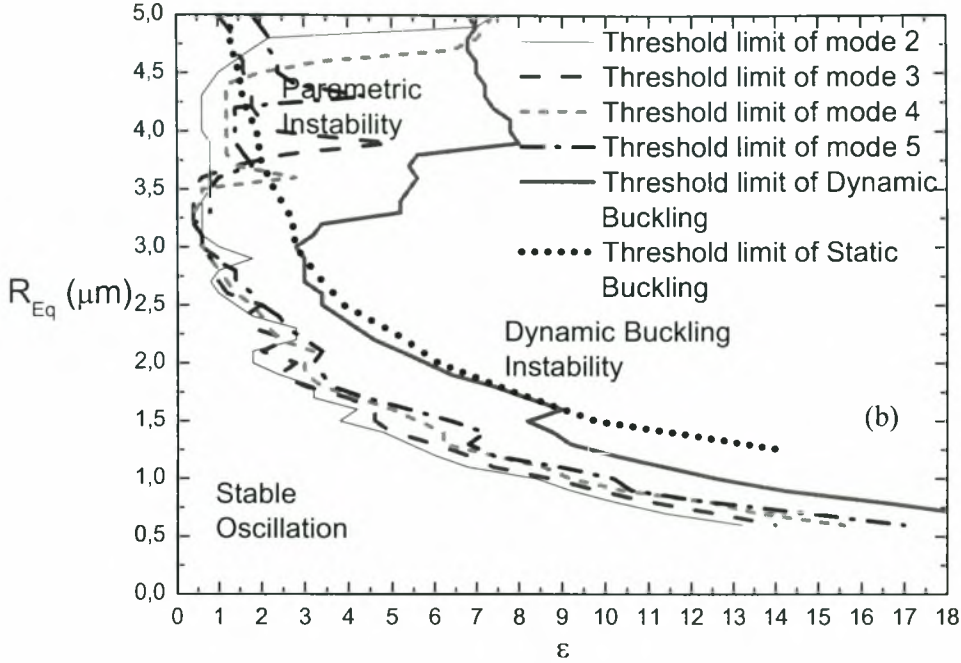


Figure VI.15: Phase diagram for an encapsulated microbubble, MP1950, with scalar bending modulus (a) $k_{B_{dim}} = 3 \cdot 10^{-14} \text{ Nm}$ and (b) $k_{B_{dim}} = 1 \cdot 10^{-13} \text{ Nm}$; $G_s = 520 \text{ MPa}$, $\delta = 1 \text{ nm}$, $\mu_s (\text{sPa}) \cdot \delta (\text{nm}) = 1.34 R_{Eq} (\mu\text{m}) - 0.69$, $b=0$, $\nu=0.5$, $\rho_l = 998 \text{ kg/m}^3$, $\mu_l = 0.001 \text{ Pa} \cdot \text{s}$, $C_l = 1540 \text{ m/s}$, $P'_{st} = 101325 \text{ Pa}$, $\sigma = 0.051 \text{ N/m}$, $\gamma=1.07$, $\nu_f = 2.4 \text{ MHz}$, far field pressure perturbation: $P'_\infty = P'_{st} \left[1 + \varepsilon \cos(2\pi\nu_f t') \right]$

In the above figures, three regions of bubble dynamic behavior can be identified. In the first one the microbubble carries out stable spherosymmetric oscillations and small perturbations on the microbubble interface will be damped. However, the microbubble cohesion can be destroyed via rupture of the membrane, if the developed in plane membrane stresses during the expansion phase of the bubble are such that the material cannot withstand. In the second region where parametric instability prevails, infinitesimal disturbances on the microbubble interface will grow period after period and finally will dominate the microbubble, possibly destroying its cohesion. In the third region, where the dynamic buckling instability dominates, the microbubble is destroyed in the first or second period of the forcing frequency through the dynamic buckling. Observing figures VI.15 (a),(b), it can be surmised that an increase in the scalar bending modulus has as consequence the broadening of the region where parametric instability takes place before dynamic buckling dominates the microbubble dynamics. In addition, the radius corresponding to resonance frequency $\nu_f = 2.4 \text{ MHz}$, is calculated from equation VI.78(a) to be $R_{Eq} \approx 3.2 \mu\text{m}$. This radius almost coincides with the radius for which the external disturbance required for parametric instability to take place is minimized, as can be observed from the above figures. This was expected since on

resonance the dynamic response is very intense. It is also worth noticing that larger microbubbles are more liable to parametric instabilities than smaller ones. The fact that larger microbubbles resonate to smaller frequencies leads to the conclusion that the parametric instability appears more easily above than below resonance. In fact, in the region of small equilibrium radii the instability threshold approaches the static buckling criterion.

It should be pointed out that if the initial interfacial disturbances are quite large then parametric instability could accelerate rupture of the microbubble within only few periods of the oscillation. This of course depends on the size and the kind of the initial interfacial disturbance. Observing the phase diagrams it can be seen that a number of modes are parametrically unstable. However, a significant region of parametric instability is dominated by modes 2 and 3. This, in conjunction with the asymmetry that is introduced when the bubble oscillates close to a solid boundary, indicates that the phenomenon of jetting is mostly observed in regions where the second mode is parametrically unstable. The phenomenon of contrast agent jetting near a solid has been observed experimentally^{114,115,116} and takes place in a similar fashion to the case of free bubbles. Two optical sequences showing jet development in encapsulated microbubbles near a solid are shown in figure VI.16. Figure VI.16(a) shows a microbubble with a radius $R_{eq} = 8.43 \mu\text{m}$ whereas Figure VI.16(b) has been captured 0.33 μs later. Liquid is propelled through the lower left and escapes from the upper right of the bubble. The mean jet velocity was calculated by the authors at about $U_{jet} = 79.4 \text{ m/s}$ and the water hammer pressure at about 60 MPa. Such a jet may penetrate any cell.

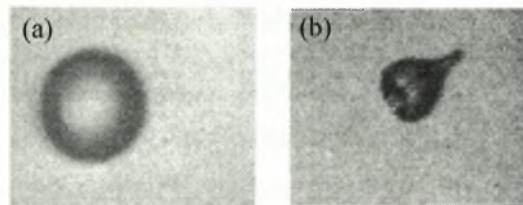
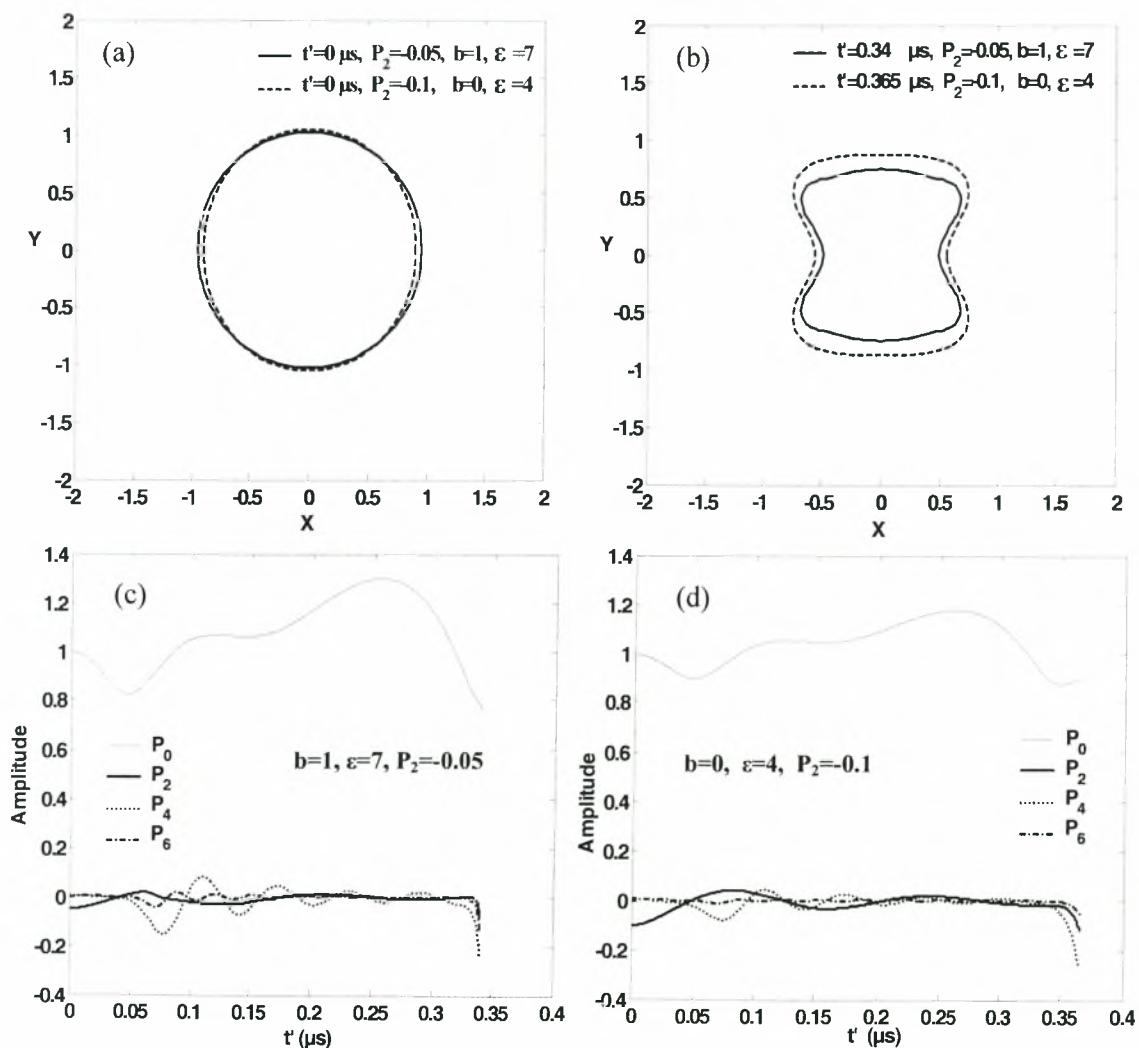


Figure VI.16: Ultrasound jet development in an experimental microbubble (Mechanical Index $MI=1.2$). Each image frame corresponds to a $38 \times 30 \mu\text{m}^2$ area. Interframe time 0.33 μs and exposure time is 10 ns. All the frames are reproduced by [116].

Experimental observations¹¹⁵ of the oscillations of an encapsulated microbubble near a solid boundary reveal 3 regions of microbubble behavior. In the first one, where the amplitude of the external disturbances is below a threshold, the microbubble carries out stable oscillations. In the second region, the microbubble exhibits jet formation and in the third region above a critical threshold the microbubble is destroyed. The three stability regions described previously fit well with these observations, if we consider that the phenomenon of jetting appears in the regions of parametric instability where the second mode is unstable. It was attempted to simulate some cases in the region where the second mode was parametrically unstable with small but finite interfacial perturbation of the second mode and considering the MP1950 microbubble.

Shapes close to the case of jetting were captured when we considered a microbubble with the characteristics of MP1950 but with slightly lower bending modulus, $k_{B_{dim}} = 1.75 \cdot 10^{-14} \text{ Nm}$ for an MR membrane with $b=1$, $\epsilon=7$ and a small initial

perturbation of the second mode, $P_2 = -0.05$. In addition, similar last shape to the previous case was captured for MR membrane with $b=0$, $\varepsilon=4$ and $P_2 = -0.1$. Under these conditions, the second mode is parametrically unstable among others. This is established from the Floquet analysis which predicts an unstable eigenvalue $\text{Im}(\mu) = 0$ and $\text{Re}(\mu) = -2.67$ for the case with $b=1$, $\varepsilon=7$ and $\text{Im}(\mu) = 0$ and $\text{Re}(\mu) = 4$ for the case with $b=0$, $\varepsilon=4$. In both cases, the simulation had to stop due to excessive growth of transverse shear q near the poles. The initial and last shapes from the simulations are shown in figures VI.17(a),(b), while the mode decomposition for the two cases are plotted in figures VI.17(c),(d), respectively. It can be seen that in both cases the most unstable mode is the fourth one. However, the second mode is also present in both cases. These numerical results were verified by stability analysis as it can be seen in figures VI.17(e), (f). In figure VI.17(g) the evolution of the dimensional velocity of the poles for the above two cases is monitored until when the simulations stop. The jet velocity seems quite large and is in the same order of magnitude reported by [116].



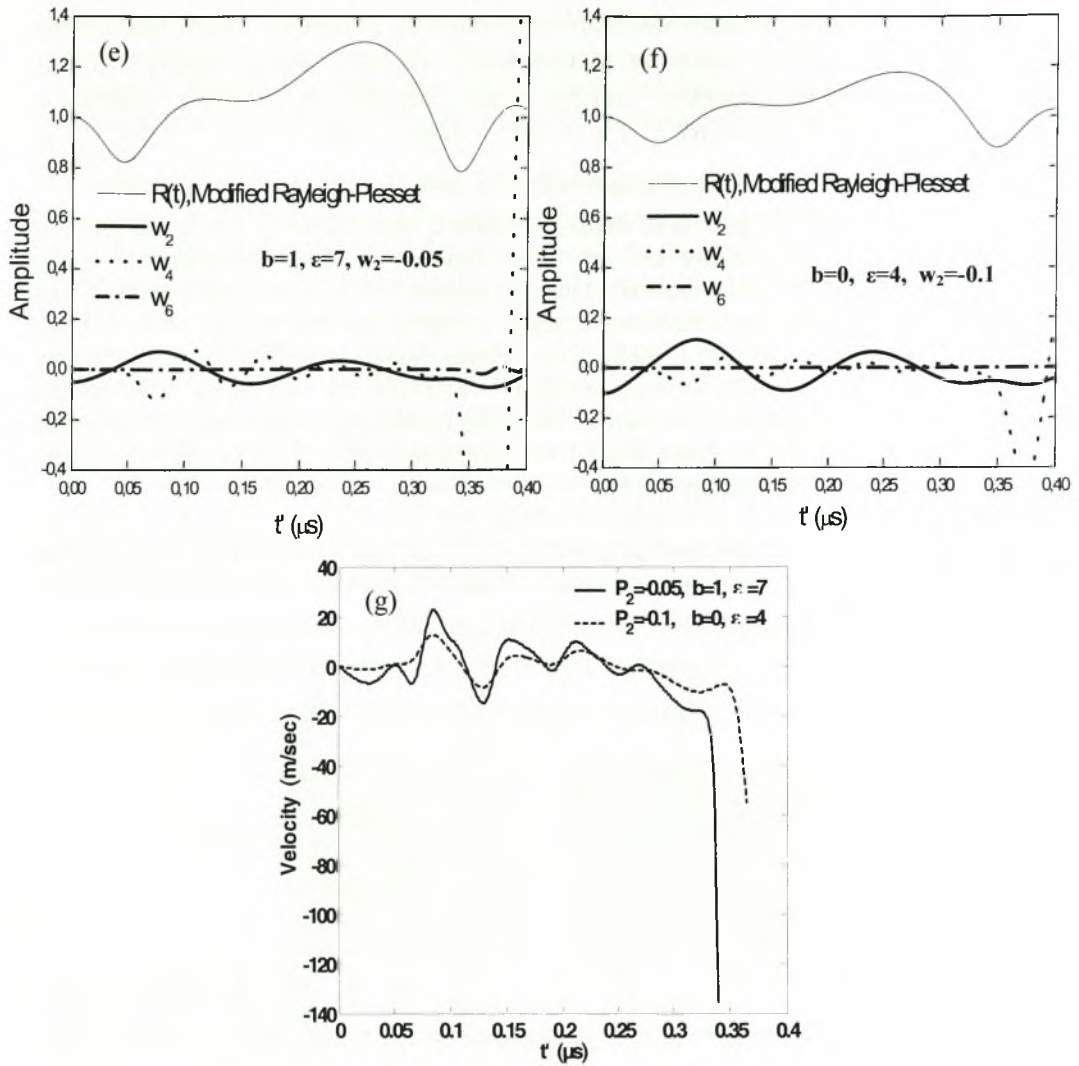


Figure VI.17: Simulation of the oscillation and collapse of the contrast agent following Mooney-Rivlin constitutive law with small initial shape perturbation of the second mode, (a) initial microbubble shapes, (b) microbubble shapes during collapse, (c)-(d) numerically obtained shape mode decomposition for the cases $b=1, \varepsilon=7, P_2=-0.05$ and $b=0, \varepsilon=4, P_2=-0.1$ respectively, (e)-(f) evolution of bubble radius and shape mode decomposition based on stability analysis for the cases $b=1, \varepsilon=7, w_2=-0.05$ and $b=0, \varepsilon=4, w_2=-0.1$, respectively, (g) time evolution of the velocity of the poles for the two cases; $S=1, R_{eq}=1.5 \mu\text{m}, G_s=590 \text{ MPa}, \delta=1 \text{ nm}, \mu_s=1.32 \text{ Pa}\cdot\text{s}, k_{\beta \text{ dim}}=1.75 \cdot 10^{-14} \text{ Nm}, \nu=0.5, \rho_l=998 \frac{\text{kg}}{\text{m}^3}, \mu_l=0, C_l \rightarrow \infty, P'_{st}=101325 \text{ Pa}, \sigma=0.051 \frac{\text{N}}{\text{m}}, \gamma=1.07, \nu_f=2.4 \text{ MHz}$, far field pressure perturbation: $P'_\infty = P'_{st} [1 + \varepsilon \cos(2\pi\nu_f t')]$

Upon reducing the amplitude of the external disturbances to $\varepsilon=5.5$ for the case with $b=1$, $P_2 = -0.05$, the second mode becomes stable while the fourth remains unstable. This has as a result that the fourth mode dominates the dynamics destroying the bubble before a jet is clearly formed. This can be seen in figure VI.18 (a) where the last shape from the simulation is plotted. In figures VI.18 (b),(c) the shape mode decomposition and the respective dynamic stability analysis are shown where it can be seen that the second mode evolves to a significantly lesser extent than the fourth one. Further reduction of the amplitude to $\varepsilon=5$ stabilizes all the modes. This can be seen in figures VI.19 (a),(b) where the mode decomposition is plotted as it is predicted by the numerical simulation and the dynamic stability analysis, respectively.

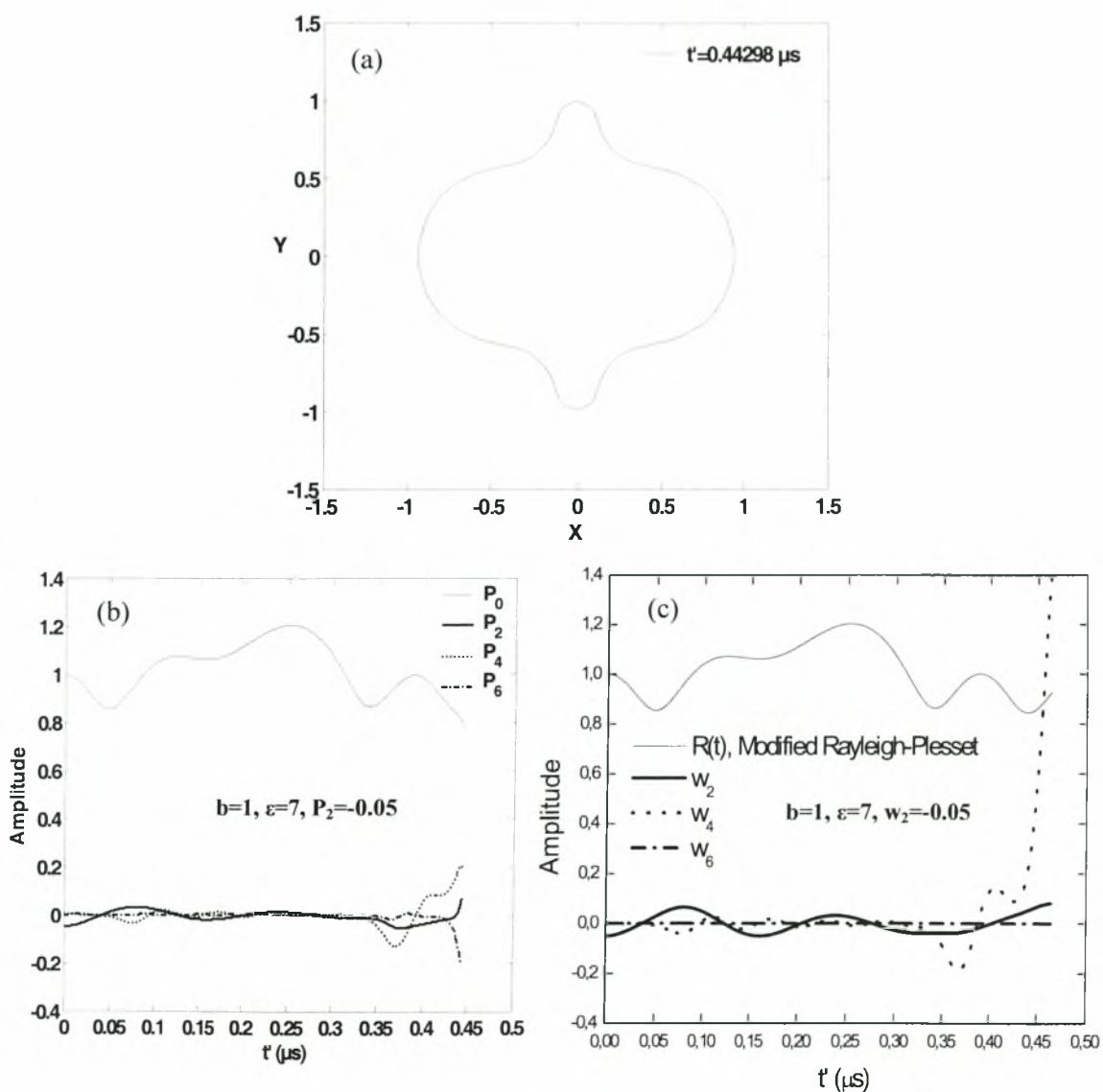


Figure VI.18: Simulation of the oscillation and collapse of the contrast agent following Mooney-Rivlin constitutive law ($b=1$) with small initial shape perturbation of the second mode, $P_2 = -0.05$, (a) microbubble shape during collapse, (b) numerically obtained shape mode decomposition, (c) evolution of bubble radius and shape mode decomposition based on stability analysis; $S=1$, $R_{Eq} = 1.5 \mu m$, $G_s = 590 MPa$, $\delta = 1 nm$, $\mu_s = 1.32 Pa \cdot s$, $k_{Bdim} = 1.75 \cdot 10^{-14} Nm$, $\nu=0.5$, $\rho_l = 998 \frac{kg}{m^3}$, $\mu_l = 0$, $C_l \rightarrow \infty$, $P'_{st} = 101325 Pa$, $\sigma = 0.051 \frac{N}{m}$, $\gamma=1.07$, $\nu_f = 2.4 MHz$, $\epsilon=5.5$, type of pressure perturbation in the far field: $P'_\infty = P'_{st} [1 + \epsilon \cos(2\pi\nu_f t')]$.

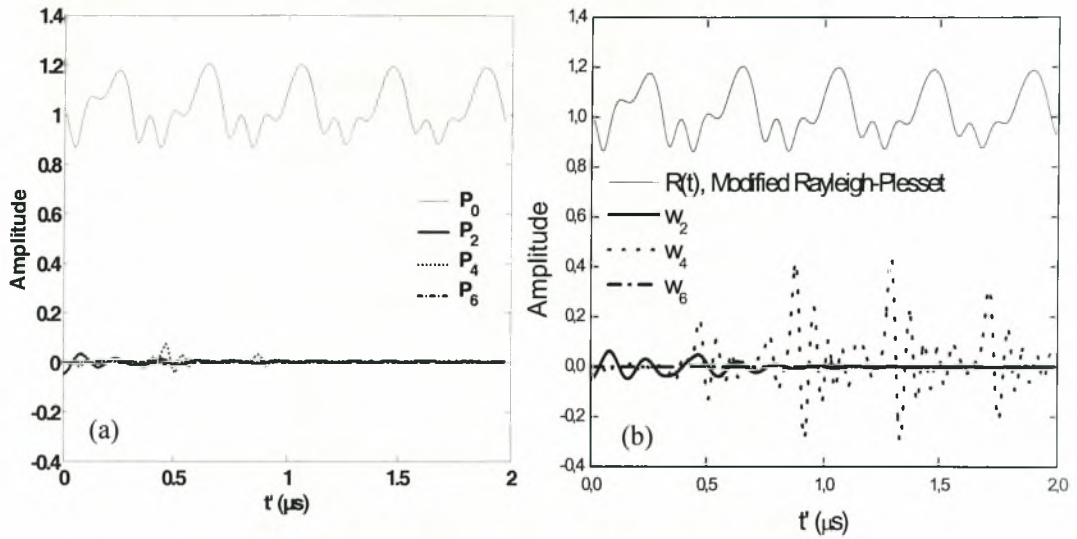


Figure VI.19: Simulation of the oscillation of the contrast agent following Mooney-Rivlin constitutive law ($b=1$) with small initial shape perturbation of the second mode, $P_2 = -0.05$, (a) numerically obtained shape mode decomposition, (b) evolution of bubble radius and shape mode decomposition based on stability analysis; $S=1$, $R_{Eq} = 1.5 \mu m$, $G_s = 590 MPa$, $\delta = 1 nm$, $\mu_s = 1.32 Pa \cdot s$, $k_{Bdim} = 1.75 \cdot 10^{-14} Nm$, $\nu=0.5$, $\rho_l = 998 \frac{kg}{m^3}$, $\mu_l = 0$, $C_l \rightarrow \infty$, $P'_{st} = 101325 Pa$, $\sigma = 0.051 \frac{N}{m}$, $\gamma=1.07$, $\nu_f = 2.4 MHz$, $\epsilon=5$, type of pressure perturbation in the far field: $P'_\infty = P'_{st} [1 + \epsilon \cos(2\pi\nu_f t')]$.

From the above analysis, it is clear that dynamic stability analysis alone cannot predict the conditions under which jet formation takes place since it cannot predict the details of the flow during the late stages of bubble oscillation. Numerical simulations of the axisymmetric model could clearly predict the onset of this phenomenon in several cases. More information about the properties of the shell and the experimental conditions where the jetting exists is necessary in order to obtain a clearer parametric dependence insight of this phenomenon. In the context of the present study, however, as

the shape deformation advanced and regions of large curvature appeared, growth of the transverse shear q rendered the numerical problem very stiff and, consequently, continuing the simulation until the very last stages of jet formation or bubble collapse was not possible.

VI.6 CONCLUSIONS

In this chapter, the dynamic behavior of an axisymmetric encapsulated microbubble was investigated. It was shown that besides the static buckling instability which appears when the forcing frequency is well below the microbubble resonance, there is also the dynamic buckling which prevails at a very fast rate near or above the resonance frequency, rupturing the microbubble due to excessive shear in regions of high curvature. It was also assumed that the material can withstand tensile tensions during the expansion phase of the bubble. Rapture of the membrane during the expansion phase of the microbubble can happen due to the excessive tensile tensions. In order to study this phenomenon, it is only needed to know the resistance of the membrane material to tensile tensions, because at every moment the elastic tensions in the membrane are known during the simulation.

In the same context, it was also shown that the mechanism behind the fragmentation of a microbubble which is insonated by very large external disturbances is not the Rayleigh-Taylor instability but, most likely, the dynamic buckling instability which is controlled by the scalar bending modulus. The axisymmetric model could predict the limit of overpressure above which buckling occurs, and it seems that it can also predict the number of the fragments that are generated, provided an accurate estimate of the material properties is available along with the proper experimental conditions. If the shell properties are not available from the literature then the present theory provides a reliable means to characterize specific contrast agents based on well designed optical experimental observations. If the scalar bending modulus and the other shell parameters are known, one can construct phase diagrams $\varepsilon - R_{\text{eq}}$ for an encapsulated microbubble and define the regions marking the onset of instability. This was done here for an MP1950 microbubble after establishing the shell properties by applying our theoretical model on the available experimental observations. Three regions of microbubble dynamic behavior were observed in a manner analogous to the case of free bubbles: Stable oscillations, parametric instability and dynamic buckling instability.

In particular, it was shown that parametric instability, which arises for less intensive external disturbances than dynamic buckling and evolves on a much longer time scale, can force an encapsulated microbubble to perform shape oscillations through resonance between the forcing frequency and the frequencies of shape modes. This effect is purely dynamic, it cannot be predicted by static considerations and arises even at low external loads. This was shown in the context of dynamic stability analysis to non-spherosymmetric disturbances and it was verified also by numerical simulations and the Floquet analysis. Parametric instability normally gives rise to unstable modes of lower order, e.g. P_2 , P_3 etc., than dynamic buckling that, however, also lead to large deformations and transverse shear as time evolves. The latter effect can also destroy the microbubble cohesion in a manner analogous to dynamic buckling, albeit on a longer

time scale. Experimental observations^{112,113,116} also reveal that microbubbles can perform shape oscillations and exhibit jet formation in many cases. In this study it was shown that jet formation is more liable to happen under conditions pertaining to parametric instability where P_2 is unstable. In fact, simulations indicate that P_2 is essential for jets to form and to acquire the speed required for medical applications. In particular, the onset of jet formation was captured by simulating the non linear response of an MP1950 microbubble to an external acoustic disturbance. Simulations could not proceed until the very last stage of jet formation because of the development of regions of large curvature that generated very large values of transverse shear and made the numerical problem very stiff. However, upon reducing the bending modulus a clearer picture of jetting were captured. In order to establish more accurate criteria for microbubble cohesion a more accurate measure of bending strain should be incorporated in the model, one that can accurately accommodate large deviations of the curvature from its value at rest and, consequently, allow for larger deformations to be captured for given bending resistance.

Further investigation with axisymmetric simulations near a solid boundary and simulations introducing 3d perturbations on an oscillating microbubble, are required in order to determine the conditions under which the jetting appears and calculate some characteristics of the jet which are useful for medical applications. Finally, the study of the interaction between a microbubble and a cell can be very useful in the definition of the parameters that determine cell deformation and opening in the method of sonoporation. Previous studies by Pelekasis & Tsamopoulos⁶⁶ on bubble bubble interaction in the presence of acoustic disturbances and by Lac et al.⁵² on the 3d interaction between a capsule and a shear flow will be useful in this direction. These are very interesting topics that are currently under investigation and will be addressed in a future study.

APPENDIX

The fundamental magnitudes of the first order on a surface⁷³, E, F, G, are defined through the derivatives of position vector, \vec{r}_s , along the surface,

$$E = \frac{\partial \vec{r}_s}{\partial s} \cdot \frac{\partial \vec{r}_s}{\partial s}, \quad \vec{t} = E^{1/2} \frac{\partial \vec{r}_s}{\partial s}, \quad G = \frac{\partial \vec{r}_s}{\partial \phi} \cdot \frac{\partial \vec{r}_s}{\partial \phi}, \quad \vec{e}_\phi = G^{1/2} \frac{\partial \vec{r}_s}{\partial \phi}, \quad F = \frac{\partial \vec{r}_s}{\partial s} \cdot \frac{\partial \vec{r}_s}{\partial \phi}. \quad (A1)$$

For a pair of orthogonal surface variables $F=0$ and the metrics along the direction associated with each one of them are defined as,

$$h_t^2 = E, \quad h_\phi^2 = G; \quad (A2)$$

in the case of the axisymmetric shape examined here $h_t = 1, h_\phi = r \sin \theta$. The fundamental quantities of the second order, L, M, N, are defined as⁷³,

$$L = \vec{n} \cdot \frac{\partial^2 \vec{r}_s}{\partial s^2}, \quad N = \vec{n} \cdot \frac{\partial^2 \vec{r}_s}{\partial \phi^2}, \quad M = \vec{n} \cdot \frac{\partial^2 \vec{r}_s}{\partial s \partial \phi}, \quad (A3)$$

with the variables involved in the above expressions bearing the significance ascribed to them in Sec. II.1 They are very important properties of a surface that are essential for the calculation of the derivatives of the unit vectors in its vicinity. In fact, for the axisymmetric surface that is investigated here, $M=0$ and

$$\frac{\partial \vec{t}}{\partial s} = L\vec{n}, \quad \frac{\partial \vec{t}}{\partial \phi} = M\vec{n} + \frac{\partial(r \sin \theta)}{\partial s} \vec{e}_\phi = \frac{\partial(r \sin \theta)}{\partial s} \vec{e}_\phi, \quad \frac{\partial \vec{t}}{\partial n} = 0, \quad (A4)$$

$$\frac{\partial \vec{e}_\phi}{\partial s} = \frac{M}{r \sin \theta} \vec{n} = 0, \quad \frac{\partial \vec{e}_\phi}{\partial \phi} = \frac{N}{r \sin \theta} \vec{n} - \frac{\partial(r \sin \theta)}{\partial s} \vec{t}, \quad \frac{\partial \vec{e}_\phi}{\partial n} = 0, \quad (A5)$$

$$\frac{\partial \vec{n}}{\partial s} = -L\vec{t} - M\vec{e}_\phi = -L\vec{t}, \quad \frac{\partial \vec{n}}{\partial \phi} = -M\vec{t} - \frac{N}{r \sin \theta} \vec{e}_\phi = -\frac{N}{r \sin \theta} \vec{e}_\phi, \quad \frac{\partial \vec{n}}{\partial n} = 0. \quad (A6)$$

In terms of the r and θ coordinates of the surface particles it can be shown that,

$$L = r\theta_s r_{ss} - r^2\theta_s^3 - 2r_s^2\theta_s - rr_s\theta_{ss}, \quad N = r \sin \theta (r_s \cos \theta - r\theta_s \sin \theta) \quad (A7)$$

where subscript s denotes partial differentiation.

In this context, we derive here the expression for shear rate in the above coordinate system:

$$\vec{t} \cdot \underline{\underline{\tau}} \cdot \vec{n} = \frac{1}{2} (\vec{t} \cdot \nabla \vec{u} \cdot \vec{n}) + \frac{1}{2} (\vec{n} \cdot \nabla \vec{u} \cdot \vec{t}) + \frac{1}{2} (\vec{t} \cdot \nabla \vec{U} \cdot \vec{n}) + \frac{1}{2} (\vec{n} \cdot \nabla \vec{U} \cdot \vec{t}) \quad (A8)$$

$$\vec{t} \cdot \nabla \vec{u} \cdot \vec{n} = \frac{\partial}{\partial s} (u_t \vec{t} + u_n \vec{n}) \cdot \vec{n} = \left(\frac{\partial u_t}{\partial s} \vec{t} + u_t \frac{\partial \vec{t}}{\partial s} + \frac{\partial u_n}{\partial s} \vec{n} + u_n \frac{\partial \vec{n}}{\partial s} \right) \cdot \vec{n} = \quad (A9)$$

$$\left(\frac{\partial u_t}{\partial s} \vec{t} + Lu_t \vec{n} + \frac{\partial u_n}{\partial s} \vec{n} - Lu_n \vec{t} \right) \cdot \vec{n} = Lu_t + \frac{\partial u_n}{\partial s}$$

$$\vec{n} \cdot \nabla \vec{u} \cdot \vec{t} = \frac{\partial}{\partial n} (u_t \vec{t} + u_n \vec{n}) \cdot \vec{t} = \left(\frac{\partial u_t}{\partial n} \vec{t} + u_t \frac{\partial \vec{t}}{\partial n} + \frac{\partial u_n}{\partial n} \vec{n} + u_n \frac{\partial \vec{n}}{\partial n} \right) \cdot \vec{t} = \quad (A10)$$

$$= \left(\frac{\partial u_t}{\partial n} \vec{t} + \frac{\partial u_n}{\partial n} \vec{n} \right) \cdot \vec{t} = \frac{\partial u_t}{\partial n}.$$

But, from irrotationality we can show that the final expressions of (A8) and (A9) are equal. As a result of this, since these expressions take exactly the same form for the vortical velocity field, the dominant contribution to the shear rate from the rotational

part of the velocity field comes from the normal derivative of its tangential component, $\frac{\partial U_t}{\partial n}$, and the condition of vanishing shear at the interface reads

$$\frac{\partial U_t}{\partial n} = -2 \frac{\partial u_t}{\partial n} = -2 \left(L u_t + \frac{\partial u_n}{\partial s} \right) = -2 \left(L \frac{\partial \Phi}{\partial s} + \frac{\partial^2 \Phi}{\partial s \partial n} \right). \quad (\text{A11})$$

In this fashion proceed all the derivations pertaining to the boundary layer equations that are valid in the vicinity of the bubble and that were presented in the previous sections. Relationships like the one shown in (A11) are very useful for the numerical calculations as well since they allow us to circumvent evaluation of normal derivatives such as $\frac{\partial u_t}{\partial n}$ that cannot be calculated solely based on surface variables; the only normal derivative that is calculated directly is that of the scalar potential Φ through the boundary integral equation (II.26). The same question can be raised for the normal derivative

$$\frac{\partial u_n}{\partial n} = \frac{\partial^2 \Phi}{\partial n^2} = \bar{\mathbf{n}} \cdot \bar{\nabla} \bar{\mathbf{u}} \cdot \bar{\mathbf{n}} \quad (\text{A12})$$

appearing in the normal force balance, Eq. (II.43), and the energy balance, Eq. (II.48). However, evaluation of continuity, in a fashion similar to the one shown above for the zero shear stress condition on the interface, gives

$$\frac{\partial u_n}{\partial n} = u_n \left(L + \frac{N}{r^2 \sin^2 \theta} \right) - \frac{1}{r \sin \theta} \frac{\partial}{\partial s} (u_t r \sin \theta), \quad (\text{A13})$$

which is much easier to evaluate, based on the numerical solution of the evolution equations (II.43) and (II.44) that produce variables as a function of arc-length s along the generating curve of the bubble's surface.

Finally, we want to point out the compatibility between the dissipative term appearing in the energy balance in Eq. (II.48), the one that involves the term

$$-\frac{2}{\text{Re}} u_n \frac{\partial u_n}{\partial n}$$

Lamb¹²⁰, for a moving surface at large Re , involving the terms $-\mu \frac{dq'^2}{dn}$ and

$2\mu \bar{\mathbf{n}} \cdot (\bar{\mathbf{u}}' \times \bar{\boldsymbol{\omega}}')$ in the integrand; in Lamb's notation q' is the magnitude of the velocity at the interface and $\bar{\boldsymbol{\omega}}'$ the vorticity. Making things dimensionless, the terms in Lamb's

formula become, $-\frac{1}{\text{Re}} \frac{\partial q^2}{\partial n} + \frac{1}{\text{Re}} \bar{\mathbf{n}} \cdot (\bar{\mathbf{u}} \times \bar{\boldsymbol{\omega}})$. Then, on introducing the decomposition

employed here we have,

$$-\frac{\partial q^2}{\partial n} = -\frac{\partial \left[(u_t + U_t)^2 + (u_n + U_n)^2 \right]}{\partial n} = \quad (\text{A14})$$

$$= -2u_t \frac{\partial u_t}{\partial n} - 2u_n \frac{\partial u_n}{\partial n} - 2 \frac{\partial (u_t U_t)}{\partial n} - 2 \frac{\partial (u_n U_n)}{\partial n}$$

Dropping terms that are lower than order 1 in (A14) we get

$$-\frac{\partial q^2}{\partial n} \approx -2u_t \frac{\partial u_t}{\partial n} - 2u_n \frac{\partial u_n}{\partial n} - 2u_t \frac{\partial U_t}{\partial n}. \quad (\text{A15})$$

By taking the outer product $\bar{\nabla} \times \bar{\mathbf{U}} = \bar{\boldsymbol{\omega}}$ we can show that

$$\vec{\omega} \approx \frac{\partial U_t}{\partial n} \vec{e}_\phi \quad (\text{A16})$$

in the boundary layer and subsequently that,

$$\vec{n} \cdot (\vec{u} \times \vec{\omega}) = u_t \frac{\partial U_t}{\partial n} \quad (\text{A17})$$

However as was shown above, $\frac{\partial U_t}{\partial n} = -2 \frac{\partial u_t}{\partial n}$ for a shear free surface, which when introduced in the above expressions gives

$$-\frac{1}{\text{Re}} \frac{\partial q^2}{\partial n} + \frac{2}{\text{Re}} \vec{n} \cdot (\vec{u} \times \vec{\omega}) = -\frac{2}{\text{Re}} u_n \frac{\partial u_n}{\partial n}. \quad (\text{A18})$$

REFERENCES

1. J. W. Strutt (Lord Rayleigh), *Philos. Mag.* **34**, 94 (1917).
2. C. E. Brennen, *Cavitation and Bubble Dynamics*, Oxford U. Press, New York (1995).
3. L. Guerri, G. Lucca & A. Prosperetti, "A numerical method for the dynamics of non-spherical cavitation bubbles", In D.H. LeCroisette (ed.) proceedings of the 2nd International Colloquium on Drops and Bubbles. Pasadena (CA): Jet Propulsion Laboratory (Publ. 82-7), 175-181 (1982).
4. J. R. Blake, B.B. Taib & G. Doherty, "Transient cavities near boundaries. Part 1. Rigid boundary", *J. Fluid Mech.* **170**, 479-497 (1986).
5. Y. Tomita & A. Shima, "Mechanisms of impulsive pressure generation and damage pit formation by bubble collapse", *J. Fluid Mech.* **169**, 535-564 (1986).
6. A. Philipp, & W. Lauterborn, "Cavitation erosion by single laser-produced bubbles," *J. Fluid Mech.* **361**, 75-116 (1998).
7. A. Pearson, J.R. Blake & S.R. Otto, "Jets in bubbles", *Journal of Engineering Mechanics* **48**, 391-412 (2004).
8. O. Lindau & W. Lauterborn, "Cinematographic observation of the collapse and rebound of a laser-produced cavitation bubble near a wall", *J. Fluid Mech.* **479**, 327-348 (2003).
9. F. D. Gaitan, L. A. Crum, C. C. Church & R. A. Roy, "Sonoluminescence and bubble dynamics for a single, stable, cavitation bubble," *J. Acoust. Soc. Am.* **91**, 3166-3183 (1992).
10. W. Lauterborn (ed.) *Cavitation and inhomogeneities in underwater acoustics*. Berlin: Springer (1980).
11. C. D. Ohl, O. Lindau & W. Lauterborn, "Luminescence from spherically and aspherically collapsing laser bubbles," *Phys. Rev. Lett.* **80**(2), 393-396 (1998).
12. R. Geisler, "Untersuchungen zur Laserinduzierten Kavitation mit Nanosekunden – Femtosekundenlasern," Ph.D Thesis submitted to the University of Goettingen (2004).
13. C. D. Ohl, T. Kurz, R. Geisler, O. Lindau & W. Lauterborn, "Bubble dynamics, shock waves and sonoluminescence," *Phil. Trans. R. Soc. Lond. A*, **357**, 269-294 (1999).
14. T. B. Benjamin & A. T. Ellis, "The collapse of cavitation bubbles and the pressures thereby produced against solid boundaries." *Phil. Trans. R. Soc. A*. **260**, 221- (1966).
15. J.R. Blake, M.C. Hooton, P.B. Robinson, & R.P Tong, 'Collapsing cavities, toroidal bubbles and jet impact,' *Phil. Trans. R. Soc. Lond. A*. **355**, 537-550 (1997).
16. J. P. Best "The formation of toroidal bubbles upon the collapse of transient cavities", *J. Fluid Mech.* **251**, 79-107 (1993).
17. A. Prosperetti, "A new mechanism for sonoluminescence", *J. Acoust. Soc. Am.* **101**(4), 2003-2007 (1997).
18. S. Hilgenfeldt, S. Grossmann & D. Lohse, "Sonoluminescence light emission," *Phys. Fluids* **11**(6), 1318-1330 (1999).
19. H. P. Brenner, S. Hilgenfeldt & D. Lohse, "Single-bubble sonoluminescence," *Rev. Mod. Physics* **74**(2), 425-484 (2002).
20. Lepoint T., De Pauw D., Lepoint-Mullie F., Goldman M. & Goldman A., 1997 "Sonoluminescence: An alternative 'electrohydrodynamic' hypothesis," *J. Acoust. Soc. Am.* **101**(4), 2012-2030.

21. Oguz H.N. & Prosperetti A. 1990 'Bubble Entrainment by the Impact of Drops on Liquid Surfaces', *J. Fluid Mechanics* **219**, 143-179.
22. Barber, B. P., Wu, C. C., Lofstedt, R., Roberts, P. H. & Putterman, S. J., 1994, Sensitivity of sonoluminescence to experimental parameters, *Phys. Rev. Lett.* **72**, 1380-1383.
23. Holt, R.G. & Gaitan D. F. 1996 'Observation of stability boundaries in the parameter space of single bubble sonoluminescence', *Phys. Rev. Lett.* **77**(18), 3791-3794.
24. Brenner M.P., Lohse D. & Dupont T.F. 1995 'Bubble shape oscillations and the onset of sonoluminescence' *Phys. Rev. Lett* **75**(5) 954-957.
25. Wu C.C. & Roberts P.H. 1998 'Bubble shape instability and sonoluminescence' *Phys. Lett. A.* **250**, 131-136 (1998).
26. J. Eggers, "Universal pinching of 3D axisymmetric free surface flow," *Phys. Rev. Lett.* **71**, 3458-3460 (1993).
27. D. Leppinen & J. R. Lister, "Capillary pinch-off in inviscid liquids," **15**, 568-578 (2003).
28. E. Klaseboer, J. Ph. Chevaillier, C. Gourdon & O. Masbernat, "Film drainage between colliding drops at constant approach velocity: Experiments and modelling," *J. Colloid Interface Sci.* **229**, 274-285 (2000).
29. D.L. Miller, "A review of the ultrasonic bioeffects of microsonation, gas-body activation, and related cavitation-like phenomena," *Ultrasound Med Biol.* **13**, 443 – 470 (1987).
30. P.N., Burns and H. Becher, "Handbook of Contrast Echocardiography" Springer, Berlin, Germany (2000).
31. K. Wei, A.R. Jayaweera, S. Firoozan, A. Linka, D.M. Skyba and S. Kaul "Quantification of Myocardial blood flow with ultrasound-induced destruction of microbubbles administered as a constant venous infusion," *Circulation* **97**, 473-483 (1998).
32. E.C. Unger, E. Hersh, M. Vannan, T.O. Matsunaga and T. Mc. Creery, "Local drug and gene delivery through microbubbles," **44**, 45-54 (2001).
33. M. Lokhandwalla and B. Sturtevant, "Mechanical haemolysis in shock wave lithotripsy (SWL): I. Analysis of cell deformation due to (SWL) flow fields," *Phys. Med. Biol.* **46**, 413-437 (2001).
34. C.C. Church, "The effects of an elastic solid surface layer on the radial pulsations of gas bubbles," *J Ac Soc Am*; **97** 1510 – 1521 (1995).
35. N. de Jong, R Cornet and C.T.Lancee, "Higher harmonics of vibrating gas-filled microspheres. Part one: simulations," *Ultrasonics* **32** 447 – 453 (1994).
36. P.J.A. Frinking and N. de Jong, "Acoustic modeling of shell-encapsulated gas bubbles," *Ultrasound Med Biol* 1998; **24**: 523 – 533.
37. Prosperetti A., "Thermal effects and damping mechanisms in forced radial oscillations of gas – bubbles in liquids.", *J. Acoust. Soc. Am.* **61**, 17-27 (1977).
38. Sboros V, MacDonald CA, Pye SD, Moran CM, Gomatam J, McDicken WN. The dependence of ultrasound contrast agents backscatter on acoustic pressure: theory versus experiment. *Ultrasonics* 2002; **40**: 579 – 583.
39. Morgan KE, Allen JS, Dayton PA, Chomas JE, Klibanov AL, Ferrara KW. Experimental and theoretical evaluation of microbubble behavior: effect of transmitted phase and bubble size. *IEEE Trans UFFC* 2000; **47**: 1494 – 1509.
40. K. Vokurka, "Comparison of Rayleigh's Herring's and Gilmore's models of gas bubbles," *Acoustica* **59**, 214-219 (1986).

41. Thurston GB. Viscoelastic properties of blood and blood analogs. In *Advanced in hemodynamics and hemorheology*, edited by T. G. Howe (JAI Press, 1996) 1 – 30.
42. D. B. Khismatullin and A. Nadim, “Radial oscillations of encapsulated microbubbles.”, *Phys. Fluids*.**14**, 3534-3556 (2002).
43. M. Postema, A. Bouakaz, M. Versluis and N. de Jong “Ultrasound-induced release from contrast agent microbubbles,” *IEEE Trans. Ultrason. Ferroelect. Freq. Contr.*, **52**(6), 1035-1041 (2005).
44. Hoff, L., Sontum, P.C. & Hovem J.M. 2000 Oscillations of polymeric microbubbles: Effect of the encapsulated shell. *J. Acoust. Soc. Am.* **107**(4), 2272-2280.
45. Edwards, D.A. Brenner, H. & Wasan, D.T. 1991 *Interfacial transport processes and rheology*. Boston: Butterworth-Heinemann.
46. Chatterjee, D. & Sarkar, K. 2003 A Newtonian rheological model for the interface of microbubble contrast agents. *Ultrasound in med. & Biol.* **29**(12), 1749-1757.
47. Sarkar, K. Shi, W.T. Chatterjee, D. & Forsberg, F. 2005 Characterization of ultrasound contrast microbubbles using in vitro experiments and viscous and viscoelastic interface models for encapsulation. *J. Acoust. Soc. Am.* **118**(1), 539-550.
48. R. Skalak, A. Tozeren, R. P. Zarda and S. Chien, “Strain energy function of red blood cell membranes,” *Biophys. J.* **13**, 245-264 (1973).
49. C. Pozrikidis, “The axisymmetric deformation of a red blood cell in uniaxial straining Stokes flow,” *J. Fluid Mech.* **216**, 231-254 (1990).
50. D. Barthès-Biesel, A. Diaz and E. Dhenin, “Effect of constitutive laws for two-dimensional membranes on flow-induced capsule deformation.”, *J. Fluid Mech.***460**, 211-222 (2002).
51. A. Diaz, D. Barthès-Biesel and N. A. Pelekasis, “Effect of membrane viscosity on the dynamic response of an axisymmetric capsule,” *Phys. Fluids*.**13**, (2001).
52. E. Lac, D. Barthes-Biesel, N. Pelekasis, and J. Tsamopoulos, “Spherical capsules in three-dimensional unbounded Stokes flows: effect of the membrane constitutive law and the onset of buckling,” *J. Fluid Mech.* **516**, 303 – 334 (2004).
53. Emelianov, S.Y. Hamilton, M.F. Ilinskii, Y.A. & Zabolotskaya, E. A. 2004 Nonlinear dynamics of a gas bubble in an incompressible elastic medium. *J. Acoust. Soc. Am.* **115**(2), 581-588.
54. Howard Leong-Poi, James Swales, Ananda R. Jayaweera, Jian-Ping Bin, Sanjiv Kaul and Jonathan R. Lindner, “Effect of microbubble exposure to ultrasound on quantitation of myocardial perfusion”. *Echocardiography*, 2005. **22**(6): p. 503-9.
55. Misch, M., T.A. Kalker, and E.H. Korsten, “Contrast echocardiography for pulmonary blood volume quantification”. *IEEE Trans Ultrason Ferroelectr Freq Control*, 2004. **51**(9): p. 1137-47.
56. Forsberg Flemming, Shi William T., Knauer Michael K, Hall Anne L, Vecchio Chris and Bernardi Richard, “Real-time excitation-enhanced ultrasound contrast imaging”. *Ultrason Imaging*, 2005. **27**(2): p. 65-74.
57. Howard Leong-Poi, Jonathan Christiansen, Peter Heppner, Christopher W. Lewis, Alexander L. Klibanov, Sanjiv Kaul, Jonathan R. Lindner, “Assessment of endogenous and therapeutic arteriogenesis by contrast ultrasound molecular imaging of integrin expression”. *Circulation*, 2005. **111**(24): p. 3248-54.
58. Azzdine Y. Ammi, Robin O. Cleveland, Jonathan Mamou, Grace I. Wang, S. Lori Bridal, and William D. O’Brien, Ultrasonic contrast agent shell rupture detected

- by inertial cavitation and rebound signals. *IEEE Trans Ultras Ferro Freq Cont.*, 2006. **53**(1): p. 126-136.
59. Stefanos Theoharis, Florentia Fostira, Andrew George, Martin Blomley. Optison Enhances gene delivery by increasing the uptake of plasmid DNA by cells. The Tenth European Symposium on Ultrasound Contrast Imaging. January 2005
 60. J. B. Keller and M. Miksis, "Bubble oscillations of large amplitude.," *J. Acoust. Soc. Am.* **68**(2), 628-633 (1980)
 61. C. Pozrikidis. Effect of membrane bending stiffness on the deformation of capsules in simple shear flow. *J. Fluid Mech.* (2001), vol.**440**, pp. 269-291
 62. M. S. Plesset. On the stability of fluid flows with spherical symmetry. *Journal Of Applied Physics*. Volume **25**, Number 1, January 1954
 63. S. Hilgenfeldt, D. Lohse & H. P. Brenner, "Phase diagrams for sonoluminescing bubbles," *Physics Fluids* **8**(11), 2608-2626 (1996); **9** 2462(E), (1996).
 64. Timoshenko, S. and Woinowsky-Krieger, S. *Theory of Plates and Shells. McGraw-Hill Companies, 1964*
 65. Zarda, P. R., Chien, S. & Skalak, R. 1997 Elastic deformations of red blood cells. *J. Biomechanics* **10**, 211-221.
 66. N. A. Pelekasis & J. A. Tsamopoulos, "Bjerknes forces between two bubbles. Part 1: Response to a step change in pressure," *J. Fluid Mech.* **254**, 467-499 (1993).
 67. T. S. Lundgren & N. N. Mansour, "Oscillations of drops in zero gravity with weak viscous effects," *J. Fluid Mech.* **194**, 479-510 (1988).
 68. N.A. Pelekasis, A. Gaki, A. Doinikov, and J.A. Tsamopoulos, "Secondary Bjerknes forces between two bubbles and the phenomenon of acoustic streamers," *J. Fluid Mech.* **500**, 313-347 (2004).
 69. Rüdiger Seydel, "From equilibrium to chaos. Practical bifurcation and stability analysis", Elsevier, 1988
 70. James E. Chomas, Paul A. Dayton, Donovan May, and John Allen. Optical observation of contrast agent destruction. *Appl. Phys. Lett.*, Vol. **77**, No. 7, 14 August 2000
 71. G. K. Batchelor, *An introduction to fluid dynamics*, Cambridge University Press, 1967
 72. N. A. Pelekasis, J. A. Tsamopoulos & G. D. Manolis, "A hybrid finite- boundary element method for inviscid flows with free surface," *J. Comp. Phys.* **101**(2), 231-251 (1992).
 73. C. A. Weatherburn, *Differential geometry of three dimensions Vol. I & II*, Cambridge University Press, 1927.
 74. J. M. Boulton-Stone & J. R. Blake, "Gas bubbles bursting at a free surface," *J. Fluid Mech.* **254**, 437-466 (1993).
 75. J. R. Blake and D. C. Gibson, "Cavitation bubbles near boundaries," *Annu. Rev. Fluid Mech.* **19**, 99(1987) .
 76. J. K. Choi and G. L. Chahine, "Noise due to extreme bubble deformation near inception of tip vortex cavitation," *Phys. Fluids* **16**, 2411 (2004).
 77. E. Canot and J.-L. Achard, "An overview of boundary integral formulations for potential flows in fluid-fluid systems," *Arch. Mech.* **43**, 453 (1991)
 78. J. M. Boulton-Stone, "A comparison of boundary integral methods for studying the motion of a two-dimensional bubble in an infinite fluid," *Comput. Methods Appl. Mech. Eng.* **102**, 213 (1993).
 79. A. H. Stroud and D. Secrest, *Gaussian Quadrature Formulas* (Prentice-Hall, Englewood Cliffs, NJ, 1966).

80. C. de Boor, *A Practical Guide to Splines* (Springer-Verlag, New York, 1978).
81. M. Abramowitz and I. A. Stegun, *Handbook of Mathematical Functions* (Dover, New York, 1972).
82. J. C. Lachat and J. O. Watson, *Int. J. Numer. Methods Eng.* **10**, 991 (1976).
83. J. F. Thompson, Z. U. Warsi & W. C. Mastin, *Numerical Grid Generation: Foundations and Applications*, North Holland, 1985.
84. M. Loewenberg & E. J. Hinch, "Numerical simulation of a concentrated suspension in shear flow." *J. Fluid Mech.* **321**, 395-419 (1996).
85. S. Abid and A. K. Chesters, "The drainage and rupture of partially-mobile films between colliding drops at constant approach velocity," *Int. J. Multiphase Flow* **3**, 613 (1994).
86. N. K. McDougald and L. G. Leal, "Numerical study of the oscillations of a non spherical bubble in an inviscid incompressible liquid. Part I: Free oscillations from nonequilibrium initial conditions," *Int. J. Multiphase Flow* **25**, 887 (1999).
87. J.-K. Choi & G. L. Chahine, "Non-spherical bubble behavior in vortex flow fields" *Computational Mechanics* **32**, 281-290 (2003).
88. B. D. Storey & A. J. Szeri, "Water vapor, sonoluminescence and sonochemistry," *Proc. R. Soc. London, Ser. A.* **456**, 1685-1709 (2000).
89. A. J. Szeri, B. D. Storey, A. P. Pearson & J. R. Blake, "Heat and mass transfer during the violent collapse of nonspherical bubbles," *Phys. Fluids* **15**(9), 2576-2586 (2003).
90. Crum, L.A. 1980 'Measurements of the growth of air bubbles by rectified diffusion' *J. Acoust. Soc. Am.* **68**, 203-211.
91. Löffstedt, R., Barber, B. P. & Putterman S.J. 1993 'Towards a hydrodynamic theory of sonoluminescence' *Phys. Fluids A* **5**, 2911-2928.
92. Storey, B.D. 2001 'Shape stability of sonoluminescence bubbles: Comparison of theory to experiments' *Phys. Rev. E* **64** 017301, 1-3.
93. A. Prosperetti and A. Lezzi, "Bubble dynamics in a compressible liquid, Part I. First-order theory," *J. Fluid Mech.* **168**, 457-478 (1986).
94. C. Herring, "Theory of the pulsations of the gas bubble produced by an underwater explosion," OSRD Rep. No. **236** (1941).
95. F. R. Gilmore, "The collapse and growth of a spherical bubble in a viscous compressible liquid," California Institute of Technology Hydrodynamics Laboratory, Rep. No. 26-4 (1952).
96. C. Pozrikidis, "Boundary Integral and Singularity Methods for Linearized Viscous Flow," Cambridge University Press, Cambridge, 1992.
97. D. Barthes-Biesel and J. M. Rallison, "The time dependent deformation of a capsule freely suspended in a linear shear flow," *J. Fluid Mech.* **113**, 251-267 (1981).
98. A. E. Green and W. Zerna, *Theoretical Elasticity*, Dover Publications, New York, 2002.
99. S. Hilgenfeldt and D. Lohse, "The acoustics of diagnostic microbubbles: dissipative effects and heat deposition," *Ultrasonics* **38**, 99-104 (2000).
100. J. M. Gorce, M. Arditi, and M. Schneider, "Influence of Bubble Size Distribution on the Echogenicity of Ultrasound Contrast Agents. A Study of SonoVue™," *Investigative Radiology*, **35**, 661-671 (2000).
101. De Jong, N. & Hoff, L. 1993 Ultrasound scattering of Albunex® microspheres *Ultrasonics*, **31** 175-.
102. D. Cosgrove, "Echo enhancers and ultrasound imaging," *Eur. J. Radiol* **26**, 64-76 (1997)

103. Tsamopoulos, J. A. & Brown, R. A. 1983. Nonlinear oscillations of inviscid drops and bubbles. *J. Fluid Mech.* **127**, 519-537.
104. Hilgenfeldt, S., Lohse, D. & Zomack, M. 1998. Response of bubbles to diagnostic ultrasound: a unifying theoretical approach. *Eur. Phys. J. B.* **4**, 247-255.
105. P. N. Burns, D. H. Simpson and M. Averkiou, "Nonlinear imaging," *Ultrasound Med. Biol.* **26** S19 (2000).
106. K. W. Commander and A. Prosperetti, "Linear pressure waves in bubbly liquids: Comparison between theory and experiments," *J. Acoust. Soc. Am.* **85** 732-746 (1989).
107. J.J. Deng, B.D. Viers, A.R. Esker, J.W. Anseth and G.G. Fuller, "Phase behavior and viscoelastic properties of trisilanolcyclohexyl-POSS at the air/water interface," *Langmuir* **21**(6), 2375-2385 (2005).
108. Steigmann, D. J. Fluid films with curvature elasticity. *Arch. Rat. Mech.* **150**, 127-152.
109. Tatsuzo Koga and Nicholas J. Hoff, "The axisymmetric buckling of initially imperfect complete spherical shells", *Int. J. Solids Structures*, 1969. Vol. **5**, pp. 679 to 697.
110. Carl M. Bender, Steven A. Orszag, "Advanced Mathematical methods for scientists and engineers", Mc Graw-Hill, 1978
111. L. Gary Leal, "Laminar flow and convective transport processes", Butterworth-Heinemann, 1992
112. M. Versluis, S.M. van der Meer, D. Lohse, P. Palanchon, D. Goertz, C.T. Chin, N. de Jong, "Microbubble surface modes", *IEEE Ultrasonics Symposium*, 2004
113. B. Dollet, P. Palanchon, D. Goertz, S. van der Meer, I. Heitman, M. Versluis, N. de Jong and D. Lohse, Surface modes and sound emitted by bubbles in an acoustic field, *Abstracts Vol. 2* pp. 338, *Euromech Fluid Mechanics Conference 6*, June 26-30 2006.
114. Michiel Postema, Annemieke van Wamel, Folkert J. ten Cate, Nico de Jong, "High-speed photography during ultrasound illustrates potential therapeutic applications of microbubbles", *Medical Physics*, Vol. **32**, No. 12, December 2005
115. Shukui Zhao, Katherine W. Ferrara, and Paul A. Dayton, "Asymmetric oscillation of adherent targeted ultrasound contrast agents", *Appl. Phys. Lett.* **87**, 134103 (2005)
116. Michiel Postema, Annemieke Van Wamel, Charles T. Lancee and Nico De Jong, Ultrasound-induced encapsulated microbubble phenomena, *Ultrasound in Med. & Biol.*, Vol. **30**, No. 6, pp. 827-840, 2000
117. Susannah H. Bloch, Mingxi Wan, Paul A. Dayton, and Katherine W. Ferrara, "Optical observation of lipid- and polymer-shelled ultrasound microbubble contrast agents", *Applied Physics Letters*, Volume **84**, Issue 4, pp. 631-633
118. Karen E. Morgan, John S. Allen, James E. Chomas, Paul A. Dayton, Katherine W. Ferrara, "Experimental and Theoretical Analysis of Individual Contrast Agent Behavior", *IEEE Ultrasonics Symposium*, 1999
119. Τσαμασφύρος, 'Μηχανική Παραμορφώσιμων Σωμάτων II', Εκδόσεις Συμμετρία, 1991
120. H. Lamb, *Hydrodynamics*, Cambridge University Press, Cambridge, 1932.



ΠΑΝΕΠΙΣΤΗΜΙΟ
ΘΕΣΣΑΛΙΑΣ



00400008584 1